

Optimal Dynamic Operation of Power to Ammonia Processes Joachim Weel Rosbo

PhD Thesis



Optimal Dynamic Operation of Power to Ammonia Processes

PhD Thesis August, 2025

Βv

Joachim Weel Rosbo

Copyright: Reproduction of this publication in whole or in part must include the cus-

tomary bibliographic citation, including author attribution, report title, etc.

Cover photo: Vibeke Hempler, 2012

Published by: DTU, Department of Chemial Engineering, Søltofts Plads, Building 228A,

2800 Kgs. Lyngby Denmark

www.kt.dtu.dk

ISSN: [0000-0000] (electronic version)

ISBN: [000-00-0000-00] (electronic version)

ISSN: [0000-0000] (printed version)

ISBN: [000-00-0000-000-0] (printed version)

Approval

This thesis has been prepared over 3 years at the Process and System Engineering Center, Department of Chemical and Biochemical Engineering, at the Technical University of Denmark, DTU, in fulfillment of the requirements for acquiring a PhD in Chemical and Biochemical Engineering.

The project was funded by DTU and Mission Green Fuels as part of the Dynflex project.

The thesis consists of eleven chapters, including references to the academic articles and contributions prepared during this project, which have been peer-reviewed and published or submitted to scientific journals.

Joachim Weel Rosbo - s164114

01/09/2025

Date

Abstract

The Power-to-Ammonia (PtA) process is widely regarded as a key pathway to decarbonise global ammonia production and enable carbon-free energy storage of renewable power. Ammonia is synthesised from hydrogen and nitrogen via the Haber–Bosch (HB) process, which has traditionally operated under stable conditions to maximise production efficiency. However, the fluctuating nature of renewable energy introduces an entirely new operating regime for HB plants, requiring frequent and rapid load changes. This is particularly challenging because ammonia reactors exhibit highly non-linear dynamics and open-loop instabilities when subjected to such disturbances.

This thesis aims to develop modelling frameworks, optimisation strategies, and control architectures for flexible operation of the HB process in PtA plants, enabling integration with intermittent renewable power.

A dynamic model of a fixed-bed ammonia reactor is developed as the foundation of this work. The model uses a novel efficient formulation of the underlying partial differential algebraic equations, enabling fast simulation compared to traditional methods. The model captures the nonlinear dynamics and complex thermal behaviour of ammonia reactors subjected to variable conditions.

The model was extended to represent an adiabatic quench-cooled reactor (AQCR), incorporating heat exchangers and mixers. Simulations revealed the onset of oscillatory behaviour and extinction phenomena under load disturbances, highlighting the instability risks of flexible operation. Optimisation studies explored the trade-off between conversion efficiency and stability, and a basic control strategy was proposed to maintain safe reactor operation under load ramps of up to 1% per minute.

The analysis was expanded to include two additional industrial reactor configurations: the adiabatic indirect-cooled reactor (AICR) and the internal direct-cooled reactor (IDCR). The three reactor types were compared across an operating range of 30–130% of nominal load. The AICR and IDCR consistently achieved higher conversions than the AQCR and exhibited more favourable dynamic and stability characteristics.

To assess the impact of reactor integration with the synthesis loop, a rigorous dynamic model of the full HB loop is developed, including an AICR, compressors, steam turbines, and flash separators. Steady-state optimisation of the synthesis loop power consumption identified loop pressure as the most influential operating parameter, varying from 220 bar at high load to around 110 bar at low load. However, anti-surge constraints in the main feed compressor were found to limit power efficiency at low load, creating a strong incentive for design improvements.

Building on these findings, the study investigates the synthesis-loop compressor configuration, focusing on designs with multiple parallel compressor trains. The study demonstrates that adding parallel compressors for both feed and recycle compression can significantly reduce power penalties from anti-surge recycling at low load, achieving power reductions of 55%, 74% and 84% for two, three and four parallel compressor trains, respectively. An economic analysis further evaluates the trade-off between added capital cost and operational energy savings, identifying the most cost-effective configurations for flexible PtA operation. Designs with two, three and four compressor trains in parallel all reduced the total cost of the compressor units by about 20% compared to the single-train configuration.

The study investigates the HB synthesis loop for self-optimising variables. Using sensitivity analysis, the study identifies controlled variables that minimise economic loss when

kept constant across the load range. Maintaining constant reactor bed inlet temperatures and H_2/N_2 -ratio results in near-optimal power efficiency, whereas fixed loop pressure causes significant energy penalties at the upper and lower load extremes. These findings support a hybrid control strategy where some variables are controlled to constant set-points across the load range, while the loop pressure is continuously updated through real-time optimisation.

The dynamic behaviour of the full HB synthesis loop is analysed through open-loop simulations for step changes in key manipulated variables, including feed and recycle compressor power and reactor bed split fraction. The simulations reveal strong nonlinear dynamics and significant process interactions across multiple input—output pairs. These insights form the basis for designing a control architecture that provides stable and efficient operation across the full load range.

A control architecture is developed for the HB synthesis loop, combining real-time optimisation with self-optimising control (SOC). Controlled and manipulated variable pairings were determined using relative gain analyses, supported by open-loop dynamic simulations. To reduce interaction between control loops, decoupling strategies were incorporated. Dynamic simulation results show that the proposed control system achieves stable and efficient operation across the entire load range (10–120% of nominal) with accurate tracking of rapid load changes of up to 3% per minute. The self-optimising control strategy maintained energy consumption close to the optimal benchmark, while reducing the need for frequent set-point adjustments, extending equipment lifetime while maintaining high energy efficiency.

Overall, this thesis provides new insights into the dynamic behaviour of ammonia reactors and synthesis loops under renewable-driven operation. It introduces efficient modelling strategies, identifies key optimisation and design trade-offs, and proposes practical control solutions to enable the transition from conventional steady-state plants to future flexible PtA systems.

Resume

Power-to-Ammonia (PtA)-processen fremhæves i stigende grad som en central løsning til at gøre den globale ammoniakproduktion fri fra fossile energikilder og samtidig muliggøre lagring af vedvarende energi i et kulstoffrit brændstof. Ammoniak fremstilles af brint og kvælstof gennem Haber–Bosch (HB)-processen, der traditionelt drives under stabile driftsforhold med fokus på maksimalt udbytte af ammoniak. Når produktionen derimod skal baseres på vind- og solenergi, ændres driften markant, hvor hyppige og hurtige lastændringer er nødvendige. Dette er en udfordring, fordi ammoniak reaktorer udviser komplekse, ulineære dynamikker, som kan medføre ustabil adfærd, hvis driften forstyrres.

Formålet med afhandlingen er at udvikle modeller, optimeringsmetoder og kontrolstrategier, som gør HB-processen fleksibel nok til at kunne integreres i PtA-anlæg drevet af fluktuerende vedvarende energi.

Som fundament udvikles en dynamisk model af en fixed-bed reaktor. Modellen er formuleret på en ny og effektiv måde, så de underliggende differential-algebraiske ligninger kan simuleres væsentligt hurtigere end med traditionelle metoder. Samtidig beskriver modellen nøjagtigt de centrale ulineære og termiske effekter for ammoniakreaktoren.

Denne model udvides til en adiabatisk quench-kølet reaktor (AQCR) med en varmevekslere til forvarmning af reaktorføden med reaktorudstrømningen. Simulationerne viser, at systemet kan udvikle både oscillerende dynamik og risikere slukning ved lastændringer. Optimeringsstudierne demonstrerer afvejningen mellem høj konvertering af reaktanter og stabil drift. En enkel kontrolstrategi foreslås, der kan fastholde stabil drift ved lastændringer op til 1 % pr. minut.

Analysen udvides derefter til to andre reaktordesigns: den adiabatiske indirekte kølede reaktor (AICR) og den internt direkte kølede reaktor (IDCR). De tre reaktor konfigurationer sammenlignes på tværs af et driftsområde fra 30 til 130 % af nominallast. Resultaterne viser, at både AICR og IDCR konsekvent leverer højere konvertering og mere stabil dynamik end AQCR.

For at vurdere reaktorernes samspil med den øvrige proces opstilles en detaljeret dynamisk model af hele Haber-Bosch processen, inklusive en AICR, kompressorer, dampturbiner og separatorer. Stationær optimering af HB-processens strømforbrug viser, at processens tryk er den mest afgørende driftsvariabel og varierer fra ca. 220 bar ved høj last til ca. 110 bar ved lav last. Samtidig viser analyserne, at anti-surge-begrænsninger i fødekompressoren hæmmer effektiviteten ved lav last.

På denne baggrund undersøges forskellige kompressorkonfigurationer med flere parallelle kompressortoge. Det påvises, at parallel kompression markant reducerer de energitab, som anti-surge-recirkulation medfører ved lav last. For to, tre og fire parallelle kompressortoge reduceres kompressorernes elforbrug med henholdsvis 55 %, 74 % og 84 %. En økonomisk analyse viser samtidig, at kapitalomkostningerne i høj grad opvejes af lavere driftsudgifter, og at konfigurationer med flere parallelle kompressorer samlet set reducerer de totale kompressonomkostninger med ca. 20 % i forhold til enkelt-tog design.

Afhandlingen undersøger selv-optimerende kontrol (SOC) for HB-processen. Med sensitivitsanalyser identificeres styrevariable, der kan holdes konstante på tværs af lastområdet uden at forårsage store økonomiske tab. Det gælder især reaktorindløbstemperaturerne og H₂/N₂-forholdet, som giver tæt på optimal energieffektivitet, når de holdes konstante over lastområdet. Omvendt medfører konstant tryk markante energitab ved lav og høj last. Dette underbygger en hybrid strategi, hvor selv-optimerende kontrol anvendes på udvalgte variable, mens processtrykket optimeres i realtid.

Den dynamiske adfærd af hele HB-processen undersøges gennem åbensløjfe simulationer af stepændringer i nøglevariable såsom kompressoreffekt og splitfraktioner af strømmene i reaktoren. Disse simulationer viser signifikante ulineariteter og stærke procesinteraktioner, hvilket fremhæver de udfordringer, der er forbundet med fleksibel drift. Disse simulationer danner grundlaget for udviklingen af en kontrolarkitektur, der kan sikre stabil og energieffektiv drift i hele lastområdet.

Til dette formål udvikles en kontrolarkitektur, der kombinerer realtidsoptimering (RTO) med selv-optimerende kontrol. Valg af styrede- og manipulerede variable baseres på "relative gain"-analyser og open-sløjfe simuleringer. For at reducere interaktion mellem reguleringssløjfer indføres afkoblingsstrategier. Dynamiske simuleringer viser, at det foreslåede system kan sikre stabil drift fra 10 til 120 % last, fastholde energiforbruget tæt på det teoretiske optimum og håndtere hurtige lastændringer på op til 3 % pr. minut. SOC-strategien reducerer samtidig behovet for hyppige setpunktændringer, hvilket forlænger levetiden af kritisk udstyr og opretholder høj energieffektivitet.

Samlet set giver afhandlingen nye indsigter i ammoniakreaktorers og Haber-Bosch processens dynamiske adfærd under drift baseret på vedvarende energikilder. Den introducerer effektive modelleringsstrategier, identificerer centrale optimerings- og design tradeoffs og foreslår praktiske kontrolarkitekturer. Således kan dette studie forhåbentlig hjælpe med at bane vejen fra konventionelle stationære ammoniak anlæg til fremtidens fleksible PtA-systemer.

Acknowledgements

This PhD journey started already during my master's in Chemical Engineering, when I worked on my thesis project under the supervision of John and Jakob. It quickly became clear to me that a PhD would be a unique opportunity, and I am glad that John and Jakob were open to continuing the collaboration with a PhD. When I started the PhD, Anker also joined as a supervisor, adding his expertise on ammonia reactors and catalysts to the team. Thank you all for your invaluable guidance and input. I have truly enjoyed working with you, and our meetings have always been productive, inspiring, and motivating. I am also grateful for the trust and flexibility you showed me, which made it possible for me to pursue my dream of competing in biathlon at the international level alongside my PhD.

I also feel very fortunate to have collaborated with highly experienced and competent people outside DTU. A special thank you to Sigurd from NTNU, Trondheim, for welcoming me to collaborate, providing the necessary resources to make it happen, and hosting me in Trondheim. I learned a lot from you, and your contributions were invaluable in advancing this thesis in the right direction. I am equally grateful for the warm welcome I received during my stay and for the great friends I made in the Process Systems Engineering group.

I am deeply thankful as well for the amazing friends and colleagues at PROSYS. All the social activities, conferences, and daily fun made the PhD three fantastic years! A special thanks goes to my office mates - definitely the fastest and probably the funniest office at DTU.

Finally, to my friends and family: thank you for your continuous support throughout my PhD studies.

Nomenclature

Roman Symbol

```
\bar{H}
         Enthalpy flux [J (m^2 s)^{-1}]
\Delta V
         Finite-volume cell size [m<sup>3</sup>]
\dot{H}
         Enthalpy flow [J s^{-1}]
         Mass flow [kg s^{-1}]
\dot{m}
         Volumetric enthalpy [J m<sup>-3</sup>]
\hat{h}
         Volumetric internal energy [J m<sup>-3</sup>]
\hat{u}
         State vector
X
         Algebraic variable vector
У
\mathcal{G}
         Gibbs energy function
\mathcal{H}
         Enthalpy function
\mathcal{S}
         Entropy function
\mathcal{U}
         Internal energy function
\mathcal{V}
         Volume function
         Chemical potential [J mol<sup>-1</sup>]
\mu
         Cross-sectional area [m<sup>2</sup>]
A_c
         Heat-exchanger area [m<sup>2</sup>]
A_{\mathsf{hex}}
         Concentration [mol m<sup>-3</sup>]
c
         Molar heat capacity [J (mol K)^{-1}]
c_p
F
         Total molar flow [kmol s^{-1}]
         Total Gibbs energy [J]
G
H
         Total enthalpy [J]
l
         Axial spatial coordinate [m]
L_B
         Bed length [m]
         Molar mass [kg mol<sup>-1</sup>]
M
         Molar flux [kmol (m^2 s)^{-1}]
N
         Mole vector [mol]
n
P
         Pressure [bar]
P_{\text{feedcomp}} Feed-compressor power [W]
```

Total Haber-Bosch loop power [W]

P_{loopcomp} Recycle/loop-compressor power [W]

 P_{HB}

```
P_{\mathsf{loop}} Loop pressure [bar]
```

*P*_{rankine} Rankine-cycle power generation [W]

 $P_{\text{refrigeration}}$ Refrigeration power consumption [W]

- q_R Reactor feed split (quench/bypass) [–]
- R Production rate per gas volume [mol $(m^3 s)^{-1}$]
- S Total entropy [J K^{-1}]
- T Temperature [K]
- t Time [s]
- U Total internal energy [J]
- U_{hex} Overall heat-transfer coefficient [W (m² K)⁻¹]
- v Interstitial gas velocity [m s⁻¹]
- V_B Bed volume [m³]
- V_R Reactor volume [m³]
- *x* Mole fraction [–]

Greek symbols

- α Catalyst activity factor [–]
- α_v Valve opening coefficient [–]
- ϵ Heat-exchanger effectiveness [–]
- ϵ_B Bed void fraction [–]
- η Dynamic viscosity [Pa s]
- η_{rankine} Rankine-cycle efficiency [–]
- η_S Compressor isentropic efficiency [–]
- ρ Density [kg m⁻³]

Superscripts

- g Gas phase
- l Liquid phase
- n Time step index
- s Solid phase

Subscripts

- c Cold stream
- f Make-up feed
- h Hot stream
- Species index
- in Inlet

k Cell index (axial discretisation)

out Outlet

R Reactor (combined gas and solid)

Rf Reactor feed

S Process stream index

sep Separator

Abbreviations

AICR Adiabatic Indirect-Cooled Reactor

AQCR Adiabatic Quench-Cooled Reactor

ASU Air Separation Unit

BMC Bare Module Cost

CAPEX Capital Expenditures

CF Capacity Factor

COP Coefficient of Performance

DAE Differential-Algebraic Equation

EB Energy Balance

EOS Equation of State

HB Haber-Bosch

HL Hydrogen Load

IDCR Internal Direct-Cooled Reactor

MB Material Balance

NTU Number of Transfer Units

OPEX Operating Expenditures

P2A Power-to-Ammonia

P2X Power-to-X

PDAE Partial Differential-Algebraic Equation

RTO Real-Time Optimisation

SOC Self-Optimising Control

Contents

	Preface	ii
No	omenclature	vii
1	Thesis overview 1.1 Motivation	5
2	Background & Literature Study 2.1 Ammonia production 2.2 Power-to-Ammonia 2.3 Ammonia applications 2.4 Investments in PtA 2.5 Ammonia reactor types 2.6 Reactor modelling and simulation 2.7 Reactor optimisation 2.8 Conventional control structure design for the ammonia process 2.9 Scheduling, Design and Economics of the PtA plants 2.10 Flexible operation of Haber-Bosch process	11 12 13 14 14 15 17
3	Catalytic bed model 3.1 Introduction 3.2 Thermodynamics 3.3 Catalytic fixed-bed model 3.4 Numerical solutions 3.5 The simulation case 3.6 Results: Steady-State 3.7 Results: Dynamic analysis 3.8 Discussion 3.9 Conclusion	22 24 27 30 30 31 37
4	Adiabatic Quench Cooled Reactor for Power-to-Ammonia 4.1 Introduction 4.2 AQCR model 4.3 The case study 4.4 Results: Reactor system (Boundary 1) 4.5 Results: Synthesis loop (Boundary 2) 4.6 Dynamic control for flexible operation 4.7 Discussion 4.8 Conclusion	40 43 44 50 56 59
5	Reactor comparison and design for Power-to-Ammonia	65

	5.2	Reactor models	
	5.3	The Case Study: Ammonia reactors in 100 MW PtA plant	. 70
	5.4	Reactor optimisation and heat transfer design for PtA	. 72
	5.5	Steady state and stability comparison	
	5.6	Open loop transient simulations of the reactors	. 82
	5.7	Reactor optimisation across the operating window	. 86
	5.8	Discussion	. 94
	5.9	Conclusion	. 96
6		elling and optimisation of a Haber-Bosch synthesis loop for Power-	
		nonia	99
	6.1	Introduction	
	6.2	Mathematical model for the synthesis loop	
	6.3	The Case Study: 100 MW PtA synthesis loop	
	6.4	Optimisation problem	
	6.5	Optimisation at nominal load	
	6.6 6.7	Optimisation across the operating window	
	0.7	Conclusion	. 113
7	•	em design of compressor structure for PtA operation	115
	7.1	Introduction	
	7.2	Compressors in parallel	
		Economic Comparison	
	7.4	Conclusion	. 121
8		sitivity analysis and self	400
	-	mising variables	123
	8.1 8.2	Introduction	
	8.3	Sensitivity to process disturbances	
	8.4	Self-optimising variables for control	
	8.5	Conclusion	
	0.5		
9	-		137
	9.1	Introduction	
	9.2	Step-responses to manipulated variables	
	9.3	Open-loop load change	
	9.4	Conclusion	. 145
10		trol of a Haber-Bosch synthesis loop for load-flexible operation	147
		Introduction	
		Control architecture design	
		Load-flexible operation	
	10.4	Conclusion	. 158
11		ussion	161
		Operating window	
		Model assumptions	
		Integration with the entire PtA process	
		Process electrification	
	11.5	Next steps toward enabling PtA	166

12	Conclusion	169
Α	Explicit ODE system for the fixed bed	185
В	Steady-State solution method (Newton's Method)	189
С	Derivation of Equation (5.18) in the main manuscript.	191
D	Vapour-Liquid Equilibrium: H ₂ , N ₂ , NH ₃ , Ar	193
Е	Influence of catalyst activity on synthesis loop power	195

Chapter 1

Thesis overview

This chapter provides a general overview of the PhD project, with emphasis on its key contributions. It begins with a brief introduction to the motivation, challenges, and prospects of Power-to-Ammonia (PtA). The project objectives and the overall structure of the thesis are also outlined. Finally, the chapter summarises dissemination activities and highlights the main achievements of the research.

1.1 Motivation

Climate change and greenhouse gas emissions represent some of the most pressing challenges of our time. Rising global temperatures are widely attributed to increasing concentrations of greenhouse gases, particularly carbon dioxide, in the atmosphere. In response, political and international institutions are investing in a coordinated global strategy to reduce emissions. A substantial initiative in this direction is the Paris Agreement, adopted in 2015 by 196 countries responsible for 55% of global carbon emissions. The agreement legally binds the signatories to limit global warming to well below $2\,^{\circ}\text{C}$, preferably $1.5\,^{\circ}\text{C}$, relative to pre-industrial levels (Delbeke et al., 2019).

In alignment with the Paris Agreement, the European Union (EU) has committed to at least a 40% reduction in greenhouse gas emissions by 2030 compared to 1990 levels, and aims to become carbon-neutral by 2050 (European Council, 2014). This target has since been revised upward, with the EU now pursuing a 55% reduction by 2030 (European Union, 2020). These ambitious goals have motivated government-led investments in green technologies to facilitate the decarbonisation of society.

It is widely agreed that renewable energy is at the core of transitioning to a carbon-neutral society, with wind and solar energy predicted to be some of the main energy sources in the future. However, their intermittent nature necessitates robust and scalable energy storage solutions. For long-term storage, chemical energy carriers are considered particularly promising for depositing excess green energy (Liu et al., 2020; MacFarlane et al., 2020). The conversion of renewable electricity into chemical products, commonly referred to as Power-to-X (PtX), enables surplus renewable energy to be stored and utilised in other sectors. Most PtX pathways begin with the generation of hydrogen via water electrolysis using renewable electricity. This green hydrogen is a truly carbon-neutral energy vector, in contrast to carbon-based synthetic fuels (lkäheimo et al., 2018).

Unfortunately, hydrogen as an energy carrier is technically challenging and economically costly due to its low volumetric energy density and high diffusivity in many materials (Verleysen et al., 2021; Fahr et al., 2023). A viable alternative is to convert hydrogen into more stable and energy-dense molecules such as methane (CH₄), methanol (CH₃OH), or ammonia (NH₃). Among these, Power-to-Ammonia (PtA) is especially attractive. Ammonia is carbon-free, has high volumetric energy density, and can be stored as a liquid under moderate conditions (8–10 bar at ambient temperature), making it practical for large-scale storage and transport (Quintero-Masselski et al., 2022; Rouwenhorst and Brown, 2023). Figure 1.1 illustrates the volumetric energy density of a range of fuel options. The figure highlights the clear advantage of chemically based storage compared to battery technologies for large-scale energy storage. Among the carbon-free storage options, ammonia stands out as the most energy-dense carrier, only slightly less energy-dense than methanol. In addition to the lower energy density, hydrogen storage requires either extremely high pressures in the compressed state or energy-intensive cooling for cryogenic liquid storage.

Ammonia is the second most produced chemical globally, with annual production exceeding 180 million tonnes (Kong et al., 2024). Its primary use is in nitrogen-based fertilisers, which support food production for nearly half of the global population (Liu et al., 2020; Nayak-Luke and Bañares-Alcántara, 2020). In addition, ammonia is a precursor for manufacturing plastics, explosives, fabrics, and dyes (Erisman et al., 2008). Virtually all ammonia is synthesised through the Haber–Bosch process, where nitrogen and hydrogen are catalytically converted to ammonia at high temperature (350–500 °C) and pressure (100-250 bar) (Erisman et al., 2008; Rouwenhorst et al., 2021). The conventional pro-

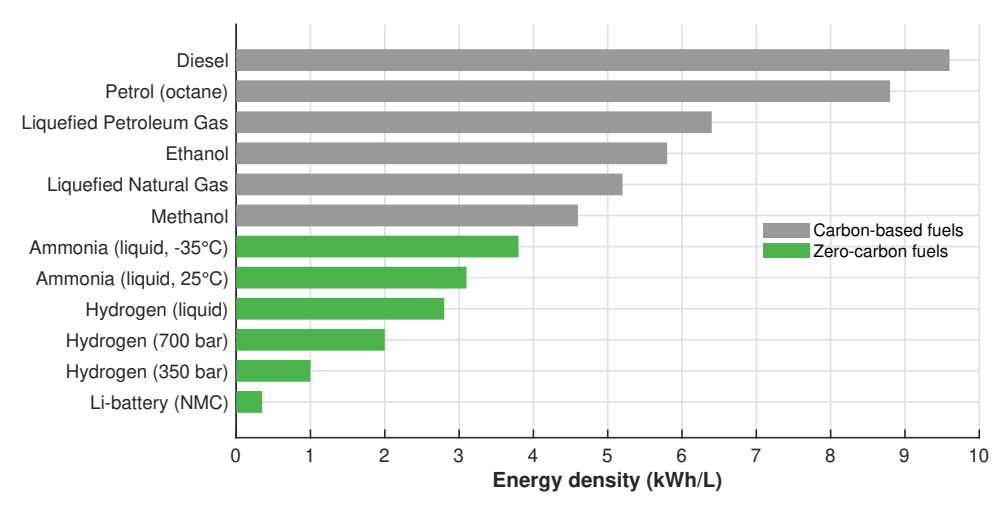


Figure 1.1: The volumetric energy density of a range of fuel options (Bird et al., 2020).

duction of hydrogen via steam-methane reforming is highly energy-intensive. As a result, ammonia synthesis accounts for approximately 2% of global carbon dioxide emissions (Smith et al., 2020).

Therefore, decarbonising ammonia production is essential, not only to reduce the emissions of today's large-scale fertiliser industry but also to enable green ammonia to serve as an energy storage medium and carbon-free fuel for sectors such as maritime transport, where it is considered one of the most promising alternatives to fossil fuels (Al-Aboosi et al., 2021).

Figure 1.2 illustrates the projected growth in global ammonia production capacity up to 2050 as reported in IRENA and AEA (2022). Over this period, the ammonia market is expected to more than triple, with fossil-based production gradually being phased out in favor of renewable pathways.

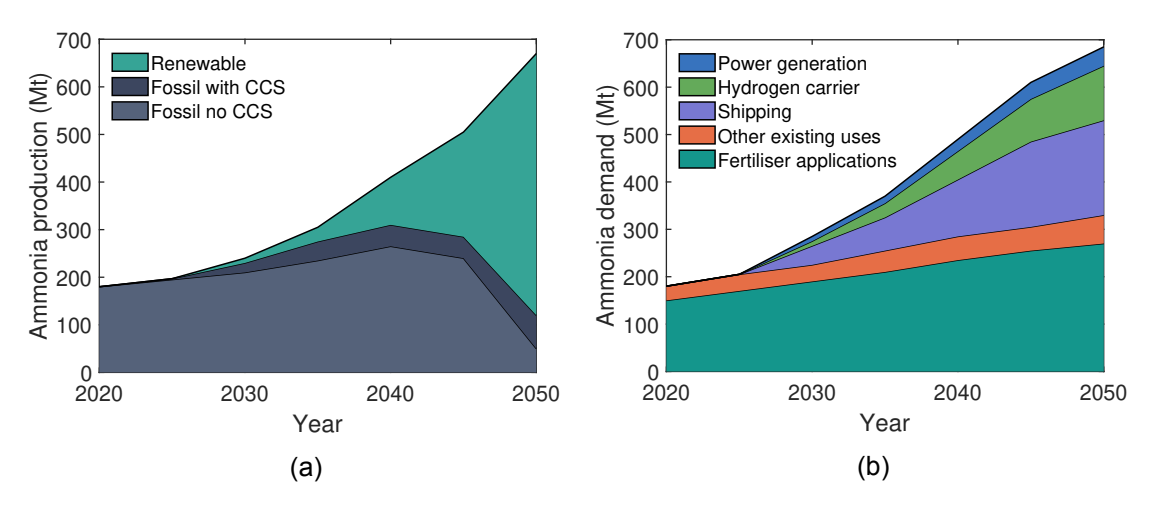


Figure 1.2: a) Expected ammonia production capacity by feedstock source up to 2050. b) Projected markets for ammonia (IRENA and AEA, 2022).

To meet the rising demand, several renewable ammonia plants are planned, and after 2025, renewable-based production is expected to dominate new capacity additions. Glob-

ally, more than 60 PtA projects have been announced, with a combined capacity of 15 Mt per year, corresponding to about 6% of total ammonia production by 2030 (IRENA and AEA, 2022).

Currently, the largest green hydrogen plants operate at the 100 MW scale, with the 260 MW Kuqa facility in northwest China being the world's largest (Zhai et al., 2024). However, Power-to-Ammonia (PtA) facilities have yet to progress beyond demonstration scale. The world's first dynamic, megawatt-scale PtA plant, based on a 10 MW electrolyser, is under construction in Denmark (Ravn, 2020). The project, led by Skovgaard Energy in collaboration with Topsoe and Vestas, is scheduled to be operational by 2025 and will be powered by 12 MW of wind energy and 50 MW of solar energy (Atchison, 2022).

Despite its potential, integrating ammonia synthesis with renewable energy presents significant technical challenges. Industrial ammonia plants are typically designed for continuous, steady-state operation, supplied with a stable stream of H_2 and N_2 from fossil sources (Smith et al., 2020). In contrast, PtA systems must operate flexibly under highly variable renewable energy input. The most critical component of a PtA system is the ammonia synthesis reactor. Under dynamic conditions, the reactor is exposed to rapid and frequent transients that can lead to instability, thermal stress, catalyst degradation, and reduced efficiency (Verleysen et al., 2021).

Historical evidence underscores the severity of this issue. For example, during an incident in Germany in 1989, an unexpected drop in reactor pressure triggered severe temperature oscillations of up to 200 K in an industrial ammonia reactor (Naess et al., 1992). Such events highlight the complex and often unstable dynamics of ammonia reactors under variable operating conditions, which will be an integral part of operation in a PtA facility.

While several studies have examined the steady-state operation and optimisation of ammonia reactors (Khademi and Sabbaghi, 2017; Gaines and Gani, 1977; Cheema and Krewer, 2020), comprehensive investigations that combine rigorous modelling with dynamic simulations to analyse reactor behaviour under load-changing conditions are still lacking.

Similarly, although basic control strategies have been proposed for handling minor disturbances in conventionally operated ammonia reactors (Araújo and Skogestad, 2008; Zhang et al., 2010; Luyben, 2012), the optimal operation and control of the ammonia synthesis loop across the wide load range required in PtA systems is not sufficiently explored.

With the current wave of investments in green ammonia, including numerous projects already underway, there is a notable lack of studies addressing the dynamics of the ammonia synthesis process under load-changing operation. Moreover, dedicated control architectures are required to enable fast, robust, and efficient synthesis loop operation under highly flexible load conditions. To address these gaps, this work aims to answer and fulfil the following objectives:

1.2 Thesis Objective and Goals

This PhD project aims to investigate and develop strategies that enable flexible, safe, and efficient operation of the ammonia synthesis loop in a Power-to-Ammonia (PtA) context. To achieve this, the thesis develops a detailed model of an ammonia synthesis process. This model captures the nonlinear dynamics and complex thermal behaviour inherent to ammonia synthesis under variable load conditions.

Using this model, the work performs transient simulations of the ammonia synthesis process to analyse its dynamic behaviour under load-changing scenarios. The aim is to

assess the stability of the ammonia reactor system, identify critical operating regions, and define margins for safe operation. The model is also used to perform steady-state optimisation, exploring the trade-offs between conversion efficiency and operational stability. This leads to the formulation of the first research question:

Research question 1

How does an ammonia reactor dynamically respond to load changes in a PtA system? Can load variability lead to open-loop instabilities or unsafe operating conditions?

Ammonia reactors exist in three general configurations, with previous studies such as Khademi and Sabbaghi (2017) focusing on their steady-state performance under conventional operation. This work aims to evaluate the reactors under conditions relevant to PtA, comparing them in terms of conversion efficiency, dynamic behaviour, stability, and controllability. This is captured in the second research question:

Research Question 2 Among the three general reactor types, which configuration offers the best combination of stability, conversion efficiency, and controllability for flexible operation in a PtA system?

To achieve optimal reactor operation in PtA, it is also essential to understand how the surrounding synthesis loop behaves under changing loads. A detailed process model of the Haber–Bosch synthesis loop is developed, allowing optimisation across the full PtA operating window. This leads to the third research question:

Research question 3

What are the optimal operating parameters for a Haber-Bosch synthesis loop across the PtA operating envelope? How sensitive are the optimisation results to process disturbances?

Ensuring robust and safe operation under fluctuating conditions requires appropriate control strategies for the ammonia synthesis loop. A final objective of this work is to propose a control architecture that enables highly flexible yet stable reactor operation, minimising stress on critical equipment. This leads to the fourth research question:

Research question 4

How can a control architecture be developed that supports fast, robust, and efficient load-flexible operation of the Haber–Bosch synthesis loop? Can the control strategy be designed to reduce mechanical and thermal stress on process equipment while maintaining near-optimal operation?

1.3 Thesis Outline and Contributions

The thesis is divided into the following chapters:

• Chapter 2, Background: This chapter provides a literature review of conventional ammonia reactor modelling, optimisation strategies, and reactor control methods. It outlines the historical development and limitations of steady-state reactor designs and conservative operation strategies. The chapter also presents recent technoeconomic assessments of Power-to-Ammonia (PtA) systems, focusing on integration with renewable energy sources and their implications for plant flexibility. Special emphasis is placed on emerging research into dynamic operation and control of ammonia reactors under fluctuating power inputs. This review identifies key knowledge gaps in flexible reactor operation and motivates the need for advanced modelling, optimisation, and control strategies addressed in the following chapters.

- Chapter 3, Catalytic bed model: This chapter presents the model for the catalytic
 fixed-bed reactor, which forms the core of all ammonia synthesis systems. A novel
 implementation approach is introduced, based on a partial differential-algebraic equation (PDAE) formulation that integrates rigorous non-ideal thermodynamics with detailed reaction kinetics. The model captures the strong nonlinearities and spatial gradients characteristic of ammonia reactors. A comparative analysis against conventional models demonstrated significant improvements in computational efficiency for
 the developed model.
- Chapter 4, Quench Cooled Reactor for Power-to-Ammonia: This chapter presents the full dynamic model of the adiabatic quench-cooled reactor (AQCR). A case study based on a 100 MW average power plant is defined to evaluate the reactor performance under renewable energy conditions. The model includes rigorous thermodynamic and kinetic formulations, enabling detailed steady-state and stability analysis. Optimisation strategies are applied across a wide operating window, and sensitivity studies are conducted to assess robustness to process disturbances. Transient simulations offer insight into reactor dynamics and limitations, and a simple feedback control strategy is implemented to demonstrate the potential for flexible reactor operation.
- Chapter 5, Reactor comparison and design for Power-to-Ammonia: This chapter introduces a modular model library comprising the three main types of ammonia reactors: AQCR, AICR (adiabatic indirect cooled reactor), and IDCR (internal direct cooled reactor). The models are analysed under PtA-relevant conditions. Stability margins and transient behaviour are compared to identify critical reactor vulnerabilities. Based on dynamic simulations and bifurcation analysis, the chapter discusses trade-offs in reactor design and performance under variable load operation. Recommendations are made for selecting the most suitable reactor type for integration in PtA plants.
- Chapter 6, Modelling and optimisation of a Haber-Bosch synthesis loop for Power-to-Ammonia: This chapter expands the reactor modelling into a full Haber-Bosch synthesis loop including all key subsystems: compressors, heat exchangers, flash separators, steam turbines, and reactor beds. The synthesis loop is optimised to minimise total power consumption, constrained by compressor surge and choke limits, minimum steam temperature, and maximum loop pressure. The optimisation is performed across the load range 10–120% of nominal capacity, revealing particularly compressor surge constraints increase power consumption at low loads.
- Chapter 7, System design of compressor structure for PtA operation: This
 chapter presents a system design study of the synthesis loop compressor structure,
 evaluating configurations with multiple parallel compressor trains. It is shown that
 parallel compressor designs significantly reduce power consumption at low loads.
 An economic analysis is carried out to identify the most cost-effective compressor
 configuration.
- Chapter 8, Optimisation, sensitivity and SOC analysis: This chapter continues
 the synthesis-loop analysis by optimising operation across the full PtA load window.
 The sensitivity of the optimal operation is evaluated for process disturbances such
 as catalyst deactivation, changes in argon content, and variations in cooling water
 temperature. Additionally, candidate variables for self-optimising control (SOC) are
 evaluated to maintain performance near optimality across the operational window.

- Chapter 9, Open-loop simulations of the Haber–Bosch synthesis loop: This chapter investigates the dynamic behaviour of the ammonia synthesis loop through open-loop simulations. Step responses are performed for key manipulated variables, showing the responses for the controlled variables identified in Chapter 8. The analysis highlights complex and nonlinear dynamics.
- Chapter 10, Control of a Haber–Bosch synthesis loop for load-flexible operation: Building on the dynamic simulations in Chapter 9, this chapter proposes a control architecture for the synthesis loop. A hierarchical control strategy is introduced, combining real-time optimisation (RTO) and self-optimising control with regulatory layers to manage fast load changes. Simulation results demonstrate effective tracking of load set-points while maintaining high power efficiency.

1.4 Peer-reviewed articles and conference proceedings

The following provides a list of journal articles and conference proceedings published or submitted as part of this PhD project

1.4.1 Published journal articles

- Rosbo, J. W., Ritschel, T. K. S., Hørstholt, S., Huusom, J. K., Jørgensen, J. B. (2023). Flexible operation, optimisation and stabilising control of a quench cooled ammonia reactor for Power-to-Ammonia. Computers & Chemical Engineering, Volume 176(108316). doi: https://doi.org/10.1016/j.compchemeng.2023.108316
- Rosbo, J.W., Jensen, A.D., Jørgensen, J.B., Huusom, J.K., (2024). Comparison, operation and cooling design of three general reactor types for Power-to-Ammonia processes. Chemical Engineering Journal, Volume 496(153660). doi:https://doi.org/10.1016/j.cej.2024.153660.

1.4.2 Submitted journal articles

Rosbo, J.W., Jørgensen, J.B., Jensen, A.D., Skogestad, S., Huusom, J.K., (2025).
 Optimisation and Robust Control of a Load-Flexible Haber-Bosch Ammonia Synthesis Loop. Submitted to Computer Computers & Chemical Engineering

1.4.3 Published conference proceedings

- Rosbo, J.W., Jensen, Ritschel, T. K.S. Hørsholt, S., A.D., Jørgensen, J.B., Huusom, J.K., (2023). Optimal power distribution in a PtA plant. Computer Aided Chemical Engineering. volume 52, pages 1777–1782.
- Rosbo, J.W., Jensen, A.D., Jørgensen, J.B., Huusom, J.K., (2024). Optimal flexible operation of an AICR for PtA. Computer Aided Chemical Engineering. volume 53, pages 1771–1776.
- Rosbo, J.W., Jensen, A.D., Jørgensen, J.B., Huusom, J.K., (2024). Efficient Numerical Methods for Dynamic Simulation of Fixed-bed Reactors, Computer Aided Chemical Engineering. volume 53, pages 1111–1116.
- Rosbo, J.W., Jørgensen, J.B., Jensen, A.D., Skogestad, S., Huusom, J.K., (2025).
 Optimisation of a Haber-Bosch Synthesis Loop for PtA. Systems Control Transactions 4, 1126–1132. doi:https://doi.org/10.69997/sct.122254.

Chapter 2

Background & Literature Study

This chapter provides background on ammonia production and its role in the transition toward a carbon-neutral future. It begins with a brief historical overview of ammonia synthesis and discusses its conventional uses, as well as its emerging potential as a carbon-free energy carrier.

The concept of Power-to-Ammonia (PtA) is then introduced, with an outline of the overall process and a description of the key operating units, particularly the ammonia reactor systems. A brief overview of major ongoing Power-to-X projects in Europe is also included to illustrate current industrial and research initiatives.

The second part of the chapter presents a literature review. It begins with modelling, simulation, and optimisation studies of ammonia reactors within conventional ammonia synthesis. This is followed by a review of techno-economic studies on green ammonia production. Finally, literature addressing the challenges and strategies for flexible operation of the Haber-Bosch process in PtA systems is presented.

The chapter is written using content from the following three journal articles:

- Rosbo, J. W., Ritschel, T. K. S., Hørstholt, S., Huusom, J. K., Jørgensen, J. B. (2023). Flexible operation, optimisation and stabilising control of a quench cooled ammonia reactor for Power-to-Ammonia. Computers & Chemical Engineering, Volume 176(108316). doi: https://doi.org/10.1016/j.compchemeng.2023.108316
- Rosbo, J.W., Jensen, A.D., Jørgensen, J.B., Huusom, J.K., (2024). Comparison, operation and cooling design of three general reactor types for Power-to-Ammonia processes. Chemical Engineering Journal, Volume 496(153660). doi:https://doi.org/10.1016/j.cej.2024.153660.
- Rosbo, J.W., Jørgensen, J.B., Jensen, A.D., Skogestad, S., Huusom, J.K., (2025). Optimisation and Robust Control of a Load-Flexible Haber-Bosch Ammonia Synthesis Loop. Submitted to Computer Computers & Chemical Engineering

2.1 Ammonia production

In the 19th and early 20th century, nitrogen-containing compounds were primarily sourced from natural deposits such as guano, the accumulated excrement of seabirds and bats. Rich in nitrates and ammonia, guano was collected from tropical islands, especially off the coasts of Peru and Chile, and served as a crucial agricultural fertiliser throughout the 19th century. However, these natural reserves were limited and increasingly depleted by the early 20th century, raising global concern over the future of food production in a growing population.

The lack of natural ammonia sources drove the search for a synthetic method to produce ammonia from the abundant nitrogen in the atmosphere. The breakthrough came in 1909, when German chemist Fritz Haber successfully demonstrated a laboratory-scale method for synthesising ammonia from nitrogen (N_2) and hydrogen (H_2) under high pressure and temperature, using an iron-based catalyst.

Shortly thereafter, Carl Bosch at BASF undertook the challenge of scaling up Haber's process from the laboratory to industrial-scale reactors. This required solving significant engineering problems, including the development of high-pressure reactors, durable materials, and efficient catalysts. However, in 1913, the first industrial ammonia plant was operational in Oppau, Germany. The industrial process was named the Haber–Bosch process after its inventors (Rouwenhorst et al., 2021).

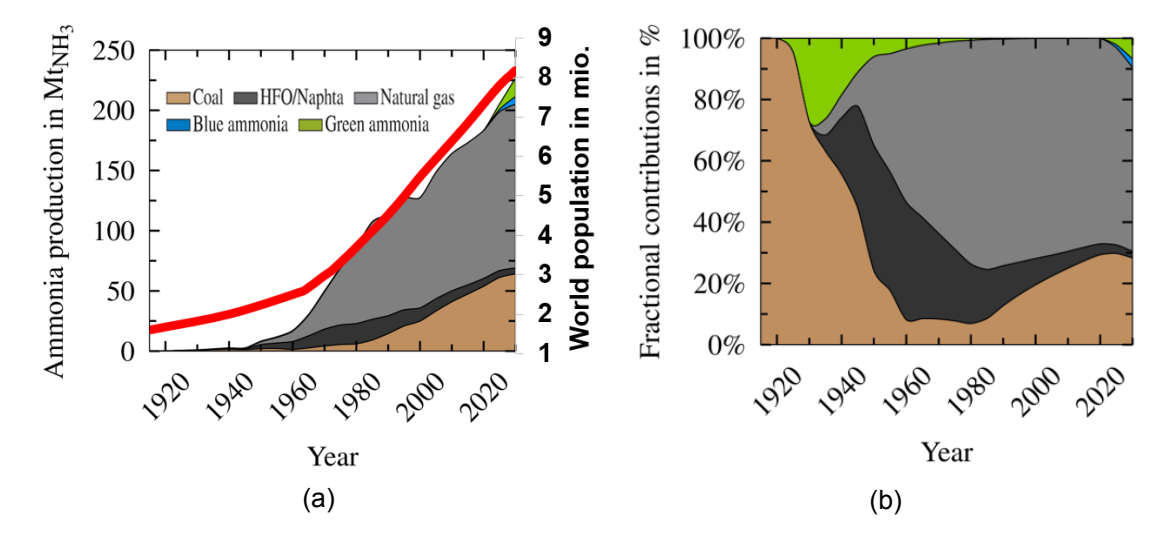


Figure 2.1: a) Historical ammonia production by feedstock, and expected production until 2030. Coal: coal gasification, HFO: heavy fuel oil gasification, Naphtha: naphtha reforming; Natural gas: steam methane reforming, Blue: steam methane reforming with carbon capture and storage (CCS), Green: renewable electricity. b) fractional distribution of feedstocks for ammonia production (Rouwenhorst et al., 2022)

The Haber–Bosch process revolutionised agriculture by enabling the large-scale production of nitrogen-based fertilisers. As shown in Figure 2.1a, the development of this process marked the beginning of a dramatic increase in global ammonia production, which closely mirrors the rise in world population over the same period. This correlation clearly illustrates ammonia's important role in supporting food production. Today, it is estimated that synthetic ammonia sustains nearly half of the global population. With continuing population growth, global demand for ammonia-based fertilisers is projected to rise by approximately 25% by 2050 (Saygin et al., 2023).

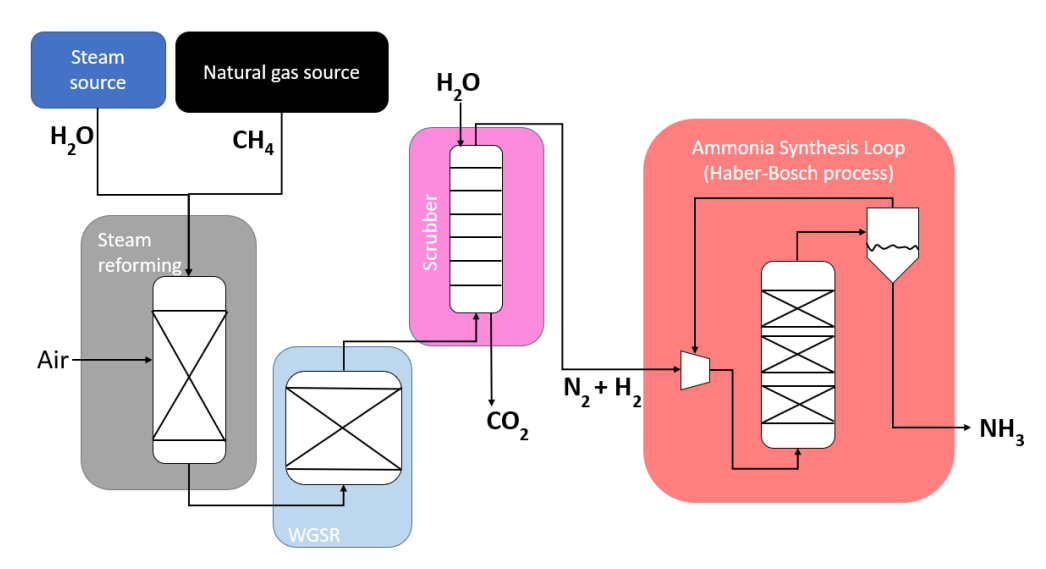


Figure 2.2: Schematic illustration of the main units of a conventional ammonia plant. Grey: Steam reforming, Light blue: Water-gas shift reactor (WGSR), Rosa: CO₂ scrubbing, Red: Ammonia synthesis loop (Haber-Bosch process).

Figure 2.1b illustrates the historical evolution of feedstocks used for ammonia production. Initially, coal gasification was the dominant route, but over time, production methods transitioned toward natural gas (methane) as the preferred feedstock. This shift eliminated the need for the gasification step but retained heavy reliance on fossil fuels for hydrogen production. As a result, conventional ammonia synthesis has become one of the most carbon-intensive processes in the chemical industry.

Figure 2.2 provides a schematic of a conventional ammonia plant. In this process, methane undergoes steam reforming and a water-gas shift reaction to produce hydrogen and carbon dioxide. The carbon dioxide is typically removed through scrubbing and released into the atmosphere. The steam reforming reaction is highly endothermic; thus, air is introduced into the reformer, where part of the methane is combusted to provide the necessary heat. This air also serves as the nitrogen source for ammonia synthesis.

Interestingly, Figure 2.1b also highlights that by 1930, approximately 30% of global ammonia production was based on electrolysis-derived hydrogen powered by renewable hydropower. This demonstrates that the concept of Power-to-Ammonia (PtA) is not new. However, electrolytic production was largely abandoned as fossil-based methods became more economically competitive.

2.2 Power-to-Ammonia

Figure 2.3 illustrates the main process units in a PtA plant consisting of renewable energy producers (wind and solar power), water electrolysis, air separation unit (ASU), hydrogen storage, and the Haber-Bosch synthesis loop. The intermittent nature of renewable energy sources, such as solar and wind, necessitates high operational flexibility across the PtA process. Hydrogen production via water electrolysis exhibits both a broad operating range and fast ramping capabilities, making it well-suited to accommodate the fluctuating output of renewable power (Nayak-Luke et al., 2018; Armijo and Philibert, 2020). The flexibility of air separation units (ASUs) is an active area of research. Industrial providers such as Linde report that their flexible ASU systems can ramp between 20% and 100% load within approximately ten minutes (Linde, 2023; Klein et al., 2021).

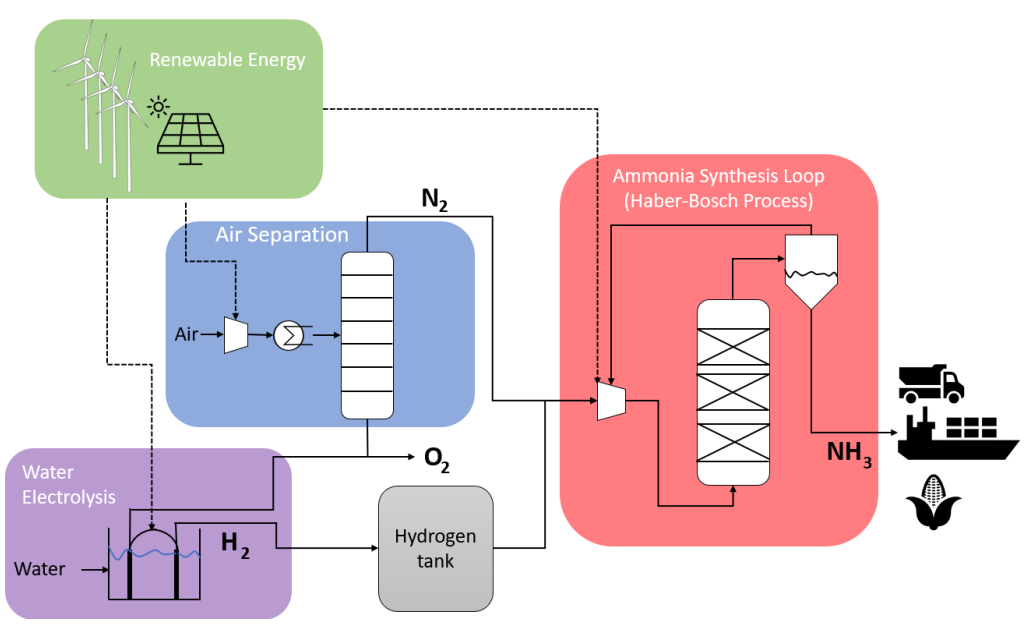


Figure 2.3: Schematic illustration of the main units of a P2A plant. Green: Renewable energy. Purple: Water electrolyser. Blue: Air separation unit. Red: Ammonia synthesis loop.

2.3 Ammonia applications

As mentioned in Section 1.1, ammonia is currently the second most produced chemical in the world. Table 2.1 summarises the main new and traditional applications of ammonia, while Figure 1.2b shows the projected future ammonia demand by sector (IRENA and AEA, 2022). Among the new applications of ammonia is its use as a storage of renewable energy. Several research groups and companies are actively developing gas turbines, combustion engines, and fuel cells for generating electricity through ammonia combustion (Valera-Medina et al., 2018; Sánchez et al., 2021). The potential reduction in greenhouse gas (GHG) emissions through the transition to a renewable energy sector, with ammonia serving as backup energy storage, is significant. However, quantifying the exact GHG reduction potential is uncertain and contingent upon various factors. These include the capacity of renewable energy sources, the level of electrification in industries, and the efficiency of utilising ammonia as a fuel for power generation.

The maritime shipping industry perceives ammonia as the most economical fuel candidate for decarbonising maritime transportation (Al-Aboosi et al., 2021). Maritime transportation is responsible for 2-3% of global GHG emissions illustrating the significant climate potential of transitioning this sector from fossil fuels to ammonia (Ash and Scarbrough, 2019). Furthermore, an ammonia transition can eliminate toxic pollutants from the combustion of heavy fuel oils. Thus, intensive research is being conducted in developing ship engines running on ammonia (Laursen, 2018). Another application of ammonia as a fuel is direct combustion of ammonia or ammonia-fossil-fuel blends in industrial processes where high-temperature heating is needed (Valera-Medina et al., 2018).

PtA is expected to replace conventional ammonia production gradually (European Gas Hub; Saygin et al., 2023). Currently, ammonia production accounts for 1.5-2% of global greenhouse gas emissions (Nayak-Luke et al., 2018). The largest fraction (>80%) of produced ammonia is used directly or after further processing as fertiliser in agriculture (Afif et al., 2016). Other traditional uses of ammonia include refrigeration, explosives, and

as a cleaning agent.

Table 2.1: The main new and traditional applications of ammonia. The table reports the GHG reduction potential for transitioning to green ammonia in each application.

Ne	ew applications	Traditional applications		
Application	Climate potential in % reduction of global GHG emmision	Application	Climate potential in % reduction of global GHG emmision	
Energy storage	Uncertain	Fertiliser in Agriculture	1.5 - 2%	
Martime transportation	2 - 3%	Refrigerantion, Explosives, Cleaning	< 0.2%	
Heating in industry	Uncertain			

2.4 Investments in PtA

Figure 1.2 illustrates that global ammonia production is expected to triple by 2050, with renewable ammonia gradually outphasing fossil-based production. This trend is consistent with several reviews of PtX projects worldwide. Chehade et al. (2019) reviewed 192 Power-to-X demonstration projects across 32 countries, showing a strong acceleration in announced projects within the last decade. In China, Zhai et al. (2024) presented several large-scale PtX projects above 100 MW, including Sinopec's 260 MW Kuqa facility in northwest China—the world's largest green hydrogen plant—operational since 2023.

Australia's sunny climate makes it well-suited for large-scale solar-powered PtX hubs. The country hosts multiple planned projects, the two largest being the Asian Renewable Energy Hub (AREH) in Pilbara and the Western Green Energy Hub (WGEH) in Western Australia (IRENA and AEA, 2022). Together, these sites are expected to produce up to 30 Mt of renewable ammonia annually, based on 76 GW of combined onshore wind and solar energy capacity.

In Europe, massive investments are being directed towards PtX projects, with more than 300 initiatives either ongoing or planned (Araya et al., 2022; Wulf et al., 2020, 2018). For example, in the Netherlands, the ELYgator project led by Air Liquide involves a 200 MW electrolyser and aims to be operational before 2030 (Innovation fund, 2020). Denmark, in particular, seeks to establish itself as a leading PtX hub, with the government identifying PtX as a strategic export market (Danish Ministry of Climate, 2022; Dansk Energi, 2020). More than 40 PtX projects are currently underway in Denmark alone.

Among these, the world's first dynamic megawatt-scale PtA facility (10 MW electrolyser) is under construction in Ramme, Western Denmark (Ravn, 2020). The project, led by Skovgaard Energy in partnership with Topsoe and Vestas, is scheduled for operation in 2025 and will be powered by 12 MW of wind and 50 MW of solar energy (Atchison, 2022). Skovgaard Energy is also one of the partners in the Dynflex project, which financially supports this PhD study. Figure 2.4 shows an aerial photograph of the PtA plant located in Lemvig, Western Denmark. In the background, the renewable mix of photovoltaic panels and wind turbines is visible. The ammonia reactor is the vertical tube to the right of the main building, while the electrolyser and air separation unit (via pressure-swing adsorption) are housed inside the building. Although a 10 MW power input is significant compared to typical electrolyser capacities, Skovgaard Energy still considers the Ramme plant a demonstration facility. For comparison, conventional ammonia plants operate at scales of several gigawatts of power input (Appl, 2006), highlighting the substantial gap



Figure 2.4: Air photografy of Skovgaard Energy's 10 MW PtA plant under construction in Ramme, Denmark.

between current green ammonia projects and the scale required to meet global ammonia demand.

Looking ahead, Denmark is also planning its first gigawatt-scale PtA facility in the city of Esbjerg on the west coast. Construction is expected to begin in 2025, with operations planned for 2028/29 (HøstP2X, 2021).

2.5 Ammonia reactor types

Figure 2.3 shows a generic representation of the catalytic ammonia reactor. At a general level, ammonia reactors can be categorised into three different types: adiabatic quench cooled reactor (AQCR), adiabatic indirect cooled reactor (AICR), and internal direct cooled reactor (IDCR) (Inamuddin et al., 2020). Figure 2.5 displays schematic illustrations of the three reactor types. The reactor types differ by the cooling method for the reactor bed(s). The cooling is applied to counteract the exothermic ammonia synthesis reaction. The AQCR and AICR consist of multiple beds with inter-bed cooling. For the AQCR the interbed cooling is achieved by injecting a fraction of the cold reactor feed stream (quench) between each bed. The AICR achieves cooling between the beds via the inter-bed heat exchangers, most commonly with feed synthesis gas as the cooling medium. Configurations utilising cooling water and steam generation in the inter-bed heat exchangers also exist. In the IDCR the catalyst at the shell side is cooled along the reactor by counter-current flow with the cold reactor feed at the tube side.

From a conversion standpoint, the IDCR and AICR generally outperform the AQCR, as the entire feed passes through all catalyst beds, whereas part of the feed in the AQCR bypasses the earlier beds (Khademi and Sabbaghi, 2017). However, due to the simpler and cheaper design, the AQCR was originally the most common in industry. Today, modern plants are installed with AICRs and decommissioned AQCRs are continuously being replaced by AICRs (Inamuddin et al., 2020).

2.6 Reactor modelling and simulation

Steady-state simulations of industrial ammonia reactors with heat integration are well established in the literature. One of the earliest contributions was made by van Heerden (1953), who studied an internal direct-cooled reactor (Figure 2.5a) and demonstrated the

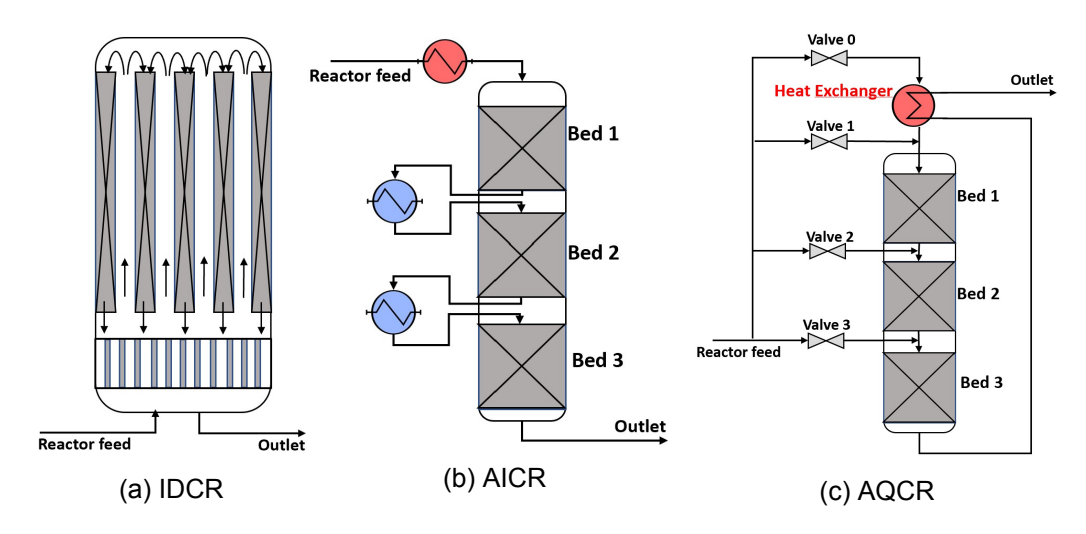


Figure 2.5: Tree ammonia reactor types: a) Internal direct cooled reactor (IDCR), b) Adiabatic indirect cooled reactor (AICR), and c) Adiabatic quench cooled reactor (AQCR).

existence of multiple steady-state solutions, as illustrated in the frequently cited van Heerden plot.

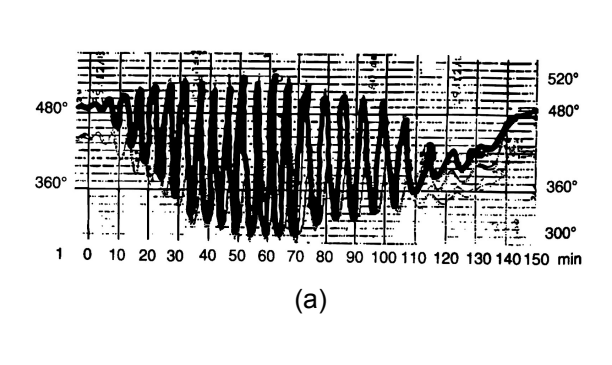
Modelling of the packed beds typically builds on a 1D Plug-Flow-Reactor (PFR) model incorporating detailed reaction kinetics. This has proven an accurate model for industrial reactors in several studies (Reddy and Husain, 1982; Baddour et al., 1965; Singh and Saraf, 1979; Froment and De Wilde, 2010).

Due to the typically stable operation of conventional ammonia plants, relatively few studies have focused on the dynamic behaviour of ammonia reactors. However, quench-cooled ammonia reactors exposed to unexpected disturbances have been observed to exhibit unstable transient responses. Figure 2.6a, show severe temperature oscillations, up to 200 K, reported by Naess et al. (1992), following a sudden pressure drop in an industrial ammonia reactor in Germany in 1989. This oscillatory behaviour was later reproduced through dynamic simulation by Morud and Skogestad (1998) (Figure 2.6b). Further studies by Andersen (1999), Rabchuk et al. (2014), and Jinasena et al. (2018) on single-bed ammonia reactors with heat integration confirmed the existence of sustained limit cycle oscillations, highlighting the potential for unstable dynamic phenomena in these systems. These studies used a 1D PFR model for the ammonia reactor but did not account for temperature-dependent thermodynamic properties and real-gas behaviour at high pressure.

Large temperature oscillations pose a significant risk to ammonia reactors as it can lead to thermal stress on the reactor structure and catalyst deactivation. Andersen (1999) reported that an unexpected period of temperature oscillations not only reduced production rates but also caused damage to the reactor insulation, underscoring the operational hazards if the reactor systems are not well controlled.

2.7 Reactor optimisation

Several papers have studied the design and optimisation of the three general reactor types. Gaines and Gani (1977), Cheema and Krewer (2020), and Straus (2018) present steady-state models and optimisation of the AQCR. El-Gharbawy et al. (2021), Shamiri and Aliabadi (2021), and Akpa and Raphael (2014) described optimisation of the AICR



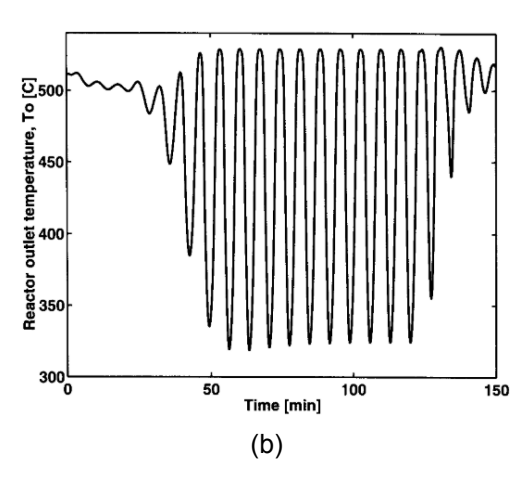


Figure 2.6: a) Temperature recording from the industrial ammonia reactor at the reactor outlet (Naess et al., 1992). b) Simulational reconstruction of the observed oscillation (Morud and Skogestad, 1998).

system. Anh-Nga et al. (2017) and Baddour et al. (1965) model and optimise the IDCR to maximise conversion of reactants. Azarhoosh et al. (2014) optimised and compared conversion for an AQCR and an AICR reactor for identical catalyst packing, while Jorqueira et al. (2018) performed a similar study for an AICR and an IDCR. Finally, Khademi and Sabbaghi (2017) optimised and compared all three reactor types, ranking the reactors in terms of conversion with the IDCR and AICR achieving significantly higher conversions than the AQCR. Figure 2.7a) shows nitrogen conversion along the normalised reactor length for the different reactor types, while 2.7b) shows the corrosponding temperature profile for the solutions reported in (Khademi and Sabbaghi, 2017).

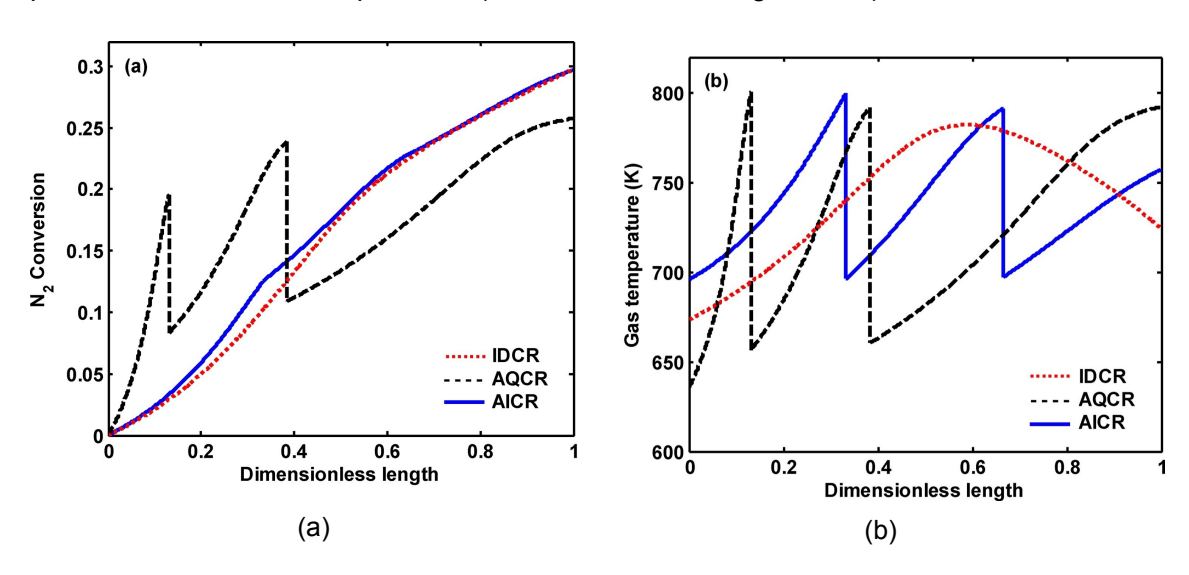


Figure 2.7: A comparison between the optimised IDCR, 3-bed AQCR and 3-bed AICR in terms of a) nitrogen conversion, and b) temperature profile along the normalised reactors lengths (Khademi and Sabbaghi, 2017).

Generally, the literature about modelling and optimisation of ammonia reactors focuses on steady-state maximisation of reactant conversion at full load, which is the most relevant performance indicator for conventional ammonia plants with a stable reactant supply. The

studies often report notable optimisation potentials in the range of 5–10%. However, only a few works, such as Baddour et al. (1965) and Straus (2018), have briefly addressed concerns regarding the proximity of the optimal operating point to unstable regions or the risk of blowout due to runaway reaction kinetics. In conventional ammonia plants, safe and stable operation typically takes precedence over strict optimality. This inherent trade-off may partly explain the relatively large optimisation potential identified in the literature.

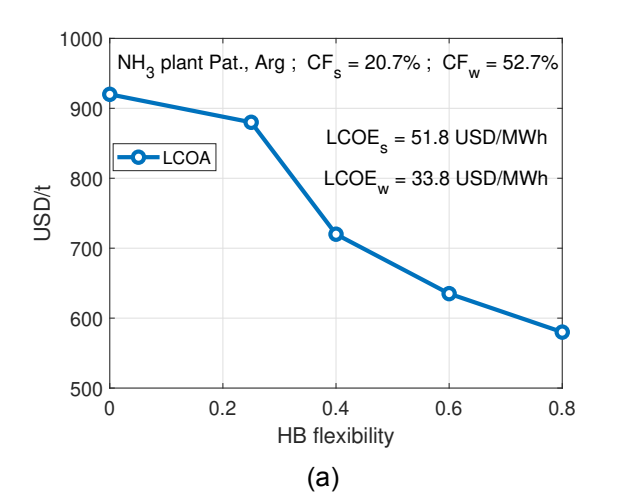
2.8 Conventional control structure design for the ammonia process

Few authors have addressed the control of ammonia plants. Among the existing studies, Araújo and Skogestad (2008), Zhang et al. (2010), and Luyben (2012) have examined plant-wide control structures using a stable, though not necessarily optimal reactor configuration, considering only small disturbances. In contrast, Recke et al. (2000), Rovaglio et al. (2001), and Straus et al. (Straus and Skogestad, 2017, 2018; Straus et al., 2019) have focused on controlling the oscillatory behaviour observed in AQCRs. Rovaglio et al. (2001) proposed a basic control scheme targeting the inlet temperature of the first AQCR bed, while Straus et al. (Straus and Skogestad, 2017, 2018; Straus et al., 2019) explored a range of advanced optimisation-based control strategies, employing the bed splitting fraction as a manipulated variable to mitigate instability and improve performance.

2.9 Scheduling, Design and Economics of the PtA plants

Enhancing the down- and upscaling flexibility of the HB-process can significantly reduce the required hydrogen storage capacity. Armijo and Philibert (2020) demonstrated that, depending on the geographical location in Argentina, the levelised cost of green ammonia (LCOA) can be reduced by more than 40% if the Haber-Bosch process is capable of ramping down to 20% of its nominal load and can be completely shut down when necessary. This trade-off is illustrated in Figure 2.8, which shows (a) the levelised cost of ammonia (LCOA) and (b) the optimal hydrogen storage size as functions of Haber-Bosch (HB) process flexibility. The case study considers Patagonia, Argentina, a region with highly favourable wind resources, as reflected by the high wind capacity factor ($CF_W = 52.7$) and relatively low levelised cost of wind power (LCOE_W = 33.8 USD/MWh). The results demonstrate that increasing the HB process flexibility significantly reduces the need for hydrogen storage and lowers the overall production cost. In the maximum flexibility scenario (down to 20% load), the LCOA falls below 600 USD/t, approaching current market price levels of 300-500 USD/t (Business analytiq, 2025; Jiang et al., 2025). Similarly, Wang et al. (2023) reported a 30% reduction in LCOA for a moderately flexible HB plant (with a 60% minimum load) compared to a completely inflexible configuration. Pistolesi et al. (2025) investigated the sensitivity of HB-process flexibility on the LCOA and demonstrated up to 40% reduction in LCOA for a HB-process with an operating window from 20% to 100% load compared to an inflexible HB-process.

Schulte Beerbühl et al. (2015), Ikäheimo et al. (2018), Smith and Torrente-Murciano (2024), Nayak-Luke et al. (2018), Salmon and Bañares-Alcántara (2023), Allman and Daoutidis (2018) and Allman et al. (2019) investigated the optimal design and scheduling of units in power-to-ammonia (PtA) systems using surrogate models to evaluate both capital and operational cost. Sánchez and Martín (2018a,b) examined the scale-up and scale-down challenges associated with renewable ammonia production, concluding that green ammonia is likely to become cost-competitive in the future, assuming continued reductions in the cost of electrolysers and solar panels.



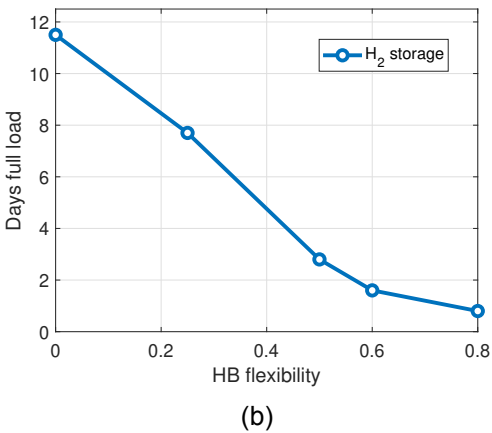


Figure 2.8: a) Optimal LCOA of green ammonia as a function of the flexibility of the Haber-Bosch process for a case in Tahtal, Argentina. b) Shows the corrosponding optimisal size of the hydrogen storage in day of full load operation (Armijo and Philibert, 2020).

Morgan et al. (2014) investigated a case with renewable energy and small-scale PtA for electricity generation in islanded communities. The study found a significant economic profit in the renewable PtA case compared with diesel-generated electricity.

In summary, numerous studies have addressed the high-level economic optimisation for scheduling and design of PtA plants integrated with renewable energy sources. The literature suggests that the most cost-effective configuration combines a relatively small hydrogen storage capacity with highly flexible operating units. These studies typically employ surrogate models to represent PtA units to reduce the computational requirements of the optimisation problem. Thus, the dynamic operation of these units under flexible load conditions is often simplified by applying assumptions regarding ramping capabilities and operational limits. Furthermore, linear relationships are often assumed for the power utility of the PtA units as a function of the load. However, Fahr et al. (2025), Schiedeck et al. (2025) and Rosbo et al. (2025b) demonstrated that the power consumption of the HB-process is highly non-linear with the load due to compressor instability limitations at low-load operation.

2.10 Flexible operation of Haber-Bosch process

Relatively few studies are available on the detailed behaviour of the Haber-Bosch process and the ammonia reactor during load-flexible operation. However, a few studies present steady-state models of the ammonia reactor at different operating points relevant for PtA operation.

Cheema and Krewer (2018) investigated the operational sensitivity of an ammonia reactor to disturbances in several operating parameters. Hereby, they identified strategies to enable part-load operation of the ammonia reactor. Building on this work, Cheema and Krewer (2020) explored the operating envelope of an ammonia synthesis loop by varying process conditions. Their findings revealed that adjusting the N_2/H_2 ratio in the reactor feed offers the greatest potential for reducing ammonia production, with reductions of up to 70%.

Fahr et al. (2023) investigated the flexible operation of an adiabatic indirect cooled reactor (AICR) under varying feed flow conditions and proposed to enable low-load operation by decreasing the reactor conversion through a reduction of the reactor operating pressure and reducing the inter-bed cooling. The authors suggested controlling the reactor pressure by opening a recycle valve around the compressor unit. This strategy has also been proposed in patents by Topsoe (Speth et al., 2023) and Casale (Maurizio, 2022). Expanding on this work, Fahr et al. (2024) developed an economic framework to quantify the additional cost associated with load-flexible PtA operation. Their findings indicate that reactor operation down to 10% part load is feasible with a cost increase of less than 7%. Moreover, the primary limitation to part-load operation was identified as insufficient heat recovery within the reactor system.

The dynamic operation of an ammonia synthesis loop under load-flexible conditions is only sparsely addressed in the literature. Sun et al. (2024) presented a rigorous dynamic model of a PtA plant and simulated load variations between 90% and 110% of the nominal synthesis loop load. In their study, the authors proposed controlling the HB-loop pressure via the hydrogen make-up feed flow. However, this approach appears questionable, as the hydrogen make-up flow is constrained by the availability of renewable power and cannot be freely manipulated.

Schiedeck et al. (2025) presents an interesting work on the heat integration of Solide Oxide Electrolyser Cells (SOECs) with a Haber-Bosch process across an operating window from 10% to 100% load. The part-load operation was achieved with the pressure reduction strategies proposed in Fahr et al. (2023), where loop pressure is controlled via recycling around the compressor unit. A key finding was the interaction between the increased compressor power demand and the thermal needs of the SOECs at part load, as the waste heat generated could be efficiently utilised by the SOECs.

Fahr et al. (2025) set up a dynamic simulator of the HB-process in UniSim® Dynamics R491. The simulator was employed to demonstrate the load-change strategies proposed in their previous works (Fahr et al., 2023, 2024). The study demonstrated load change rates up to 3%/min and safe operation down to 10% load defined based on the hydrogen make-up feed flow.

Kong et al. (2024) demonstrated nonlinear model predictive control (NMPC) on a simulated HB-process with a quench cooled reactor. The study demonstrated flexible operation between 50% and 100% of the nominal load by varying the make-up feed flow. The set-point for the reactor feed temperatures were updated to maximise reactor conversion as a function of the load. The loop pressure was maintained within ±5 bar of the nominal value and controlled via manipulation of the outlet gas flow from the separator.

In summary, a few studies have addressed the load-flexible operation of ammonia reactors, whereas the load-changing operation of the full Haber-Bosch synthesis loop has been described only in a handful of papers.

Chapter 3

Catalytic bed model

The intermittent nature of renewable energy sources requires Power-to-X (PtX) plants to operate flexibly, in contrast to the traditionally stable operation associated with fossil feedstocks. This emphasises the need for accurate and computationally efficient dynamic models of PtX plants.

In this chapter, a partial differential—algebraic equations (PDAEs) model is developed for a fixed-bed gas-phase reactor. The model is discretised in space using the finite volume method (FVM). Dispersion effects from back-mixing in the bed are not implemented directly in the FVM formulation but are instead approximated through numerical diffusion by selecting an appropriate number of discretisation cells. Five different numerical implementations of the Euler time-integration step are investigated: one traditional explicit scheme and four implicit formulations, which differ in the number of algebraic equations and variables treated implicitly. The performance of these numerical schemes is evaluated by simulating the reactor response to a step change in inlet temperature. Significant differences in computational efficiency are observed, with the most efficient implicit method achieving a speed-up of approximately five times compared to the explicit scheme, while the slowest implicit method is about six times slower.

This chapter contains material from the article:

Rosbo, J.W., Jensen, A.D., Jørgensen, J.B., Huusom, J.K., (2024). Efficient Numerical Methods for Dynamic Simulation of Fixed-bed Reactors, Computer Aided Chemical Engineering. volume 53, pages 1111–1116.

3.1 Introduction

Catalytic fixed-bed reactors are among the most widely used reactor types for synthesising large-scale chemicals such as methanol, ammonia, and sulphuric acid. Consequently, the mathematical modelling of fixed-bed reactors is a core component of chemical engineering education and is covered in several classical textbooks (Froment and De Wilde, 2010; Rawlings and Ekerdt, 2013). Traditionally, literature and textbooks have focused on steady-state modelling, as chemical plants have historically been designed for stable operation with minimal production fluctuations. However, with the current shift away from fossil-based feedstocks toward renewable energy sources, new challenges have emerged for chemical plant operation. In particular, the dynamic and flexible operation of Power-to-X (PtX) plants is required to accommodate the intermittent nature of renewable energies such as wind and solar power. This shift underscores the importance of dynamic models, which are essential for simulating renewable-powered chemical plants and fundamental for advanced process control.

Steady-state models of industrial fixed-bed reactors for ammonia and methanol production are well established in the literature. These models typically employ a one-dimensional plug-flow reactor (1D PFR) formulation, which has been shown to provide accurate predictions for industrial reactors in several studies (Baddour et al., 1965; Shamiri and Aliabadi, 2021). Building on 1D PFR models, several studies have presented dynamic models for fixed-bed ammonia and methanol reactors (Morud and Skogestad, 1998; Jinasena et al., 2018). Morud and Skogestad (1998) and Jinasena et al. (2018) discretised the governing partial differential equations (PDEs) in space using the finite volume method, whereas Manenti and Bozzano (2013) applied a finite difference scheme. All three studies employed an explicit Euler method for the temporal discretisation. While these models qualitatively reproduce transient behaviour observed in fixed-bed ammonia and methanol reactors, their quantitative accuracy has not been addressed. Moreover, the models assume constant thermodynamic properties and neglect deviations from ideal gas behaviour in the high-pressure range (up to 250 bar).

To address these limitations, this work develops a dynamic fixed-bed reactor model that incorporates real-gas behaviour and variable thermodynamic properties, enabling more accurate simulation of high-pressure operation. The model is formulated as a system of partial differential—algebraic equations (PDAEs) and discretised in space using the finite volume method. In contrast to previous studies relying solely on explicit time integration schemes, several implicit temporal discretisation schemes are investigated to improve numerical stability and computational efficiency.

3.2 Thermodynamics

3.2.1 Fluids

The model for the ammonia synthesis loop and its components consists of mass and energy balances as well as equations describing thermo-physical properties, reaction stoichiometry, and reaction kinetics (Hangos, 2001). In Section 3.3.1, the energy balance is expressed in terms of internal energy, rather than modifying it in terms of temperature, as is common in textbooks and literature (Rawlings and Ekerdt, 2013; Froment and De Wilde, 2010). Expressing the energy balance in terms of internal energy implicitly incorporates temperature, pressure, and composition dependencies. With modern thermodynamic software, it is possible to evaluate state functions for the gas phase, e.g. internal energy U and enthalpy H, applying more advanced equations of state (EOS) such as Soave-Redlick Kwong (SRK) and Peng-Robinson (PR) equation.

Ammonia reactors are operated at high pressures (>150 bar); therefore, a real-gas equation of state (EOS) is required to describe the gas phase. This work uses the Peng-Robinson EOS. The thermodynamic software ThermoLib to evaluate the state functions for the gas phase (Ritschel et al., 2016, 2017). Given a system with temperature T, pressure P and molar vector n, functions for the system volume, \mathcal{V} , enthalpy, \mathcal{H} , and internal energy, \mathcal{U} , is defined as,

$$V = \mathcal{V}(T, P, n),$$
 $\left[\mathsf{m}^3\right],$ (3.1a)

$$H = \mathcal{H}(T, P, n), \tag{3.1b}$$

$$U = \mathcal{U}(T, P, n) = \mathcal{H} - P\mathcal{V}$$
 [J], (3.1c)

where V denotes the absolute system volume, H the absolute enthalpy and U the absolute internal energy. The system concentration vector, c, is by definition,

$$c = \frac{n}{V}. (3.2)$$

The state functions are all homogeneous 1st order functions wrt. to the molar vector. Thus, the volume-specific values are obtained by evaluating the thermodynamic functions with the concentration vector,

$$\hat{v} = \mathcal{V}(T, P, c) \tag{3.3a}$$

$$\hat{h} = \mathcal{H}(T, P, c)$$
 $\left[\mathsf{J/m^3} \right],$ (3.3b)

$$\hat{u} = \mathcal{U}(T, P, c)$$
 $\left[\mathsf{J/m^3} \right],$ (3.3c)

in which lower-case-"hat" symbols denote volume-specific values. For a molar flow vector, F [mol/s], the corresponding transported properties are identified by "dot"-notation,

$$\dot{V} = Q = \mathcal{V}(T, P, F)$$
 $\left[\mathbf{m}^3 / \mathbf{s} \right],$ (3.4a)

$$\dot{H} = \mathcal{H}(T, P, F)$$
 [J/s], (3.4b)

$$\dot{U} = \mathcal{U}(T, P, F)$$
 [J/s], (3.4c)

where Q is also used to represent the volumetric flow rate. Given a molar flux vector, N [mol/(s m²)], evaluating the thermodynamic functions yields the associated flux,

$$\bar{V} = v = \mathcal{V}(T, P, N)$$
 [m/s], (3.5a)

$$\bar{H} = \mathcal{H}(T, P, N)$$
 $\left[\mathsf{J}/(\mathsf{s}\;\mathsf{m}^2) \right],$ (3.5b)

$$\bar{U} = \mathcal{U}(T, P, N)$$
 $\left[\mathsf{J}/(\mathsf{s}\;\mathsf{m}^2) \right],$ (3.5c)

Evidently, "bar"-notation denotes fluxes. The flow velocity is also denoted by v.

3.2.2 Solids

The solid catalyst is assumed not to change its volume with changes in temperature and pressure. Thus, the internal energy density of the solid catalytic, \hat{u}^s , is purely a function of the temperature,

$$\hat{u}^{s}(T) = \hat{u}^{s}(T_{0}) + \int_{T_{0}}^{T} \rho_{s} c_{p,s}(T) \quad [\mathsf{J/m^{3}}]$$
(3.6)

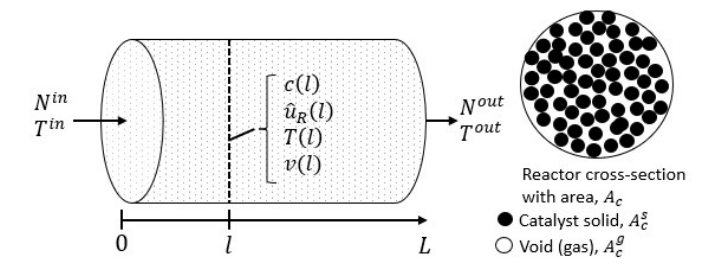


Figure 3.1: Schematic illustration of the catalytic fixed-bed.

in which ρ_s is the solid density, $c_{p,s}$ is the specific heat capacity, and T_0 is a reference temperature. The value of $\hat{u}_s(T_0)=0$ and the reference temperature can be set arbitrarily. Therefore Setting $\hat{u}_s(T_0)=0$ J/m³ at $T_0=0$ K, and assuming $c_{p,s}$ is independent of temperature,

$$\hat{u}^s(T) = \rho_s c_{p,s} T \tag{3.7}$$

Gas and solid

The internal energy density of the reactor, \hat{u}_R , consisting of a combined solid and gas system, is,

$$\hat{u}_R = \epsilon \hat{u}^g + (1 - \epsilon)\hat{u}^s \tag{3.8}$$

3.3 Catalytic fixed-bed model

Figure 3.1 displays a schematic illustration of the catalytic fixed-bed. For the packed bed reactor, the porosity, ϵ_B , is defined as the void fraction of the reactor volume,

$$\epsilon_B = \frac{V^g}{V_R}, \quad 1 - \epsilon_B = \frac{V^s}{V_R}$$
 (3.9)

where V^g is the gas volume, V^s is the solid catalyst volume, and V_R is the total reactor bed volume. The reaction takes place within the solid catalyst phase, but material is transported via the gas phase. Thus, the factor,

$$\frac{1 - \epsilon_B}{\epsilon_B} [=] \frac{\mathsf{m}^3 \text{ cat.}}{\mathsf{m}^3 \text{ gas}}, \tag{3.10}$$

is used to convert basis from catalyst to gas phase.

3.3.1 Bed model

The bed is modelled as a 1-dimensional packed bed reactor with the following assumptions:

- **A1** The reactor beds are adiabatic as the reactor is well isolated.
- **A2** The reactor is isobaric both in time and space. Compared with the very high operating pressure, the pressure drop over each reactor bed is negligible. This also entails that the system is at mechanical equilibrium.
- A3 The particle and gas phase are isothermal.

In the most general form, the material and energy balance for the fixed-bed reactor is given by the two partial differential equations,

$$\frac{\partial c}{\partial t} = -\frac{\partial N}{\partial l} + R \tag{3.11a}$$

$$\frac{\partial \hat{u}_R}{\partial t} = -\epsilon \frac{\partial \bar{H}}{\partial l} \tag{3.11b}$$

where c is the gas phase concentration vector, l is the spatial coordinate, N is the molar flux vector, and R is the production rate vector per gas volume. The component molar flux, N, consists of an advection and dispersion term,

$$N = vc - D_L \frac{\partial c}{\partial l} \tag{3.12}$$

in which v is the interstitial flow velocity and D_L is the axial dispersion. The velocity is positive in the direction defined by the spatial coordinate, l, and negative for flow in the opposite direction. In the energy balance, \bar{H} denotes the flux of enthalpy, which is given by,

$$\bar{H} = \mathcal{H}(T, P, N) \tag{3.13}$$

Assumption **A3** of isothermal particle and gas-phase allows for modelling the energy balances (3.11b) of the two phases (gas and solid catalyst) as a single pseudo-homogeneous phase. The combined volumetric internal energy, \hat{u}_R , of the gas and particle phase is a function of the gas phase concentrations, c, the temperature, T, and pressure, P,

$$\hat{u}_R = \epsilon_B \hat{u}^g(T, P, c) + (1 - \epsilon_B)\hat{u}^s(T) \tag{3.14}$$

where the gas phase internal energy is determined from an equation of state (see Section 3.2). Additionally, the equation of state must always be satisfied in the entire bed domain. In this work, satisfying the EOS is required through the volume function,

$$\mathcal{V}(T, P, c) = 1 \tag{3.15}$$

Equations (3.11)-(3.15) define the bed model as a partial differential algebraic equations system (PDAEs).

Catalyst reaction

The ammonia synthesis follows the Haber-Bosch reaction scheme,

$$N_2 + 3 H_2 \rightleftharpoons 2 NH_3 \tag{3.16}$$

Thus, with the species sequence [N₂, H₂, NH₃, Ar] the stoichiometric vector is,

$$\nu = [-1 \quad -3 \quad 2 \quad 0] \tag{3.17}$$

Nielsen et al. (1964) studied the elementary steps occurring during ammonia synthesis on iron catalysts and found the nitrogen adsorption to be rate-determining. Hereby, the reaction rate of 3.16 can be described by a single rate expression. This work uses the Temkin-Pyzhev rate equation,

$$r = k_1 P_{N_2} \left(\frac{P_{H_2}^3}{P_{NH_3}^2}\right)^a - k_{-1} \left(\frac{P_{NH_3}^2}{P_{H_2}^3}\right)^b \quad [=] \quad \frac{\text{kmol N}_2}{\text{h m}^3 \text{ cat.}}, \tag{3.18}$$

in which the rate r is defined relative to N₂. For exponents a and b are applied, $a = b = \frac{1}{2}$ (Morud and Skogestad, 1998; Jinasena et al., 2018; Araújo and Skogestad, 2008). The forward and the backward rate constants are given from Arrhenius' equation

$$k_i = A_i \exp\left(\frac{-E_{a,i}}{R_{gas}T}\right) = A_i \exp\left(\frac{B_i}{T}\right)$$
 (3.19)

with $B_i = -E_{a,i}/R_{gas}$ for $i \in \{1, -1\}$. The ideal gas constant is $R_{gas} = 8.314 \text{J}/(\text{mol} \cdot \text{K})$ and the Arrhenius parameters are,

$$E_{a,1} = 87,090 \frac{\mathsf{J}}{\mathsf{mol}}, \quad A_1 = 1.79 \cdot 10^4 \frac{\mathsf{kmol} \ \mathsf{N}_2}{\mathsf{h} \ \mathsf{m}^3 \ \mathsf{cat}}. \tag{3.20a}$$

$$E_{a,-1} = 194,464 \frac{\mathsf{J}}{\mathsf{mol}}, \quad A_{-1} = 2.57 \cdot 10^{16} \frac{\mathsf{kmol} \ \mathsf{N}_2}{\mathsf{h} \ \mathsf{m}^3 \ \mathsf{cat}}. \tag{3.20b}$$

$$E_{a,-1} = 194,464 \frac{\mathsf{J}}{\mathsf{mol}}, \quad A_{-1} = 2.57 \cdot 10^{16} \frac{\mathsf{kmol} \ \mathsf{N}_2}{\mathsf{h} \ \mathsf{m}^3 \ \mathsf{cat}}.$$
 (3.20b)

Eq. (3.18) is given per catalyst volume. Thus, the production rates per gas volume, R, are obtained via.

$$R = \frac{1 - \epsilon_B}{\epsilon_B} \nu' \alpha r \tag{3.21}$$

The value of the activity factor, α , is adopted from (Morud and Skogestad, 1998),

$$\alpha = 4.75 \tag{3.22}$$

which takes into account advances in modern catalyst with higher activity compared to pre 1940 catalysts available for Temkin and Pyzhev (Morud and Skogestad, 1998). The partial pressure, P_i , is given by Dalton's law,

$$P_i = Px_i \tag{3.23}$$

where x_i is the mole faction of the i'th species,

$$x_i = \frac{c_i}{\sum_i c_i} \tag{3.24}$$

The influence of temperature and the extent of reaction on the overall reaction rate is illustrated in Figure 3.2, which shows contours of constant reaction rate in the temperatureconversion plane. The plot is constructed for a gas mixture of hydrogen and nitrogen at the stoichiometric ratio (3:1) at a pressure of 200 bar. The conversion, X, is defined as,

$$X_i = \frac{n_{0, i} - n_i}{n_{0, i}},\tag{3.25}$$

where n_i and $n_{0,i}$ is respectively the current and initial amount of component, i. Note that for a stoichiometric mixture, the conversion is independent of the component it is based on. As expected from Arrhenius kinetics, the overall reaction rate generally increases with temperature. However, at sufficiently high temperatures, the rate of the backward reaction increases sharply, leading to a net reaction rate of zero. This corresponds to the contour line of zero, defining the equilibrium line. This behaviour is consistent with Le Chatelier's principle, which states that increasing the temperature of an exothermic reaction shifts the equilibrium toward the reactants, thereby limiting the extent of ammonia formation.

Boundary and initial condition

The material and energy balances of the reactor bed, (3.11a) and (3.11b), are supplemented by a set of boundary conditions related to the bed inlet,

$$F|_{z=0} = F_{in}$$
 (3.26a)

$$\dot{H}|_{z=0} = \mathcal{H}(T_{in}, P, F_{in})$$
 (3.26b)

Furthermore, the initial state of the system is required, which is usually a steady-state solution to (3.11a) and (3.11b).

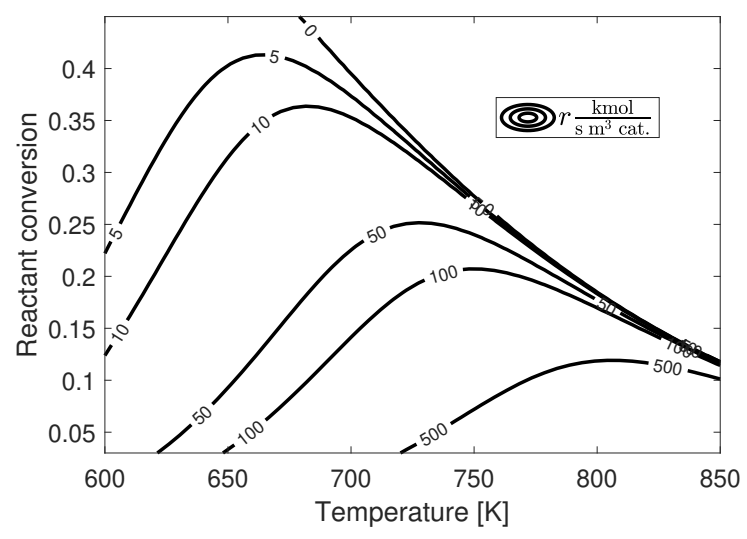


Figure 3.2: Contours of reaction rate of (3.18) in the temperature-conversion plane for a stoichiometric gas mixture of hydrogen and nitrogen at 200 bar pressure.

3.4 Numerical solutions

The PDAE model describing the fixed-bed reactor can be solved by discretising the spatial coordinate. This converts the problem to a system of ordinary differential algebraic equations (DAEs). This study uses the finite volume method (FVM) where the bed is divided into K cells as illustrated in Figure 3.3. Each cell is assumed to be perfectly mixed. The states and algebraic variables are defined in nodes at the cell centres, while the molar and energy fluxes are defined at the nodes at the cell interfaces. The material and energy balances expressed over a finite volume with length, Δl , are,

$$\frac{dc_k}{dt} = \frac{N_{k-1/2} - N_{k+1/2}}{\Delta l} + R_k,$$
(3.27a)

$$\frac{d\hat{u}_{R,k}}{dt} = \epsilon_B \frac{\bar{H}_{k-1/2} - \bar{H}_{k+1/2}}{\Delta l}.$$
 (3.27b)

The mole and enthalpy flux over the interfaces of cell k and k+1 are indexed as k+1/2 and given by an upwind scheme,

$$N_{k+1/2} = v_{k+1/2}c_k$$

$$\left[\frac{\mathsf{mol}}{\mathsf{s}}\right], \tag{3.28a}$$

$$\bar{H}_{k+1/2} = H(T_k, P_k, N_{k+1/2})$$
 $\left| \frac{\mathsf{J}}{\mathsf{s} \, \mathsf{m}^2} \right|,$ (3.28b)

where $v_{k+1/2}$ is the interstitial flow velocity over the cell interfaces. It is deliberately chosen not to include the dispersion term. The FVM method introduces numerical diffusion as the discretisation error, which is exploited to represent the physical dispersion (Froment and De Wilde, 2010). In each cell, the equation of state is invoked by the volume equation,

$$V(T_k, P_k, c_k) = 1. (3.29)$$

Additionally, Eq. (3.30) relates the cell internal energy with the cell temperature, pressure and concentration,

$$\hat{u}_{R,k} = \epsilon_B \hat{u}^g(T_k, P_k, c_k) + (1 - \epsilon_B)\hat{u}^s(T_k).$$
 (3.30)

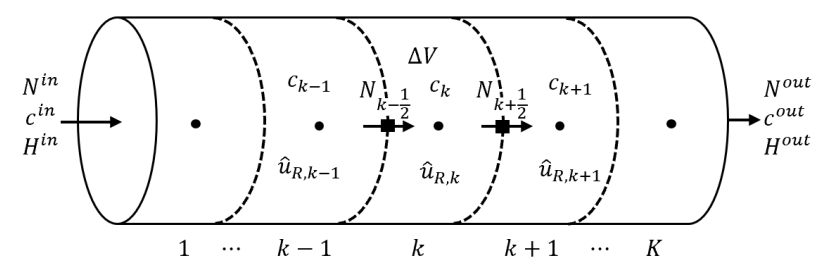


Figure 3.3: Finite volume discretisation of the reactor bed.

3.4.1 DAEs formulation

The governing equations (MBs, EBs and EOSs) for the adiabatic fixed bed and countercurrent cooled reactors constitute a differential algebraic equations (DAEs) system. The states, \mathbf{x}_k , and algebraic variables, \mathbf{y}_k , of the k'th volume element is defined as,

$$\mathbf{x}_k = [c_k, \ \hat{u}_{R.k}],$$
 (3.31a)

$$\mathbf{y}_k = [T_k, v_{k+1/2}, x_k].$$
 (3.31b)

The system is expressed in the general form of a semi-explicit differential algebraic equation,

$$\dot{\mathbf{x}} = f(\mathbf{x}, \mathbf{y}),\tag{3.32a}$$

$$0 = g(\mathbf{x}, \mathbf{y}), \tag{3.32b}$$

in which f constitute the mass and energy balances, and g represents the algebraic equations. For the DAE of the bed,

$$f = \begin{bmatrix} \frac{N_{k-1/2} - N_{k+1/2}}{\Delta l} + R_k \\ \epsilon_B \frac{\bar{H}_{k-1/2} - \bar{H}_{k+1/2}}{\Delta l} \end{bmatrix}$$
(3.33a)

$$g = \begin{bmatrix} x_k c_{tot, k} - c_k \\ \hat{u}_{R,k} - U_R(T_k, P, c_k) \\ \mathcal{V}(T_k, P, c_k) \end{bmatrix}$$
(3.33b)

Solving Eq. (3.32) involves integrating the balance equations while satisfying the algebraic equations. As (3.32) is a highly nonlinear DAE, a numerical solution method is employed.

3.4.2 Solving in time

A first-order Euler scheme is applied for the discretisation in time of the material and energy balance. The Euler step can be solved either explicitly or implicitly, depending on whether the spatial derivatives are approximated at the current or future time step as illustrated in Eq. (3.34).

Explicit:
$$\mathbf{x}^{n+1} = \mathbf{x}^n + f(\mathbf{x}^n, \mathbf{y}^n) \Delta t$$
, (3.34a)

Implicit:
$$\mathbf{x}^{n+1} = \mathbf{x}^n + f(\mathbf{x}^{n+1}, \mathbf{y}^{n+1}) \Delta t$$
, (3.34b)

where Δt is the size of the Euler step.

Explicit method

The studied literature has exclusively utilised the explicit Euler method for integrating i. The explicit method is simple to implement but the stability of the algorithm is restricted by the Courant number, Co,

$$Co = \frac{v\Delta t}{\Delta L},$$
 (3.35a)

for stability :
$$Co \le 1$$
, (3.35b)

Where ΔL is the length of the discretisation cell. Thus, for stability, the time step must be smaller than the residence time of the cell.

In the explicit method, the algebraic equations are used to find explicit relations between the state variables to the algebraic variables.

Implicit Euler method

The implicit Euler method evaluates f and g at the next time step. Thus, (3.34b) and (3.32b) constitute an equation system. The residual function, **R**, is defined as,

$$\mathbf{z} = \begin{bmatrix} \mathbf{x} \\ \mathbf{y} \end{bmatrix},$$
 (3.36a)

$$\mathbf{R} = \mathbf{R}(\mathbf{z}^{n+1}) = \mathbf{R} \begin{pmatrix} \begin{bmatrix} \mathbf{x}^{n+1} \\ \mathbf{y}^{n+1} \end{bmatrix} \end{pmatrix}$$

$$= \begin{bmatrix} \mathbf{x}^{n+1} - \mathbf{x}^n - f(\mathbf{x}^{n+1}, \mathbf{y}^{n+1}) \Delta t \\ g(\mathbf{x}^{n+1}, \mathbf{y}^{n+1}) \end{bmatrix},$$
(3.36b)

A solution to the implicit Euler step is the roots of \mathbf{R} . In this work, Newton's method is used to solve $\mathbf{R} = \mathbf{0}$. Newton's iteration matrix, M, is constructed via the partial derivatives,

$$M = \frac{\partial \mathbf{R}}{\partial \mathbf{z}} = \begin{pmatrix} \frac{\partial \mathbf{R}}{\partial \mathbf{x}} & \frac{\partial \mathbf{R}}{\partial \mathbf{y}} \end{pmatrix} = \begin{pmatrix} I - \frac{\partial f}{\partial \mathbf{x}} \Delta t & -\frac{\partial f}{\partial \mathbf{y}} \Delta t \\ \frac{\partial g}{\partial \mathbf{x}} & \frac{\partial g}{\partial \mathbf{y}} \end{pmatrix}.$$
 (3.37)

where I is the identity matrix. Newton's iteration method starts with an initial guess for the solution, \mathbf{z}_0^{n+1} . A better approximation is obtained at iteration w+1 via,

$$\mathbf{z}_{w+1}^{n+1} = \mathbf{z}_{w}^{n+1} - \left(M\left(\mathbf{z}_{w}^{n+1}\right)\right)^{-1} \mathbf{R}\left(\mathbf{z}_{w}^{n+1}\right),$$
 (3.38)

When the infinity norm for the absolute value of the normalized elements in $\bf R$ is smaller than a predetermined value, e, the solution is assumed to have converged,

$$L_{\infty} \left| \frac{\mathsf{R}}{\mathsf{R}^{norm}} \right| \le e, \tag{3.39}$$

The normalization vector \mathbf{R}^{norm} insures equal weighting of the equations contained in \mathbf{R} . In this work, a tolerance of $e=10^{-5}$ was used. This is at least two orders of magnitude smaller than the discretisation error.

In the implicit formulation, the algebraic equations and variables can be kept as a part of the equation system or expressed explicitly. The implicit handling of the algebraic variables involves a larger system of equations. On the other hand, expressing the algebraic variables explicitly reduces the number of equations but typically also leads to a denser iteration matrix and steeper derivatives.

3.5 The simulation case

The dimensions of the bed are adopted from Rosbo et al. (2023b), where dynamic simulation of a 3-bed quench-cooled ammonia reactor with heat exchange was investigated. The bed dimensions and feed gas properties in table 3.1 and 3.2 correspond to the first reactor bed in Rosbo et al. (2023b).

Table 3.1: Bed dimensions.

$\overline{\text{Length, }L,}$	Diameter, D_R , [m]	Bed porosity, ϵ_B	Particle diameter, d_p
1.24 m	1.2 m	0.33	8 mm

Table 3.2: Bed feed conditions.

Temperature, T_{in} [K]	670
Pressure, P [bar]	200
Feed flow, F_{in} , [kmol/(s)]	1.922
Compositions:	
$N_2, x_{N_2},$	0.2326
$H_2, x_{H_2},$	0.6977
NH_3 , x_{NH_3} ,	0.0405
Ar, x_{Ar} ,	0.0293

3.6 Results: Steady-State

The steady-state solution for the fixed-bed can be found by solving,

$$0 = f(\mathbf{x}, \mathbf{y}), \tag{3.40a}$$

$$0 = q(\mathbf{x}, \mathbf{y}), \tag{3.40b}$$

Eq. (3.40) is solved via Newton's method, similar to the solution procedure described in Section 3.4.2. The full algorithm is provided in Appendix B. The steady-state is solved for the case defined in Section 3.5 with K=80 discretisation cells. Figure 3.4a shows the steady-state profiles of the bed temperature and hydrogen conversion, $X_{\rm H_2}$, along the reactor length. The exothermic ammonia formation leads to a continuous temperature rise, which accelerates the reaction rate, as reflected by the initially steepening slope of the conversion profile. However, the reaction equilibrium soon restricts the rate, limiting the overall hydrogen conversion to approximately 18%. This effect is further illustrated in Figure 3.4b, which plots conversion against temperature and highlights the sharp decline in reaction rate as equilibrium conditions are approached.

Figure 3.5 illustrates the bed outlet temperature and hydrogen conversion as functions of the bed inlet temperature. As expected, the outlet temperature increases nonlinearly with the inlet temperature. The hydrogen conversion, however, shows a more interesting behaviour, revealing a distinct optimum around $T_{bed,\,in}=670\,\mathrm{K}$ (corresponding to the base case with profiles presented in Figure 3.4). This reflects the trade-off between operating at lower inlet temperatures, which provides more "room" for conversion before equilibrium is reached but also slows down the reaction rate, and higher inlet temperatures, which accelerate the initial reaction but quickly push the system to equilibrium.

Figures 3.6a and 3.6b show the temperature and conversion profiles along the reactor length for different inlet temperatures. At a low bed inlet temperature, the reaction rate

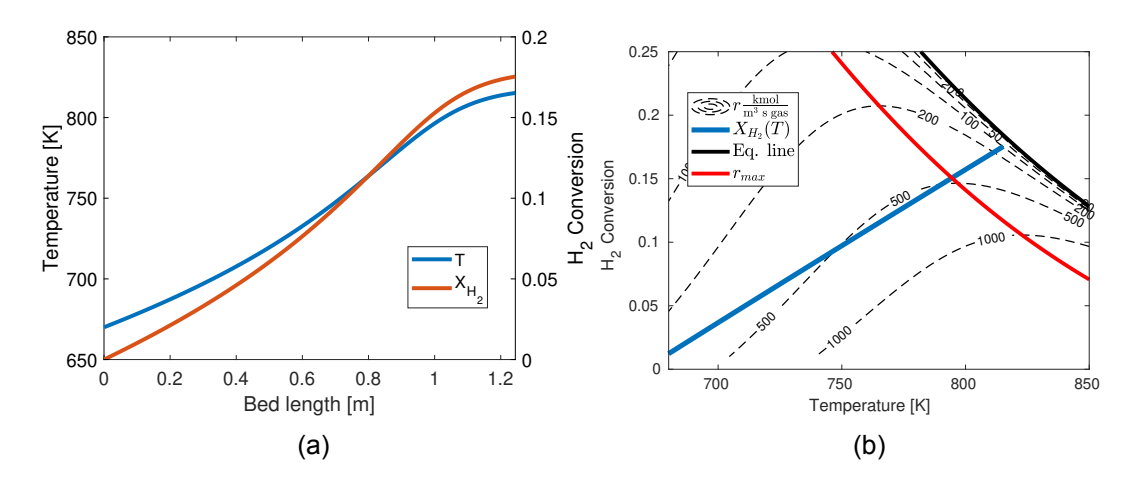


Figure 3.4: a) Steady-state profiles for bed temperature and reactant conversion along the bed length. b) Bed outlet temperature and conversion for varying inlet temperature (K=80 cells).

is too slow and conversion remains limited throughout the bed (See curve for $T_{bed,\,in}=630\,\mathrm{K}$). In contrast, at high bed inlet temperature, conversion rises rapidly towards equilibrium near the inlet, leaving a substantial portion of the reactor volume underutilised, as illustrated by the curve corresponding to $T_{bed,\,in}=720\,\mathrm{K}$.

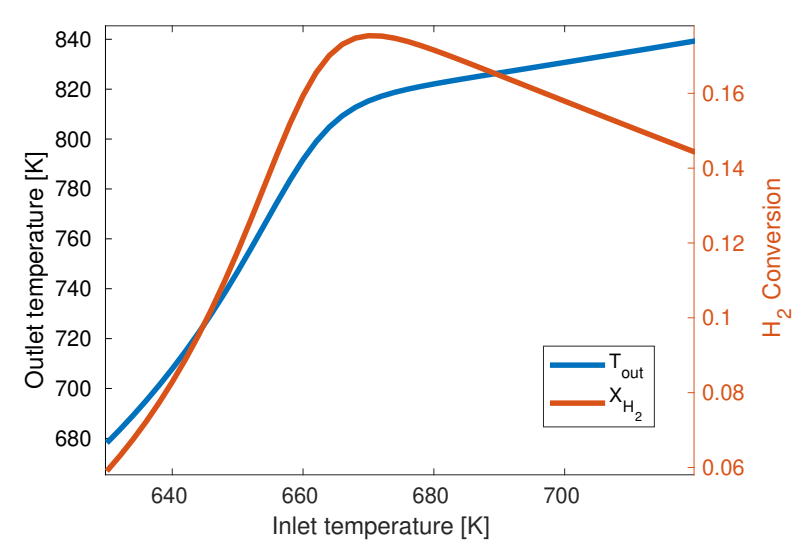


Figure 3.5: Bed outlet temperature and conversion for varying inlet temperatures. (K=80 cells)

3.7 Results: Dynamic analysis

The study investigates the system response to a step disturbance of 10 K in the feed temperature, T_{in} . The system is simulated for 3 min of physical time.

3.7.1 Size of the time step

Equation (3.35a)-(3.35b) defines the stability limit of the explicit method. Inserting the feed properties in the volume function in ThermoLib and dividing by the void cross-sectional

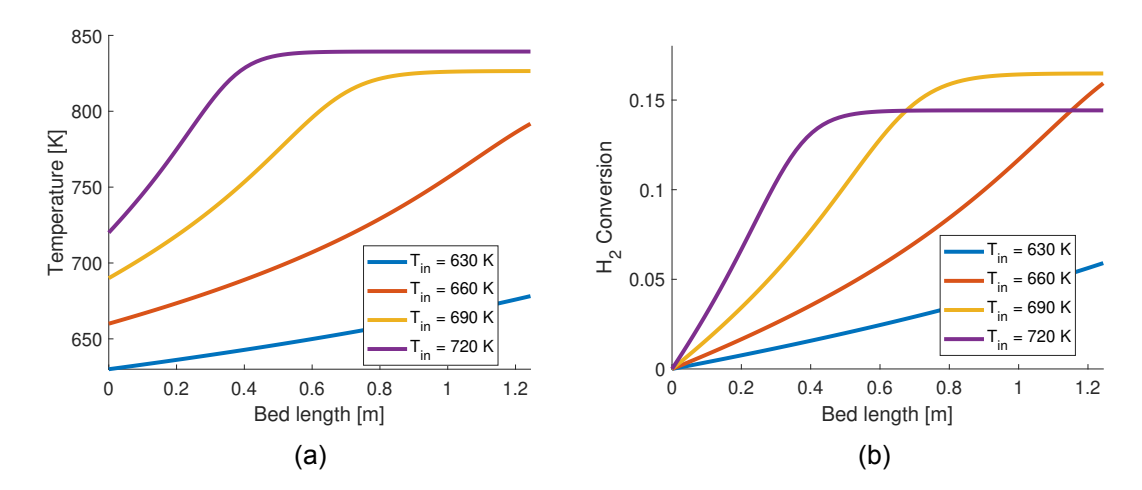


Figure 3.6: a) Steady-state profiles of bed temperature and b) conversion for different bed inlet temperatures. (K = 80 cells)

area, A_c^g , yields the interstitial gas velocity at the inlet to the bed,

$$v_{in} = \frac{\mathcal{V}(T_{in}, P, F_{in})}{A_c^g} = \mathcal{V}(T_{in}, P, N_{in}) = 0.92 \text{m/s}$$
 (3.41)

Considering the interstitial velocity and the length of the bed, the residence time of the reactor bed, τ , is approximately,

$$au pprox rac{L}{v_{in}} = rac{1.24 \text{m}}{0.92 \text{m/s}} = 1.35 \text{s}$$
 (3.42)

The flow velocity increases only slightly throughout the bed, as the acceleration caused by the temperature rise is largely counterbalanced by the net consumption of molecules in reaction (3.16). Consequently, when using a fixed time step of $\Delta t = 1/K$ for the explicit method, the step size remains below the numerical stability limit. For the implicit methods, larger time steps are feasible from a stability perspective, but this comes at the expense of numerical accuracy.

Figure 3.7a displays the simulated step response of the bed outlet temperature for an increasing size of the time step (with K=80 cells). The response shows an initial decrease in the bed outlet temperature (inverse response) to the 10 K step increase in the inlet temperature. This is a known phenomenon for exothermic fixed-bed reactors. The maximum numerical error compared to a refined solution is shown in Figure 3.7b. The dotted line has unit slope, illustrating the first-order global error of the Euler scheme. It is observed that for a step size of $\Delta t=20/K$, the maximum error is well below 1 K, and the bed response is almost identical to those with smaller time steps. This accuracy with $\Delta t=20/K$ is below the errors expected from the simplifying assumption A1-A3. For $\Delta t=100/K$ the bed response begins to deviate significantly from the finer temporal discretisations and the inverse response, i.e. the initial temperature drop, is not captured properly. In summary, the analysis indicates that integrating with a time step less than $\Delta t=20/K$ appears to yield reasonable numerical accuracy in the simulations. Thus, in the following analysis, a time step of $\Delta t=10/K$ is used for the implicit methods, yielding a good trade-off between numerical accuracy and computational efficiency.

3.7.2 Spatial refinement

Figure 3.8 displays the bed outlet temperature response to the 10 K inlet temperature step change for increasing refinement of the spatial discretisation. The inverse temperature

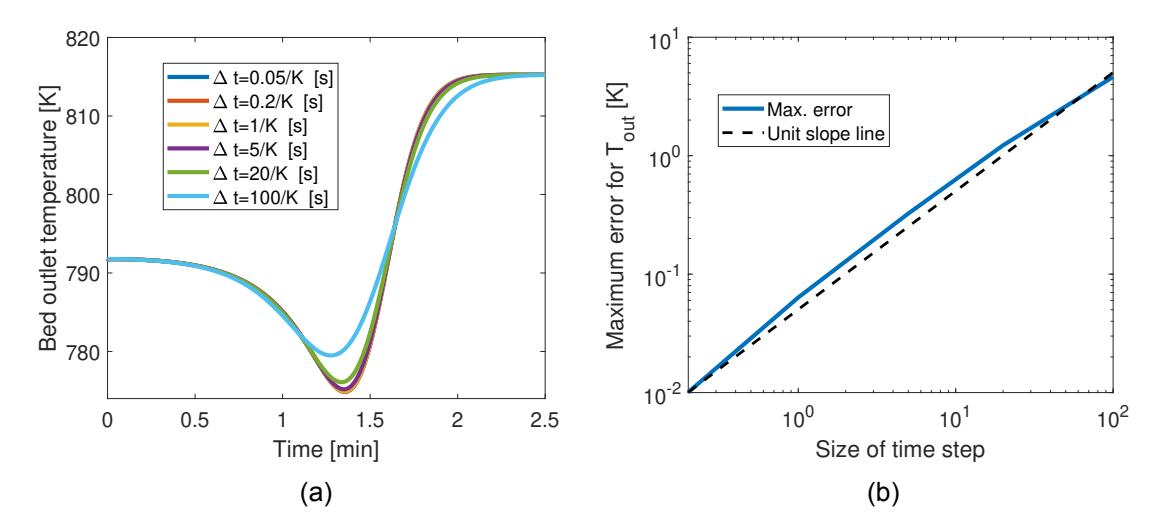


Figure 3.7: a) Bed outlet temperature response to a 10 K step increase in the inlet temperature simulated with different temporal discretisations. b) Maximum error in the outlet temperature as a function of the time step size.

response is larger and narrower for a higher number of cells. The FVM method introduces numerical diffusion as the truncation error of the spatial discretisation (Froment and De Wilde, 2010).

Nummerical diffusion

The numerical diffusion is not identical to a physical dispersion term, but the properties of the solution are very similar. The broadening of the inverse response when simulating with a coarse spatial discretisation resembles the effect of large axial dispersion. Froment and De Wilde (2010) suggests simulating the physical dispersion with numerical diffusion by using an equal standard deviation of the residence time distribution for a series of perfectly mixed reactors (cells) and the analytical solution to a pure diffusion/advection problem. The Peclet number, Pe, is a dimensionless quantity reflecting the ratio between advective and dispersive transportation,

$$Pe = \frac{vL}{D_L} \tag{3.43}$$

where, D_L , is the axial dispersion and L is the bed length. For a given Peclet number, when the Reynolds number, Re, is larger than 2, using

$$K \cong Pe/2 + 1/2 \quad Re > 2$$
 (3.44)

discretisation cells yields an identical standard deviation to the analytical solution of the diffusion/advection problem. At high Reynolds numbers (${\rm Re}>2000$) the axial dispersion from backmixing in packed beds can be approximated by Delgado (2006); Edwards and Richardson (1968),

$$D_L = \frac{1}{2}vd_p \quad \text{Re} > 2000$$
 (3.45)

in which d_p is the diameter of the catalyst particles. Given the properties of the bed feed gas, the Reynolds number at the bed inlet is,

$${\rm Re} = \frac{v d_p \rho^g}{\mu^g} = \frac{0.92 \ {\rm m/s} \cdot 8 \cdot 10^{-3} \ {\rm m} \cdot 33.86 \ {\rm kg/m^3}}{2.78 \cdot 10^{-5} \ {\rm Pa \ s}} = 13,407 \tag{3.46}$$

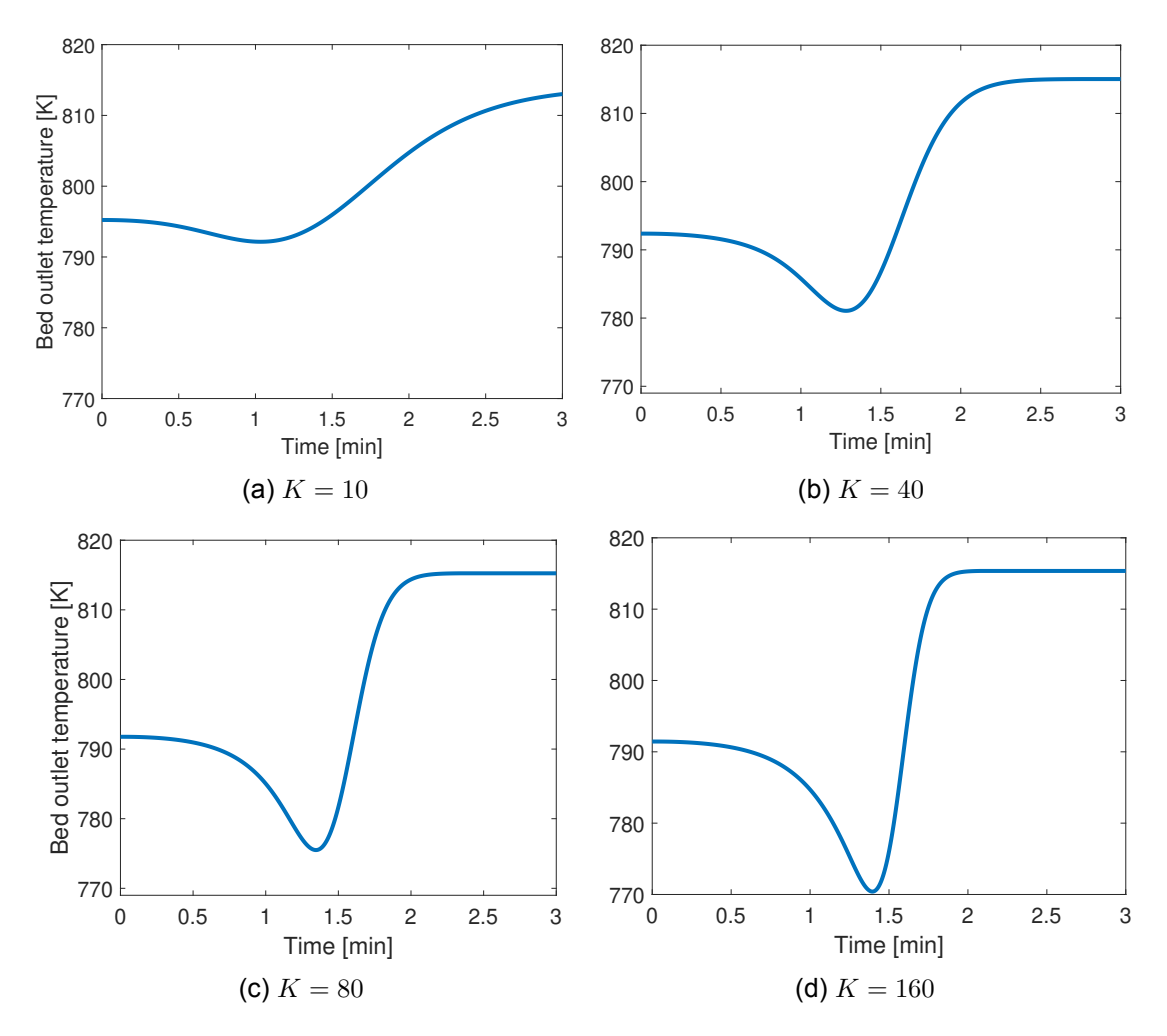


Figure 3.8: Step response for the bed outlet temperature to a 10 K step change in inlet temperature with spatial discretisation of a) 10 cells, b) 40 cells, c) 80 cells, and d) 160 cells.

here ρ^g is the gas density and μ^g is the gas viscosity calculated with the correlations presented in Poling et al. (2001). Through the bed, the Reynolds number is only increasing (as the flow velocity increases). Thus, the bed is well within the regime where (3.45) is applicable. Inserting (3.43) and (3.45) in (3.44),

$$K = \frac{\text{Pe}}{2} + \frac{1}{2} = \frac{vL}{2D_L} + \frac{1}{2} = \frac{L}{d_p} + \frac{1}{2} = \frac{1.2441\text{m}}{8.00 \cdot 10^{-3}\text{m}} + \frac{1}{2} = 156.0$$
 (3.47)

Therefore, to accurately approximate physical dispersion through numerical diffusion, the bed must be discretised into 156 cells. In typical fixed-bed gas-phase reactions, the ratio of bed length to particle diameter, L/d_p , is between 100 and 500. If the physical dispersion term were to be explicitly included in the model, a substantially finer discretisation would be required to sufficiently suppress the influence of numerical diffusion.

3.7.3 Computational efficiency

Section 3.7.2 showed that typically 100–500 discretisation cells are required to approximate physical dispersion through numerical diffusion. Such a fine discretisation entails considerable computational effort. Consequently, it is essential to identify numerical methods that allow fast and efficient dynamic simulations of the fixed-bed DAE system.

Numerical formulations

In section 3.4.2, the bed model was presented as a DAE model with concentration and internal energy as the state variables, $\mathbf{x}_k = [c_k, \ \hat{u}_{R,k}]$, and temperature, interfacial velocities, and mole fractions as the algebraic variables, $\mathbf{y}_k = [T_k, \ v_{k+1/2}, \ x_k]$. As mentioned in Section 3.1, the literature often employs explicit schemes, expressing the system as a pure ODE by eliminating the algebraic equations. The fixed-bed model in ODE form is,

$$\frac{dc_k}{dt} = \frac{N_{k-1/2} - N_{k+1/2}}{\Delta l} + R_k, \tag{3.48a}$$

$$\frac{dT_k}{dt} = \frac{A^g \hat{h}_{k-1} v_{k-1/2} - A^g \hat{h}_k v_{k+1/2} - \left(\frac{\partial U_k^g}{\partial n}\right) (a_k - A^g c_k v_{k+1/2})}{\left(\frac{\partial U_k}{\partial T}\right)},$$
(3.48b)

in which, a_k , is defined as,

$$a_k = A^g c_{k-1} v_{k-1/2} + V_k^g R_k. (3.49)$$

And the velocity across the cell surfaces

$$v_{k+1/2} = \frac{\phi_T \,\hat{h}_{k-1} \,v_{k-1/2} \,+\, \frac{\phi_n}{A_g} \,a_k}{\phi_T \,\hat{h}_k \,+\, \phi_n \,c_k} \tag{3.50}$$

with

$$\phi_{T} = \frac{\left(\frac{\partial V_{k}^{g}}{\partial T}\right)}{\left(\frac{\partial U_{k}}{\partial T}\right)}, \qquad \phi_{n} = \left(\frac{\partial V_{k}^{g}}{\partial n}\right) - \frac{\left(\frac{\partial V_{k}^{g}}{\partial T}\right)}{\left(\frac{\partial U_{k}}{\partial T}\right)} \left(\frac{\partial U_{k}^{g}}{\partial n}\right)$$
(3.51)

Equations (3.48)-(3.51) are not trivial to derive, but the derivation is presented in Appendix A.

When integrating the bed DAE with an implicit Euler method, the solution already requires solving a system of equations, as described in Section 3.4.2. Hence, the algebraic equations may be retained and included in the equation system.

In this work, five different numerical implementations of the Euler step are investigated, as summarised in Table 3.3. This includes one explicit Euler scheme and four implicit Euler schemes, which differ in the number of algebraic equations and variables incorporated into the solution system.

Table 3.3: Numerical implementation methods

Method	E1	11	12	13	
States	c, T	c, \hat{u}_R	c, \hat{u}_R	c, \hat{u}_R	$ c, \hat{u}_R $
Algebraic Variables	-		T, x	$\mid T, v \mid$	$\overline{\mid T, x, v \mid}$

Figure 3.9 displays the size and sparsity of the iteration matrices for the implicit formulations. The iteration matrices are all illustrated for a discretisation with K=10 cells. Naturally, the size of the derivative matrix increases when more algebraic equations and variables are included in the formulation. However, eliminating algebraic variables leads to a denser structure of the iteration matrix. Figure 3.9a show the matrix structure for a formulation where only T is incorporated as an algebraic variable. Observe that, especially

expressing the flow velocities as a function of c and T (Eq. 3.50) increases the number of dense elements in the iteration matrix. Changes in the states in the upstream cell are influencing the velocities down the bed – hence the staircase structure. Figure 3.9c and 3.9d show the iteration matrix structure when solving for v during the implicit Euler step. These matrices are sparser than 3.9a and 3.9b, and therefore better performance is expected for these formulations.

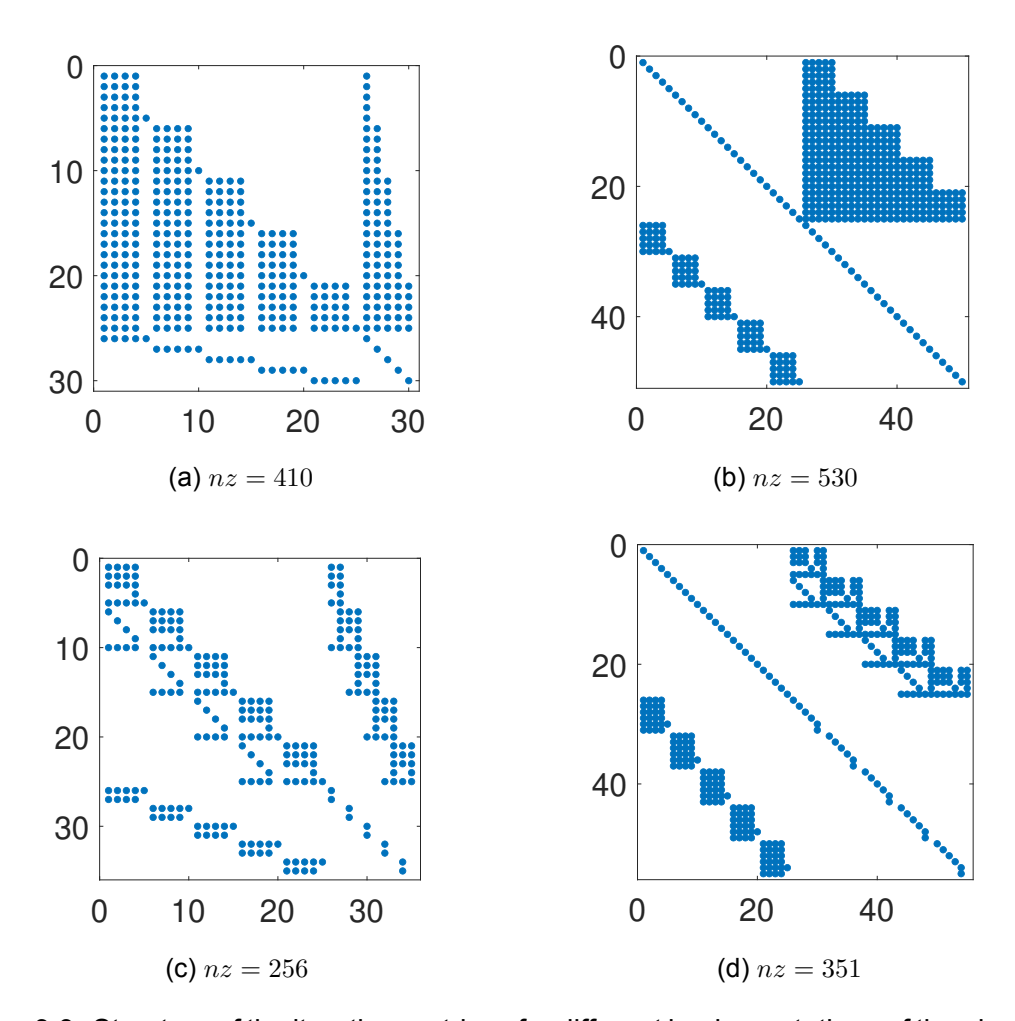


Figure 3.9: Structure of the iteration matrices for different implementations of the algebraic equations in g: a) I1, b) I2, c) I3, and d) I4. The number, nz, denotes the number of non-zero elements.

Comparison of integration time

Figure 3.10 shows the computational time required to simulate the three-minute step response as a function of the number of discretisation cells for each numerical formulation. The results reveal substantial differences in algorithmic efficiency. The methods that calculate flow velocity via Eq. (3.50) are significantly more computationally demanding due to the lack of sparsity in their iteration matrices. As illustrated in Figures 3.9a and 3.9b, the number of non-zero elements for I1 and I2 scales with the square of the number of discretisation cells, K^2 , which leads to a steep increase in computational cost as the spatial resolution is refined.

The computational time of the sparse methods (I3 and I4) scales approximately linearly with the number of discretisation cells, with I3 demonstrating slightly better performance

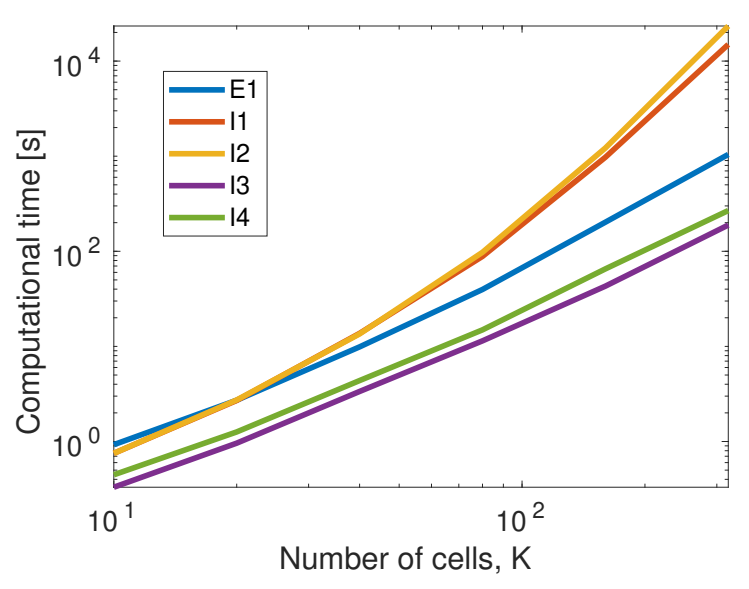


Figure 3.10: Computational time versus the number of cells for simulating 3 min physical time of a step response. The curves represent the five different numerical formulations. For the explicit method, $\Delta t = 1/K$, while for the implicit methods, $\Delta t = 10/K$.

than I4. Compared to the traditional explicit method (E1), both I3 and I4 are approximately an order of magnitude faster. Thus, for finer discretisations, the implicit methods, particularly I3, offer a significant computational advantage over the traditional explicit approach.

3.8 Discussion

Section 3.7.2 concludes that a spatial discretisation of 156 cells is necessary to adequately capture the physical dispersion caused by back-mixing in the bed. Figure 3.10 shows that, with 156 cells, the traditional explicit method requires approximately 200 seconds to simulate a 3-minute step response. In contrast, the implicit method I3 completes the same simulation in about 40 seconds. For applications such as advanced control, particularly nonlinear model predictive control (NMPC), it is essential that the model can simulate faster than real time. For a multi-bed ammonia reactor with up to four beds, this becomes particularly challenging when using explicit methods, even with high-performance computing resources. Furthermore, ammonia catalyst manufacturers such as Topsøe report particle sizes in the range of 1.5–3 mm (Topsoe, 2008), which, according to Eq. (3.47), demands even finer spatial discretisation, further increasing the computational load.

One possible approach to achieve feasible computational times is to use a coarser spatial discretisation. While this reduces resolution, the inverse response still appears, but with a smaller peak and broader profile. However, Rosbo et al. (2023b) investigated the stability of ammonia reactors and highlighted that the inverse response plays a critical role in determining the overall stability of the reactor system with inter-bed heat exchange. Therefore, relying on coarse discretisation may lead to an underestimation of key dynamic behaviours, potentially overlooking important stability concerns in the ammonia synthesis loop.

3.9 Conclusion

This chapter developed a partial differential—algebraic equation (PDAE) model for a fixed-bed gas-phase reactor, discretised in space using the finite volume method (FVM). Dispersion effects from back-mixing were not implemented explicitly, but instead approximated through numerical diffusion, requiring more than 100 cells. This highlighted the importance of efficient numerical methods. Five numerical schemes for the Euler time-integration step were evaluated: one traditional explicit formulation and four implicit formulations differing in the number of algebraic equations and variables treated implicitly. The performance of these schemes was assessed by simulating the reactor response to a step change in inlet temperature. The results revealed substantial differences in computational efficiency, with the most efficient implicit method achieving a speed-up of approximately five times compared to the traditional explicit scheme, while the slowest implicit method was about six times slower. These findings underscore the importance of selecting an appropriate numerical formulation when simulating the reactor model for dynamic studies.

Chapter 4

Adiabatic Quench Cooled Reactor for Power-to-Ammonia

This chapter discusses the operation of an ammonia reactor system for a Power-to-Ammonia (PtA) plant. A dynamic model is developed for the reactor system, consisting of a three-bed quench-cooled adiabatic reactor and a feed-effluent heat exchanger. The reactor bed model is formulated as a system of differential-algebraic equations (DAEs). Rigorous thermodynamic properties of the high-pressure ammonia reactor are modelled using the Thermolib software package.

A case study is presented for an ammonia synthesis loop in a PtA plant connected to a 250 MW renewable energy source with a capacity factor of 0.4. Static optimisation and stability analysis are carried out for the reactor system, identifying an optimal operating point located close to the stability boundary. Dynamic simulations confirm the presence of unstable operating regions, where severe oscillations arise under small perturbations.

Due to the fluctuating nature of renewable energy, the ammonia reactor is required to operate across a wide operating window ranging from 20–120% of nominal capacity. A strategy is formulated for varying the feed supply of hydrogen and nitrogen to the synthesis loop, based on the available renewable power. Open-loop simulations show that load changes in the synthesis feed result in dynamic oscillations in the reactor system. To mitigate this, a regulatory control structure is proposed to stabilise the reactor response. The control architecture incorporates an optimisation algorithm that determines the desired reactor set-point at each change in synthesis loop load. As a result, fast regulatory control and accurate tracking of the reactor set-points are achieved, ensuring stable and efficient operation of the ammonia reactor under highly flexible conditions.

In summary, this chapter provides the answers to research question 1.

This chapter contains material from the article:

Rosbo, J. W., Ritschel, T. K. S., Hørstholt, S., Huusom, J. K., Jørgensen, J. B. (2023). Flexible operation, optimisation and stabilising control of a quench cooled ammonia reactor for Power-to-Ammonia. Computers & Chemical Engineering, Volume 176(108316). doi: https://doi.org/10.1016/j.compchemeng.2023.108316

4.1 Introduction

As outlined in Sections 2.7 and 2.8, previous research on optimisation and control of ammonia reactors has primarily focused on conventional large-scale plants. These studies generally consider only small and infrequent disturbances, consistent with traditional operation where hydrogen is supplied from steam methane reforming. In contrast, green power-to-ammonia (PtA) plants are directly coupled to intermittent renewable energy, resulting in continuously fluctuating energy availability. Consequently, the reactor feed flow can vary significantly on an hourly basis, requiring operation across the entire load range, from 20% up to 120% of nominal capacity (Armijo and Philibert, 2020). Such variability is fundamentally incompatible with the conservative operating strategies employed in traditional plants (Verleysen et al., 2021).

This creates a clear need for new strategies that enable stable and efficient reactor operation under flexible conditions. To address this, the present chapter investigates an adiabatic quench-cooled ammonia reactor within a 100 MW PtA plant. The reactor is modelled by combining the fixed-bed model developed in Chapter 3 with a heat-exchanger model. Dynamic simulations demonstrated the complex nonlinear dynamics of the AQCR, illustrating key challenges such as oscillatory dynamics and reactor shutdowns.

A detailed stability analysis is conducted to identify unstable regions and define safe operating margins. Building on this, the reactor is optimised across a wide range of feed flows to establish an optimal load-change strategy. Finally, this strategy is coupled with a control structure that enables robust dynamic regulation of the reactor system across the full operating envelope.

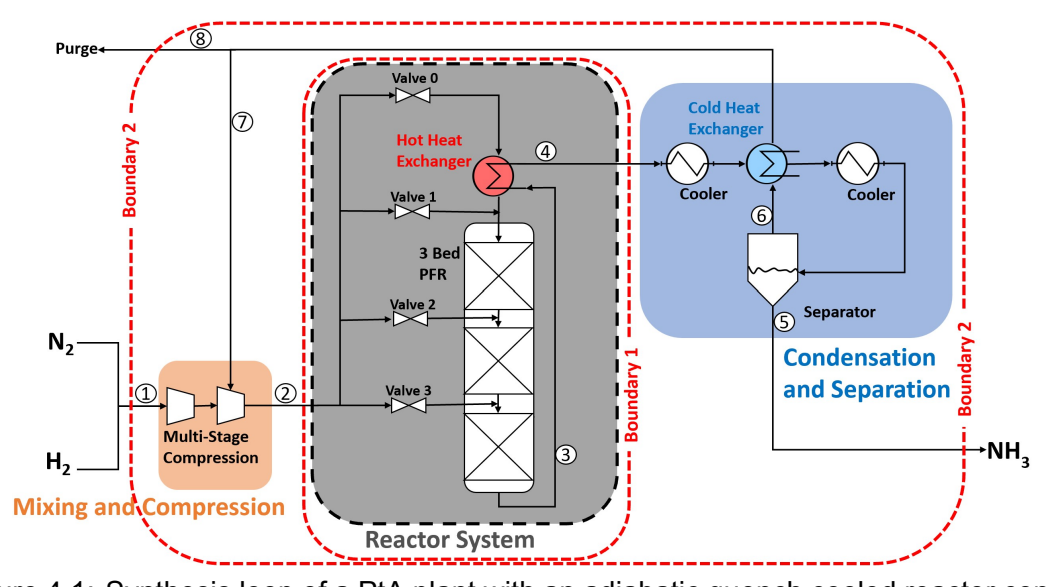


Figure 4.1: Synthesis loop of a PtA plant with an adiabatic quench cooled reactor configuration. A *boundary* is defined around the reactor system with stream 2 and 4 as respectively the inlet and outlet streams. The synthesis loop is supplied with a fresh feed stream (1) while material is exiting boundary 2 via the purge stream (8) and ammonia product stream (5).

4.2 AQCR model

Figure 4.1 present a schematic illustration of the synthesis loop in a PtA plant. The reactor is an AQCR configuration as AQCRs are the most common reactor type in the industry

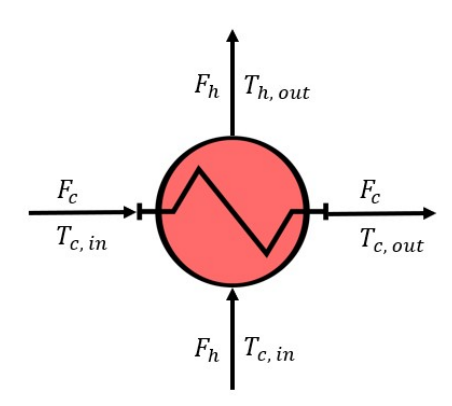


Figure 4.2: Illustration of the flows in and out of the heat exchangers.

and well described in the literature (Inamuddin et al., 2020; Morud and Skogestad, 1998; Cheema and Krewer, 2018; Rabchuk et al., 2014). The reactor system consists of 3 concurrent reactor beds with an injection of a quench stream between beds. The heat released from the ammonia synthesis reaction is partly recovered via the feed-effluent heat exchanger. The exit from the feed-effluent exchanger (Stream 4), is further cooled and enters the separator where liquid ammonia is recovered.

Due to equilibrium limitations, the single-pass conversion of the reactor is around 25%. Hence, a relatively large recycling of reactants is required. A fraction of the recycle is purged (stream 8) to avoid accumulating inert gasses (argon).

4.2.1 Fixed-bed

The fixed-bed model is described in Chapter 3.

4.2.2 Heat exchangers

Heat integration of the HB process is used at several points within the reactor system (iHex 1 and 2) and for pre-heating of the reactor feed (eHex 1). The heat exchangers are counter-current units with two feeds; a hot side inlet flow F_h with temperature $T_{h,\ in}$, and a cold side inlet flow F_c with temperature $T_{c,\ in}$. Figure 4.2 displays a diagram of the heat exchanger unit.

The dynamics of the heat exchangers are fast relative to the catalytic beds. Therefore, the heat exchanger is assumed at steady-state. The heat exchangers are modelled with the ε -NTU model, which has often been used for modelling heat exchange in ammonia synthesis (Cheema and Krewer, 2018; Morud and Skogestad, 1998). The ε -NTU model gives outlet temperatures via,

$$T_{c, out} = \varepsilon T_{h, in} + (1 - \varepsilon) T_{c, in}, \tag{4.1a}$$

$$T_{h, out} = T_{h, in} - C(T_{c, out} - T_{c, in}),$$
 (4.1b)

in which ε is the effectiveness. For counter-current flow an analytical expression for ε has been derived, Holman (2002),

$$\varepsilon = \frac{1 - \exp\left(-\mathsf{NTU}(1-C)\right)}{1 - C \exp\left(-\mathsf{NTU}(1-C)\right)}. \tag{4.2}$$

The number of transfer units, NTU, and the heat capacity ratio, C, are calculated from,

$$\mathsf{NTU} = \frac{U_{hex} A_{hex}}{C_{p,\,c}},\tag{4.3a}$$

$$C = \frac{C_{p, c}}{C_{p, h}},$$
 (4.3b)

in which \mathcal{C}_p is the absolute heat capacity of the streams. The absolute heat capacity is the derivative of the enthalpy with respect to temperature,

$$C_{p, c} = \frac{\partial \mathcal{H}}{\partial T}(\bar{T}_c, P, F_c),$$
 (4.4a)

$$C_{p, h} = \frac{\partial \mathcal{H}}{\partial T}(\bar{T}_h, P, F_h).$$
 (4.4b)

where \bar{T} is the mean temperature given by,

$$ar{T_c} = rac{T_{c, in} - T_{c, in}}{2}$$
 (4.5a)

$$ar{T_h} = rac{T_{h, in} - T_{h, out}}{2}.$$
 (4.5b)

Eq. (4.1) are solved as algebraic equations with $T_{c, out}$ and $T_{h, out}$ as algebraic variables.

4.2.3 Mixing

The mixing of streams is especially relevant for introducing the quench flows in the AQCR. Given streams m1 and m2 entering a mixing point and stream m3 exiting, the mixing material energy balances are,

$$F_{m3} = F_{m1} + F_{m2},$$
 (4.6a)

$$\mathcal{H}(T_{m3}, P, F_{m3}), = \mathcal{H}(T_{m1}, P, F_{m1}) + \mathcal{H}(T_{m2}, P, F_{m2}).$$
 (4.6b)

The temperature after mixing, T_{m3} , is found by solving Eq. (4.6b) via Newton's method.

Reactor feed split

The split of the reactor feed stream for introducing the AQCR quench between beds are numbered 0-3. The feed split over valve j is described mathematically by the split fraction, q_{Rj} ,

$$F_{Rfj} = q_{Rj}F_{Rf}, (4.7)$$

where F_{Rfj} is the total flow through valve j.

4.2.4 Separator and purge

The large difference in boiling points between NH₃ and the other components (H₂, N₂, Ar) justifies assuming the ammonia product stream (S5) is pure. Thus, one may model the separator by a simple split model where a fraction q_S of the NH₃ from the reactor product stream (S3) is condensed

$$F_{S5, NH_3} = q_S F_{S4, NH_3},$$
 (4.8a)

$$F_{S6, NH_3} = (1 - q_S)F_{S4, NH_3}.$$
 (4.8b)

The purge stream, F_{S8} , is a splitting from the recycle stream, F_{S6} , by the purge fraction q_p ,

$$F_{S7} = (1 - q_p)F_{S6},$$
 (4.9a)

$$F_{S8} = q_p F_{S6}.$$
 (4.9b)

4.3 The case study

The case study is based on a 250 MW full-load renewable energy source with a capacity factor (CF) of 0.4. That is, an average power of 100 MW is supplied to the PtA plant. In compliance with the studied literature, the electrolyser unit is assumed to utilise 92% of the generated electrical energy at stoichiometric H_2/N_2 feed ratio (Rosbo et al., 2023a; Armijo and Philibert, 2020). Hydrogen is assumed to be produced in the electrolyser at a cost of 48 MWh/ton, corresponding to an electrolyser efficiency of 67% compared with the low heating value of H_2 . Thus the average production of H_2 is,

$$\langle \dot{m}_{\rm H_2} \rangle = \frac{100 {\sf MW} \cdot 92\%}{48 {\sf MWh/ton}} = 1.92 {\sf ton/h}$$
 (4.10)

The ammonia reactor size is scaled 20% larger relative to the average hydrogen feed flow to enable operation during periods that exceed the average hydrogen feed flow. This reactor volume is likely to represent an economically reasonable catalyst volume in the context of PtA operations (Maggi et al., 2023). This yields a NH₃ full-load capacity of,

$$\dot{m}_{\rm NH_3}^{FL} = \langle \dot{m}_{\rm H_2} \rangle \cdot 120\% \cdot \frac{2M_{\rm NH_3}}{3M_{\rm H_2}} = 10.80 \ {\rm ton/h}. \tag{4.11}$$

With this, the capacity factor of the ammonia reactor is $CF_{Reac.} = \frac{1}{120\%} = 0.833$.

4.3.1 Reactor system dimensions

The full-load capacity of the ammonia reactor is denoted as the nominal operating point. The reactor size and feed flow are scaled relative to the ammonia production rate reported in Morud and Skogestad (1998) for a commercial-size plant. This yields the reactor dimensions and feed flow as tabulated in Table 4.1. Additionally, argon, omitted by Morud and Skogestad (1998), is added to the reactor feed, and the flow rates are converted to kmol/h to comply with the mathematical description of the bed model. Note, the hydrogen feed flow given in Eq. 4.10 refers to the synthesis loop feed (Figure 4.1: Stream 1), while the flow given in table 4.1 relates to the reactor feed (Figure 4.1: Stream 2).

The splitting of the reactor feed through the quench valves is given in (4.12).

$$q_R = [0.579, 0.195, 0.118, 0.108]$$
 (4.12)

Properties of the catalyst bed are for consistency likewise adopted from Morud and Skogestad (1998) and displayed in Table 4.2.

Table 4.1: Bed dimensions and reactor feed gas conditions.

Specification	Bed 1	Bed 2	Bed 3
Length, L [m]	1.24	1.79	2.83
Diameter, D_{in} [m]	1.20	1.20	1.20
Bed porosity, ϵ_p	0.33	0.33	0.33

Reactor feed condition	Value
Temperature [°C]	250
Pressure [bar]	200
Total flow, F_{fR} , [kmol/h]	5846
x_{N_2} [mol%]	23.6
x_{H_2} [mol%]	69.7
x_{NH_3} [mol%]	4.1
x_{Ar} [mol%]	2.9

The values of the heat transfer coefficient, U_{hex} , and heat exchanger contact area, A_{hex} , are given in Table 4.3.

Table 4.2: Catalyst properties.

Catalyst properties	
Туре	Metalic iron on Fe ₃ O ₄
Density [kg/m ³]	3284
Heat capacity [J/(kg K)]	1100
Particle hydraulic diameter [mm]	6-10

Table 4.3: Properties of the heat exchanger

Heat Transfer Coefficient, U_{hex}	Heat exchanger area, A_{hex}
${}$ 536 $\left[\frac{W}{m^2K}\right]$	61.0 [m ²]

4.4 Results: Reactor system (Boundary 1)

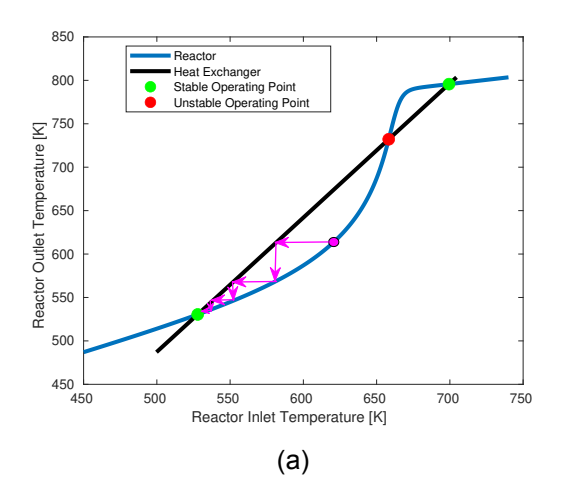
Consider the reactor system part of the ammonia synthesis defined by the boundary around the grey box in Figure 4.1. The reactor system is the main bottleneck of the synthesis loop as the reactor conversion governs the ammonia production rate.

4.4.1 Reactor system steady-state

The steady-state (SS) equation system of a reactor bed can be found by setting the time derivative of the material (3.11a) and energy (3.11b) balance equal to zero. A possible steady-state solution for the reactor system exists when both the reactor and heat exchanger equations are satisfied. The van Heerden plot seen in Figure 4.3a plots the steady-state reactor outlet versus inlet along with the line of the heat exchanger. A feasible steady-state solution for the reactor system exists at the intersections between the reactor curve and the heat exchanger line. Clearly, three possible steady-state solutions exist; a cold extinguished solution, a hot ignited solution, and an intermediate not fully ignited solution. By van Heerden's analysis, the upper and lower static solutions are stable, while the intermediate steady-state is unstable. The stability of steady-state solutions can be deduced by the stepwise trajectory of a point on the reactor curve, as illustrated via the purple arrows in Figure 4.3a. Figure 4.3b displays the temperature profile along the reactor beds for the upper steady-state. The temperature rise accelerates through the first bed as the reaction rate increases with temperature. In contrast, both the second and third bed approach equilibrium conditions, indicated by the flattening of the temperature profiles towards the outlet of the beds. A comparison of the reactor temperature profile for the model defined in this work and the model used in Morud and Skogestad (1998) is presented in Section 4.7.2.

4.4.2 Multiple steady-states

Returning to the van Heerden plot in Figure 4.3a. One can imagine that varying an operating parameter, e.g. the operating pressure, feed flow rate, and feed temperature, may displace or reshape the reactor curve. The possible static solutions of the reactor system are mapped for an operating parameter by projecting the steady-state solutions onto the y-axis. Figure 4.4 display the S-shaped reactor characteristic constructed by varying the feed temperature. Additionally, Figure 4.4 illustrates the existence of an extinction and ignition point enclosing the region of multiple steady-states. Beyond the ignition and extinction point, only a fully ignited or extinguished solution exists. In the van Heerden plot, the ignition and extinction points correspond exactly to the case where the heat exchanger



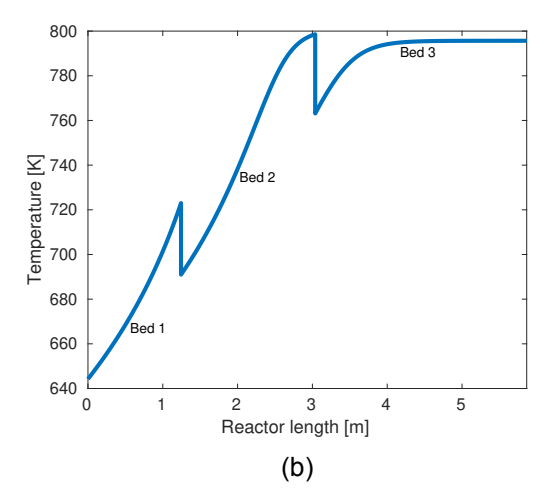


Figure 4.3: a) van Heerden plot depicting the reactor inlet versus outlet temperature and the heat exchanger line. Three possible steady-states exist; A stable upper ignited state, a stable lower extinguished state and a middle unstable state. b) Temperature along the reactor beds for the upper ignited steady-state.

line tangentially touches the reactor curve and the upper or lower steady-state coincides with the intermediate static solution.

4.4.3 Reactor system transient simulations

The classical van Heerden analysis predicts stable reactor operation in the upper steady-state solution branch shown in Figure 4.4, with extinction occurring once the system passes the extinction point. However, subsequent studies have shown that this picture is incomplete. Both industrial observations and detailed simulations (Naess et al., 1992; Morud and Skogestad, 1998) report the onset of self-sustained oscillations in the vicinity of the extinction point. These oscillatory dynamics, branching from the upper steady-state solution, highlight that the van Heerden analysis alone is insufficient for describing reactor stability.

The reactor dynamics is investigated by solving the transient models for the reactor system described in Section 4.2. Figure 4.5 displays the transient response of the reactor outlet temperature and N_2 conversion to step disturbances in the feed temperature. The feed temperature is decreased stepwise by 10 K three times and finally restored to the nominal value. The reactor outlet temperature converges towards a slightly lower steady-state for the initial step disturbance, but clearly displays damped oscillations. The same pattern is observed for the N_2 conversion, but with a negative gain as the conversion is increased. The second step disturbance decreases the feed temperature just above the extinction point, which, according to van Heerden's analysis, is a stable operating point. However, substantial temperature oscillations are observed, confirming the instabilities from Morud and Skogestad (1998). After around 2.5 hours, the oscillations repeat at a stable limit cycle with temperature variations around 200 K and an oscillation period of 7.22 min.

Further decreasing the temperature below the extinction point amplifies the oscillations up to 300 K rather than extinguishes the reactor. This agrees with Naess et al. (1992) observations for an industrial plant and suggests that a region of stable limit cycles exists beyond the extinction point. Andersen (1999) mapped the regions of stable limit cycle behaviour for a single-bed ammonia reactor and even found the stable oscillatory regions

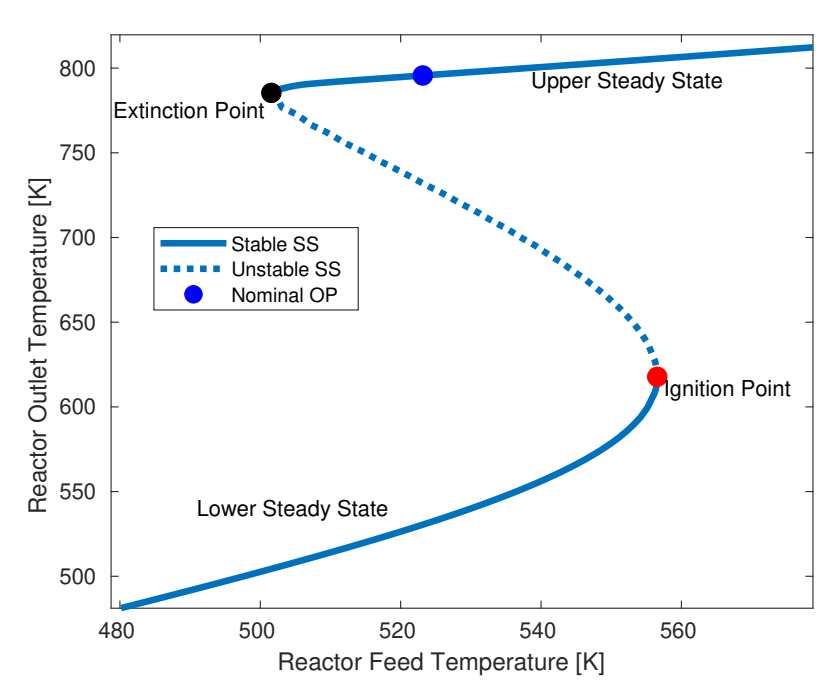


Figure 4.4: Mapping of the possible SS solutions for the reactor outlet temperature by varying feed temperature.

to overlap with the stable steady-state regions. Finally, returning to Figure 4.5, observe that increasing the feed temperature to the nominal value suppresses the oscillations and restores the original steady-state.

4.4.4 Reactor stability and bifurcation analysis

The transient simulation performed above clearly illustrates some concerning stability issues of the ammonia reactor system. Heavy temperature oscillations, like those observed in Figure 4.5, are at high risk of damaging the ammonia reactor casing and catalyst packing due to thermal stress. Thus, knowing the stable operating window and cause of the oscillatory behaviour is paramount. Consider the magnified view in Figure 4.5 displaying the outlet temperature transient for each bed during the initial 8 min after the step disturbance. An initial temperature rise is observed for all the reactor beds. This inverse response is a known phenomenon for exothermic reactions in packed bed PFRs caused by differential flow of matter and heat (Yakhnin and Menzinger, 1999). The thermal inertia of the heavy catalyst packing slows down the transportation of heat through the bed by multiple orders of magnitude compared to the material flow. The residence time of a material wave, τ , and temperature wave, τ_T , travelling through a reactor bed is defined as,

$$au = rac{L}{v_s} = rac{A_c^g L}{Q^{in}}, \quad au_T = rac{A_c^s L
ho_p c_p^s}{c_p^g N^{in}}, ag{4.13}$$

where v_s denotes the gas velocity at the inlet of the bed. Table 4.4 summarises the material and temperature wave residence times for each of the three beds. Note that the residence times of the material flow are in seconds while the temperature wave travels through the beds in minutes.

The inverse response arises when a step decrease in feed temperature initially cools the bed inlet. This cooling lowers the reaction rate and thereby the reactant conversion in the

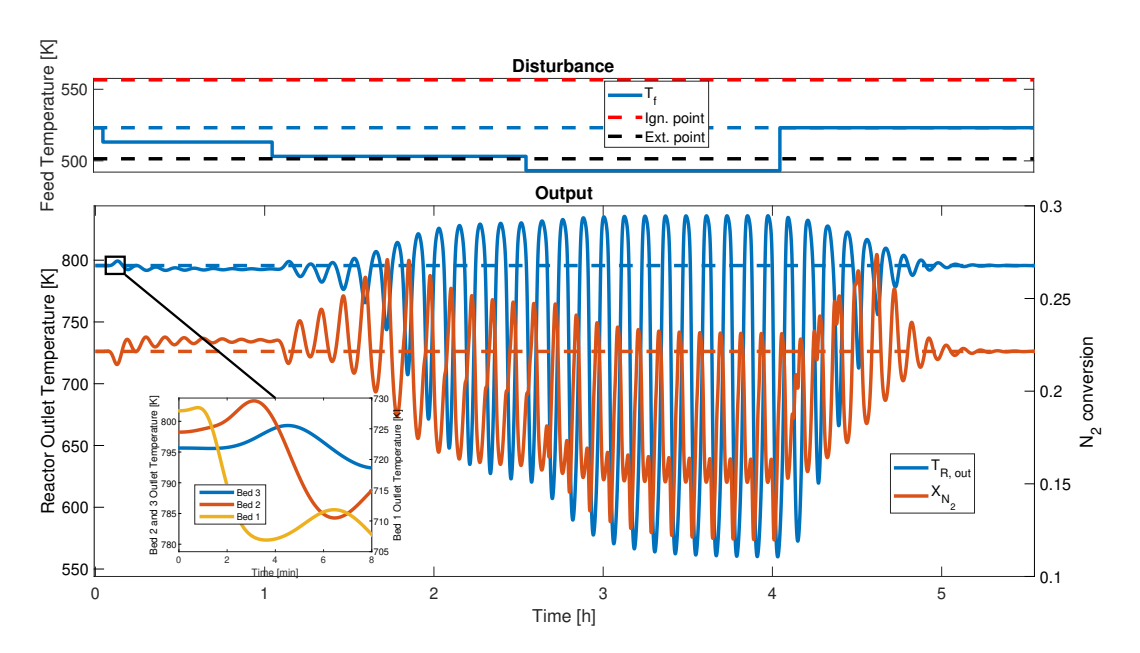


Figure 4.5: Reactor outlet temperature and N_2 conversion response to step disturbances in the reactor feed temperature.

Table 4.4: Residence times of the gas and temperature wave in the reactor beds.

	Bed 1	Bed 2	Bed 3	Total
$ au_T$ [S] $ au_T$ [min]	1.38	1.63	2.14	5.15
	1.56	1.90	2.62	6.08

front section of the bed. As the gas continues downstream, it is reheated by the catalyst, which remains hot further along the bed. Consequently, the gas reaches the outlet less converted but at a higher temperature, which temporarily increases the reaction rate near the bed exit. This effect produces the initial rise observed in the outlet temperature. Eventually, the cooling front propagates through the bed and lowers the outlet temperature, as observed in all reactor beds. As expected, the temperature wave arrives progressively later in the downstream beds, consistent with the cumulative residence times reported in Table 4.4.

The oscillatory transient of the reactor system is caused by the heat integration as the inverse response is fed back to the reactor inlet through the feed-effluent heat exchanger. Hereby, one can imagine a self-reinforcing effect as observed in Figure 4.5.

Bifurcation analysis

The stability of the reactor systems can be determined from the eigenvalues of the linearisation matrix, A, when linearising the reactor system in the form,

$$\dot{\mathbf{x}} = A\mathbf{x},\tag{4.14}$$

where, \mathbf{x} , is the system states. The linearisation matrix is obtained from the Jacobian of f and g in the DAE system via (Martinsen et al., 2023),

$$A = \frac{\partial f}{\partial x} - \frac{\partial f}{\partial y} \left(\frac{\partial g}{\partial y}\right)^{-1} \frac{\partial g}{\partial x}.$$
 (4.15)

A bifurcation analysis is carried out by evaluating the system stability as a single so-called bifurcation parameter, μ , is varied.

The bifurcation points are encountered when an eigenvalue or a complex pair of eigenvalues crosses the imaginary axis. In this work, two types of bifurcations are encountered, (Andersen, 1999):

- **Fold bifurcation**: The fold bifurcation arises when a purely real eigenvalue crosses into the right half-plane.
- Hopf bifurcation: The Hopf bifurcation is encountered when two complex conjugate eigenvalues cross the imaginary axis. The presence of two imaginary eigenvalues in the right half-plane gives rise to an unstable periodic solution.

The bifurcation analysis is carried out along the upper static solution curve of the S-shaped reactor characteristic in Figure 4.4. Figure 4.6a show how the system eigenvalues move towards the right-hand plane as the feed temperature is decreased. Two complex conjugate poles cross the imaginary axis in a Hopf-bifurcation before the extinction point, which gives rise to the unstable oscillatory transient discovered in Figure 4.5. Quantitatively the Hopf-bifurcation occurs at a feed temperature of 509.15 K where the imaginary part (frequency) of the complex conjugate pair is

$$\omega = \operatorname{Im}(\lambda_{\text{max}}) = \pm 0.0146 \operatorname{rad/s} \tag{4.16}$$

corresponding to a time period au_{osc} of the arising oscillations to

$$au_{osc} = \frac{2\pi}{\omega} = 430$$
s = 7.16 min (4.17)

which is consistent with the time period of the oscillations observed in Figure 4.5 and the calculated cumulative migration time of the temperature wave (Table 4.4).

Figure 4.6b illustrates the stability characteristics of the upper steady-state solution. The reactor loses stability at the Hopf bifurcation point, giving rise to a relatively wide range of unstable steady states. The distance between the nominal operating point and this instability threshold can be defined as the safety margin. At nominal conditions, the reactor operates with a safety margin of approximately 15 K in terms of feed temperature. Nevertheless, higher conversions can be achieved closer to the extinction point, even within the unstable region, though at the expense of operational robustness.

Finally, Figure 4.6a shows that a purely real eigenvalue crosses into the right-hand plane at a feed temperature corresponding exactly to the extinction point, confirming the occurrence of a fold bifurcation.

4.4.5 Optimisation

Figure 4.6b revealed that the nominal operating point of the ammonia reactor is not located at the point of maximum conversion but rather at a significant safety margin from the extinction point. This operation is consistent with the reactor being scaled from a conservatively operated commercial plant.

From Figure 4.6b observe that the conversion is increased at the upper steady-state for lower feed temperature, with a maximum located very close to the extinction point. It is possible to achieve a similar effect to lowering the feed temperature by adjusting the reactor quench fractions. The quench fractions configuration yielding the maximum reactant conversion can be obtained by setting up an optimisation problem for minimising the flow of nitrogen at the reactor outlet, F_{Rout, N_2} . However, by directly employing the

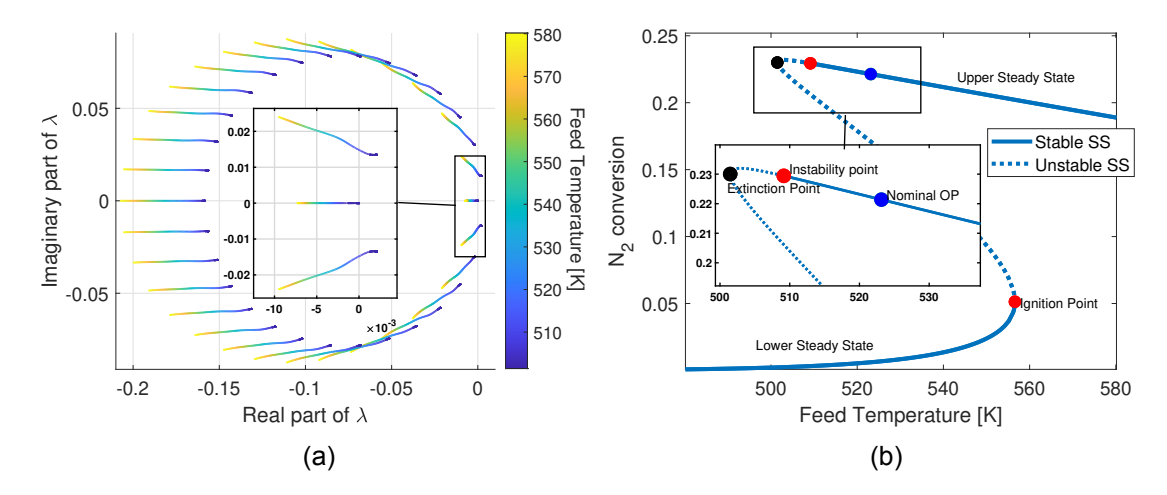


Figure 4.6: a) Eigenvalues λ and b) Bifurcation diagram for the optimal reactor configuration with T_f employed as the bifurcation parameter. The upper static solution becomes unstable below 509.15 K when a complex pair of eigenvalues crosses into the rhs-plane in a Hopf-bifurcation.

quench fractions as the design variables, the algorithm is required to solve the entire reactor system (Reactor + Heat exchanger) for each iteration. Alternatively one may regard the heat exchanger feed fraction, q_{R0} , and bypass fraction, q_{R1} , as a combined bed 1 quench fraction,

$$q_{R01} = q_{R0} + q_{R1} (4.18)$$

Hereby, the inlet temperature to bed 1, $T_{bed1,;in}$, is included as a design variable. The final formulation of the optimisation problem is therefore given as,

$$min. \quad F_{Rout, N_2}(T_{bed1, in}, q_{R01}, q_{R2}, q_{R3}),$$
 (4.19a)

$$s.t. \quad q_{R01} + q_{R2} + q_{R3} = 1.$$
 (4.19b)

Introducing $T_{bed1,\ in}$ as a design variable relieves the optimisation algorithm of solving the entire reactor system simultaneously. Instead, the heat exchanger equations are solved only once for the quench fractions q_{R0} and q_{R1} . The Matlab function fminsearch was used to perform the optimisation with the solution:

$$T_{bed1, in}^{opt} = 636.4 \text{ K},$$
 (4.20a)

$$[q_{R01}, q_{R2}, q_{R3}]^{opt} = [0.391, 0.304, 0.305].$$
 (4.20b)

Subsequently, solving the heat exchanger equation identifies the optimal bypass over the heat exchanger,

$$q_R^{opt} = [0.183, 0.208, 0.304, 0.305].$$
 (4.21)

The optimal reactor quench fractions yield a reactor N_2 conversion of 25.3%, which is a rather substantial increase compared to the original configuration with a conversion of 22.2%. Figure 4.7 display a traditional plot of conversion versus temperature along the reactor beds for both the nominal and optimal configuration. The optimal configuration utilises each reactor bed more efficiently, as a significantly larger conversion is reached, particularly in bed 1 and bed 3.

A bifurcation analysis with the feed temperature as the bifurcation parameter is performed for the optimal reactor configuration. Figure 4.8 displays the reactor S-curve with stable

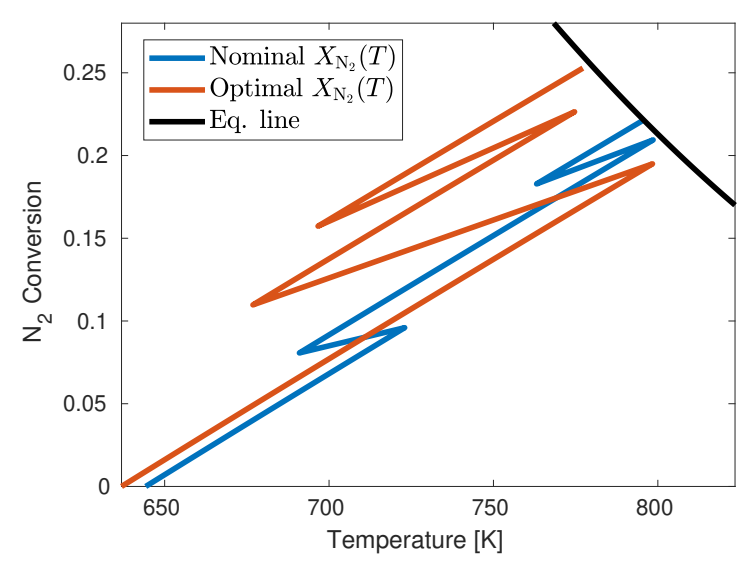


Figure 4.7: N_2 conversion versus temperature along the reactor beds for the nominal and optimal reactor configuration.

and unstable ranges. The optimal operating point is located close to the extinction point but just outside the unstable range.

Furthermore, Figure 4.8 reveals a trade-off between optimal and safe operation of the reactor system. Operating at the point of maximum conversion can easily lead to unstable oscillations due to process disturbances. Commercial plants traditionally avoid this by non-optimal operation at a safe distance from the instability point.

Non-optimal operation with less conversion per reactor pass entitles a larger recycling stream to achieve an equivalent utilisation of the synthesis feed. The larger recycling stream increases the electrical work for recompression and thus lowers the energy efficiency of the ammonia plant. Electrical availability is not a concern for a commercial plant, and the extra recompression work is insignificant compared to the energy input of steam reforming. However, for a PtA plant, the energy supply is purely electrical and non-optimal utilisation of the electricity directly reduces ammonia production. Furthermore, the flexible operation of PtA plants requires a control structure, which can stabilise operation at the optimal operating point. Stabilising control of the AQCR is discussed further in Section 4.6.

4.5 Results: Synthesis loop (Boundary 2)

This section considers the whole ammonia synthesis loop, including separation and recycling as defined by boundary 2 in Figure 4.1. The streams of the synthesis loop (1, 5, 6, 8) are solved given a steady-state solution for the reactor system (boundary 1). That is, the synthesis loop is solved "backwards" by determining the feed stream, separation and purge fraction satisfying a solution to the reactor system. One may regard stream 2 entering the reactor system (boundary 1) as an outlet from boundary 2 and stream 4 as an inlet to boundary 2. The material balance for component i over the synthesis loop boundary is then,

$$F_{S1} + F_{S4} - F_{S2} - F_{S5} - F_{S8} = 0 (4.22)$$

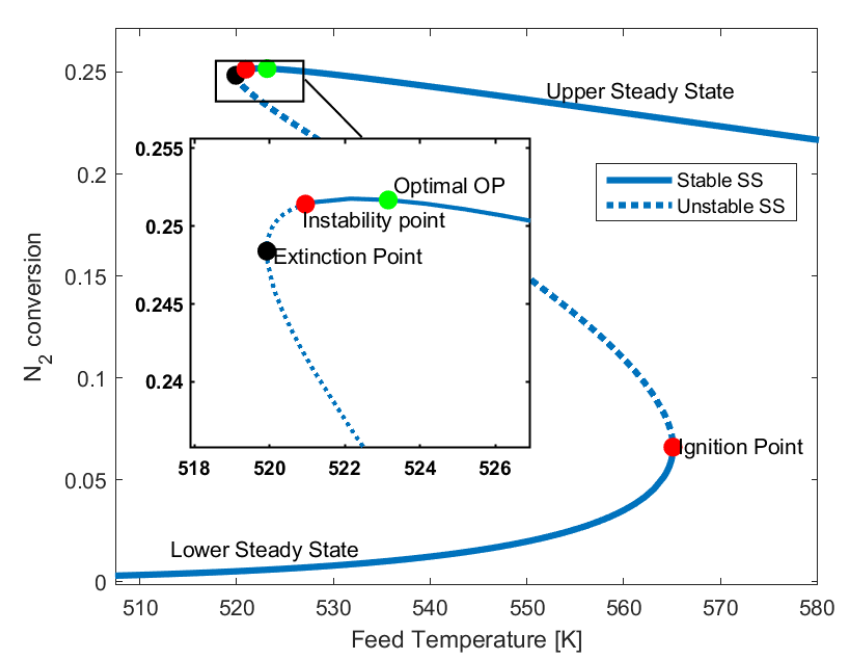


Figure 4.8: Bifurcation diagram for the optimal reactor configuration with T_f employed as the bifurcation parameter. The optimal operating point is clearly located very close the instability and extinction point.

For NH₃ and the light components [N₂, H₂, Ar] respectively,

$$F_{S1, NH_3} = 0$$
 (4.23a)

$$F_{S5, [N_2, H_2, Ar]} = 0 {(4.23b)}$$

Expressing the mole flows of the light component in stream 8 via the purge fraction and rearranging (4.22) a bit,

$$F_{S1, [N_2, H_2, Ar]} - F_{S4, [N_2, H_2, Ar]}q_p = F_{S2, [N_2, H_2, Ar]} - F_{S4, [N_2, H_2, Ar]}$$
 (4.24)

Additionally, assuming the argon is supplied with the nitrogen from the ASU at a rate of $0.0125 \text{ mol Ar/mol } N_2$,

$$F_{S1,Ar} = 0.0125 F_{S1,N_2} \tag{4.25}$$

 $F_{S2,\;i}$ and $F_{S4,\;i}$ are known from the reactor system SS-solution. Hence, equation (4.24) and (4.25) constitute a linear equation system, which is easily solvable for the component flow of feed stream 1 and the purge fraction, q_p . The separation fraction is found by inserting (4.8a) and (4.8b) in (4.9a) and solving for q_s ,

$$F_{S7, NH_3} = (1 - q_p)(1 - q_s)F_{S4, NH_3}$$
 (4.26)

Table 4.5 summarizes the flows of streams (1-8) for the nominal steady-state. The purge and separation fraction are respectively,

$$q_p = 0.0270$$
 $q_s = 0.736$ (4.27)

The ammonia yield in the product stream 5 is 11.5 ton NH₃/h. As the reactor system is optimized compared to the original scaling basis in (Morud and Skogestad, 1998), the

Table 4.5: Component stream flow

Stream	1	2	3	4	5	6	7	8
$\overline{F_{N_2}}$ [kmol/h]	370	1360	1018	1018	0	1018	990	27.5
F_{H_2} [kmol/h]	1109	4078	3052	3052	0	3052	2969	82.5
F_{NH_3} [kmol/h]	0	237	921	921	678	243	237	6.57
F_{Ar} [kmol/h]	4.62	171	171	171	0	171	166	4.62

plant produces more ammonia than estimated in Section 4.3. Consequently, more hydrogen is required than reported in Section 4.3, which increases the power demand of the PtA plant. Thus, for the optimized reactor configuration the PtA power consumption is 117 MW based on the calculation procedure presented in Section 4.3. This corresponds to an energy consumption of 10.11 kWh/kg NH₃. Relative to the lower heating value of ammonia this converts to a total energy efficiency of 51.7% for the PtA plant.

4.5.1 Load variation strategies

The synthesis loop is operated flexibly to comply with the intermittent renewable energy supply. As the electrolyser consumes most of the electrical energy, it is reasonable to assume the electrical load of the PtA plant is scaled proportionally with the synthesis feed of fresh hydrogen. The load factor (LF) on the synthesis loop is hence given by,

$$LF = \frac{F_{S1, H_2}}{F_{S1n H_2}} \tag{4.28}$$

where F_{S1n, H_2} denotes the nominal flow of fresh H₂. It is convenient to define the hydrogen efficiency of the synthesis loop as the amount of fresh synthesis feed H₂ converted to NH₃ in the product stream 5,

$$\eta_{\rm H_2} = \frac{3F_{S5, \, \rm NH_3}}{2F_{S1, \, \rm H_2}} \tag{4.29}$$

In this way, the hydrogen efficiency reflects how effectively the renewable electricity is converted to NH₃.

Here, two strategies for scaling the load factor are investigated:

Strategy 1: The total reactor feed flow (stream 2) is scaled stoichiometrically with the available energy, such that the H₂/N₂ ratio remains constant.

Strategy 2: Only the H_2 reactor feed flow is scaled, while the N_2 flow is kept constant. As a result, the reactor feed deviates from the stoichiometric ratio.

It should be noted that the scaling strategies are applied to the reactor system and not directly to the synthesis loop load factor. To clarify, the reactor load is defined as the relative amount of H_2 entering the reactor compared to nominal conditions:

$$RL = \frac{F_{S2, H_2}}{F_{S2n, H_2}} \tag{4.30}$$

The corresponding synthesis load factor is found by solving the equation system (4.24)-(4.26).

Figure 4.9 illustrates the effect of the two scaling strategies on the hydrogen efficiency of the synthesis loop. For each data point, the reactor configuration has been optimised. The top diagram shows the produced ammonia (stream 5) in ton/h as a function of load factor, while the middle diagram displays the hydrogen efficiency. Across the full operating

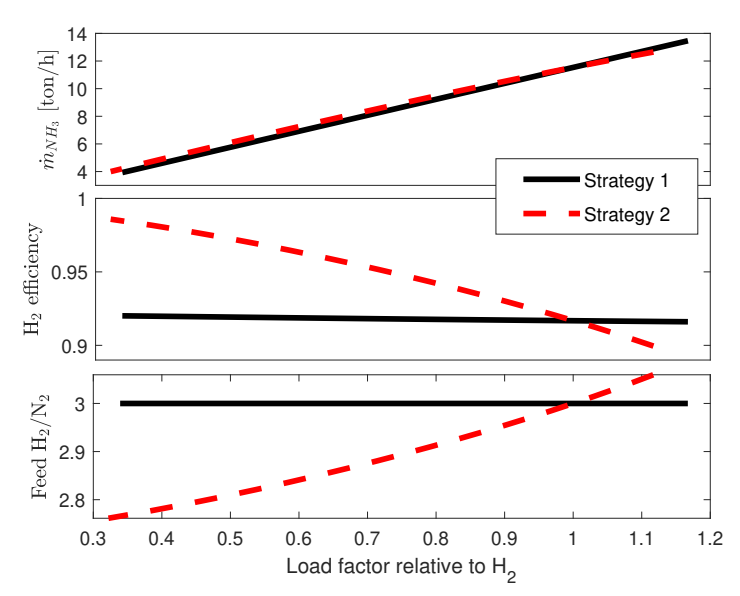


Figure 4.9: Comparison of scaling *Strategy 1* and 2. For varying load factor, the diagrams depict: Top: Ammonia flow in product (stream 5). Middle: Hydrogen efficiency. Bottom: H_2/N_2 ratio in the feed stream.

window, more than 90% of the hydrogen feed is converted, indicating efficient utilisation of the feedstock. The hydrogen efficiency highlights the relative performance of the two scaling strategies, which is important since hydrogen is far more costly to produce via electrolysis than nitrogen via air separation.

The results show that $Strategy\ 2$ yields higher hydrogen efficiency at loads below nominal, while $Strategy\ 1$ is superior above nominal load. At low load, reducing only the H_2 feed flow ($Strategy\ 2$) enables higher hydrogen utilisation since excess N_2 facilitates more H_2 conversion before equilibrium is reached. In addition, the lower hydrogen fraction in the recycle stream reduces purge losses. Consequently, Figure 4.9 suggests employing $Strategy\ 2$ for down-scaling PtA load and $Strategy\ 1$ for up-scaling above nominal load.

The bottom diagram in Figure 4.9 shows the H_2/N_2 ratio in feed stream 1 under the two strategies. Interestingly, even for *Strategy 2* at low loads, where the reactor feed ratio approaches 1:1, the synthesis feed ratio remains close to stoichiometric. This is due to the large recycle stream in the synthesis loop, which strongly amplifies deviations from stoichiometry in the synthesis feed.

Figure 4.10a shows the optimal bed inlet temperature for *Strategy 1* and *Strategy 2* over synthesis loop load from 0.3 to 1.15 of the nominal load. Observe that the proposed combination of *Strategy 1* and *Strategy 2* yields the most constant optimal inlet temperature for all the beds over the synthesis load range. Thus, in terms of dynamic operations, the bed temperatures are always close to the optimum, which simplifies the control task and reduces time at non-optimal operation during load transitions. The optimal configuration of the quench valves for the combined scaling strategy is shown in Figure 4.10b. At low loads, a large fraction of the reactor feed is directed to the heat-exchanger as the excessive flow of nitrogen requires a higher inlet temperature. Similarly, a higher inlet temperature is required at higher loads with increased reactor flowrates. Data for the optimal bed inlet temperatures and reactor quench fractions are also presented in Table 4.6. Additionally, Table 4.6 contains data for the open loop safety margin in terms of feed tem-

perature, $T_{Rfn} - T_{Rf,\ instab}$, and the distance to the extinction point, $T_{Rfn} - T_{Rf,\ ext.}$. The optimal points all show a bifurcation diagram similar to that in Figure 4.8 for the nominal case. That is, the distance to the instability point and extinction point is around 2-4 K.

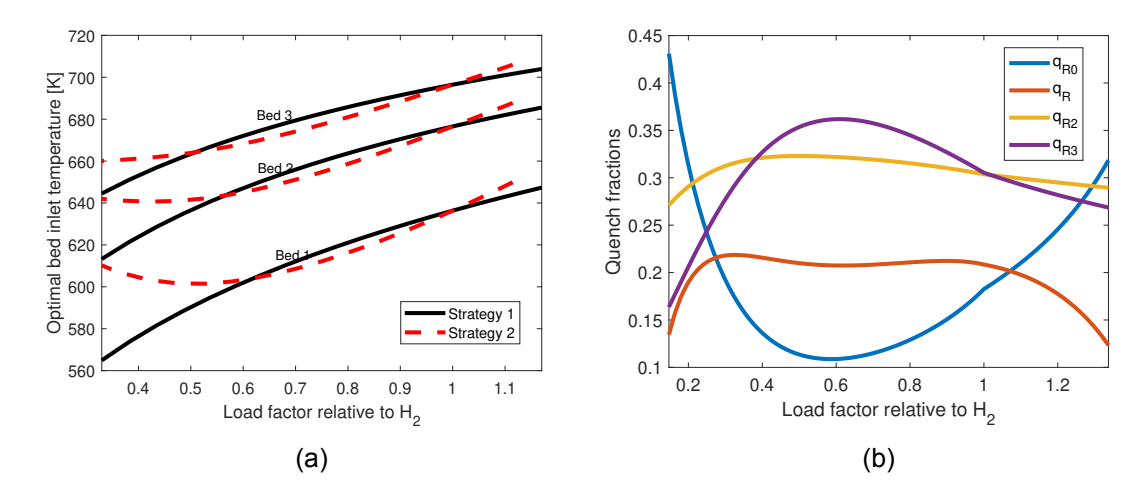


Figure 4.10: a) Optimal bed inlet temperatures for load scaling *Strategy 1* and *Strategy 2*. b) The optimal reactor quench fractions versus synthesis load employing the proposed combination of scaling *Strategy 1* and *Strategy 2*.

Table 4.6: Optimal bed 1 inlet temperature and reactor quench fractions for a range of load factors.

Load factor	T_1^{in} [K]	T_2^{in} [K]	T_3^{in} [K]	q_{R0}	q_{R1}	q_{R2}	q_{R3}	$T_f^n - T_f^{instab.}$ [K]	$T_f^n - T_f^{ext.}$ [K]
0.15	637.3	645.4	654.3	0.42	0.14	0.27	0.17	2.4	3.8
0.20	628.3	645.3	657.3	0.31	0.19	0.29	0.21	2.2	3.6
0.25	620.1	644.2	658.9	0.24	0.21	0.30	0.24	2.2	3.6
0.30	613.3	642.7	659.7	0.19	0.22	0.31	0.28	2.2	3.6
0.35	608.0	641.5	660.3	0.16	0.22	0.32	0.31	2.2	3.6
0.40	604.3	640.7	661.1	0.14	0.22	0.32	0.33	2.2	3.4
0.45	602.2	640.7	662.3	0.12	0.21	0.32	0.34	2	3.4
0.50	601.4	641.5	663.9	0.11	0.21	0.32	0.35	2	3.4
0.55	601.8	643.0	665.9	0.11	0.21	0.32	0.36	2	3.2
0.60	603.3	645.2	668.3	0.11	0.21	0.32	0.36	2	3.2
0.65	605.6	647.9	671.0	0.11	0.21	0.32	0.36	2	3.2
0.70	608.6	651.1	674.1	0.11	0.21	0.32	0.36	2	3
0.75	612.2	654.7	677.4	0.12	0.21	0.32	0.35	1.8	3
0.80	616.3	658.6	680.9	0.13	0.21	0.32	0.34	1.8	3
0.85	620.8	662.8	684.6	0.14	0.21	0.31	0.34	1.8	2.8
0.90	625.7	667.3	688.5	0.15	0.21	0.31	0.33	1.8	2.8
0.95	630.9	671.8	692.4	0.17	0.21	0.31	0.32	1.8	2.8
1.00	636.4	676.5	696.5	0.18	0.21	0.30	0.31	1.8	2.8
1.05	639.7	679.3	698.8	0.20	0.20	0.30	0.30	1.8	3
1.10	643.0	682.0	701.0	0.21	0.20	0.30	0.29	1.8	2.8
1.15	646.1	684.5	703.1	0.23	0.19	0.30	0.29	1.8	2.8
1.20	649.1	687.0	705.1	0.25	0.18	0.30	0.28	2	2.8
1.25	652.0	689.3	707.1	0.27	0.16	0.29	0.28	2	3
1.30	654.8	691.5	708.9	0.29	0.14	0.29	0.27	2.2	3.2

4.5.2 Open-loop stability of the load scaling strategies

bifurcation parameter, using the recommended combination of Strategies 1 and 2. The reactor quench fractions are fixed at their optimal configuration for nominal load. The resulting bifurcation diagram in Figure 4.11 therefore illustrates the feasible operating window of the ammonia reactor without re-optimisation of the quench flows as a function of load.

Unlike the familiar S-shaped curves obtained in earlier bifurcation diagrams (Figures 4.6b and 4.8), varying the reactor load does not reveal an ignition point. Instead, two extinction points are encountered: one during down-scaling and one during up-scaling of the load. The lower-load extinction occurs due to excessive quenching of the reactor, as an oversupply of N_2 relative to H_2 suppresses the reaction. At the upper extinction point, the high flow rate reduces the residence time to the extent that conversion is insufficient to sustain operation, effectively "blowing out" the reactor. A small discontinuity appears at RL=1, corresponding to the transition between Strategy 2 (down-scaling) and Strategy 1 (up-scaling).

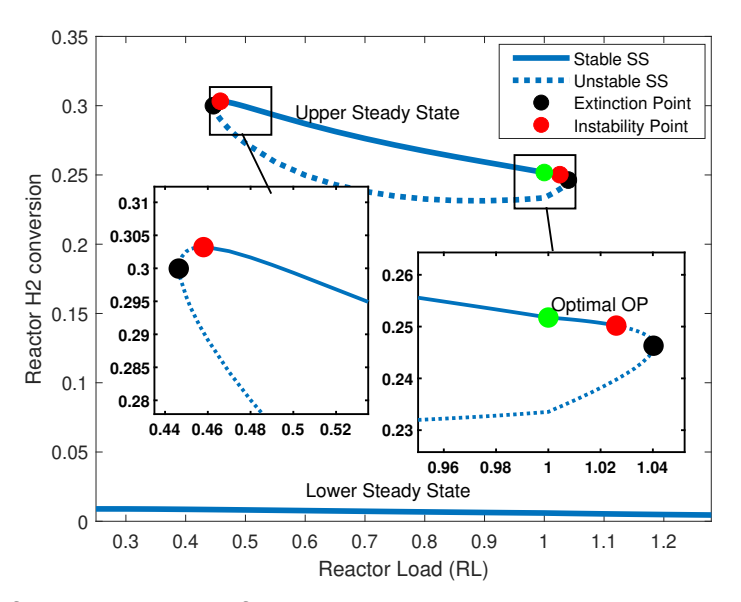


Figure 4.11: Bifurcation diagram for varying reactor load applying the recommended combination of scaling *Strategy 1* and 2. Instability and extinction points are encountered both by up and down-scaling the load.

4.5.3 Synthesis loop transient simulation

Considering the bifurcation analysis in Figure 4.11, it is naturally of interest to investigate the dynamic response of the synthesis loop when up- and down-scaling the load towards the instability regions. Figure 4.12a displays the transient of the reactor load and reactor outlet temperature for scaling up the load factor. For increasing the load above nominal operation, scaling *Strategy 1* is employed, implying the feed flow increases at the stoichiometric ratio. The higher supply of fresh feed instantly raises the load on the reactor by an amplified factor due to the recycling. The increased reactor flow pushes the reactor system into the unstable range and, as predicted by the bifurcation analysis, an oscillating unstable solution arises. Reestablishing the nominal synthesis feed flow damps the oscillations and regenerates the stable optimal operating point.

Figure 4.12b shows the response of down-scaling the load factor by applying scaling Strat-

egy 2. Initially decreasing the synthesis load factor to 0.55, the reactor system remains stable, displaying an asymptotic path towards the new steady-state. Further decreasing the synthesis load, the reactor load moves beyond the instability point, which causes small but growing unstable oscillations. Finally, by re-establishing the nominal feed flowrate, the reactor system does not return to the nominal steady-state. Instead, the oscillatory behaviour is amplified and the reactor system is attracted towards a stable limit cycle. The acceleration of the oscillations can be explained from the temperature plot in Figure 4.12b. At low load, the reactor outlet temperature, and, as such, the entire reactor, is at a lower temperature state than at nominal operation. As a result, when restoring the nominal flow, the cold reactor does not convert the increased reactant flow sufficiently. This causes the ammonia reactor system to become unstable and transition towards a region of sustained limit cycles. Thus, Figure 4.12b illustrates some additional issues with quickly increasing the load of the synthesis loop.

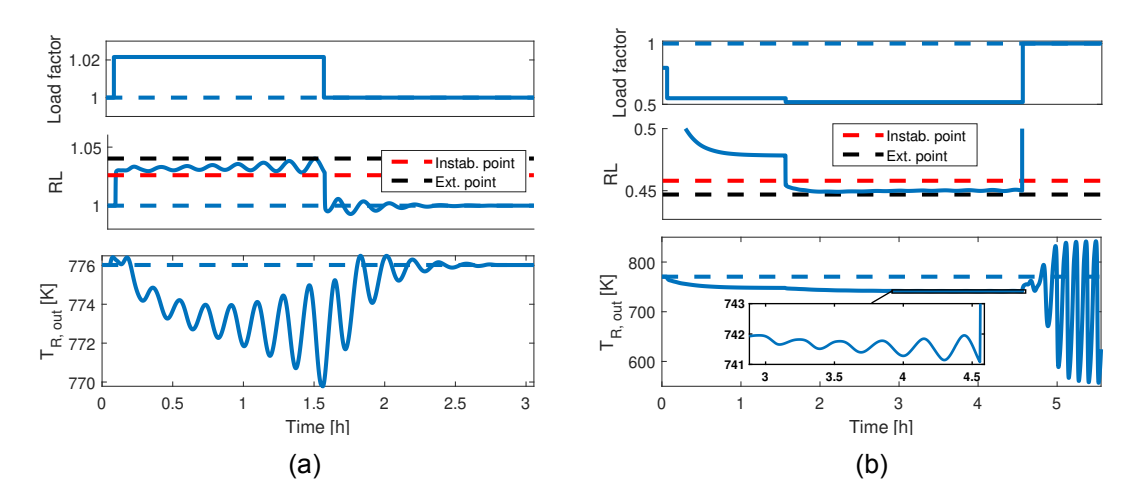


Figure 4.12: Transient simulation of the synthesis loop subjected to a) scale up of production into the upper unstable range b) scale down towards the lower instability point followed by a sudden regeneration of the nominal load.

4.6 Dynamic control for flexible operation

The transient simulations in Section 4.5.3 clearly demonstrate the necessity of a control strategy when the synthesis loop is operated flexibly between 20–120% of nominal load. The optimal operating points identified in Section 4.5.1 are located close to instability and extinction boundaries. A control structure is therefore required to stabilise operation in these regions.

As shown in Figure 4.1, five immediate manipulated variables can be identified in the synthesis loop: the four quench valves and the purge valve. For simplicity, it is assumed that valve adjustments directly and instantaneously determine the corresponding quench and purge fractions, allowing them to be treated as manipulated variables. This reduces the effective degrees of freedom by one, since the quench fractions must sum to unity. In addition, the separation fraction and the operating pressure represent two further degrees of freedom, though neither can be adjusted instantaneously, as they depend dynamically on the cooling utility and compressor power. In total, six manipulated variables are available within the synthesis loop for an advanced multi-input–multi-output (MIMO) control strategy.

The design of such a comprehensive MIMO control system for the full synthesis loop is, however, not the scope of this chapter. Instead, to illustrate the interplay between varying the PtA load, updating the optimal reactor configuration, and applying regulatory control, a simplified single-input—single-output (SISO) scheme is implemented. This control structure is used to stabilise the reactor and steer it towards the optimal operating point.

4.6.1 Regulatory SISO control

Consider the comparison of scaling strategies 1 and 2 in Figure 4.9. The reactor system is optimised for each value of the load factor, and the corresponding purge and separation fractions are calculated. The optimal solutions in Figure 4.9 provide a mapping of the optimal synthesis loop configuration for varying load. This optimal map is used to determine the reactor set-point when the synthesis load is changed. The reactor outlet temperature is perhaps, by first impulse, the most obvious choice for the controlled variable (CV). However, due to the observed inverse response and slow response time, the reactor outlet temperature is strongly advised against as CV (Morud and Skogestad, 1998; Naess et al., 1992; Manenti and Bozzano, 2013). Instead, the literature suggests using the bed 1 inlet temperature, $T_{bed1, in}$, as CV. The inlet temperature to bed 1 is a simple mixing of streams; thus, the response can be measured immediately and with no inverse response. Furthermore, recall the setup of the optimisation algorithm, which exactly finds the optimal temperature for $T_{bed1, in}$.

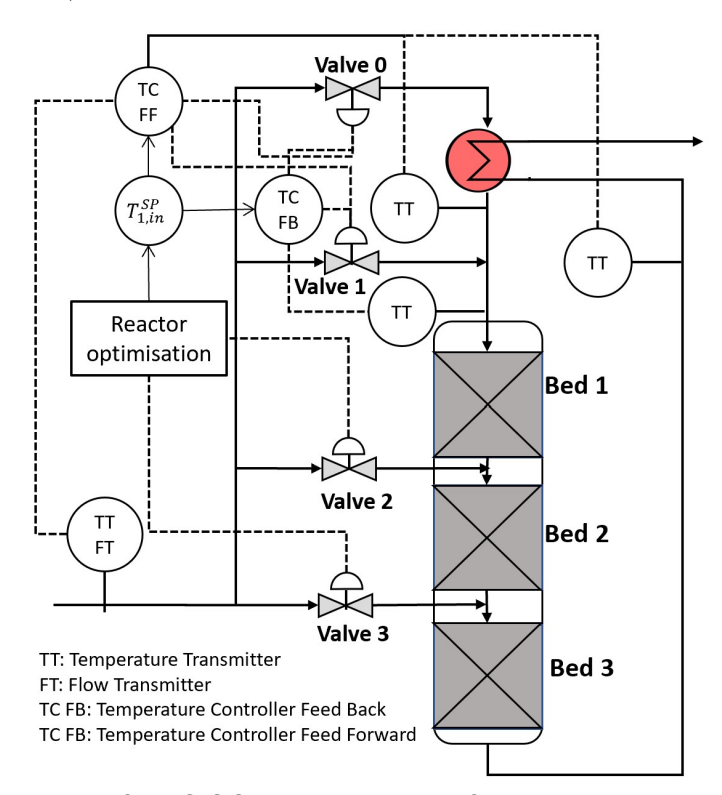


Figure 4.13: Schematic of the SISO control structure for the reactor system. The controller action consists of a combined output from feed-forward and feed-back control.

Figure 4.13 illustrates the proposed control structure for the reactor system. At the supervisory level, available renewable energy is monitored and forecasted to determine the optimal flow of fresh N_2 and H_2 feed into the synthesis loop. From the reactor's perspective, changes in the feed flow represent disturbances. These are detected by a flow meter on the reactor feed stream, which transmits the measurement to the reactor optimisation algorithm. Based on this, the algorithm computes the optimal steady-state targets for

 $T_{bed1:in}$ and for the quench fractions of valves 2 and 3 (From Table 4.6).

The feed-forward controller then receives the updated $T_{bed1,;in}$ set-point, the change in feed flowrate, and a temperature signal from the reactor outlet. Using these inputs, the feed-forward controller solves the heat exchanger and mixing equations to determine q_{R0} and q_{R1} . To reflect model–plant mismatch, the feed-forward heat exchanger model assumes a heat transfer coefficient 5% larger than the actual system.

A feedback loop is included on the bed 1 inlet temperature to correct any steady-state error left by the feed-forward controller. Because the optimisation constrains the sum of q_{R0} and q_{R1} , the feedback is implemented as a split-range controller, with q_{R0} and q_{R1} acting in opposite directions. The feedback loop is realised as a PI controller with parameters $K_c = 3.38 \cdot 10^{-4}$, K^{-1} and $\tau = 1$, s.

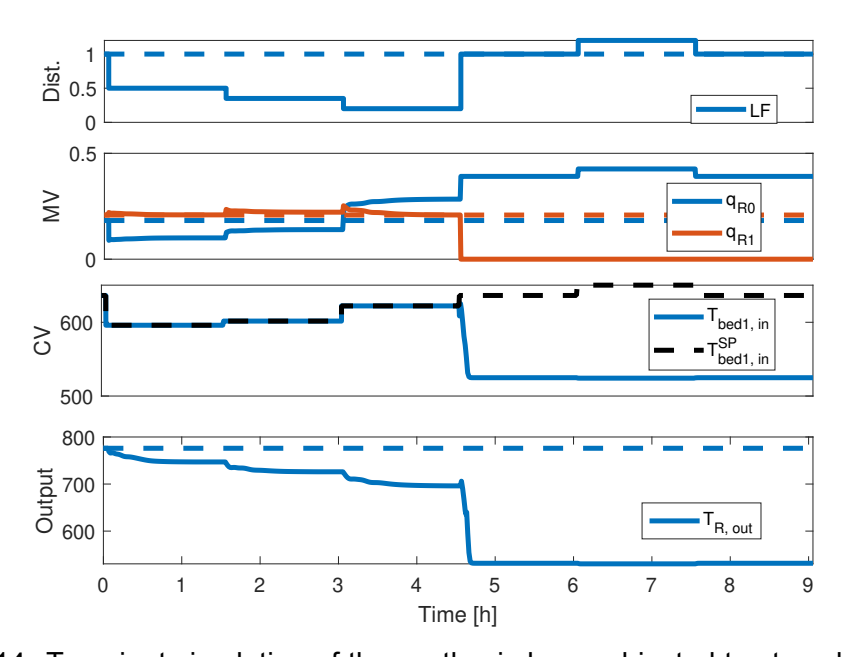


Figure 4.14: Transient simulation of the synthesis loop subjected to step changes in the load. The reactor system is controlled via a combination of feed-forward and feed-back control on the bed 1 inlet temperature.

The action of the supervisory controller is simulated by varying the load factor (disturbance) step-wise in the range from LF = [0.2, 1.2] at 1.5 h intervals. Figure 4.14 shows the corresponding responses of the manipulated variables (MVs), the bed 1 inlet temperature (CV), and the reactor outlet temperature. The feed-forward controller responds efficiently to the first three scale-down steps in load. Each disturbance is promptly counteracted by adjusting the quench fractions, which shifts $T_{bed1::in}$ toward its new set-point. The small remaining offset is eliminated by the PI feedback loop, ensuring accurate temperature control. However, the return to nominal load (LF = 1) from the lowest operating point (LF = 0.2) at t = 4.5; h is poorly controlled due to actuator saturation. At low load, the reactor operates at reduced temperatures (see Section 4.5.3), and when the feed flow is increased back to nominal, the required $T_{bed1,:in}$ cannot be achieved even with valve 0 fully open, directing maximum flow through the heat exchanger. The combination of a cold reactor state and an increased feed flow results in insufficient conversion, ultimately causing a reactor blowout. Once extinguished, the reactor requires a dedicated restart procedure with external heat input to reignite the catalyst. Furthermore, the catalyst packing and reactor casing risk damage by thermal stress at a sudden cold stop. For these reasons, blowout scenarios are highly undesirable and underscore the importance of carefully designed load-change strategies and control margins.

Substantial step changes of the load as investigated in Figure 4.14 reflect the most demanding case for the controllers and are not a viable operating method. In practice, variations in the load are restricted by a maximum rate of change. It is assumed the synthesis load can change by a maximum of 10% load per 10 min relative to the nominal load. Figure 4.15 shows the synthesis loop's closed-loop response when applying the ramp restriction on the load. In this way, the controllers can keep up with the change in set-point for $T_{bed1,\ in}$, and efficient system control is achieved.

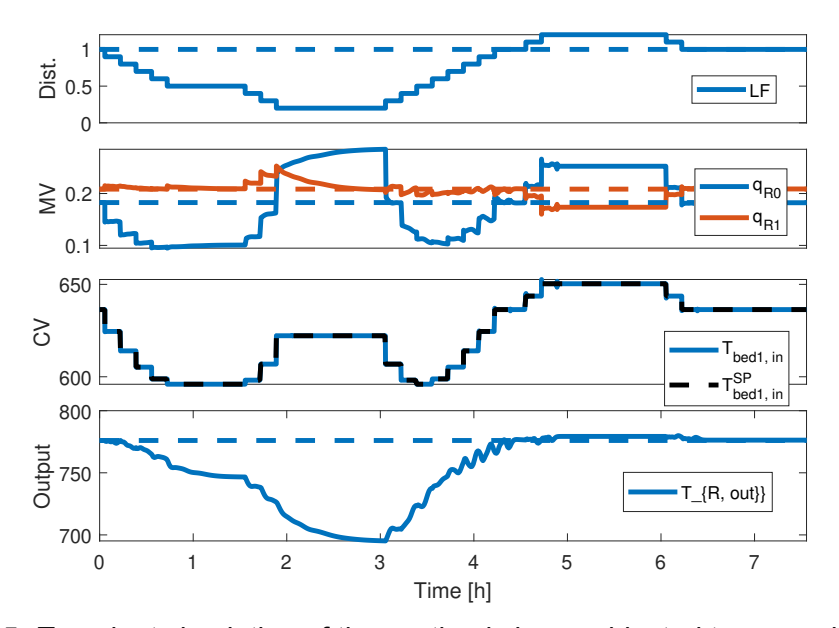


Figure 4.15: Transient simulation of the synthesis loop subjected to ramp changes in the load. The reactor system is controlled via a combination of feed-forward and feed-back control on the bed 1 inlet temperature.

4.7 Discussion

This chapter has examined the steady-state and dynamic behaviour of an adiabatic quench-cooled reactor under conditions relevant to PtA operation. The analysis demonstrated pronounced nonlinear characteristics, including severe temperature oscillations. Furthermore, the steady-state optimum was consistently found near the stability limit across the entire operating window. While the study primarily focused on the qualitative dynamics of the reactor system, the narrow stability margins highlight the importance of assessing model fidelity and understanding how small modelling errors could impact reactor performance.

4.7.1 Model validation

To validate the accuracy of the developed ammonia reactor model, steady-state simulation results are compared with industrial data reported in the literature. Specifically, the model predictions are benchmarked against data from Singh and Saraf (1979) and Shamiri and Aliabadi (2021). The corresponding feed gas conditions are summarised in Table 4.16.

Figure 4.16 presents the simulated steady-state profiles for temperature and hydrogen conversion, alongside industrial data points. The catalyst activity factor in the kinetic expression (Section 3.3.1) was adjusted to account for differences in catalyst properties

between the industrial cases and this study.

As shown in Figures 4.16a–b, the proposed model accurately reproduces the industrial data from Singh and Saraf (1979). This result demonstrates the model's ability to replicate plant data just by modifying the activity of the reaction kinetics. For the data set from Shamiri and Aliabadi (2021), the deviation is slightly larger (Figures 4.16c–d), which can be attributed to the unusually low operating pressure of 87 bar reported for this case. Because the Temkin–Pyzhev rate expression was developed for typical industrial pressures (150–250 bar), it does not fully capture the equilibrium behaviour at such low pressure. Nevertheless, the discrepancy remains small, resulting in only about a 2% error in outlet conversion.

Table 4.7: Data for reactor feed gas conditions from Singh and Saraf (1979) and Shamiri and Aliabadi (2021)

Singh and Saraf (1979)		Shamiri and Aliabadi (2	<u>2</u> 021)	
Pressure [bar]	226	Pressure [bar]	87	
Total flow, F_{fR} , [kmol/h]	10,810	Total flow, F_{fR} , [kmol/h]	13,391	
x_{N_2} [mol%]	22.19	x_{N_2} [mol%]	23.91	
x_{H_2} [mol%]	67.03	x_{H_2} [mol%]	62.3	
x_{NH_3} [mol%]	2.76	x_{NH_3} [mol%]	4.13	
x_{Ar} [mol%]	8.02	x_{Ar} [mol%]	9.65	

4.7.2 Comparison with Morud and Skogested (1998)

Morud and Skogestad (1998) presented a dynamic model of ammonia reactors, reproducing the reactor oscillations observed by Naess et al. (1992) through dynamic simulation. Several studies on both steady state and dynamic simulations of ammonia reactors have been based on the model proposed by Morud and Skogested, (Mancusi et al., 2001; Rabchuk et al., 2014; Mancusi et al., 2009; Wang et al., 2017; Straus, 2018; Cheema and Krewer, 2018, 2020; Wang et al., 2020; Burrows and Bollas, 2022). Morud and Skogestad (1998) modelled the reactor by assuming the material balance at steady state and thermodynamic properties, e.g. C_p and ΔH_r , constant with temperature and pressure. The model used in this work uses rigorous thermodynamics and accounts for real gas behaviour.

Figure 4.17a shows the steady-state temperature profile for the reactor configuration specified by Morud and Skogestad (1998), simulated both with the model used in this work and with the model from the original study. The current model predicts higher outlet and equilibrium temperatures in reactor beds 2 and 3, primarily due to the use of rigorous thermodynamics. Specifically, the heat of reaction, ΔH_r , in this work ranges from -100 to $-115~\mathrm{kJ/mol}$ over the reactor temperature range, whereas Morud and Skogestad (1998) uses the value at standard conditions, $\Delta H_r = -91.8~\mathrm{kJ/mol}$. As a result, more heat is released in the present model, leading to higher outlet temperatures.

These differences are further illustrated in Figure 4.17b, which plots reactant conversion versus temperature along the reactor beds. The lower heat of reaction assumed by Morud and Skogestad (1998) results in a steeper conversion—temperature curve compared to that obtained in this work. Consequently, their model reaches a significantly higher equilibrium conversion.

Additionally, Figure 4.17a suggests that the reaction proceeds faster in the model by

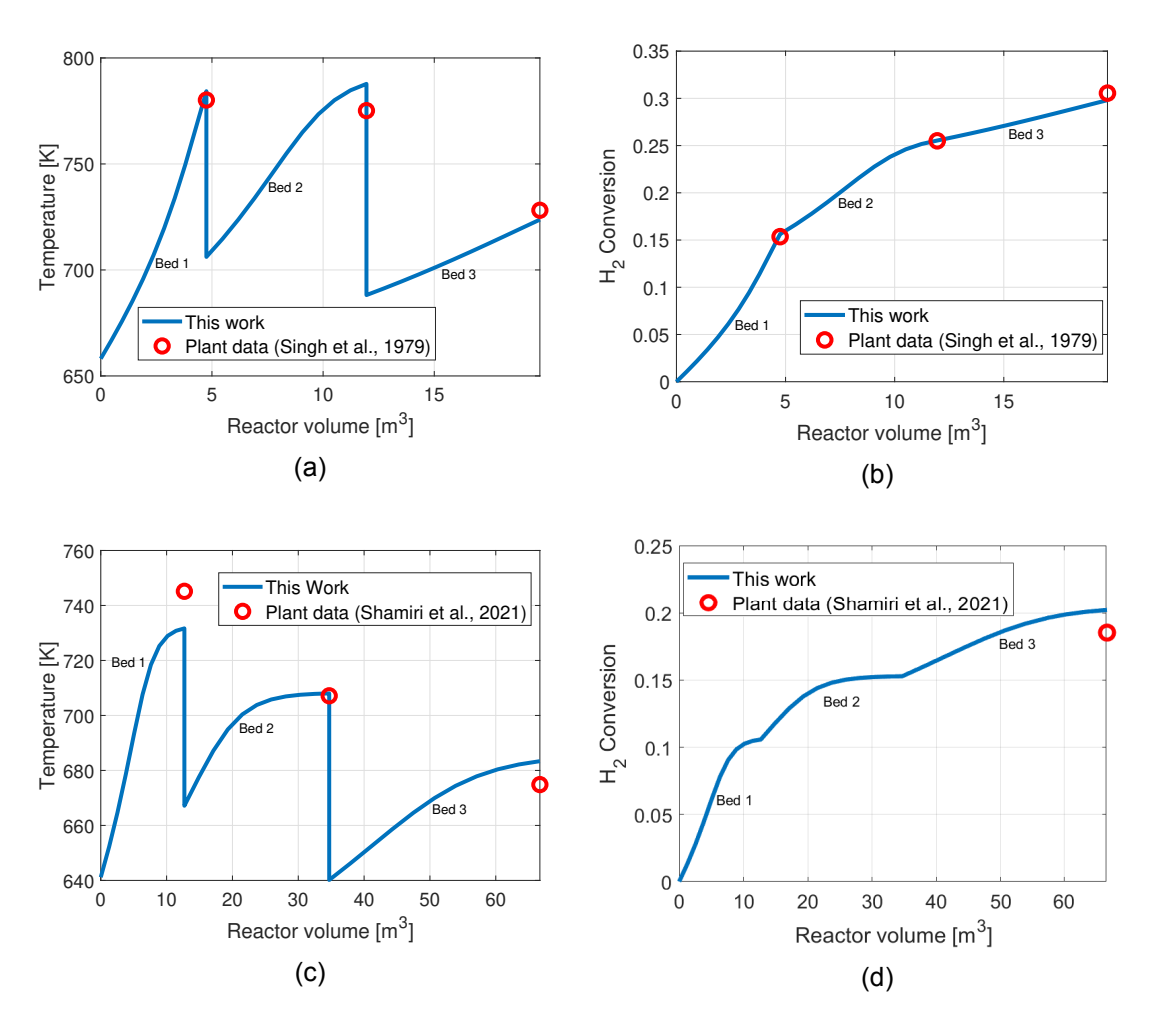


Figure 4.16: Simulated steady-state profiles for temperature and reactant conversion through the beds alongside industrial data from a-b) Singh and Saraf (1979) and c-d) Shamiri and Aliabadi (2021).

Morud and Skogestad (1998). This outcome is somewhat counterintuitive, as the more exothermic reaction in the present model should, through Arrhenius kinetics, lead to faster reaction rates. However, the discrepancy can be attributed to a numerical shortcut employed by Morud and Skogestad (1998), wherein the reaction rate in cell k is calculated based on the concentrations in cell k-1. This numerical shortcut significantly simplifies the computation of the steady-state profile, but artificially accelerates the reaction kinetics.

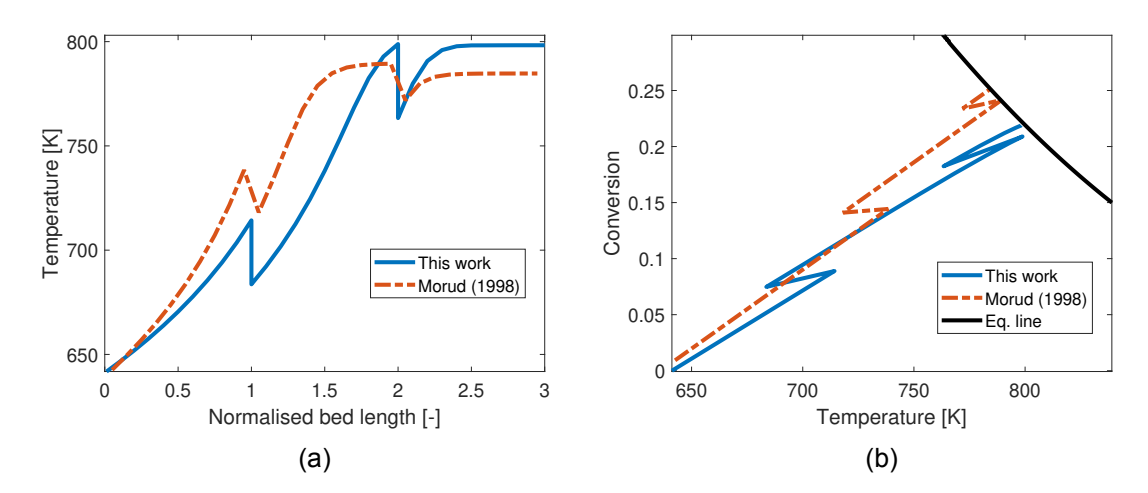


Figure 4.17: Comparison of the model used in this work and Morud and Skogestad (1998) for a) the steady-state temperature along the normalised reactor beds length and b) the conversion versus temperature map.

The numerical simplifications adopted in Morud and Skogestad (1998) influence the predicted stability limits of the reactor. Figure 4.19 compares the upper steady-state stability curve derived from the model presented in this work with that from Morud and Skogestad (1998). The latter predicts noticeably lower temperatures for both the Hopf bifurcation and extinction points. Although the deviation is only about 5 K, this difference is significant given that the optimal operating point is located at the verge of instability, as shown in Section 4.4.5.

Table 4.6 further highlights that the temperature margin between the optimal operating point and the instability threshold is only 2–4 K across the load range. Such a narrow margin is a serious concern, even when using a highly accurate reactor model, as real plant conditions are subject to disturbances and sensor bias. This issue is addressed in the next chapter, where a stability margin is introduced to shift the operating point away from the instability region.

4.8 Conclusion

This chapter modelled the steady-state and dynamic behaviour of a three-bed quench cooled adiabatic ammonia reactor for PtA. The study was based on a PtA plant connected to a renewable energy source with a capacity factor of 0.4.

Multiple steady-state solutions were identified via van Heerden analysis: A stable upper ignited state, a stable lower extinguished state, and an unstable intermediate partly ignited state. The multiple steady-state solutions existed over a wide operating window and were depicted as an s-shaped curve with a clearly defined ignition and extinction point enclosing the region of multiple steady-states.

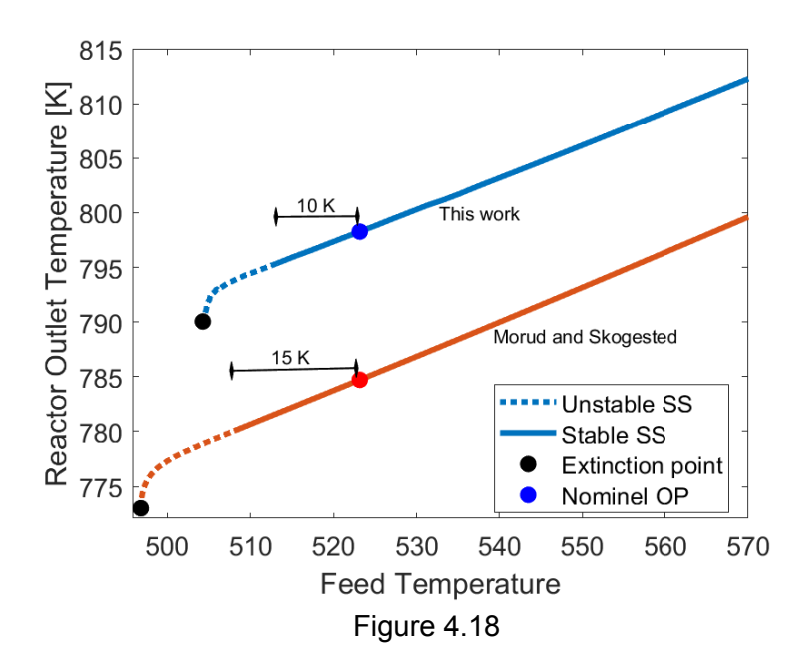


Figure 4.19: Comparison of the stability margin of the upper static solution for the model used in this work and the model presented in Morud and Skogestad (1998).

Dynamic simulations revealed the occurrence of large temperature oscillations in the reactor system when the feed temperature approached the extinction point. Decreasing the feed temperature below the extinction point did not blow out the reactor, but amplified the oscillations up to 300 K. This exposed the insufficient stability description of the van Heerden analysis. A stability analysis, performed through linearisation of the system, revealed an unstable range of the upper static solution before the extinction point, which agreed with the results of the transient simulations.

The optimal reactor configuration, determined by optimisation, increased the reactant conversion to 25.3% compared to 22.2% for the nominal configuration. However, stability analysis of the optimal reactor configuration showed that the optimal operating point is located very close to the instability range.

Two strategies for varying the reactor inlet feed to accommodate the fluctuating supply of renewable energy were assessed. *Strategy 1*: changing the reactor feed flow at the H_2/N_2 stoichiometric ratio, *Strategy 2*: keeping the reactor feed flow of nitrogen constant only changing the hydrogen flow. Strategy 2 yielded the best hydrogen efficiency for down-scaling the PtA load, while strategy 1 is recommended for up-scaling the load.

Open-loop simulations revealed that the uncontrolled reactor system becomes unstable during synthesis load changes. To address this, a regulatory control structure combining feed-forward and feedback elements was proposed to stabilise the ammonia reactor system. Closed-loop simulations were then performed for varying PtA load conditions, applying the recommended combination of Scaling Strategy 1 and 2 for up- and downscaling, respectively. The results showed effective control and accurate tracking of the optimal set points for most load transitions. However, abrupt changes from low to high load caused controller saturation, ultimately leading to reactor extinction. In contrast, when load changes were applied more gradually through ramping at 1% per minute, the controller maintained stability and ensured efficient transition to the new operating point.

Chapter 5

Reactor comparison and design for Power-to-Ammonia

The previous chapter 4 demonstrated the dynamic response and stability of an AQCR reactor during operation with varying operating parameters. However, as mentioned in the background Section 2 other types of ammonia reactors exist.

This chapter compares three reactor configurations for flexible Power-to-Ammonia (PtA) operation: the adiabatic quench-cooled reactor (AQCR), the adiabatic indirect-cooled reactor (AICR), and the internal direct-cooled reactor (IDCR). Rigorous steady-state and dynamic models are developed to evaluate their performance. At nominal load, the AICR and IDCR achieve the highest conversions (30.0% and 29.4%), while the AQCR reaches only 26.9% and exhibits unstable oscillatory behaviour. In contrast, the AICR and IDCR show stable dynamics with fast-decaying oscillations.

Across the 30–130% load range, the AICR and IDCR maintain higher conversions and better flexibility compared to the AQCR. However, all reactors operate close to extinction at optimal conditions, highlighting a risk of shutdown from small disturbances. Introducing a 15 K thermal stability margin slightly lowers conversion but markedly improves stability, enabling operation even with reduced catalyst activation.

As such, this chapter answers research question 2.

This chapter contains material from the article:

Rosbo, J.W., Jensen, A.D., Jørgensen, J.B., Huusom, J.K., (2024). Comparison, operation and cooling design of three general reactor types for Power-to-Ammonia processes. Chemical Engineering Journal, Volume 496(153660). doi:https://doi.org/10.1016/j.cej.2024.153660.

5.1 Introduction

As described in Chapter 2, ammonia reactors can generally be categorised into three types: the adiabatic quench-cooled reactor (AQCR), the adiabatic indirect-cooled reactor (AICR), and the internal direct-cooled reactor (IDCR) (Inamuddin et al., 2020). Figure 5.1 illustrates these three reactor types. In this figure, the AICR is specifically shown with the synthesis gas feed as the cooling medium in the inter-bed heat exchangers, in contrast to the more general illustration in Chapter 2, Figure 2.5. In conventional ammonia plants, cooling water may be used as the cold sink, but this requires an alternative heat source, such as the steam reformer, to preheat the reactor feed. In a PtA setting, however, the reactor bed outlet streams are the only available heat sources at the required temperature.

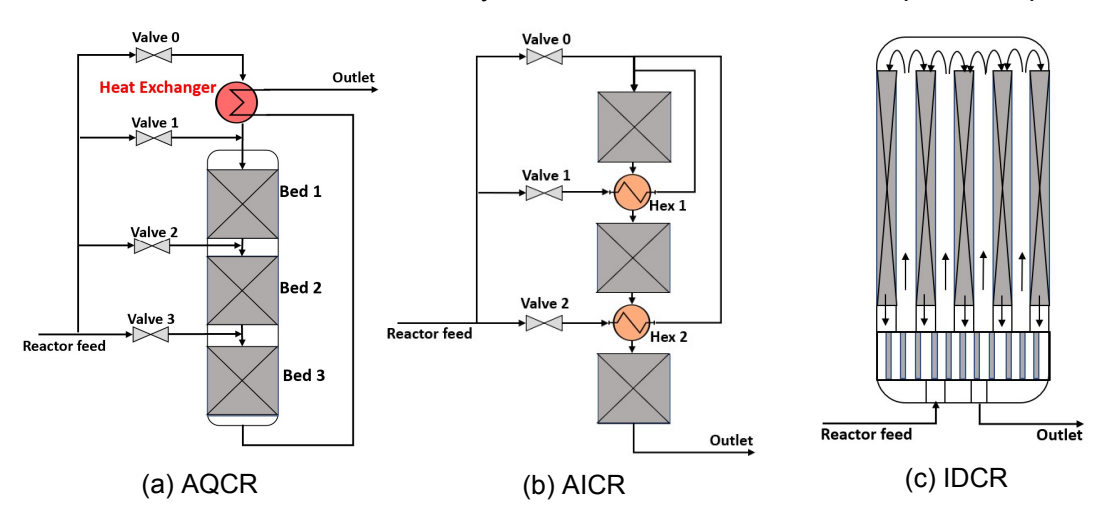


Figure 5.1: Three ammonia reactor types: a) Adiabatic quench cooled reactor (AQCR), b) Adiabatic indirect cooled reactor (AICR), and c) Internal direct cooled reactor (IDCR).

The literature has optimised and compared the three reactor types at nominal operating conditions. Azarhoosh et al. (2014) optimised and compared conversion for an AQCR and an AICR with identical catalyst packing, while Jorqueira et al. (2018) performed a similar study for an AICR and an IDCR. Khademi and Sabbaghi (2017) compared all three reactor types, ranking the IDCR and AICR significantly higher in conversion performance than the AQCR. However, there is a lack of studies evaluating these reactors across the wide operating window relevant for PtA operation, particularly concerning stability concerns under flexible loads.

The previous chapter (4) addressed this for an AQCR across an operating window from 20% to 120% of nominal load. This chapter extends the analysis in Chapter 4 to all three reactor types. Furthermore, the work suggests methods for sizing the heat exchanger areas of the ammonia reactors to enable load-flexible operation. The overall objective is to establish a fair and consistent basis for comparing reactor performance in a PtA context. To this end, optimisation is carried out across the full operating window, followed by stability analysis, open-loop transient simulations, and evaluation of operational strategies such as applying thermal stability margins for robust load switching.

5.2 Reactor models

This chapter focuses on the study on the reactor system outlined by the grey box in Figure 5.4. This allows for a direct comparison of the static and dynamic characteristics of the reactor configurations presented in Figure 5.1, independent of any recycle interactions that might otherwise obscure the system behavior.

As illustrated in Figure 5.1, all three reactor types consist of catalytic bed(s) paired with a cooling strategy. In the AQCR and AICR, cooling is implemented between the catalytic beds. In contrast, the IDCR features a counter-current heat exchange design, where the catalytic bed is located on the shell side and the feed gas serves as the cooling medium on the tube side. The material balances are identical across the three configurations. The energy balances are also similar, with the exception of the IDCR, which includes an additional term accounting for heat transfer across the reactor wall. These formulations are described in more detail in the following sections.

AQCR and AICR models

The model for the AQCR is described in Section 4.2. The AICR comprises the same unit operations as the AQCR but is configured differently, as shown in Figure 5.1b.

5.2.2 IDCR model

Material and energy balances

Figure 5.2 shows a schematic illustration of the IDCR. The reacting gas on the catalyst side of the reactor is cooled by counter-current flow with the feed gas flowing in the tubes. Assumptions A2-A3 for the fixed-bed (Section 3.3) still apply for the IDCR bed, but a term for heat flow over the tube wall, q^w , is added to the energy balance. Additionally, a material and energy balance are included to describe the tube phase yielding the PDE,

$$\frac{\partial c^r}{\partial t} = -\frac{\partial N^r}{\partial l} + R^r, \tag{5.1a}$$

$$\frac{\partial c^r}{\partial t} = -\frac{\partial N^r}{\partial l} + R^r,
\frac{\partial c^t}{\partial t} = -\frac{\partial N^t}{\partial l},$$
(5.1a)

$$\frac{\partial \hat{u}^r}{\partial t} = -\epsilon_B \frac{\partial \bar{H}^r}{\partial l} - n^t C^{ti} q^w, \tag{5.1c}$$

$$\frac{\partial \hat{u}^t}{\partial t} = -\frac{\partial \bar{H}^t}{\partial l} + n^t C^{ti} q^w. \tag{5.1d}$$

Superscript r refers to the reacting catalyst side and t refers to the tube side. n^t is the number of tubes in the reactor, and C^{ti} is the inner circumference of each tube,

$$C^t = \pi d^{ti}, (5.2)$$

where d^t is the inner tube diameter. The heat flux over the wall interface is given by the temperature driving force,

$$q^{w} = U^{w}(T^{r} - T^{t}), (5.3)$$

in which U^w is the overall wall heat transfer coefficient. The heat transfer resistance over the metal tubes is neglected, as it is small compared to the gas phase resistance on either side of the wall (Khademi and Sabbaghi, 2017). Thus, U^w is found by adding the heat transfer resistance on the shell and tube side,

$$U^w = \left(\frac{1}{\frac{d^{to}}{d^{ti}}h^r} + \frac{1}{h^t}\right)^{-1},\tag{5.4}$$

with h^r being the heat transfer coefficient on the reacting gas side, and h^t the heat transfer coefficient on the gas tube side. The ratio between inner and outer tube diameter relates h^r to the tube inner circumference used in Eq. (5.1)c-d. h^r is determined from a correlation presented for ammonia synthesis gas in packed beds (de Wasch and Froment, 1972),

$$h^r = 6.885 \cdot 10^{-4} \frac{\text{Re}^{\text{r}}}{d_p} \left[\frac{\text{J}}{\text{m}^2 \text{ s K}} \right].$$
 (5.5)

 d_p is the catalyst particle diameter and Re^r is the Reynolds number on the reacting gas side,

$$\mathsf{Re}^{\mathsf{r}} = \frac{d_p v^r \rho^{rg}}{\mu^{rg}},\tag{5.6}$$

in which ρ^{rg} and μ^{rg} are the gas density and viscosity respectively. On the tube side, the heat transfer coefficient is calculated via the Nusselt number from the Dittus-Boelter equation,

$$Nu^t = 0.023 (Re^t)^{0.8} (Pr^t)^{0.33}$$
 (5.7)

$$h^t = \frac{\mathsf{Nu}^t \lambda^{tg}}{d_t},\tag{5.8}$$

with the Prandtl number given by,

$$\mathsf{Pr} = \frac{c_p^{tg} \mu^{tg}}{\lambda^{tg}},\tag{5.9}$$

in which λ^{tg} is the thermal conductivity of the gas. In this work, $\lambda^{tg}=0.3~\frac{\text{W}}{\text{m K}}$, was used, reflecting an average value for the gas mixture over the reactor operating conditions.

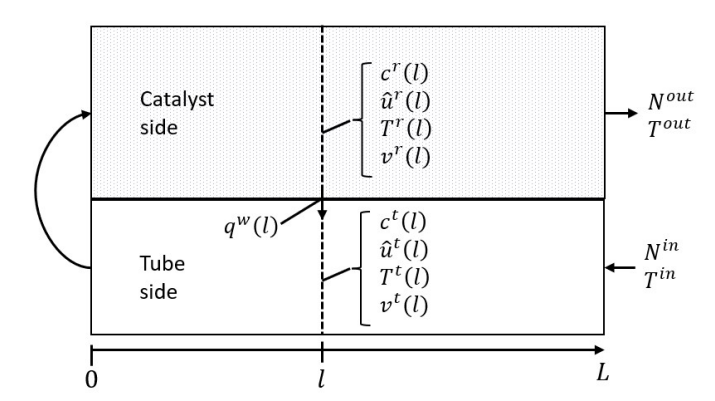


Figure 5.2: Illustration of the IDCR with feed gas used as the cooling utility in countercurrent flow.

IDCR discretization

As for the adiabatic bed, the IDCR is discretized in space by the finite volume method. Figure 5.3 illustrates the FVM for the IDCR with the cells on the catalyst side being connected to the tube side cells via the heat flux over the interface,

$$q_k^w = U_k^w (T_k^r - T_k^t). (5.10)$$

The material and energy balance for the discretized system becomes,

$$\frac{dc_k^r}{dt} = \frac{N_{k-1/2}^r - N_{k+1/2}^r}{\Delta l} + R_k,$$
(5.11a)

$$\frac{dc_k^t}{dt} = \frac{N_{k-1/2}^t - N_{k+1/2}^t}{\Delta l},\tag{5.11b}$$

$$\frac{du_k^r}{dt} = \frac{\epsilon_B \left(\bar{H}_{k-1/2}^r - \bar{H}_{k+1/2}^r\right)}{\Delta l} - n^t \frac{C^t}{A_c^r} q_k^w, \tag{5.11c}$$

$$\frac{du_k^t}{dt} = \frac{\bar{H}_{k-1/2}^t - \bar{H}_{k+1/2}^t}{\Delta l} + \frac{C^t}{A_c^t} q_k^w, \tag{5.11d}$$

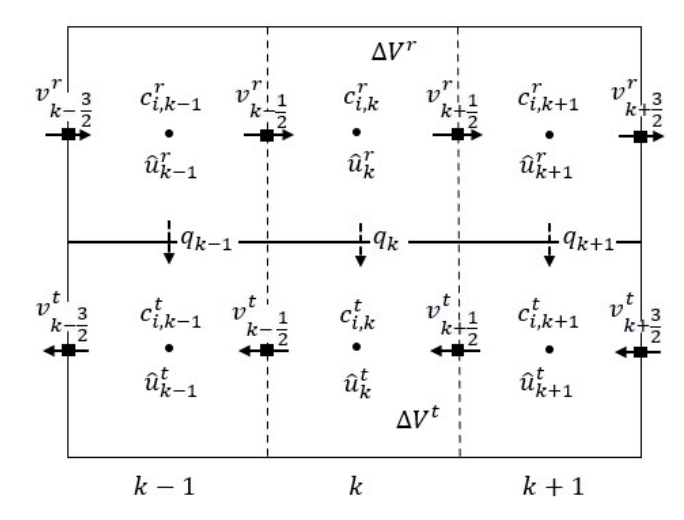


Figure 5.3: Finite volume discretization of the IDCR.

where A_c^r and A_c^t are respectively the catalyst and tube cross-sectional area. Additionally, the algebraic equations governing the IDCR are,

$$\hat{u}_k^r = \epsilon_B \mathcal{U}(T_k^r, P_k^r, c_k^r) + (1 - \epsilon_B)\hat{u}^s(T_k^r),$$
 (5.12a)

$$\hat{v}_k^r = \mathcal{V}(T_k^r, P_k^r, c_k^r) = 1, \tag{5.12b}$$

$$\hat{u}_k^t = \mathcal{U}(T_k^t, P_k^t, c_k^t),\tag{5.12c}$$

$$\hat{v}_k^t = \mathcal{V}(T_k^t, P_k^t, c_k^t) = 1. \tag{5.12d}$$

5.2.3 DAEs formulation

The governing equations (MBs, EBs and EOSs) for the adiabatic fixed bed and counter-current cooled reactors constitute a differential algebra equations (DAEs) system. Let's define the states, \mathbf{x}_k , and algebraic variables, \mathbf{y}_k , of the k'th volume element as,

$$\mathbf{x}_k = [c_k, \ \hat{u}_k],$$
 (5.13a)

$$\mathbf{y}_k = [T_k, \ v_{k+1/2}]. \tag{5.13b}$$

The system is expressed in the general form of the semi-explicit differential algebraic equation,

$$\dot{\mathbf{x}} = f(\mathbf{x}, \mathbf{y}),\tag{5.14a}$$

$$0 = g(\mathbf{x}, \mathbf{y}), \tag{5.14b}$$

in which f constitute the mass and energy balances, and g represents the algebraic equations. We apply this formulation for the DAE system as it has been demonstrated to be the most computationally effective (Rosbo et al., 2024c). Solving Eq. (5.14) involves integrating the balance equations while satisfying the algebraic equations. As (5.14) is a highly nonlinear DAE a numerical solution method is employed.

5.2.4 Numerical parameters

Each adiabatic bed has been divided into 10 cells (K=10), while the IDCR is discretized with 30 volume elements (K=30). This provides an equal number of elements per volume for the reactors. The selected time step size is, $\Delta t=1$ s, offering a good trade-off between numerical accuracy and computational efficiency (Rosbo et al., 2024c).

Table 5.1: Specifications for the reactors and nominal reactor feed flow.

Catalyst properties			Nominal reactor feed flow			
Type: Metallic iron on Fe ₃ O ₄			Pressure, P	[bar]	200	
Total Volume, V_R	[m ³]	6.63	Total flow, F_{Rfn}	[kmol/h]	5846	
Void fraction, ϵ_B		0.33	x_{N_2}		23.8%	
Catalyst density, ρ_p	[kg/m³]	3284	x_{H_2}		71.4%	
Catalyst heat capacity, c_p	[J/(kg K)]	1100	$x_{\rm NH_3}$		4.15%	
Particle hydraulic diameter, d_p	[mm]	8	x_{Ar}		0.60%	

5.3 The Case Study: Ammonia reactors in 100 MW PtA plant

The case study is presented in Section 4.3, revolving around a 100 MW average power input PtA plant. The electrolyser unit utilises approximately 90% of the electrical energy at stoichiometric H_2/N_2 feed ratio. The remaining 10% of power consumption in the PtA plant is distributed between the air separation unit for nitrogen production (2-3%) and compressor work for running the Haber-Bosch process (7-8%) Nayak-Luke et al. (2018). Therefore, in the context of PtA, ensuring the conversion of hydrogen to ammonia is important for achieving high plant efficiency.

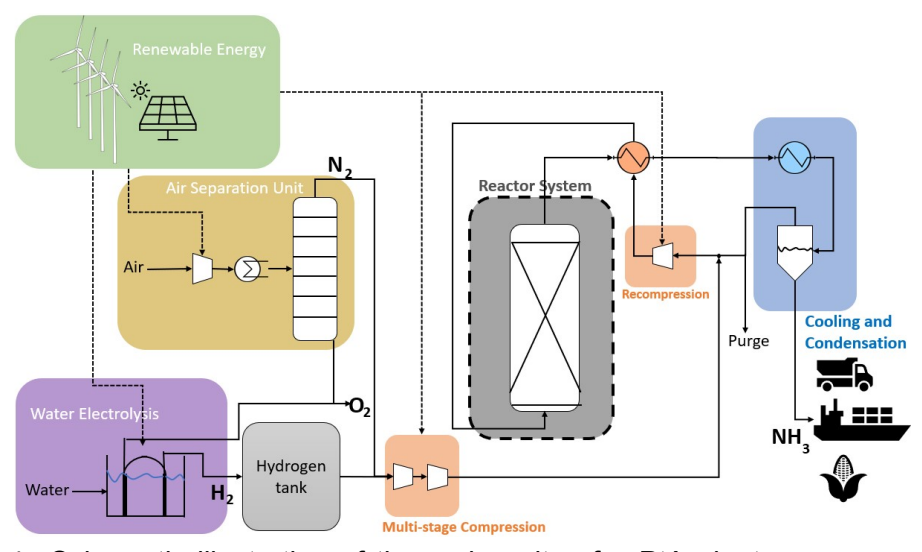


Figure 5.4: Schematic illustration of the main units of a PtA plant. green: renewable energy, purple: water electrolyser, yellow: air separation unit, grey: ammonia reactor system, blue: ammonia flash separator, orange: compressors.

Figure 5.4 provides a schematic representation of the primary operating units in the considered PtA plant. The ammonia reactor is located within the synthesis loop. To keep the analysis clean, without having to account for complicated feedback dynamics arising from the synthesis recycle, the study regards the grey box around the reactor system as the system boundary. This approach allows for a direct comparison of the reactors without the interaction effects from the recycle loop.

5.3.1 Reactor system dimensions

Table 5.1 presents the nominal reactor feed flow corresponding to a power consumption of approximately 100 MW, as described in Chapter 4. The reactors operate at a stoichiometric H_2/N_2 -ratio, with an ammonia content of about 4%, representing a typical operating condition for the vapour phase in the separator. In this case study, the argon content is

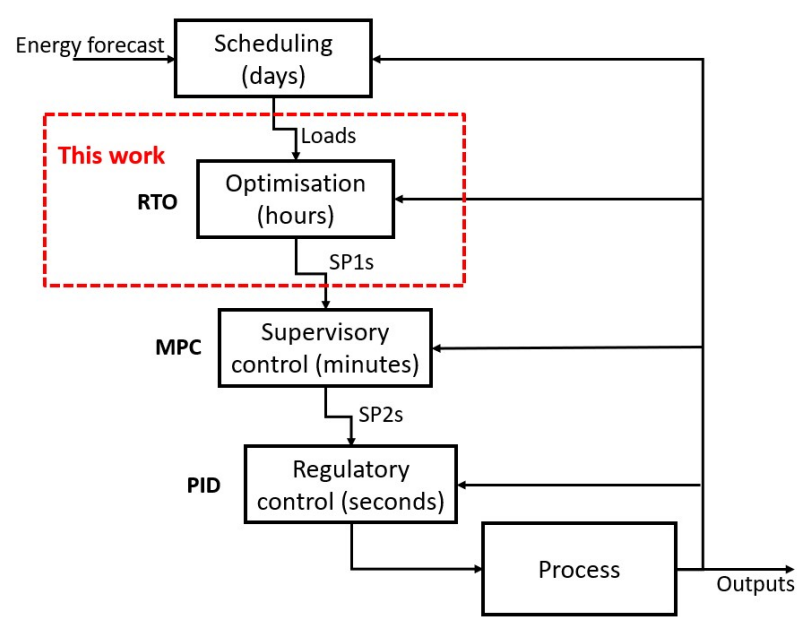


Figure 5.5: Suggested scheduling, optimisation, and control layer structure for a PtA plant.

set to 0.6%, significantly lower than in the conventional case presented in Section 4.3, which is based on literature-reported flows (Shamiri and Aliabadi, 2021; Araújo and Skogestad, 2008; Cheema and Krewer, 2020). This reduction reflects nitrogen production via an ASU rather than by air combustion in the secondary reformer of a conventional ammonia plant (Smith et al., 2020). Since the boiling points of nitrogen, argon, and oxygen are -195.8°C, -185.8°C, and -183.0°C, respectively, most argon separates with oxygen in the ASU (Klein et al., 2021).

The total catalytic reactor volume and catalyst properties follow the case in Section 4.3, which applied a scaled reactor volume based on the industrial design reported by Morud and Skogestad (1998). However, unlike in Chapter 4, where individual bed volumes were directly adopted from the literature, this chapter includes the distribution of catalyst volume among the beds as part of the optimisation in Section 5.4. In addition, Section 5.4 addresses the sizing of the reactor heat-exchanger areas to ensure load-flexible operation

5.3.2 The reactor operating window

Figure 5.5 illustrates a possible scheduling, optimisation and control strategy for a PtA plant. At the top layer, a scheduling optimisation determines the future plant loads based on forecasts for available renewable energy and plant outputs, such as the hydrogen inventory in storage. The desired plant loads are transmitted to an optimisation layer performing a real-time optimisation (RTO) of the plant units. The model-based supervisory control receives the optimised plant set point (SP1s) and calculates the optimal plant trajectory for load switching (SP2s). The supervisory control operates in cascade with an underlying regulatory control structure. As highlighted by the red box in Figure 5.5, this study focuses on the optimisation layer. Specifically, this study involves the optimisation of the reactor system. Our objective is to maximise hydrogen conversion across the reactor operating window, from 30% to 130% of the reactor load.

Reactor load

This work models the reactor system unit of the PtA plant, and thus the system boundaries are the reactor system feed, F_{Rf} , and outlet flow, $F_{R, out}$ (Figure 5.4: grey box). As approximately 92% of the total power input is consumed by the electrolysers, the reactor

load (RL) is defined based on the hydrogen feed flow to the reactor,

$$RL = \frac{F_{Rf, H_2}}{F_{Rfn, H_2}},$$
 (5.15)

where $F_{Rf,\, H_2}$ is the reactor feed flow of hydrogen and $F_{Rfn,\, H_2}$ the nominal flow. The reactor is operated at stoichiometric conditions,

$$F_{Rf, N_2} = \frac{1}{3} F_{Rf, H_2}.$$
 (5.16)

The argon molar flow in the reactor feed stream is assumed constant over the reactor operating window,

$$F_{Rf, Ar} = F_{Rfn, Ar}. ag{5.17}$$

Rosbo et al. (2023a) found an increase in synthesis loop efficiency when operating with a larger recycle ratio at reduced loads. A larger recycle ratio results in higher concentrations of inert argon in the reactor feed stream. Therefore, assuming a constant flow rate of argon over the operating range simulates operating with a larger recycle at low loads, without needing to model the entire synthesis loop. Furthermore, the argon content in the reactor feed ranges from 0.5-3% across the operational range and therefore has negligible influence on the results in this paper.

The flash tank is assumed to be operated at 20°C and 200 bar across the entire operating window. For this condition, the liquid ammonia is more than 98% pure (Michels et al., 1950). Thus, we find the equilibrium vapour mole fraction of ammonia by assuming Raoult's law applies $y_{\rm NH_3} = P_{\rm NH_3}^{\rm sat.}/P$. As the overhead gas from the flash tank flows to the reactor (see Figure 5.4) the mole fraction of ammonia in the reactor feed is assumed constant. Thus, the flow of ammonia in the reactor feed is,

$$F_{Rf, NH_3} = F_{Rfn, NH_3} \left(\frac{F_{Rf, H_2} + F_{Rf, N_2} + F_{Rf, Ar}}{F_{Rfn, H_2} + F_{Rfn, N_2} + F_{Rfn, Ar}} \right).$$
 (5.18)

Equation (5.18) is derived in the Appendix C. Equations (5.15)-(5.18) define the relationship between reactor load and reactor feed flow used throughout this paper. We explore the performance of the reactors over an operational range spanning from 30% to 130% of the nominal load. This is a good reflection of the operating envelope for a PtA plant, however, the operating limits can be somewhat different and softer depending on the specific plant.

5.4 Reactor optimisation and heat transfer design for PtA

The literature about ammonia reactor design predominantly focuses on conventional operation with a stable supply of reactants. In the context of PtA, it is important to ensure that the reactor system (catalyst bed + heat exchanger) can achieve the desirable operating temperatures over the entire operational window. With the total catalyst volume fixed as tabulated in Table 5.1, the AQCR and AICR system design involves dividing the catalyst volume between the beds and determining the size of the heat exchangers. For the IDCR, the design involves determining the required tubing heat transfer contact area. The objective of the reactor optimisation is to maximise the conversion of reactants per reactor pass. Achieving maximum conversion results in a higher fraction of ammonia in the reactor outlet, which eases separation in the flash tank (see Figure 5.4). Additionally, maximising reactant conversion per reactor pass reduces the size of the recycle stream, leading to lower pressure drop across the operating units and reduced recompression work. Therefore, optimising the reactors for reactant conversion minimises the

operational costs of the synthesis loop. It is important to note that this approach does not necessarily align with the most economical scenario when considering both capital and operational costs. However, performing a full economic optimisation of the PtA plant is beyond the scope of this work. This study aims to compare the different reactor types for PtA operation. Thus, optimising the reactors for conversion provides a fair design basis on which one can assess the static and dynamic characteristics of the reactors.

5.4.1 AQCR optimisation and heat exchanger design

Figure 5.1a illustrates the three-bed AQCR system where preheating of the feed gas occurs over the feed-effluent heat exchanger, and cooling is achieved via the quench streams. The optimal design of the AQCR to maximise reactant conversion can be determined by solving the optimisation problem,

$$\min_{T_{Rf}, q_{Rj}, V_{Bj}, A_{hex}} F_{R, out, H_2}(T_{Rf}, q_{Rj}, V_{Bj}, A_{hex}), \tag{5.19a}$$

s.t.
$$f(x,y) = 0$$
, (5.19b)

$$g(x,y) = 0$$
 (5.19c)

$$q_{R0} + q_{R1} + q_{R2} + q_{R3} = 1,$$
 (5.19d)

$$V_{B1} + V_{B2} + V_{B3} = V_R.$$
 (5.19e)

 T_{Rf} is the feed temperature, q_{Rj} are the quench fractions, V_{Bj} are the bed volumes, and A_{hex} is the heat exchanger area. Note, the optimisation problem in (5.19) differs from the AQCR optimisation performed in the previous chapter Section 4.4.5. In Section 4.4.5 the reactor feed temperature and heat-exchanger area were fixed, while (5.19) includes these in the optimisation. However, the optimisation problem (5.19) leads to unbounded values for the feed temperature and heat exchanger area, approaching negative and positive infinity, respectively. An economic objective considering the cost of the heat exchanger area versus the profit of increased conversion is beyond the scope of this work as explained in section 5.4. Nevertheless, one may assess the trade-off qualitatively by specifying a feed temperature and solving the optimisation problem (5.20),

$$\min_{T_{bed1,\ in},q_{R01},\ q_{R2},\ q_{R3},\ V_{Bj}} F_{R,\ out,\ \mathsf{H_2}}(T_{bed1,\ in},q_{R01},\ q_{R2},\ q_{R3},\ V_{Bj}), \tag{5.20a}$$

$$s.t. \quad f(x,y) = 0,$$
 (5.20b)

$$g(x,y) = 0,$$
 (5.20c)

$$q_{R01} + q_{R2} + q_{R3} = 1, (5.20d)$$

$$V_{B1} + V_{B2} + V_{B3} = V_R,$$
 (5.20e)

in which $T_{bed1, in}$ is the inlet temperature to bed 1, and $q_{R01} = q_{R0} + q_{R1}$. The heat exchanger equations are eliminated from the optimisation by defining the optimisation problem in terms of $T_{bed1, in}$ and q_{R01} . This significantly reduces the computational effort of optimising the AQCR. The solution to Eq. (5.20) is found via Matlab's optimiser fminsearch.

Subsequently, the heat exchanger area that corresponds with the optimal solution to Equation (5.20) is determined. From Figure 5.1a, observe that T_{Rf} is the cold side- and $T_{bed3,\ out}$ the hot side inlet temperature for the feed-effluent heat exchanger. $T_{bed1,\ in}$ is the temperature after mixing the cold side heat exchanger outlet and the bypass. To minimise the heat exchanger area, it is optimal to have no bypass flow. However, to provide some margin for control, the bypass quench fraction, q_{R1} , is set to 5%. The feed fraction to the heat exchanger is then $q_{R0}=q_{R01}-0.05$. The required heat exchanger area is found by expressing the bed 1 inlet temperature as a function of the heat exchanger area and

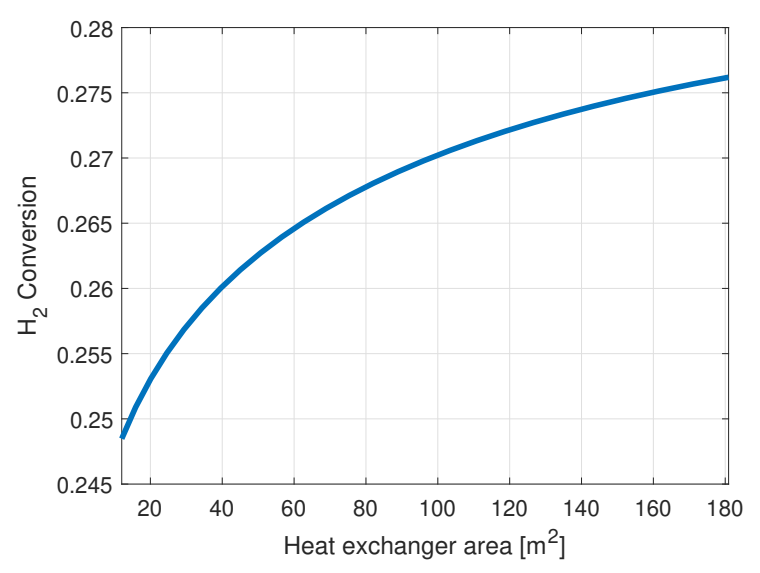


Figure 5.6: Maximum H₂ conversion versus heat exchanger area.

equating this to the optimal value from the solution to Eq. (5.20),

$$T_{bed1, in}(A_{bex}) = T_{bed1, in},$$
 (5.21a)

s.t.
$$T_{chex, out} = \text{hex}(F_f q_{R0}, T_{Rf}, F_{bed3, out}, T_{bed3, out}, A_{hex}),$$
 (5.21b)

$$T_{bed1, in} = mix(F_f q_{R1}, T_{Rf}, F_f q_{R0}, T_{chex, out}).$$
 (5.21c)

The functions hex and mix represent the solutions of the heat exchanger and mixing equations defined in Section 4.2.2 and 4.2.3. This procedure is performed over a range of feed temperatures yielding a relationship between feed temperature, maximum conversion, and heat exchanger area. Figure 5.6 shows the maximum H_2 conversion versus the corresponding heat exchanger area. Observe that the gradient of H_2 conversion decreases quickly for increasing heat exchanger area. A heat exchanger area of 100 m^2 is chosen. Note that the chosen heat exchanger area does not significantly influence the main results of this paper. With the heat exchanger area specified the solution to the optimisation problem (5.19) becomes,

$$T_{Rf} = 400.0 \text{ K}$$
 (5.22a)

$$[q_{R0}, q_{R1}, q_{R2}, q_{R3}] = [0.484, 0.050, 0.231, 0.235],$$
 (5.22b)

$$[V_{B1}, V_{B2} V_{B3}] = [0.967 \text{ m}^3, 1.98 \text{ m}^3, 3.69 \text{ m}^3].$$
 (5.22c)

The solution for the bed volumes fixes the bed volumes of the AQCR reported in Table 5.2.

Figure 5.7 shows the hydrogen conversion versus temperature along the reactor beds for the optimal AQCR configuration at nominal load. The hydrogen conversion, $X_{\rm H_2}$, along reactor bed m is defined relative to the amount of hydrogen supplied before the bed,

$$X_{\mathsf{H}_2}(l) = 1 - \frac{F_{\mathsf{H}_2}(l)}{\sum_{j=1}^m F_{f,j,\mathsf{H}_2}}.$$
 (5.23)

The temperature approaches the equilibrium curve at the end of the beds. Therefore, the quench streams are injected to cool the reacting gas and facilitate further conversion in the subsequent bed.

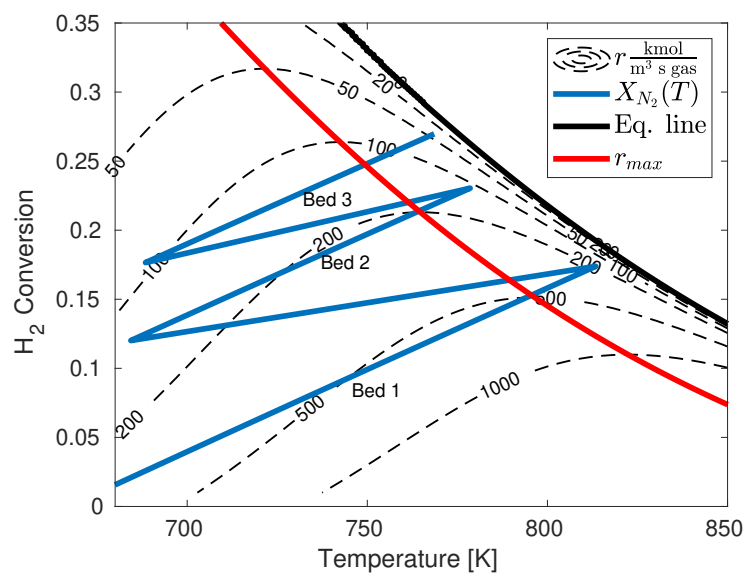


Figure 5.7: Reactant conversion versus temperature along the AQCR beds for the optimal reactor configuration at nominal load.

Table 5.2: Optimal bed and heat exchange dimensions for the reactors.

AQCR			AICR	IDCR		
Bed dimensio	ns:					
Bed diameter	[m]	1.2	1.2	Reactor length	[m]	6.64
Bed 1 volume	[m ³]	0.967	0.998	Cross sectional area	[m ²]	1.00
Bed 2 volume	[m ³]	1.98	2.13	Inner tube diameter	[cm]	3.81
Bed 3 volume	$[m^3]$	3.69	3.50	Outer tube diameter	[cm]	5.08
Heat exchang	je area:					
Hex 1	$[m^2]$	100	89.0	Number of tubes	$[m^2]$	115
Hex 2	[m ²]	-	67.4	Total inner tube area	$[m^2]$	91.3
Conversion at	t nominal load:	'		I		
		26.9%	30.0%			29.4%

5.4.2 AICR optimisation

Figure 2.5b displays the AICR configuration. Initially, consider the AICR without the heat exchangers and regard the bed inlet temperatures as unbound optimisation variables. The optimal bed inlet temperatures, $T_{bed,\ in}$, and bed volumes are determined by solving the optimisation problem in Eq. (5.24) for the nominal load,

$$\min_{T_{bed, in}, V_{Bj}} F_{R, out, H_2}, \tag{5.24a}$$

$$s.t. \quad f(x,y) = 0,$$
 (5.24b)

$$g(x,y) = 0,$$
 (5.24c)

$$V_{B1} + V_{B2} + V_{B3} = V_R. (5.24d)$$

Equation (5.25) displays the solution for the optimal bed inlet temperatures at nominal load. The solution to (5.24) sets the bed volumes of the AICR, displayed in Table 5.2.

$$[T_{bed1, in}, T_{bed2, in}, T_{bed3, in}] = [700.3 \text{ K}, 704.2 \text{ K}, 695.0 \text{ K}]$$
 (5.25)

Heat exchanger design for the AICR

The load requiring the highest absolute recovery of heat is the upper limit of the operating window due to the larger flow through the reactor system. Therefore, the heat exchangers are designed to accommodate 130% of the nominal load. With the bed volumes fixed, one can determine the optimal bed inlet temperatures for a given load by solving the optimisation problem in Eq. (5.26),

$$\min_{T_{bed, in}} F_{R, out, H_2},$$
(5.26a)

$$s.t. \quad f(x,y) = 0,$$
 (5.26b)

$$q(x,y) = 0.$$
 (5.26c)

Solving Eq. (5.26) at 130% load obtains optimal temperatures and flows for all bed inlet and outlet streams. The cooling duty required in each heat exchanger can be calculated from,

$$Q_{Hex1} = \dot{H}(T_{bed1, out}, P, F_{bed1, out}) - \dot{H}(T_{bed2, in}, P, F_{bed2, in}), \tag{5.27a}$$

$$Q_{Hex2} = \dot{H}(T_{bed2, out}, P, F_{bed2, out}) - \dot{H}(T_{bed3, in}, P, F_{bed3, in}).$$
(5.27b)

The feed temperature is determined by setting up an energy balance for the bed 1 inlet stream.

$$\dot{H}(T_{bed1, in}, P, F_f) - \dot{H}(T_{Rf}, P, F_f) = Q_{Hex1} + Q_{Hex2}.$$
(5.28)

Solving Eq. (5.28) for 130% load the required feed temperature is,

$$T_{Rf} = 513 \text{ K},$$
 (5.29)

Figure 2.5b shows that a fraction of the feed bypasses the heat exchangers. The bypass is set to 5% of the feed stream, $q_{R0} = 0.05$, for control flexibility. For a given split between q_{R1} and q_{R2} the heat exchanger areas can be found by solving Eq. (5.30),

$$T_{bed2, in}(A_{hex1}) = hex(F_f q_{R1}, T_{Rf}, F_{bed1, out}, T_{bed1, out}, A_{hex1}),$$
 (5.30a)

$$T_{bed3, in}(A_{hex2}) = hex(F_f q_{R2}, T_{Rf}, F_{bed2, out}, T_{bed2, out}, A_{hex2}).$$
 (5.30b)

Eq. (5.30) is solved over a range of splits between q_{R1} and q_{R2} . Figure 5.8 show the solution for the heat exchanger areas as a function of q_{R1} . A minimum is observed for the

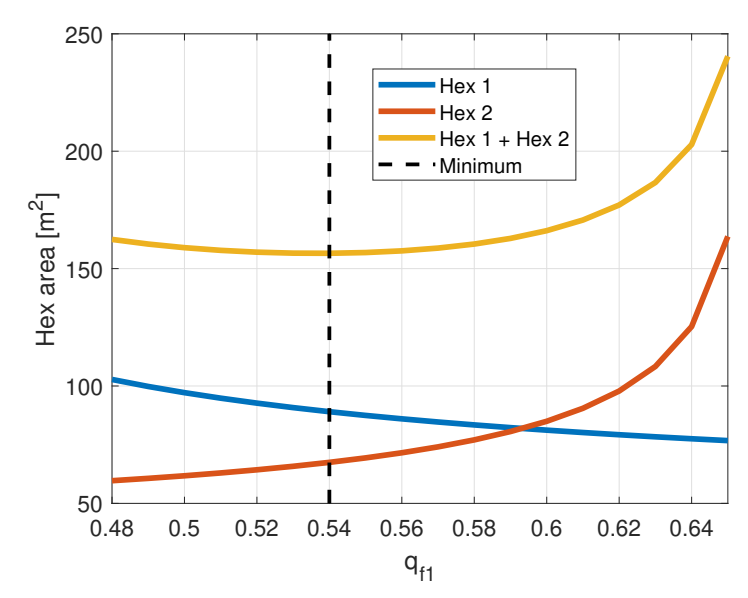


Figure 5.8: AICR heat exchanger area versus the feed split to the first heat exchanger, q_{R1} .

total heat exchanger area for a feed split to Hex 1 of $q_{R1}=0.54$. Alternatively, one could have determined the minimal heat exchanger area by solving an optimisation problem for the total heat exchanger area constrained by Equation (5.30). From Figure 5.8, observe that the gradient of the total required heat exchanger area remains relatively flat around the optimum. The "plateau" between $q_{R1} \in [0.5, 0.6]$ represents a design window where the cost function remains close to constant. This information could be valuable for a design engineer tasked with selecting heat exchanger areas based on the spatial layout of the reactor. However, in this study, this optimum was selected, as considerations related to the reactor's spatial layout are outside the scope of this manuscript. Table 5.2 tabulates the individual heat exchanger areas at the optimum.

5.4.3 IDCR

Figure 5.1c shows the IDCR configuration where heat removal is achieved along the catalyst bed by counter current flow with the feed gas on the tube side. The dimensions of the IDCR cooling tubes are scaled from Khademi and Sabbaghi (2017) and given in table 5.2.

The steady-state of the IDCR is solved by starting from a top temperature, T_{top} , and solving the steady-state IDCR equation system to obtain the reactor outlet temperature on the catalyst side and feed temperature on the tube side. Figure 5.9 shows the temperature and conversion profiles on the catalyst and tube sides for a top temperature of $T_{top} = 700~{\rm K}$ and the number of cooling tubes, $T_{top} = 110$.

The IDCR is optimised by determining the top temperature and cooling tube surface area, which maximises the conversion of the reactants. As the diameter and length of the cooling tubes are specified in Table 5.2, the area can be expressed in terms of the number of cooling tubes. Mathematically the optimisation is expressed in Eq. (5.31),

$$min. F_{R, out, H_2}(T_{top}, n_T),$$
 (5.31a)

$$s.t. \quad f(x,y) = 0,$$
 (5.31b)

$$g(x,y) = 0.$$
 (5.31c)

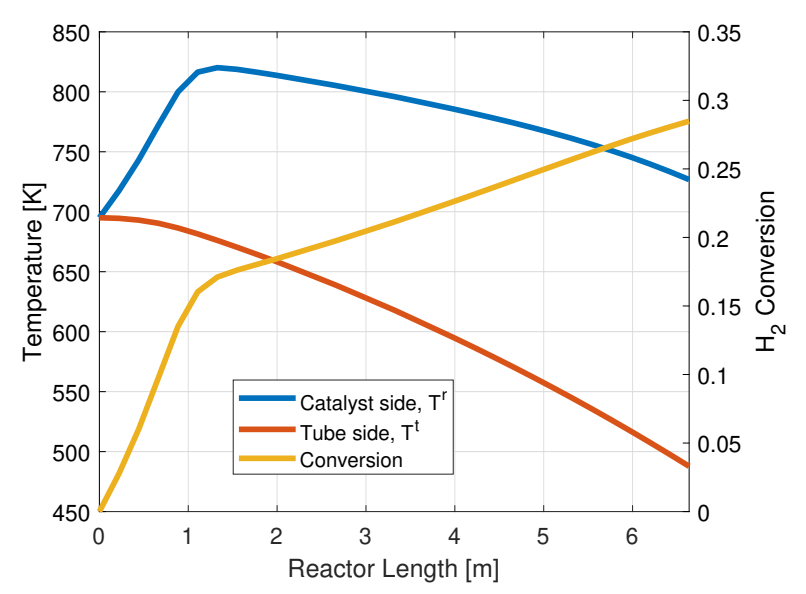


Figure 5.9: Left axis: Catalyst and tube side gas temperature. Right axis: Conversion along the IDCR. The top temperature is $T_{top} = 700$ K.

The solution to Eq. (5.31) is $T_{top}=663 \mathrm{K}$ and $n_T^{opt}=114.9$. Thus, the actual number of cooling tubes is rounded up as displayed in table 5.2. Observe, the total inner tube contact area is similar to the areas found for the heat exchangers in the AQCR and AICR configurations.

5.5 Steady state and stability comparison

Figure 5.10 shows graphs for reactant conversion versus temperature of the optimal solution at nominal load for the AQCR, AICR and IDCR. Table 5.2 summarises the total conversion per reactor pass. The AICR and IDCR yield similar conversions at around 30% per reactor pass, while the AQCR shows significantly less reactant conversion 3-4% points lower than the AICR and the IDCR. These results for conversions align with the work of Khademi and Sabbaghi (2017).

Figure 5.10 supports the preference for the AICR and the IDCR at nominal flow conditions, highlighting their advantages for conventional plants. However, in the context of PtA, the reactors also need to be capable of operating flexibly and robustly under varying loads.

5.5.1 Bifurcation analysis wrt. feed temperature

Figures 5.11 a), c) and e) show a characteristic plot displaying multiple steady-states for the AQCR, the AICR and the IDCR. All the reactors exhibit the characteristic S-curve when identifying the steady-states over a range of reactor feed temperatures from 450 K to 600 K. The regions of three steady-states are enclosed by an extinction- and an ignition point, beyond which only the fully extinct or ignited reactor states exist. It is observed that the bend at the extinction point is narrower for the AICR compared to the AQCR, and for the IDCR, the extinction point even ends in a sharp cusp shape.

As described in Section 4.4.4, the stability of the reactor systems can be determined from the eigenvalues of the linearisation matrix, A, obtained by linearising the reactor system around a steady-state operating point.

$$\dot{\mathbf{x}} = A\mathbf{x},\tag{5.32}$$

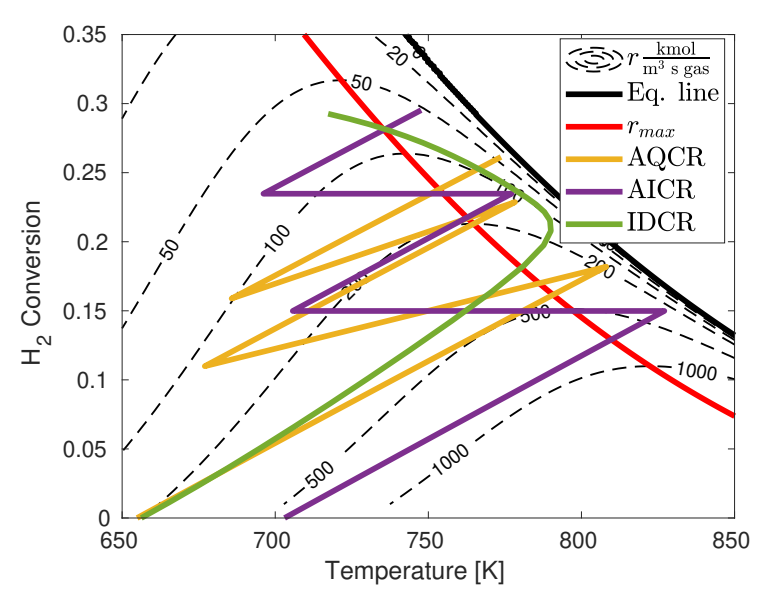


Figure 5.10: Conversion versus temperature at nominal load for the optimised AQCR, AICR and IDCR.

Figure 5.11 b), d) and f) display a bifurcation analysis of the reactor systems' upper steady states when the feed temperature is varied as the bifurcation parameter. As found in Rosbo et al. (2023b) a complex pair of eigenvalues crosses into the right-hand-side (rhs) plane for the AQCR (Figure 5.11b). Eigenvalues in the rhs plane involve a positive real part, giving rise to unstable oscillatory transients. The point of instability for the AQCR is located between the optimum and the extinction points as depicted in Figure 5.11a). Figure 5.11d) and f) show the eigenvalues for the AICR and the IDCR for the upper steady-state. A complex pair of eigenvalues approach but never crosses the y-axis for both the AICR and the IDCR. A purely real eigenvalue reaches the y-axis corresponding to the extinction point where the upper steady-state loses stability.

5.5.2 Bifurcation analysis wrt. reactor load

Figure 5.12 presents a bifurcation analysis with respect to the reactor load, as defined in Section 5.3.2. Figures 5.12a), c), and e) show the multiple steady-state solution maps for the AQCR, AICR, and IDCR reactor configurations, respectively. Unlike the classic S-shaped bifurcation curve observed in Figure 5.11, the curves here exhibit a Z-shape. This Z-shape occurs as the reactors approach blowout at high loads. The upper steady state ranges from extinction at 1.02-1.04 load and theoretically extends to the zero flow limit.

Figures 5.12b), d), and f) illustrate the evolution of the reactor eigenvalues as the load changes. For the AQCR, a stability loss is observed before extinction, as a complex conjugate pair of eigenvalues crosses into the right half-plane (positive real part), indicating the onset of oscillatory instability. In contrast, the AICR and IDCR maintain stability throughout the load range; however, their optimal operating points lie close to the extinction boundary in all cases, implying a narrow margin for safe operation.

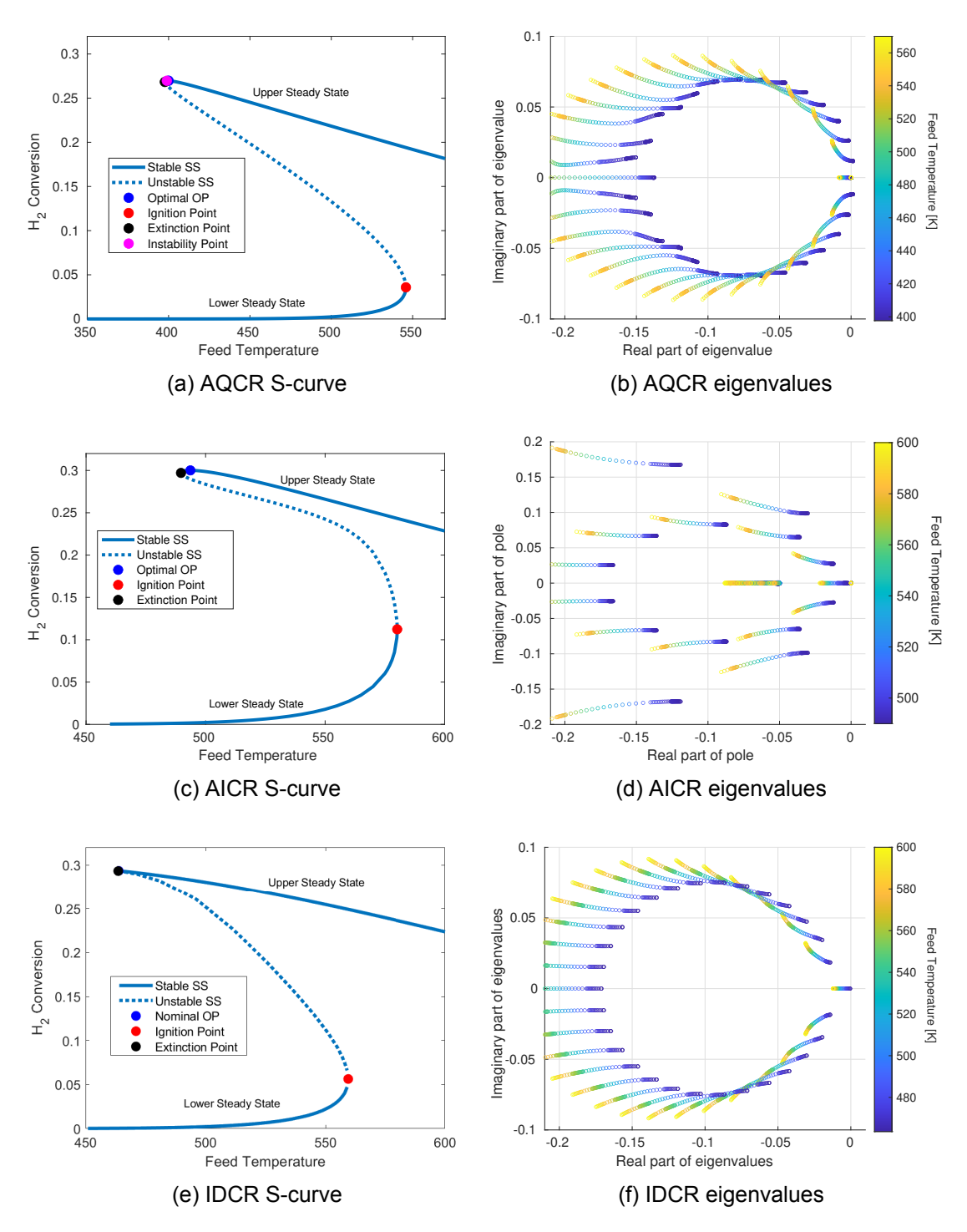


Figure 5.11: a), c) and e) Show the steady-states solutions versus reactor feed temperature, T_f , for the AQCR, AICR and IDCR. The region of multiple steady-states defines an S-curve enclosed by the extinction and ignition point. b), d) and f) display the evolution of the system eigenvalues, λ , wrt. feed temperature. An instability point is indicated in (a) for the AQCR reactor as a complex pair of eigenvalues crosses into the right hand side plane.

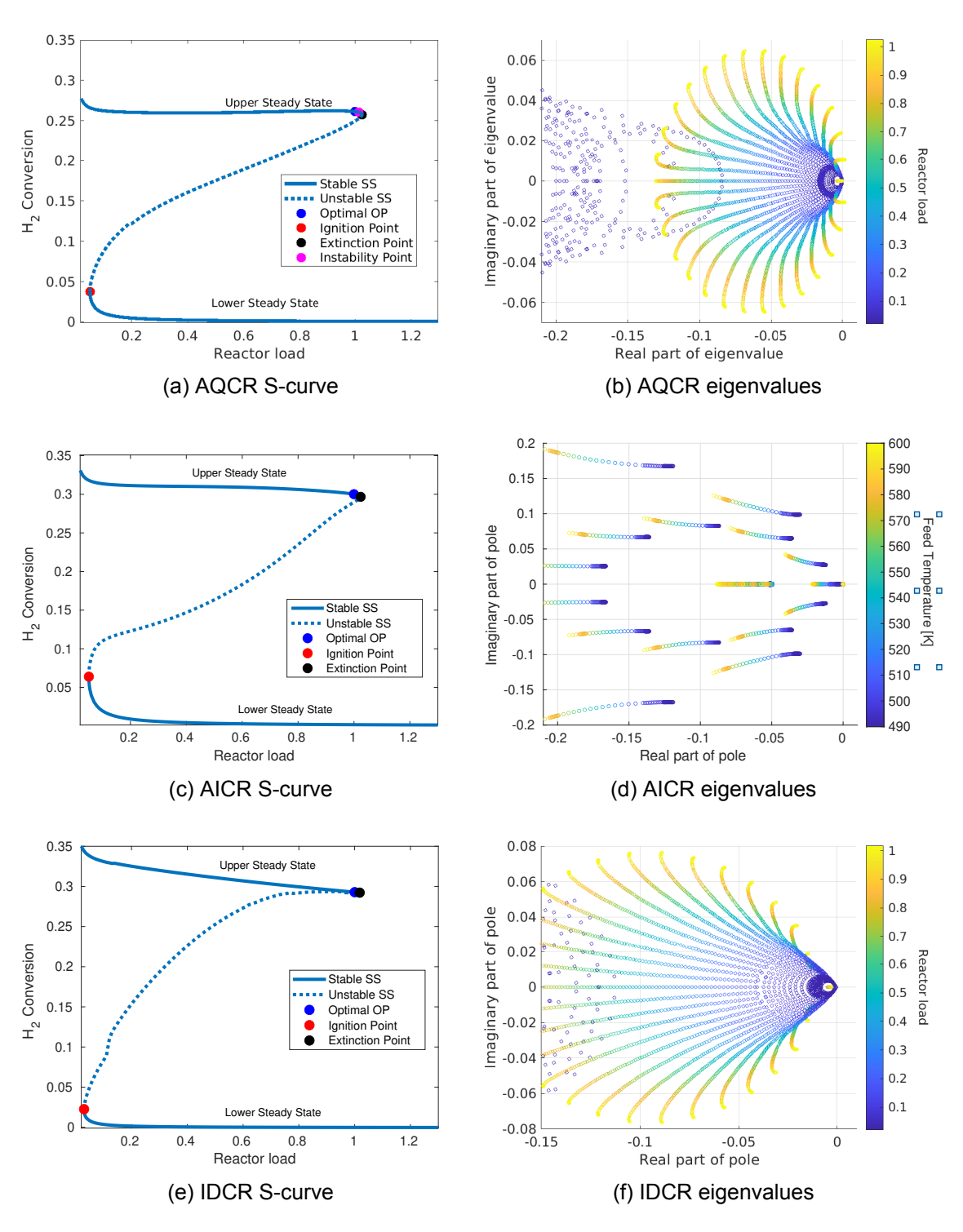


Figure 5.12: a), c) and e) Show the steady states solutions for varying reactor load, RL, of the AQCR, AICR and IDCR. The region of multiple steady states defines a Z-curve enclosed by the extinction and ignition points. b), d) and f) display the evolution of the reactor eigenvalues, λ , wrt. reactor load. An instability point is indicated in (a) for the AQCR reactor as a complex pair of eigenvalues crosses into the right half plane.

5.6 Open loop transient simulations of the reactors

5.6.1 Feed temperature disturbances

The transient behaviour of the reactor types is initially investigated by simulating the reactor responses to step changes in the reactor feed temperature. Figure 5.13 shows the responses of reactor outlet temperature and conversion for the AQCR (Figure 5.13a), AICR (Figure 5.13b) and IDCR (Figure 5.13c). All the simulations start from the optimal operation points at nominal load. The transients are initiated by a 2-5 K step increase in feed temperature, followed by a step-wise decrease of the feed temperature towards the extinction point.

The behaviour of the AQCR reactor is dominated by oscillations as predicted from Figure 5.11a) where the eigenvalues lie close to the rhs plane around the optimal operating point. Generally, good agreement is observed between the stability analysis and the transient simulations for the AQCR reactor. The initial two step changes around the optimal point cause significant but damped oscillations. Stepping the reactor feed temperature below the instability point, the AQCR exhibits growing unstable oscillations. Lastly, upon returning to the optimal feed temperature, the AQCR does not recover the stable optimal operating state; instead, it continues oscillating with growing amplitude towards a stable limit cycle. Andersen (1999) demonstrated that once the AQCR has passed beyond the instability point, it transitions to an oscillatory regime with stable limit cycles. From the oscillatory regime, a significant rise in the feed temperature is required to bring the reactor back to a stable steady-state. This was illustrated in Section 4.4.3.

Figure 5.13b) and 5.13c) display the transient responses of the AICR and IDCR respectively. Good agreement is observed between the stability analysis in Figure 5.11c)-f) and the dynamic behaviours. As predicted from the stability analysis, the step responses display stable dynamics. Moreover, it is observed that the dynamic responses of the AICR and the IDCR hardly show any oscillations. This agrees with the location of the complex eigenvalues in Figure 5.11c) and e) relatively far from the y-axis in the lhs-plane, corresponding to guickly decaying oscillations.

Returning to Figure 5.13a) and b), an inverse response is observed in the reactor outlet temperature for the AQCR and AICR. That is, a change in the feed temperature initially leads to a response in the opposite direction. In the case of the AQCR, the inverse response is fed back to the reactor beds through the feed-effluent heat exchanger, causing unstable oscillations. However, for the AICR, the inverse response is damped through the inter-bed heat exchangers. Conversely, the IDCR does not exhibit an inverse response, as a change in the feed temperature leads to a response in the same direction for the outlet temperature. An inverse response can complicate controller design and should therefore be carefully considered when designing a control scheme for AQCRs and AICRs.

5.6.2 Reactor extinction and ignition

Figure 5.11 predicts distinct ignition and extinction points that enclose a region of multiple steady states for all reactor types. This section investigates the transient behavior associated with reactor extinction and reignition. Figure 5.14 presents dynamic simulations in which the reactor feed temperature is first decreased below the extinction point and subsequently increased above the ignition point to trigger reignition.

The AICR and IDCR show similar responses when the feed temperature is stepped slightly below the extinction threshold. During the first hour following the step, the outlet temperature and conversion profiles appear stable, making it difficult to detect the destabilisation. Subsequently, particularly in the AICR, an upward bump in temperature is observed, co-

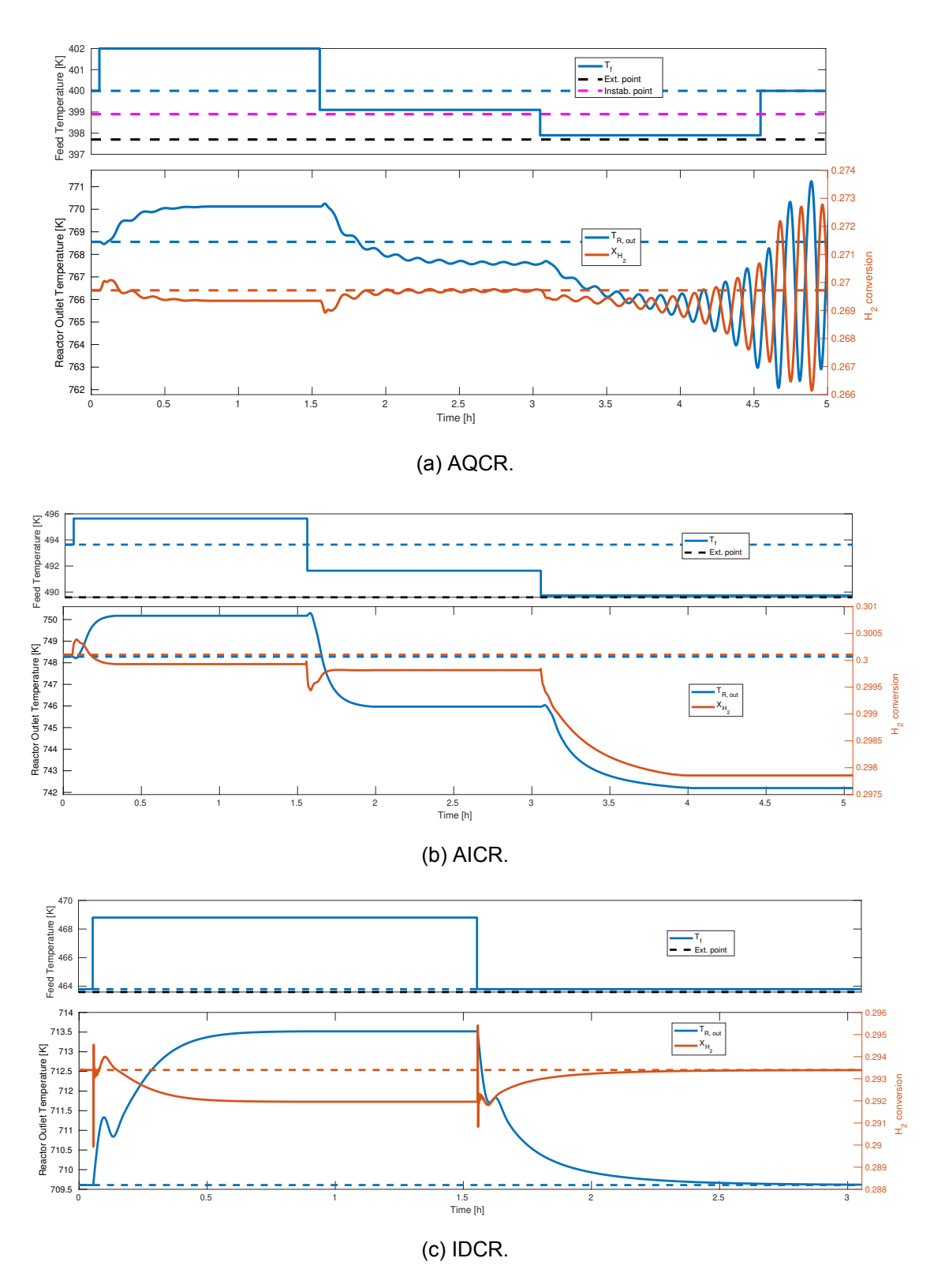


Figure 5.13: Step responses of reactor outlet temperature and conversion for the AQCR (a), AICR (b) and IDCR (c). The responses are induced by an initial step increase in the reactor feed temperature followed by step decreases towards the extinction point. The AICR and IDCR show stable responses, while the AQCR exhibits unstable oscillations as predicted in Figure 5.11.

inciding with a sharp decline in conversion. This behaviour occurs as the extinction front propagates from the inlet to the outlet of the bed. Initially, extinction at the bed inlet suppresses the reaction, reducing conversion. However, the downstream section of the bed remains hot, and the incoming, less-converted gas accelerates the reaction in this zone, releasing more heat and causing the observed temperature bump. Eventually, the extinction front reaches the bed outlet, leading to rapid and complete reactor extinction.

The same differential transport of mass and heat through the bed also explains the inverse responses seen in the AQCR and AICR. In the AQCR, this effect is further amplified by feedback through the feed-effluent heat exchanger, contributing to the observed limit-cycle behaviour. As shown in Figure 5.14a), the AQCR enters an oscillatory regime when the feed temperature drops below the extinction point. A sufficiently large temperature decrease ultimately causes full extinction of the AQCR reactor.

The reactors are reignited by increasing the feed temperature above the ignition point. For all reactor configurations, ignition typically takes around two hours before a new steady state is established. However, thermomechanical stress in the thick reactor walls and catalyst packing imposes strict limitations on the allowable heating rate during restart. Industry reports suggest that ammonia reactor restarts may require several days (Schulte Beerbühl et al., 2015; Armijo and Philibert, 2020; Institute for Sustainable Process Technology, 2017). Furthermore, extended shutdown periods pose a risk of catalyst deactivation (Matthey, 2021). As a result, an unforeseen reactor extinction event can cause prolonged downtime for a power-to-ammonia (P2A) plant, potentially leading to substantial economic losses.

5.6.3 Transient response to changes in load

The open-loop responses to changes in feed temperature provide valuable insight into the dynamic behaviour of the different reactor types, including inverse responses and oscillatory phenomena. However, in Power-to-Ammonia (PtA) systems, variations in reactor load represent the most significant disturbance affecting reactor operation.

Figure 5.15 presents the dynamic responses of the reactor systems to step changes in reactor load. During these transitions, the reactor feed splits are held constant, consistent with the bifurcation analysis presented in Section 5.5.2. The simulation results show strong agreement with the bifurcation predictions. When the load is decreased, the conversion of reactants does not significantly increase, as the reaction near the bed outlet is already close to equilibrium. Additionally, as anticipated by the bifurcation analysis, a slight increase in reactor flow beyond the nominal point leads to destabilisation. This destabilisation results in reactor blowout for the AICR and IDCR, while the AQCR exhibits oscillatory behaviour.

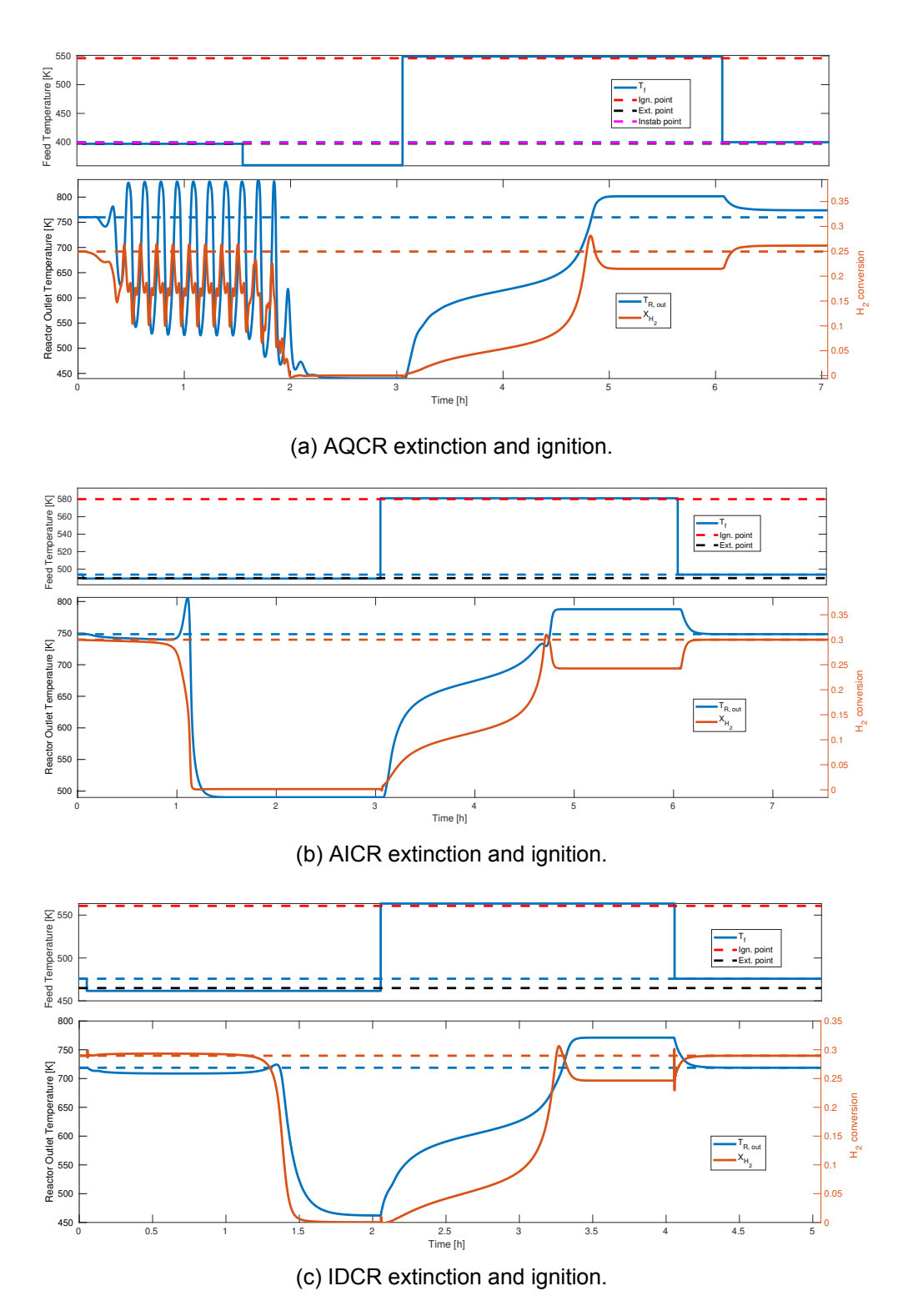


Figure 5.14: Transient simulation of reactor extinction and ignition for the AQCR (a), AICR (b), and IDCR (c). The AICR and IDCR extinguish when the feed temperature is reduced below the extinction point, while the AQCR exhibits unstable oscillations. Further reduction in feed temperature ultimately leads to extinction of the AQCR. Reignition by increasing the feed temperature above the ignition point follows a similar trajectory for all three reactor types.

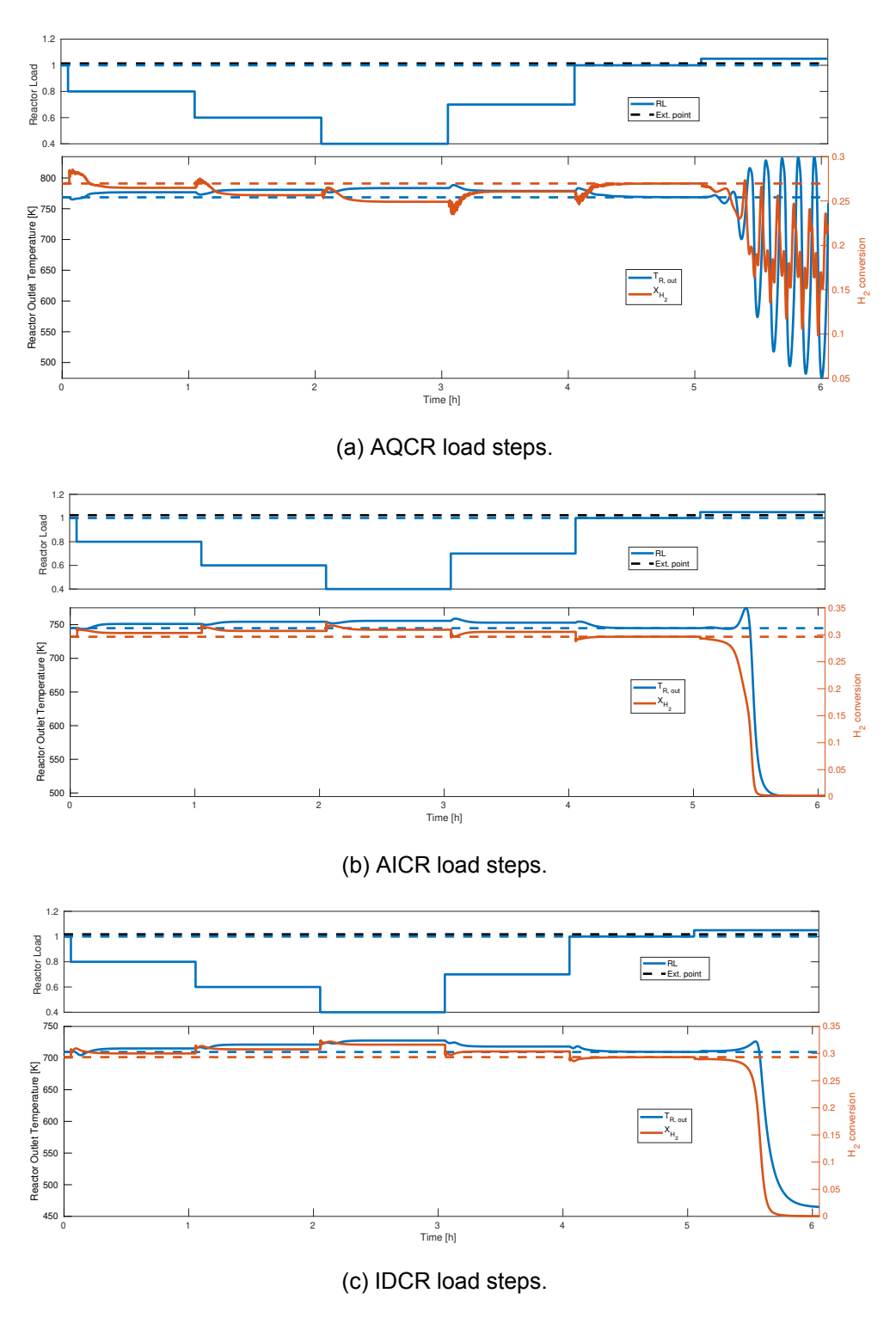


Figure 5.15: Transient response for load changes in the reactor feed flow of the AQCR (a), the AICR (b) and the IDCR (c).

5.7 Reactor optimisation across the operating window

The intermittent nature of renewable energy sources requires the ammonia reactors to operate across a wide load window. The bifurcation analysis in Section 5.11 and open-loop simulations in Section 5.6 demonstrated suboptimal operation with constant reactor

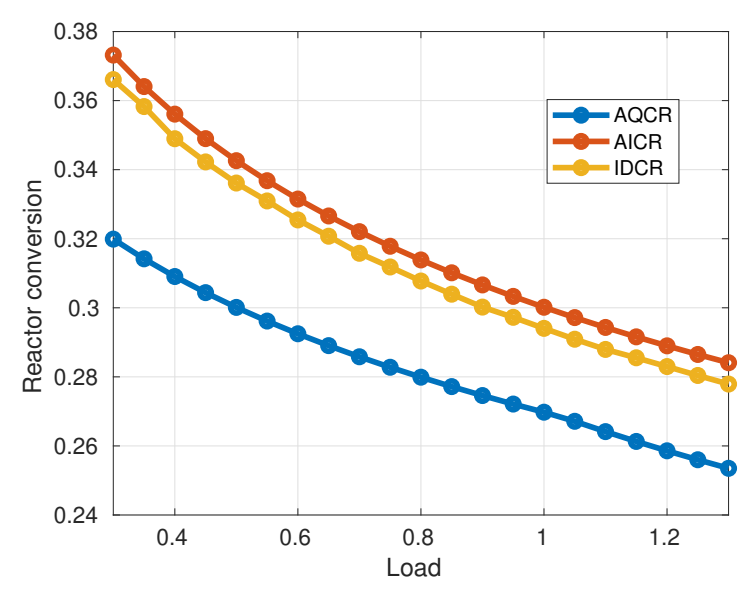


Figure 5.16: Conversion for the reactor types over the operating window. The reactors are optimised over the entire operating window. Markers indicate optimisation points.

settings. Therefore, the reactors are optimised across the operating window from 30% to 130% of the nominal load. For the AQCR, the optimal reactor feed temperature and feed splits are determined by solving the optimisation problem in Eq. (5.33).

$$\min_{T_{Rf}, q_R} F_{\mathsf{H_2}, Rout}(T_{Rf}, q_R), \tag{5.33a}$$

$$s.t. \quad f(x,y) = 0,$$
 (5.33b)

$$g(x,y) = 0,$$
 (5.33c)

$$q_{R0} + q_{R1} + q_{R2} + q_{R3} = 1,$$
 (5.33d)

$$q_{R0} \ge 0.05.$$
 (5.33e)

The constraint $q_{R0} \geq 0.05$ is imposed to ensure control space for the heat exchanger bypass.

In the case of the AICR, the optimal reactor settings are determined by solving the optimisation problem Eq. 5.26.

For the IDCR, the number of cooling tubes is fixed from the design optimisation in Eq. 5.31. Thus, the only degree of freedom for IDCR is the top temperature,

$$\begin{aligned} & \underset{T_{top}}{\min} & F_{Rout, \; \mathsf{H}_2}(T_{top}), \\ & s.t. & f(x,y) = 0, \end{aligned} \tag{5.34a}$$

$$s.t. \quad f(x,y) = 0,$$
 (5.34b)

$$g(x,y) = 0.$$
 (5.34c)

Figure 5.16 depicts the conversion profiles for the optimised configurations of all three reactor types across the entire operational window. The optimisation has been performed at 5% load intervals indicated by the dot markers in Figure 5.16. Through optimisation, the reactors achieve significantly higher conversions at reduced loads. The curves for the AICR and IDCR show similar behaviour over the load range, with the IDCR curve slightly displaced at a lower conversion level. Conversely, the AQCR exhibits a significantly smaller gradient in conversion wrt. load, indicating reduced flexibility in utilising the reactor volume at lower loads compared to the AICR and IDCR. The increased reactant conversion in the reactors is achieved by lowering the inlet temperatures of the catalyst beds.

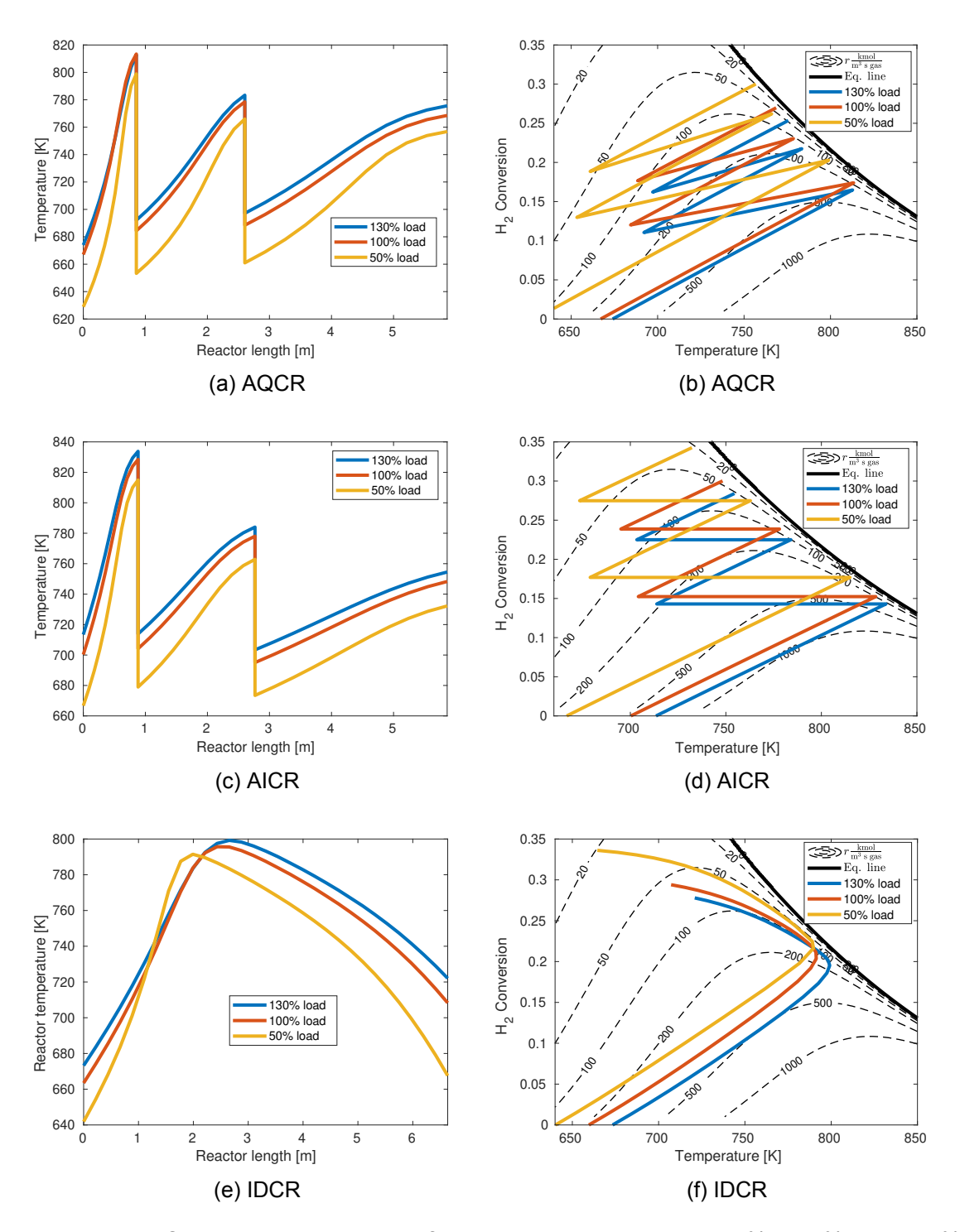


Figure 5.17: Optimal temperature profiles through the reactor at 50%, 100% and 130% reactor load for the a) AQCR, c) AICR and e) IDCR. Corresponding conversions versus temperature profiles are illustrated in b), d) and f).

Figure 5.17 demonstrates the effect of lowering the reactor temperatures. Figures 5.17a),

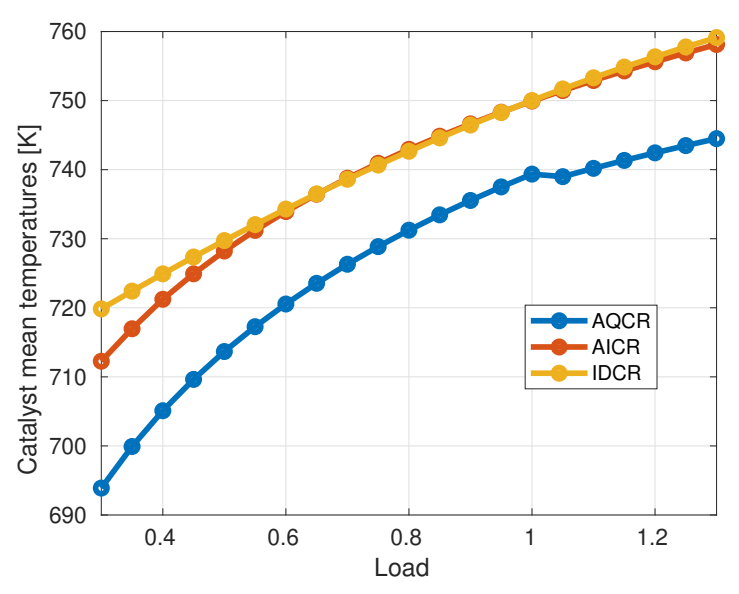


Figure 5.18: Optimal mean catalyst temperature for the optimal reactor configuration over the load range.

c), and e) show temperature profiles along the reactor for 50%, 100%, and 130% load, respectively. The reactors are generally operated at lower temperatures during reduced loads. A lower inlet temperature provides more room for reactant conversion before the reaction approaches equilibrium. Figures 5.17b), d), and f) plot H_2 conversion against reactor temperature, demonstrating the increased conversion achieved by lowering the inlet temperatures. At reduced reactor loads, the residence time within the reactor is extended due to the lower flow rate. This prolonged residence time enables the operation of the reactors at lower temperatures.

Figure 5.18 depicts the catalyst mean temperature for the reactors across the load range, confirming that the optimal reactor temperatures reduces with decreasing load. Note in Figure 5.18, that the AQCR curve exhibits a discontinuity at the nominal load. This is where the constraint $q_{R0} \ge 0.05$ of the optimisation in Eq. (5.33) becomes active.

5.7.1 Varying load operation with RTO

With sufficient hydrogen storage, a PtA plant mainly operates at stable conditions. Recall the layered scheduling, optimisation and control structure in Figure 5.5. It is assumed that a scheduling optimisation layer decides the reactor load on an hourly time scale. The results from section 5.7 are used to perform a real-time optimisation (RTO) of the reactor settings (feed splits and temperature) upon each load change. Figure 5.19 displays the reactor responses to hourly load switching and simultaneous real-time optimisation of the reactor settings. Notably, a control layer is not included in the simulations. Reducing the reactor load, the RTO method efficiently transitions the reactor systems to the optimal lower load operating points. However, increasing the reactor load induces oscillations in the AQCR, reaffirming the unstable nature of the AQCR system. In contrast, the AICR and IDCR systems with RTO show stable transitions in load across the entire operating window.

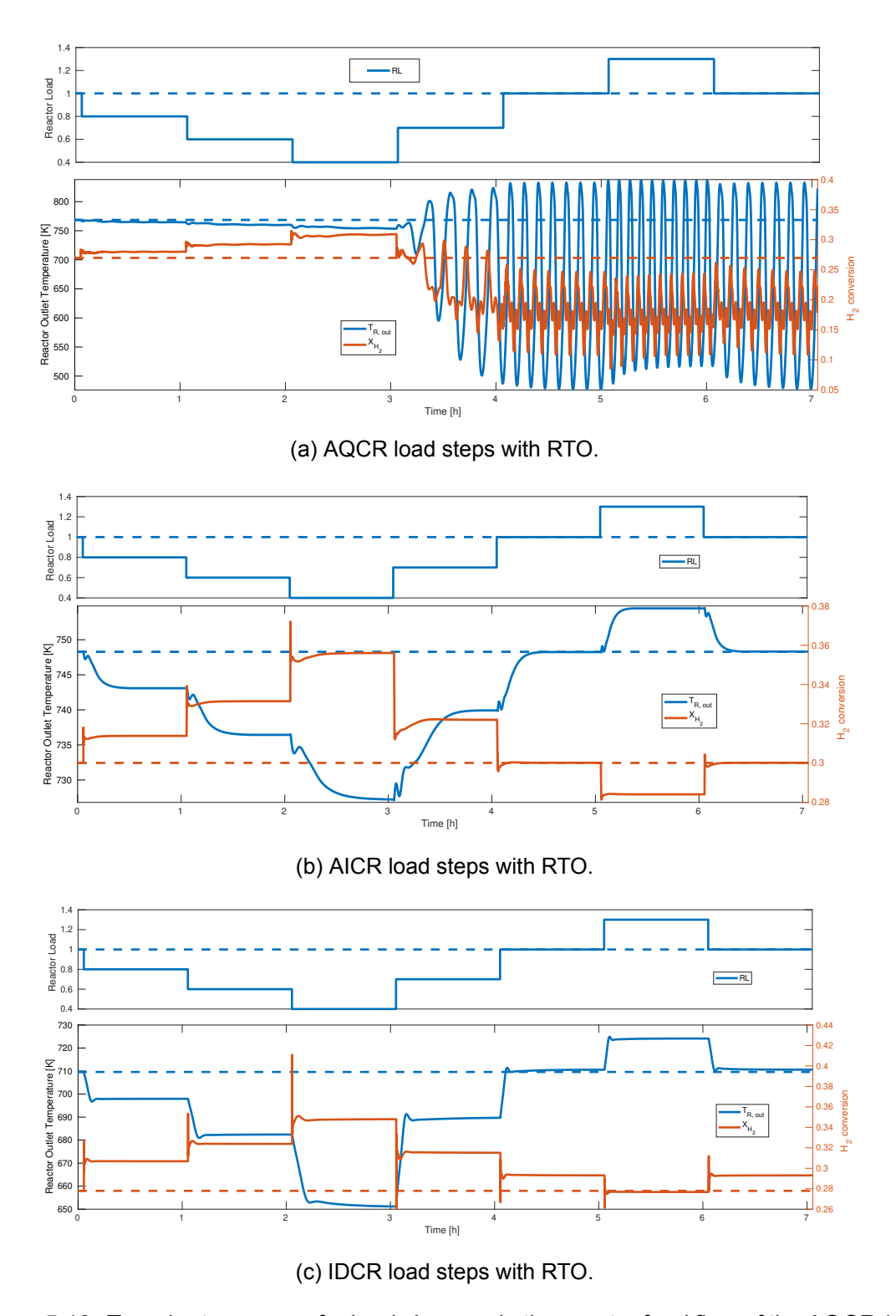


Figure 5.19: Transient response for load changes in the reactor feed flow of the AQCR (a), AICR (b) and IDCR (c). The reactor settings (Feed splits and temperature) are reoptimised at each load shift.

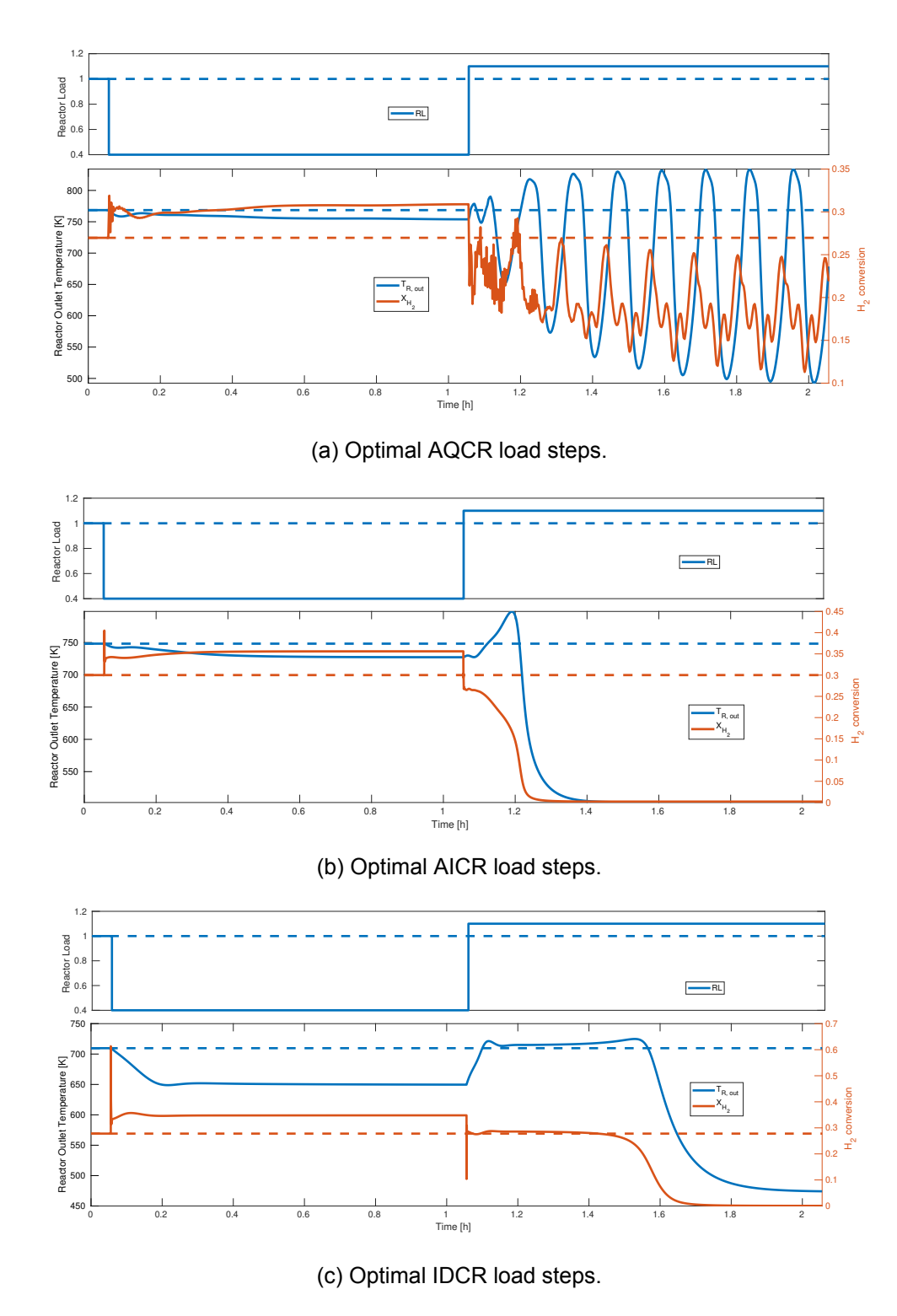


Figure 5.20: Transient response for large load changes in the reactor feed flow of the AQCR (a), AICR (b) and IDCR (c). The reactor settings (Feed splits and temperature) are reoptimised at each load shift.

Under renewable energy conditions, rapid transitions between high and low load levels are expected (Armijo and Philibert, 2020). Figure 5.20 shows the reactor transients during a scenario involving large load fluctuations. A real-time optimisation (RTO) scheme adjusts

the reactor settings based on the current load. However, aside from this adjustment, the reactor systems are operated without active control. Initially, the load decreases from nominal to 40% without issues. However, the subsequent ramp-up to 110% destabilises all three reactor types. As discussed in Section 5.7, the reactors operate at lower average temperatures during reduced load conditions. When the load is rapidly increased, this lower thermal state becomes insufficient to support the higher reactant flow. As a result, the reaction rate is too low to maintain thermal equilibrium within the reactor. This leads to oscillations in the AQCR and full reactor blowout in the AICR and IDCR.

5.7.2 Operating with a stability margin

Recall the reactor S-curves in section 5.5 Figure 5.11. The optimal operating points are located very close to the extinction point at a distance of 1-3 K from the instability and extinction points. This operating strategy is unsafe, as disturbances may push the reactor beyond the extinction point. Additionally, Section 5.6 illustrated that destabilisation of the AICR and IDCR is difficult to detect before extinction becomes imminent. Lastly, in the case of discrepancies in the model or degradation of the catalyst over its lifetime, the optimisation may locate the optimal operating point beyond the actual extinction point. Therefore, it is proposed to operate the reactors at a safe distance from the extinction points. The stability margin is defined wrt. feed temperature as the distance from the extinction or stability point. Figure 5.21a illustrates the stability margin for the AQCR. The S-curves in Figure 5.11 reveal that the conversion decreases faster with increasing reactor feed temperature for the AQCR and AICR than the IDCR. This implies that the IDCR conversion is less affected by operating with a stability margin compared with the AQCR and AICR. Figure 5.21b demonstrates this by depicting the reactor conversions versus stability margin for each reactor. Notice that the IDCR conversion curve intersects the AICR curve at a stability margin of approximately 50 K. However, the AICR curve exhibits a broader arch shape around the optimal operating point, resulting in a relatively minor decrease in conversion for stability margins below 20 K.

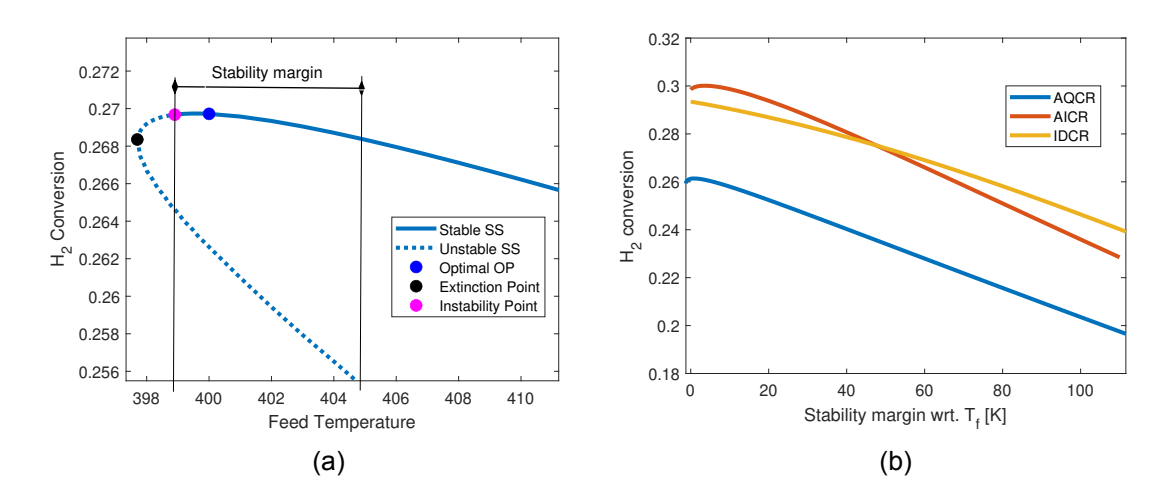


Figure 5.21: a) Definition of the stability margin wrt. reactor feed temperature for the AQCR. b) H_2 conversion versus stability margin for each reactor type at nominal load

Figure 5.21b shows that the penalty in conversion by operating with a stability margin below 20 K is relatively small, especially for the AICR and IDCR. Additionally, a higher feed temperature significantly stabilises the reactors, as evidenced in Figure 5.11b), d), and f). Increasing the reactor feed temperature significantly moves the eigenvalues away

from the right-hand-side plane (increased negative real part).

The ammonia catalyst inevitably deactivates over its lifetime (Forzatti and Lietti, 1999; Nielsen, 1953). Moghaddam and Krewer (2020) even notes the deactivation could be accelerated by variable load operation. Therefore, it is explored how a reduction in the catalyst activity affects the optimal reactor feed temperature and extinction point for the AICR. Numerically, this is implemented by multiplying the reaction rate, r, with a deactivation factor, f_{deact} .

$$r_{inhib.} = (1 - f_{deact.}) \cdot r, \tag{5.35}$$

where $r_{inhib.}$ is the inhibited reaction rate.

Figure 5.22 shows the extinction point and optimal feed temperature as functions of catalyst deactivation for the AICR operating at nominal load. As the reaction rate is inhibited, both the optimal feed temperature and the extinction temperature increase. A higher temperature compensates for the reduced activity but also shifts the operating point closer to equilibrium. As a result, the maximum achievable conversion, indicated by the yellow line, decreases with increasing deactivation. However, even with a 25% reduction in catalytic activity, the conversion drops by only about 1.8 percentage points, indicating that the process is primarily equilibrium limited rather than kinetically constrained.

A 10% reduction in catalyst activity raises the optimal and extinction feed temperatures by only 8 K. Based on this, it is proposed to operate the ammonia reactor with a 15 K stability margin in feed temperature. This margin accommodates up to a 15% loss in reaction rate without compromising reactor stability, and with only a minor reduction in conversion, as illustrated in Figure 5.21b.

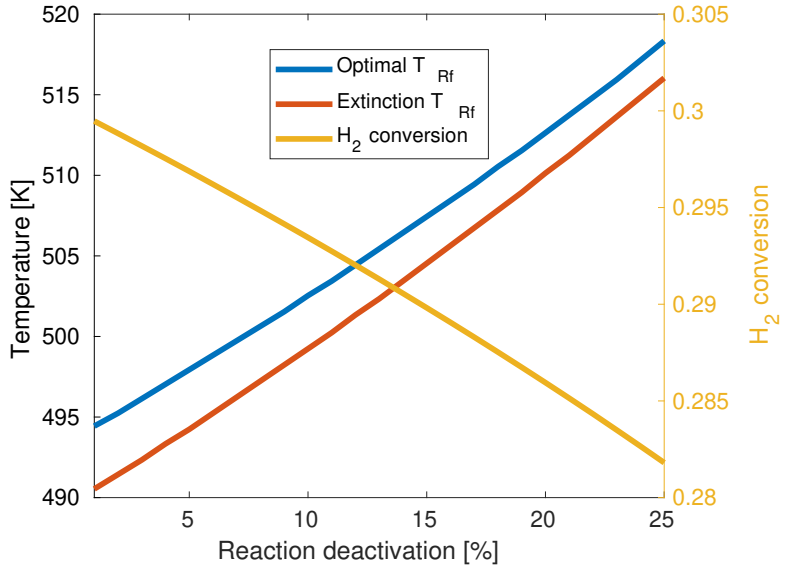


Figure 5.22: Optimal reactor feed temperature and extinction point as a function of reaction deactivation.

Figure 5.23 shows the hydrogen conversion across the operating window for the reactors when operating with a 15 K stability margin in the reactor feed temperature. The trends in Figure 5.23 closely resemble those in Figure 5.16, though the IDCR performance is now slightly closer to that of the AICR, particularly at lower loads. Notably, if a larger stability margin were applied, the IDCR conversion would eventually exceed that of the AICR, indicating its potential advantage with more conservative operating strategies.

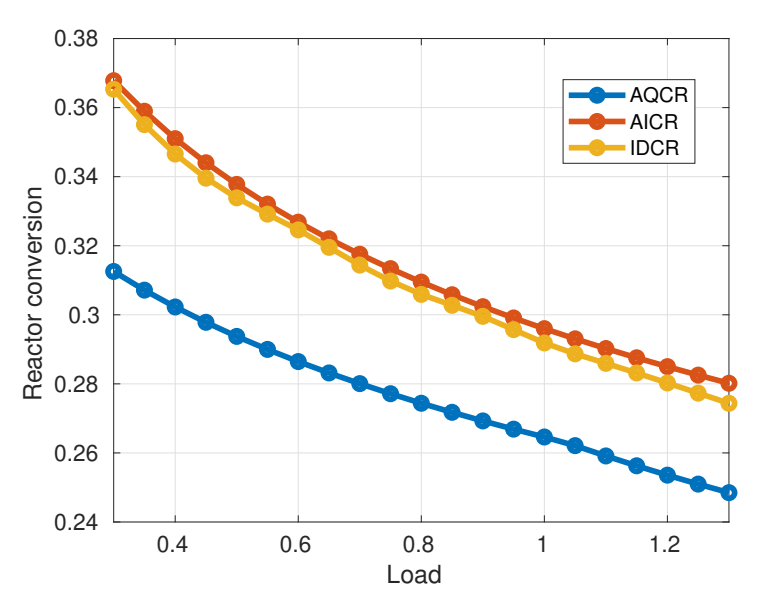


Figure 5.23: Conversion for the reactor types over the operating window when applying a stability margin of 15 K in the feed temperature.

Operating with a 15 K stability margin is tested by simulating a demanding load change scenario, identical to that causing reactor destabilisation and blowout in Figure 5.20. Figure 5.24 shows the reactor responses to the large step changes, but operating with the 15 K stability margin in the feed temperature. Contrary to the results in figure 5.20, the reactors transition from low load operation (40 %) to high load operation (110 %) without destabilisation or blowout of the reactors. This illustrates the significant stabilising effect of adding a 15 K stability margin to the optimal operating point. Furthermore note, that compared with optimal values the hydrogen conversion only decreases by approximately 0.5 %

5.8 Discussion

A comprehensive comparison of the three general types of ammonia reactors has been performed, based on both steady-state and dynamic simulations. Our objective was to identify the optimal reactor type for application in power-to-ammonia, considering the wide operating envelope and flexibility requirements in PtA. In conventional ammonia plants, the assessment of the most profitable reactor type is based on conversion at the nominal load relative to the reactor capital cost. However, in PtA, reactor conversion should be assessed over the entire operating window as depicted in Figure 5.16. This strengthens the case for the AICR and IDCR, as their conversion advantage over the AQCR becomes more pronounced at loads below nominal load.

The open-loop simulations presented in Figure 5.13 revealed severe oscillatory transients for the AQCR. This raises a concern, especially for dynamic operation with a fluctuating reactant supply from renewable energy, as this might induce oscillations. The oscillations are caused by an inverse response in the AQCR outlet temperature, which is amplified through the feed-effluent heat exchanger. The AICR also displayed an inverse temperature response but with damped oscillations. Only the IDCR showcased an attractive open-loop transient without inverse response.

Moreover, the open-loop simulations demonstrated that detecting a destabilisation of the

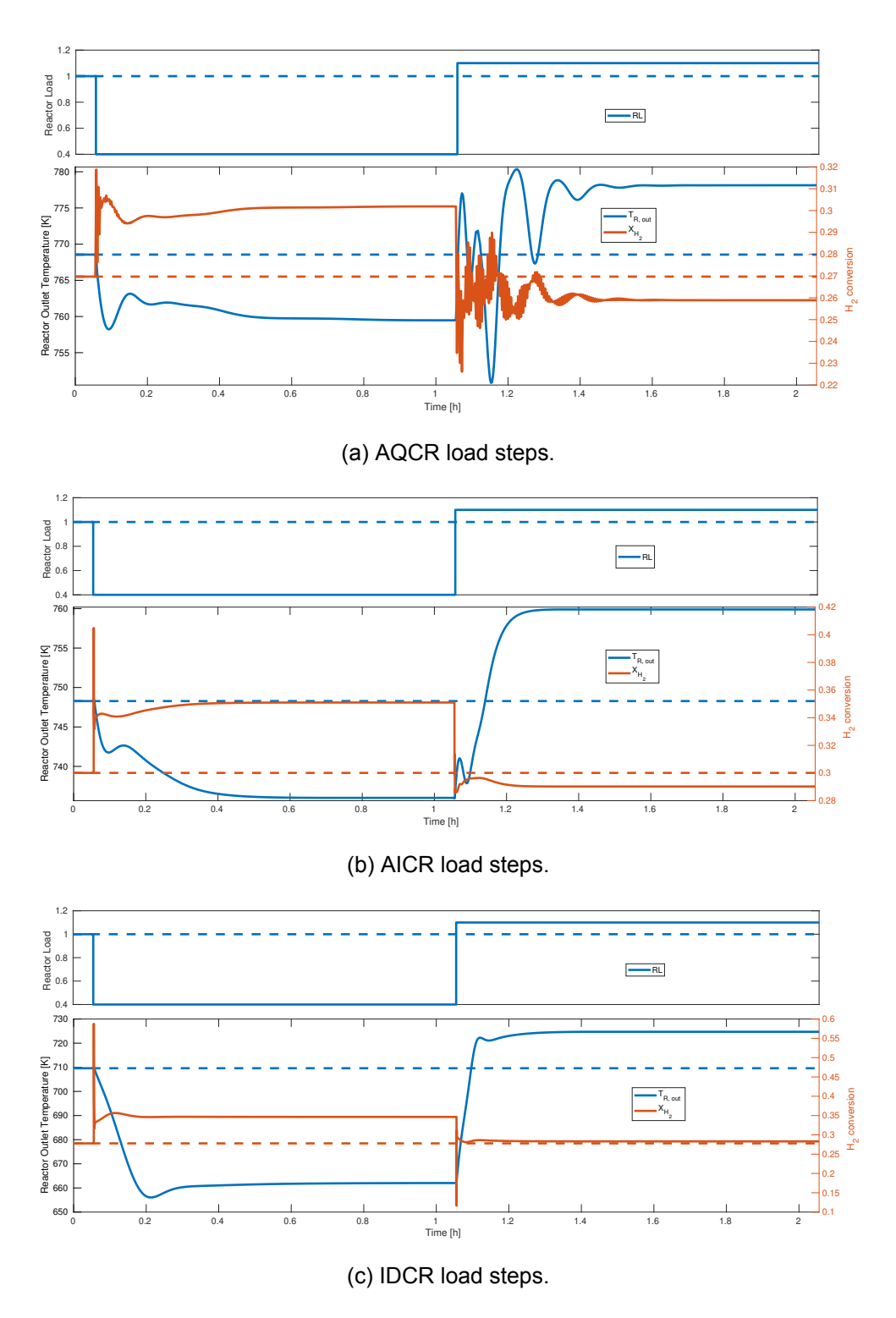


Figure 5.24: Transient response for load changes in the reactor feed flow of the AQCR (a), AICR (b) and IDCR (c). The reactor settings (Feed splits and temperature) are reoptimised at each load shift, and a stability margin of 15 K is applied for the feed temperature.

AICR and IDCR is challenging before the extinction is practically inevitable. Contrary, for the AQCR, a destabilisation of the reactor immediately induces oscillations, requiring significant action to re-stabilise. The bifurcation diagrams in Figure 5.11 revealed that the optimal operating points are situated on the verge of the instability/extinction point for all the reactors. Consequently, during optimal operation, the reactors are vulnerable to destabilisation from disturbances. This emphasises the rationale for operating the reactors at a stability margin from the optimal operating points. It is recommended to operate the reactors with a stability margin of 15 K in the feed temperature. Figure 5.11 highlights that the loss in reactor conversion is small when operating with a 15 K higher feed temperature than optimal. At lower loads, employing the 15 K stability margin decreases the AICR conversion slightly more than for the IDCR, bringing the conversion curves closer together over the operating window as shown in Figure 5.23.

Based on the conducted analysis, the AICR and IDCR outperform the AQCR in both conversion efficiency across the operating window and open-loop stability, making them more suitable for flexible operation in PtA systems. In conventional ammonia plants, the AICR is generally preferred due to its simpler structural design and proven reliability (Inamuddin et al., 2020). However, in the context of highly dynamic PtA operation, the IDCR exhibits features that make it particularly attractive. Specifically, the absence of inverse responses in the IDCR outlet temperature allows for straightforward design and tuning of a single-input, single-output (SISO) control structure.

In contrast, maintaining optimal performance of the AICR involves controlling multiple reactor bed inlet temperatures. This requires coordinated manipulation of the inter-bed split valves, leading to a multiple-input, multiple-output (MIMO) control problem. The strong dynamic coupling between these variables through the reactor and heat exchanger network introduces additional challenges for controller design. Advanced model-based control strategies such as model predictive control (MPC) could address these challenges, but implementation requires accurate dynamic models and computational resources. Note, this thesis has developed high-fidelity models of the AICR system, which could serve as a foundation for advanced control schemes in future research.

In this work, a PID-based MIMO control structure for the AICR is proposed in Chapter 10, which yields highly effective control.

5.9 Conclusion

In conclusion, this chapter examined the design and performance of three general ammonia reactor types—AQCR, AICR, and IDCR—for Power-to-Ammonia (PtA). The evaluation was based on a case study of a 250 MW renewable-powered PtA plant with a capacity factor of 0.4 and an operational window ranging from 30% to 130% of nominal reactor load. Rigorous steady-state and dynamic reactor models were applied to identify optimal operating conditions across this full load range.

At nominal load, optimisation results showed that the AICR and IDCR achieved higher reactant conversions (30.0% and 29.4%) compared to the AQCR (26.9%). However, for all reactor types, the optimal operating points were found to lie close to the extinction boundary. Open-loop transient simulations further highlighted this vulnerability as small disturbances were sufficient to extinguish the AICR and IDCR, while the AQCR displayed unstable oscillatory behaviour.

Optimising over the entire operational range (30% to 130% of nominal load), the AICR and the IDCR exhibit similar conversions. This showcases the adaptability of the AICR and the IDCR to varying loads as significantly higher conversion was achieved at low loads. The

AQCR displays less conversion increase at low load, highlighting its conversion deficiency compared to the AICR and the IDCR for P2A operation.

The reactor responses were simulated to changes in reactor load while employing a RTO strategy for updating the reactor settings upon load changes. This strategy showed promising load shifting capabilities even without a control structure. However, transitioning from a low load to a high load operating point caused reactor destabilisation.

Given the proximity of optimal operating points to the extinction limit, this work recommends the use of a 15 K feed temperature stability margin. This adjustment ensured stable reactor operation even under a 15% reduction in reaction rate, with only a marginal penalty in conversion. Moreover, the stability margin significantly improved dynamic robustness, enabling stable transitions even under demanding load increases from minimum to maximum capacity.

Chapter 6

Modelling and optimisation of a Haber-Bosch synthesis loop for Power-to-Ammonia

In this chapter, a detailed model of a Haber-Bosch synthesis loop is presented, including an AICR, compressors, steam turbines, and flash separators. A function for the total electrical power consumption of the synthesis loop is developed, accounting for power demands from compression and refrigeration, as well as power generation from steam turbines. This total power consumption serves as the cost function for optimising the synthesis loop, subject to constraints on compressor surge and choke limits, minimum steam temperature, and maximum loop pressure.

The optimisation problem considers six degrees of freedom: the inlet temperatures of the three reactor beds, the H_2/N_2 ratio in the reactor feed, the separator temperature, and the loop pressure. For a given hydrogen make-up feed flow, the total power utility is minimised, and the PtA load is varied by adjusting the hydrogen feed from 10% to 120% of the nominal value. Across this load range, various operational constraints become active, with the compressor surge limit becoming particularly critical at low loads, leading to a significant increase in power consumption.

Thus, this chapter answers the first part of research question 3.

This chapter contains material from the articles:

-Rosbo, J.W., Jørgensen, J.B., Jensen, A.D., Skogestad, S., Huusom, J.K., (2025). Optimisation and Robust Control of a Load-Flexible Haber-Bosch Ammonia Synthesis Loop. Submitted to Computer Computers & Chemical Engineering

-Rosbo, J.W., Jørgensen, J.B., Jensen, A.D., Skogestad, S., Huusom, J.K., (2025). Optimisation of a Haber-Bosch Synthesis Loop for PtA. Systems Control Transactions 4, 1126–1132. doi: https://doi.org/10.69997/sct.122254.

6.1 Introduction

The background in Section 2 highlighted that several studies have investigated steadystate optimisation of ammonia reactors, particularly focusing on conversion efficiency and reactor comparison at high-capacity operation. However, little attention has been given to the optimisation and dynamic behaviour of ammonia reactors across a wide range of load conditions relevant for PtA applications. This motivated the extensive comparison performed in Chapter 5.

Chapter 5 exclusively modelled the reactor section of the Haber-Bosch synthesis loop. While this allowed for a clear comparison between different reactor types, it did not capture the full system-level dynamics. In particular, the strong coupling between the reactor inlet and outlet via the large internal recycle stream can significantly affect reactor stability and performance in a full-loop configuration.

To address this, the present chapter introduces a detailed model of the complete Haber-Bosch synthesis loop, incorporating catalytic beds, compressors, steam turbines, heat exchangers, and flash separators. As illustrated in Figure 6.1, the model includes an adiabatic indirect cooled reactor (AICR) for ammonia synthesis. The AICR is widely used in modern ammonia plants (Appl, 2006) and, as demonstrated in Chapter 5, performs robustly under the flexibility requirements imposed by PtA operation.

The model provides a function for the total power consumption of the synthesis loop, enabling system-wide optimisation. Previous work by Schiedeck et al. (2025) and Fahr et al. (2025) showed that the power consumption of the Haber-Bosch process is highly non-linear with respect to load, primarily due to compressor surge limitations during low-load operation. Fahr et al. (2025) demonstrated that the part-load power consumption of the synthesis loop could be reduced by decreasing the loop pressure. However, these studies did not identify the optimal operating parameters. In this chapter, the ammonia synthesis loop is optimised in terms of power consumption across the entire PtA load range.

6.2 Mathematical model for the synthesis loop

Figure 6.1 illustrates the ammonia synthesis loop, commonly referred to as the Haber–Bosch process. The make-up gas, composed of hydrogen and nitrogen, is compressed to the high loop pressure (>100 bar) and preheated before entering the adiabatic indirect cooled ammonia reactor (AICR). The ammonia synthesis reaction is highly exothermic, enabling the generation of steam in the Rankine cycle. The ammonia product is separated from the reactants by condensation. A second flash tank is used to recover a portion of the hydrogen dissolved in the ammonia product by reducing the pressure. Since the reactor achieves a single-pass conversion of only 20–30% of the reactants, a substantial fraction of unreacted gases is recycled through the recompression stage.

6.2.1 Reactor bed model

The reactor bed model without pressure drop is described in Chapter 3. This chapter extends the bed model by incorporating pressure drop across the catalytic bed. Including pressure drop is essential when modelling the entire synthesis loop, as pressure differences govern the flow between units. Compared to the high operating pressure of the synthesis loop (approximately 200 bar), the pressure drop across the reactor is relatively small (typically 1–3 bar). Therefore, modelling the pressure drop was unnecessary when exclusively studying the reactor systems in Chapters 3-5.

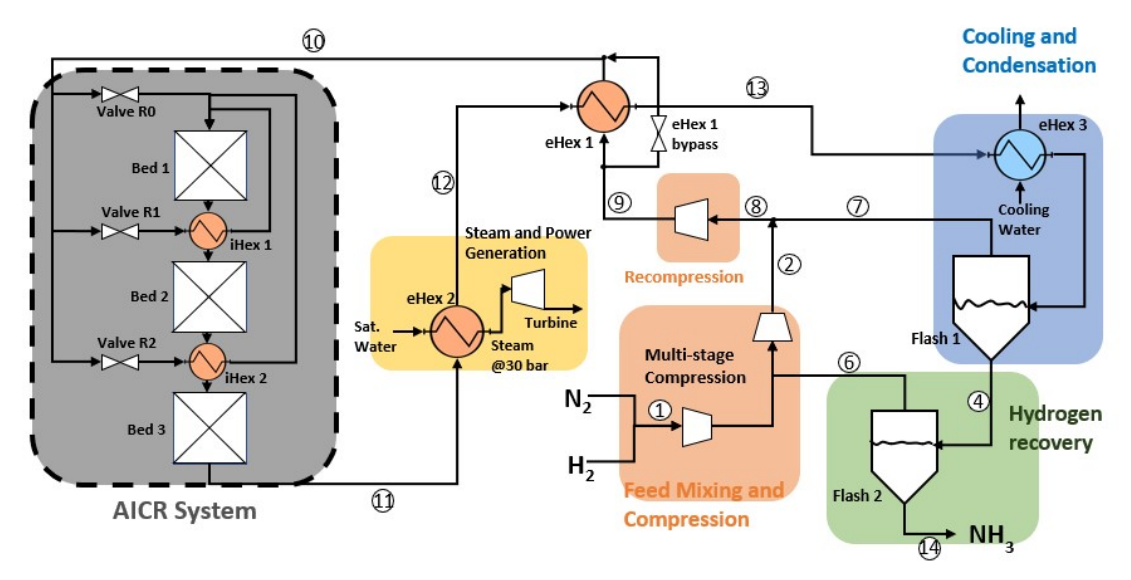


Figure 6.1: Illustration of the Haber-Bosch process. grey: adiabatic indirect cooled ammonia reactor system, orange: compressors, blue: primary flash tank, green: 2nd flash tank for hydrogen recovery, yellow: Rankine cycle

The pressure drop across the catalyst bed is described using Ergun's equation,

$$\frac{dP}{dl} = \frac{180\eta^g}{d_p^2} \frac{(1-\epsilon)^2}{\epsilon_B^3} v_s + \frac{1.75\rho^g}{d_p} \frac{1-\epsilon_B}{\epsilon_B^3} v_s^2, \tag{6.1}$$

in which P is the pressure, η^g is the gas viscosity, ρ^g is the gas density, d_p is the hydraulic diameter of the catalyst particles and v_s is the superficial gas velocity.

Adiabatic bed spatial discretisation

As described in Chapter 3, the partial differential algebraic equation (PDAE) system is transformed into a differential algebraic equation (DAE) system by discretisation using the finite volume method (FVM). The material and energy balances are already presented in Chapter 3. However, in this extended model, the flow velocity across the cell surfaces is governed by the discretised form of Ergun's equation,

$$\frac{P_{k+1} - P_k}{\Delta l} = \frac{180\eta^g}{d_p^2} \frac{(1 - \epsilon_B)^2}{\epsilon_B^3} v_{k+1/2} + \frac{1.75\rho^g}{d_p} \frac{1 - \epsilon_B}{\epsilon_B^3} v_{k+1/2}^2, \tag{6.2}$$

6.2.2 Mixing/volume model

Figure 6.1 shows that multiple mixing points are present in the Haber-Bosch synthesis loop. These are modelled using the mixer model illustrated in Figure 6.2, where each mixing point is modelled as a control volume with, n, inlet streams. The mass and energy balances over the mixer volume are given by,

$$\frac{dc}{dt} = \frac{\sum_{n} F_{in, n} - F_{out}}{V_{vol}},\tag{6.3a}$$

$$,\frac{d\hat{U}}{dt} = \frac{\sum_{n} \dot{H}_{in,\,n} - \dot{H}_{out}}{V_{vol}}, \tag{6.3b}$$

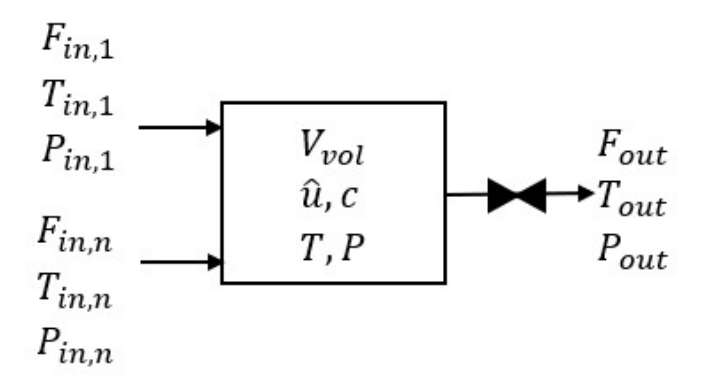


Figure 6.2: Illustration of volume element model.

where the summation represents the addition of all the inlet streams. The enthalpy flows are given by,

$$\dot{H}_{in, n} = \mathcal{H}(T_{in, n}, P_{in, n}, F_{in, n}), \quad \begin{bmatrix} \mathsf{J} \\ \mathsf{s} \end{bmatrix}, \tag{6.4a}$$

$$\dot{H}_{out} = \mathcal{H}(T, P, F_{out}), \tag{6.4b}$$

The algebraic equations for the volume element are,

$$0 = \hat{u} - \mathcal{U}(T, P, c), \tag{6.5a}$$

$$0 = 1 - \mathcal{V}(T, P, c), \tag{6.5b}$$

The outlet volume flow, Q_{out} , from the volume element is driven by the pressure difference across the outlet valve shown in Figure 6.2. Assuming turbulent flow across the valve, the valve equation is (Woolf, 2009),

$$0 = \alpha_v (P - P_{out}) - R_v Q_{out}^2, (6.6a)$$

$$F_{out} = cQ_{out}, (6.6b)$$

where P_{out} represents the pressure of the upstream unit, Q_{out} is the volumetric outlet flow, and R_v is a coefficient reflecting the flow resistance across the valve. α_v denotes the opening of the outlet valve in the range [0,1], where zero represents a fully closed valve and one a fully open valve. Note that the outlet valve from the mixer volume is often not manipulable and that the valve equation in practice often represents the pressure drop of the outlet pipe.

6.2.3 Stream split model

Stream splits occur in the ammonia synthesis loop around the external heat exchanger (eHex 2) and within the reactor system, where the reactor feed is distributed between the internal heat exchangers. The splitter model is characterised by the split fractions q_j , defined as,

$$F_{out, j} = q_j F_{in}, (6.7)$$

$$\sum_{j} q_j = 1 \tag{6.8}$$

where F_{in} is the flow entering the split module and $F_{out, j}$ is the flow of split stream j. For the reactor system, we denote the split factors as $q_{R, j}$ and the external heat exchanger bypass as q_{eHex} .

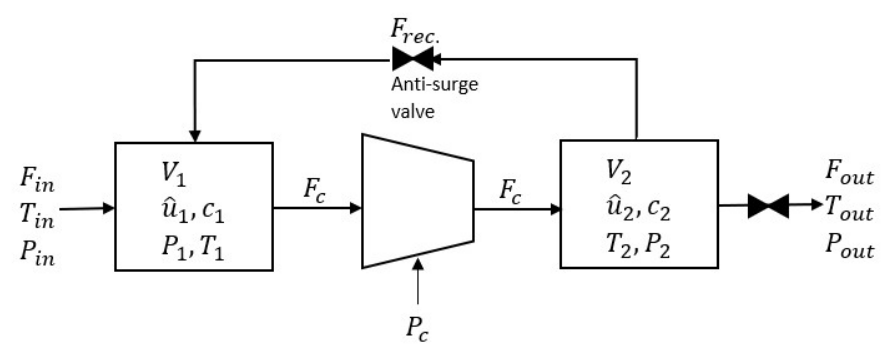


Figure 6.3: Schematic illustration of the dynamic compressor model

6.2.4 Compressor model

Centrifugal compressors are used in the ammonia synthesis loop to compress the makeup feed gas and recompress the recycle stream (Morgan et al., 2014; Inamuddin et al., 2020). Figure 6.3 illustrates the components in the dynamic compressor model. The dynamic part of the compressor module is captured via the two volume elements, one before and one after the compressor unit. The material and energy balances for the volume elements are.

$$\frac{dc_1}{dt} = \frac{F_{in} - F_c + F_{rec.}}{V_1},\tag{6.9a}$$

$$\frac{dc_2}{dt} = \frac{F_c - F_{out} - F_{rec.}}{V_2},\tag{6.9b}$$

$$, \frac{d\hat{U}_{1}}{dt} = \frac{\dot{H}_{in} - \dot{H}_{1} + \dot{H}_{rec.}}{V_{1}},$$
 (6.9c)

$$\frac{d\hat{U}_2}{dt} = \frac{\dot{H}_{in} - \dot{H}_1 + \dot{H}_{rec.}}{V_2},\tag{6.9d}$$

where the enthalpy flows are given by,

$$\dot{H}_{in} = \mathcal{H}(T_{in}, P_{in}, F_{in}),$$
 (6.10a)

$$\dot{H}_1 = \mathcal{H}(T_1, P_1, F_c),$$
 (6.10b)

$$\dot{H}_c = \mathcal{H}(T_c, P_2, F_c), \tag{6.10c}$$

$$\dot{H}_2 = \mathcal{H}(T_2, P_2, F_{out}),$$
 (6.10d)

In compliance with the volume model (Sec. 6.2.2) the algebraic equations for each volume element are,

$$0 = \hat{U}_1 - \mathcal{U}(T_1, P_1, c_1), \tag{6.11a}$$

$$0 = \hat{U}_2 - \mathcal{U}(T_2, P_2, c_2), \tag{6.11b}$$

$$0 = 1 - \mathcal{V}(T_1, P_1, c_1), \tag{6.11c}$$

$$0 = 1 - \mathcal{V}(T_2, P_2, c_2), \tag{6.11d}$$

The outlet flow from volume 2 is driven by the pressure driving force across the outlet valve,

$$0 = \alpha_{v,out}(P_2 - P_{out}) - R_v Q_{out}^2, \tag{6.12a}$$

$$F_{out} = c_2 Q_{out}, \tag{6.12b}$$

Similarly, the recycling flow across the anti-surge valve is manipulated via the opening of the anti-surge valve,

$$0 = \alpha_{v, rec}(P_2 - P_1) - R_v Q_{rec}^2, \tag{6.13a}$$

$$F_{rec.} = c_2 Q_{rec.}, \tag{6.13b}$$

We assume the centrifugal compressor unit can be modelled by steady-state equations as the dynamics of the compressor is fast compared to the transients of other units in the synthesis loop. The compressor model is based on isentropic compression from pressure P_1 to pressure P_2 ,

$$0 = \mathcal{S}(T_s, P_2, F_C) - \mathcal{S}(T_1, P_1, F_C), \tag{6.14a}$$

$$0 = \mathcal{H}(T_s, P_2, F_C) - \mathcal{H}(T_1, P_1, F_C) - \eta_S P_C, \tag{6.14b}$$

where $T_{\mathcal{S}}$ is the isentropic compression temperature, P_C is the compressor power and η_S is the isentropic efficiency further described in Eq. 6.15. The real compressor outlet temperature, T_C , satisfies,

$$0 = \mathcal{H}(T_C, P_2, F_C) - \mathcal{H}(T_1, P_1, F_C) - W_C, \tag{6.14c}$$

We assess the compressor efficiency from a qualitative fit of a compressor map generated with Concept NREC® design software for the relevant $[N_2,H_2,Ar,NH_3]$ gas mixture. The efficiency is assumed to follow a second order polynomial expression as a function of the corrected flow, $F_{C,cor}$,

$$\eta_S(F_{C, cor.}) = -0.44 \left(\frac{F_{C, cor.}}{F_{Cn}}\right)^2 + 0.8 \frac{F_{C, cor.}}{F_{Cn}} + 0.35,$$
(6.15)

where F_{Cn} is the nominal compressor flow at the design point. The corrected flow is given by, $F_{cor} = \frac{P_1}{P_{1n}} F_C$, with P_{1n} being the inlet pressure at the design point. Figure 6.4 displays a simplified compressor map, illustrating the isentropic efficiency as a function of the corrected flow. As indicated, we assume the compressor operating window is bounded by compressor surge and choke at respectively 60% and 140% of the nominal compressor flow. However, for safety, the practical operational window is restricted to 65-130%, consistent with the assumptions in Schiedeck et al. (2025). Consequently, anti-surge recycle control is activated when the corrected compressor flow falls below 65%.

The hydrogen and nitrogen feed gases are assumed to be supplied at 5 bar, as reported in Sánchez and Martín (2018b) and Verleysen et al. (2021). Thus, the make-up gas must be compressed by several orders of magnitude to reach the synthesis loop pressure (100–250 bar). To achieve this, multistage compression trains are employed, with a maximum compression ratio of three per stage. Inter-stage cooling is provided via cooling water, assumed at a temperature of 15°C.

6.2.5 Separator model

The separation of the ammonia product can be achieved at high purity by a series of two flash separators (see Figure 6.1), due to the large difference in boiling points between ammonia and the synthesis gas. The material and energy balance over the flash tank is,

$$\frac{dn}{dt} = F_{in}^g + F_{in}^l - F_{out}^g - F_{out}^l, {(6.16a)}$$

$$\frac{dU}{dt} = H_{in}^g + H_{in}^l - H_{out}^g - H_{out}^l$$
 (6.16b)

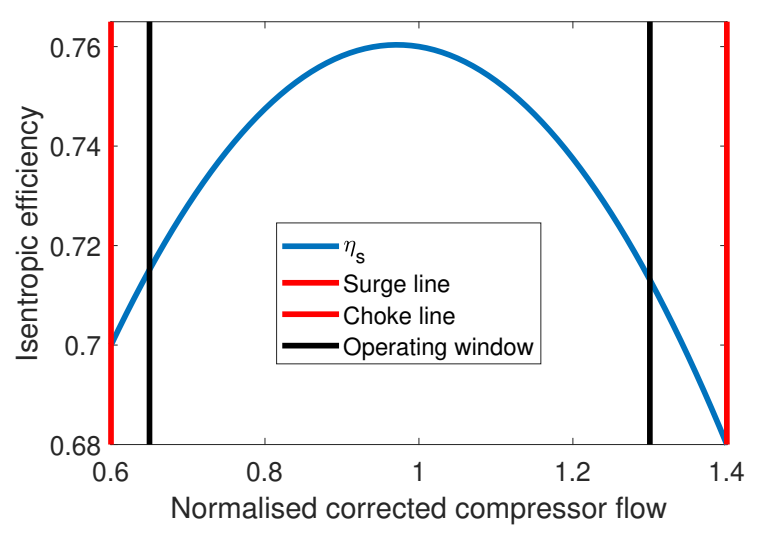


Figure 6.4: Simplified compressor map for the compressors in the ammonia synthesis loop. The compressor operating window is limited between 65% and 130% of the nominal flow.

where n is a vector for the total molar hold-up in the tank, and U is the combined total internal energy of liquid and vapour hold-up inside the flash tank. F_{in}^l and F_{in}^g are, respectively, the liquid and gas flow entering the flash unit. Correspondingly, F_{out}^l and F_{out}^g denote the outlet liquid and gas flows. The outlet flow of the gas phase is governed by the pressure driving force across the outlet valve,

$$0 = P - P_{out}^g - R_v Q_{out}^{g-2}, (6.17a)$$

$$0 = P - P_{out}^g - R_v Q_{out}^{g^2},$$

$$F_{out}^g = \frac{n^g}{V^g} Q_{out}^g,$$
(6.17a)

$$H_{out}^g = \mathcal{H}^g(T, P, F_{out}^g) \tag{6.17c}$$

where n^g is the gas-phase molar hold-up, V^g is the gas volume inside the flash tank, Pis the tank pressure, and H^g_{out} is the enthalpy flow of the outlet gas. The volumetric liquid outlet flow, Q_{out}^l , controls the liquid level in the flash tank via the liquid outlet pump,

$$F_{out}^g = \frac{n^l}{V^l} Q_{out}^l, \tag{6.18a}$$

$$H_{out}^{l} = \mathcal{H}^{l}(T, P, F_{out}^{l})$$
(6.18b)

in which, n^l is the liquid-phase molar hold-up, V^l is the liquid volume, and H^l_{out} is the enthalpy flow of the outlet liquid. We assume Q^l_{out} can be manipulated directly.

The vapour-liquid equilibrium of the flash tank is modelled via the Gibbs energy of the system. The total Gibbs energy of the separator, G, is a sum of gas and liquid Gibbs free energies,

$$G = G^{g} + G^{l} = \mathcal{G}^{g}(T, P, n^{g}) + \mathcal{G}^{l}(T, P, n^{l})$$
(6.19)

in which the Gibbs energy of the phases, G^g and G^l , are functions of the separator temperature, T, pressure, P, and respective phase hold-ups, n^g and n^l . At the vapour-liquid equilibrium, the total Gibbs energy is minimised subject to the following constraints, (Ritschel

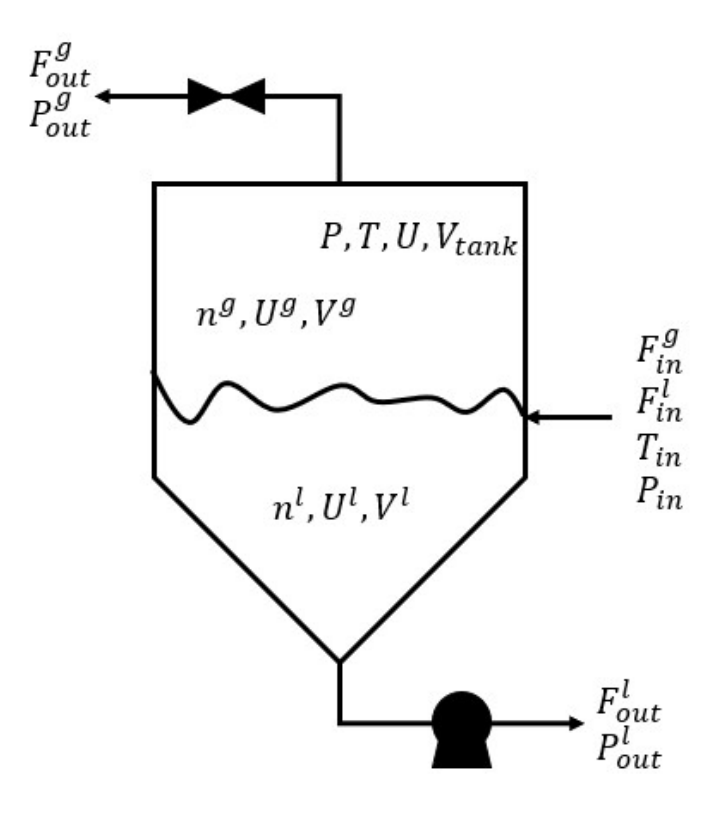


Figure 6.5: Schematic illustration of the flash tank.

et al., 2018),

$$\min_{n^g, \ n^l, \ T, \ P} G = G^g + G^l \tag{6.20a}$$

s.t.
$$n = n^l + n^g$$
 (6.20b)

$$U = \mathcal{U}^l(T, P, n^l) + \mathcal{U}^g(T, P, n^g)$$
(6.20c)

$$0 = V_{tank} - \mathcal{V}^g(T, P, n^g) - \mathcal{V}^l(T, P, n^l)$$
 (6.20d)

Eq. (6.20b) and (6.20c) represent, respectively, the mass and energy constraint coupled to Eq. the differential equations (6.16a) and (6.16b). Eq. (6.20d) imposes the volume constraint of the flash tank. The molar derivatives of the Gibbs energies define the chemical potentials,

$$\frac{d\mathcal{G}^g}{dn_i^g} = \mu_i^g,\tag{6.21a}$$

$$\frac{dG^l}{dn_i^l} = \mu_i^l, \tag{6.21b}$$

The minimisation of Equation (6.20) is achieved when the component chemical potentials of the vapour and liquid phases are identical,

$$0 = \mu_i^g(T, P, n^g) - \mu_i^l(T, P, n^l), \tag{6.22}$$

Eq. 6.22 should be satisfied for all components which corresponds to the KKT first-order optimality conditions for the constrained minimisation in Eq. (6.20). The chemical potentials of the gas and liquid mixtures are calculated with the thermodynamic tool Thermolib

(Ritschel et al., 2016, 2017). Appendix D provides a validation of the vapor-liquid equilibrium (VLE) simulations. The simulated VLE of the [H₂, N₂, NH₃, Ar]-mixture matches very well with experimental data in the relevant temperature and pressure range.

In summary, the dynamic separator model consists of five states: the four total molar hold-ups, n, and the total internal energy, U. These are described by the material and energy balance (6.16). The twelve algebraic variables, n^g , n^l , V^g , V^l , Q_{out} , $P_{sep.}$ governed by the algebraic equations (6.20)-(6.22).

6.2.6 Heat-exchangers

The heat-exchanger model is presented in Chapter 4 Section 4.2.2.

6.2.7 Cooling and refrigeration

Cooling is performed before the flash tank and between the stages for the make-up gas compression. We assume that cooling water is available at 15 °C, and that the heat exchangers are designed for a minimum temperature approach of 10 °C. consequently, cooling below 25 °C requires the use of a refrigeration cycle. We assume the coefficient of performance (COP) for the refrigeration is three, which is typical for refrigeration from ambient temperatures (20 °C) down to approximately 0°C (Balmer, 2011b). The required refrigeration power for cooling before the flash tank is then,

$$P_{refrigiation} = \frac{\mathcal{H}(25.0^{\circ}\text{C}, P_{S13}, F_{S3}) - \mathcal{H}(T_{S3}, P_{S3}, F_{S3})}{COP}$$
(6.23)

The enthalpy flow of Stream 3 is for two-phase flow. Note that the inlet conditions to the flash unit (Sec. 6.2.5) are specified as a two-phase flow accordingly. The VLE of the Stream 3 at the temperature T_{S3} is solved via Equations (6.20)-(6.22).

6.2.8 Rankine cycle

The hot reactor outlet temperature (Figure 6.1: Stream 11) is in the range 770-820 K. This temperature enables the generation of superheated steam at 30 bar ($T_{sat}^{@30bar} = 507.0$ K), driving a turbine in a Rankine cycle. We assume a heat-to-electric power efficiency, $\eta_{rankine}$, of 40%, reflective of a high-efficiency cycle with superheated steam (Balmer, 2011a). The electrical power generated in the rankine cycle is,

$$P_{rankine} = \eta_{rankine}(\mathcal{H}(T_{S11}, P_{S11}, F_{S11}) - \mathcal{H}(T_{S12}, P_{S12}, F_{S12}))$$
(6.24)

where H is the enthalpy flow of the stream at the temperature, T, pressure, P, and flow, F. Subscripts S11 and S12 refer to the streams entering and exiting the steam generator eHex 2 as illustrated in Figure 6.1. Downstream, Stream 12 is used to preheat the reactor feed (Stream 10) via the external heat exchanger eHex 1. The temperature of Stream 12 is restricted to provide a bypass of eHex 1 of $q_{ex}=0.2$. This provides flexibility for control of the reactor temperatures without saturation of the bypass valve, as will be further demonstrated in Section 10.3.

6.2.9 Numerical parameters

Each adiabatic bed has been divided into 10 cells (K=10). This is sufficient to capture the non-linear behaviour of the beds, and introduces a numerical diffusive error term of the same magnitude as the dispersive backmixing in the beds (Morud and Skogestad, 1998). The system then comprises 180 states and differential equations, and 160 algebraic variables and equations. For dynamic simulations, the DAEs system of the HB synthesis loop is integrated in time via the implicit Euler method,

$$\mathbf{x}^{n+1} = \mathbf{x}^n + f(\mathbf{x}^{n+1}, \ \mathbf{y}^{n+1})\Delta t,$$
 (6.25a)

$$0 = g(\mathbf{x}^{n+1}, \mathbf{y}^{n+1}), \tag{6.25b}$$

where **x** is a vector containing all the system states and **y** contains the combined algebraic variables. f represents the rate function, while g contains the algebraic equations. The selected time step size is, $\Delta t = 1$ $S \approx \min(Q_{reac.}/\Delta V_{reac})$, approximately equal to the smallest residence time of the discretised bed volume elements. Chapter 3 showed this integration time provided a good trade-off between numerical accuracy and computational efficiency.

6.3 The Case Study: 100 MW PtA synthesis loop

The dimensions of the synthesis loop are based on the case presented in Chapter 4 and 5 for a 100 MW average power PtA plant supplied by a 250 MW renewable energy source (wind and solar). Figure 6.1 illustrates that the PtA synthesis loop is designed without a purge stream, which is usually included in the conventional Haber-Bosch process (Araújo and Skogestad, 2008). Elimination of the purge stream is feasible because the nitrogen feed, produced via air separation, is more than 99.9% pure in nitrogen. Thus, the argon content, $f_{\rm Ar}\approx 0.1\%$, is significantly lower than around 1.2% typical in conventional ammonia plants where nitrogen is provided from combusted air. As a result, the trace amounts of Argon in the nitrogen feed can be removed by dissolution in the ammonia product (Klein et al., 2021; Smith et al., 2020).

6.3.1 System dimensions

Rosbo et al. (2024b) found the optimal sizing of catalyst bed volumes and heat exchanger surface areas for the AICR in the 100 MW PtA case. Table 6.1 displays the dimensions for the process units in the synthesis loop case study. For the heat exchangers in the Haber–Bosch synthesis loop, a pressure drop of 1 bar at nominal flow is assumed, in accordance with Araújo and Skogestad (2008). The flash tanks are assumed to exhibit significantly lower pressure losses, with a nominal drop of 0.1 bar. For all units, deviations from nominal flow are modelled by assuming that the pressure drop is proportional to the square of the flow velocity, as outlined in Section 6.2.

The make-up feed is assumed to be supplied at a temperature of 25 °C and 5 bar pressure (Sánchez and Martín, 2018b; Verleysen et al., 2021). Hydrogen and Nitrogen are supplied close to the stoichiometric value, but may deviate slightly due to differences in solubility in the ammonia product stream.

6.3.2 Synthesis loop load

As described in the introduction, enhancing the flexibility of the ammonia synthesis loop can significantly reduce the levelised cost of green ammonia. Electrolysis accounts for approximately 90% of the total power consumption in PtA systems (Cheema and Krewer, 2020). Therefore, the synthesis loop load is defined based on the make-up hydrogen feed, referred to here as the hydrogen load (HL),

$$HL = \frac{F_{f, H_2}}{F_{fn, H_2}},$$
 (6.26)

where F_{Ff,H_2} is the hydrogen make-up feed flow and F_{Ffn,H_2} the nominal design flow. In this study, we optimise and demonstrate load-flexible operation of the synthesis loop across a hydrogen load range of 10% to 120%.

Table 6.1: HB-synthesis loop design specifications

Table 6.1. The synthesis loop design	gir opcomoa	110113
Reactor:		
Beds:		
Bed diameter	[m]	1.2
Bed 1 volume	$[m^3]$	0.998
Bed 2 volume	$[m^3]$	1.98
Bed 3 volume	$[m^3]$	3.69
Internal heat exchangers:		
ihex 1 area	$[m^2]$	89
ihex 2 area	$[m^2]$	67.4
Catalyst:		
Type: Metallic iron		
Void fraction		0.33
Catalyst density	[kg/m³]	3284
Catalyst heat capacity, c_p	[J/(kg·K)]	1100
Particle hydraulic diameter, d_p	[mm]	8
External heat exchangers:		
eHex 1 area	$[m^2]$	300
eHex 2 area	$[m^2]$	212
eHex 3 area	$[m^2]$	112
Cooling water		
T_{cool}	[°C]	15
Rankine cycle		
T_{steam}	[K]	507
P_{steam}	[bar]	30
Flash tanks:		
Flash 1 volume	$[m^3]$	10
Flash 2 volume	$[m^3]$	5
Compressors:		
Two parallel compressor trains.		
Four-stage feed compressor trains.		
Nominal power feed compressors	[MW]	2.78
Nominal power loop compressors	[MW]	0.12
Make-up feed:		
T_{feed}	[°C]	25
P_{feed}	[bar]	5
Nominal composition:		
Hydrogen.		74.92%
-		24.98%
Nitrogen.		Z T .30 /0
Nitrogen. Ammonia		0%

6.4 Optimisation problem

In PtA the only utility costs are electrical power and cooling water. Assuming that cooling water is a negligible operational cost, the electrical utility alone represents the cost function. In this work, we focus on optimising the Haber-Bosch synthesis loop, since this represents a general optimum independent of the electrolysis method used for hydrogen production or the method for air separation. The electrical power consumption of the Haber-Bosch process consists of power for feed compression, $P_{feedcomp}$, loop recycle compressor, $P_{loopcomp}$, and refrigeration, $P_{refrigiation}$, while the steam turbine generates electricity, $P_{rankine}$. The net external power requirement of the HB-loop, P_{HB} , is then,

$$J = P_{HB} = P_{feedcomp} + P_{loopcomp} + P_{refrigiation} - P_{rankine}.$$
 (6.27)

Section 6.3 explains the design of the synthesis loop without a purge stream. Consequently, all hydrogen and nitrogen leave the synthesis loop by conversion to ammonia. Therefore, given a hydrogen make-up feed flow, minimising the cost function, $J=P_{HB}$, represents the optimal solution. We optimise across six degrees of freedom (DOF): three reactor bed inlet temperatures, $T_{bed,\ in}$, loop pressure, P_{loop} , reactor feed H₂/N₂-ratio, $R_{\rm H_2/N_2}$, and separator temperature, $T_{sep.}$. The DOFs are defined in a vector, ν ,

$$\nu = [T_{bed1, in}, T_{bed2, in}, T_{bed3, in}, P_{loop}, R_{H_2/N_2}, T_{sep.}].$$
(6.28)

The loop pressure P_{loop} is defined as the pressure after the loop recycle compressor (Stream 9 in Figure 6.1). The optimal solution is found by minimising the objective function across the six DOFs,

$$\min_{U} J = P_{HB}, \tag{6.29a}$$

s.t.
$$f(x,y) = 0$$
, $g(x,y) = 0$, (6.29b)

$$0.65 \le F_{cor.}/F_{n.comp.} \le 1.3,$$
 (6.29c)

$$0 \le q_R \le 1,$$
 (6.29d)

$$0 \le q_{ex} \le 1,$$
 (6.29e)

$$P_{loop} \le 250 \text{ bar.}$$
 (6.29f)

Equation (6.29b) represents the steady-state solution of the ammonia synthesis loop, where f and g denote the rate function and the algebraic equations for the units described in Section 6.2. Eq. (6.29c) represents the compressor operating window defined in Section 6.2.4. Eq. (6.29d)-(6.29e) is the constraints on the reactor feed split fractions, q_R , and the bypass of eHex 1 (see Figure 6.1). The maximum loop pressure is 250 bar. We solve the optimisation problem via Matlab's constrained minimisation algorithm, fmincon. The specific HB-power requirement for producing ammonia is defined as,

$$E_{\mathsf{NH}_3} = \frac{P_{HB}}{\dot{m}_{\mathsf{NH}_2}},\tag{6.30}$$

Where \dot{m}_{NH_3} is the product mass flow of ammonia after the 2nd flash tank (Figure 6.1: Stream 14).

6.5 Optimisation at nominal load

Table 6.2 summarises the optimal operating parameters and the corresponding power distribution when solving the optimisation in Equation (6.29a) at nominal load. The feed compression consumes most of the electrical utility with 5.50 MW, while the recycle compression only constitutes 0.18 MW. The optimal separator temperature of 25 °C is at the

lower bound for water cooling, avoiding refrigeration power. A relatively large fraction of the electrical utility for compression is regained through the Rankine cycle delivering 3.6 MW, corresponding to 60% of the total electrical utility for compression. This sums to a total of 2.11 MW of external electrical utility required to power the HB-loop.

Table 6.2: Optimal operating parameters and power distribution at nominal load.

Optimal parameters		Power distribution	
Bed inlet temperatures [K]	[717, 700, 691]	Feed compression	5.65 MW
loop pressure	213.3 bar	Recycle compression	0.22 MW
Separator temperature	25 °C	Steam generator	3.50 MW
Reactor	2.68	Refrigeration power	0 MW
		HB-loop power	2.37 MW

6.6 Optimisation across the operating window

The optimisation problem of Eq. (6.29a) is performed across the synthesis loop operating window from 10% to 120% of the nominal hydrogen flow. Figure 6.6a illustrates the optimal distribution of power throughout this operating window. At the same time, Figure 6.6b presents the normalised corrected make-up feed and recycle flows across the operating envelope. The compressor power decreases with reduced hydrogen feed, as both the make-up and recycle flows decrease with the dashed lines indicating the surge limit of the compressors. At 65% hydrogen load, the reduction in compressor power becomes markedly constrained. This effect corresponds to the activation of anti-surge recycling, which is initiated below 65% of total normalised compressor flow load. Thus, for hydrogen loads below the surge line feed compressor power remains almost constant.

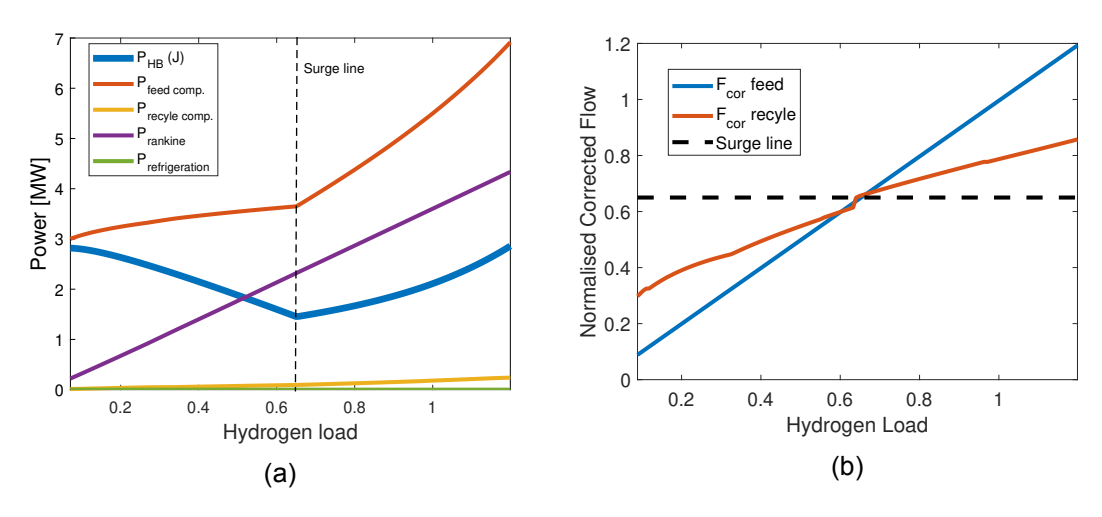


Figure 6.6: a) Optimal distribution of power in the HB-loop across the operating envelope. b) Normalised corrected flow for the feed and recycle compressors across the operating envelope.

From Figure 6.6a, it can be observed that the total HB-loop power demand, somewhat counterintuitively, increases as the load decreases when compressor anti-surge recycling is activated. This behaviour arises because the power output from the steam turbine decreases approximately linearly with the hydrogen feed rate, while the compressor power

exhibits only a modest reduction due to the anti-surge recycling. This significantly affects the specific ammonia production cost illustrated in Figure 6.7a. For the optimised PtA loop, the specific cost of ammonia production at reduced loads is up to ten times higher than at nominal load.

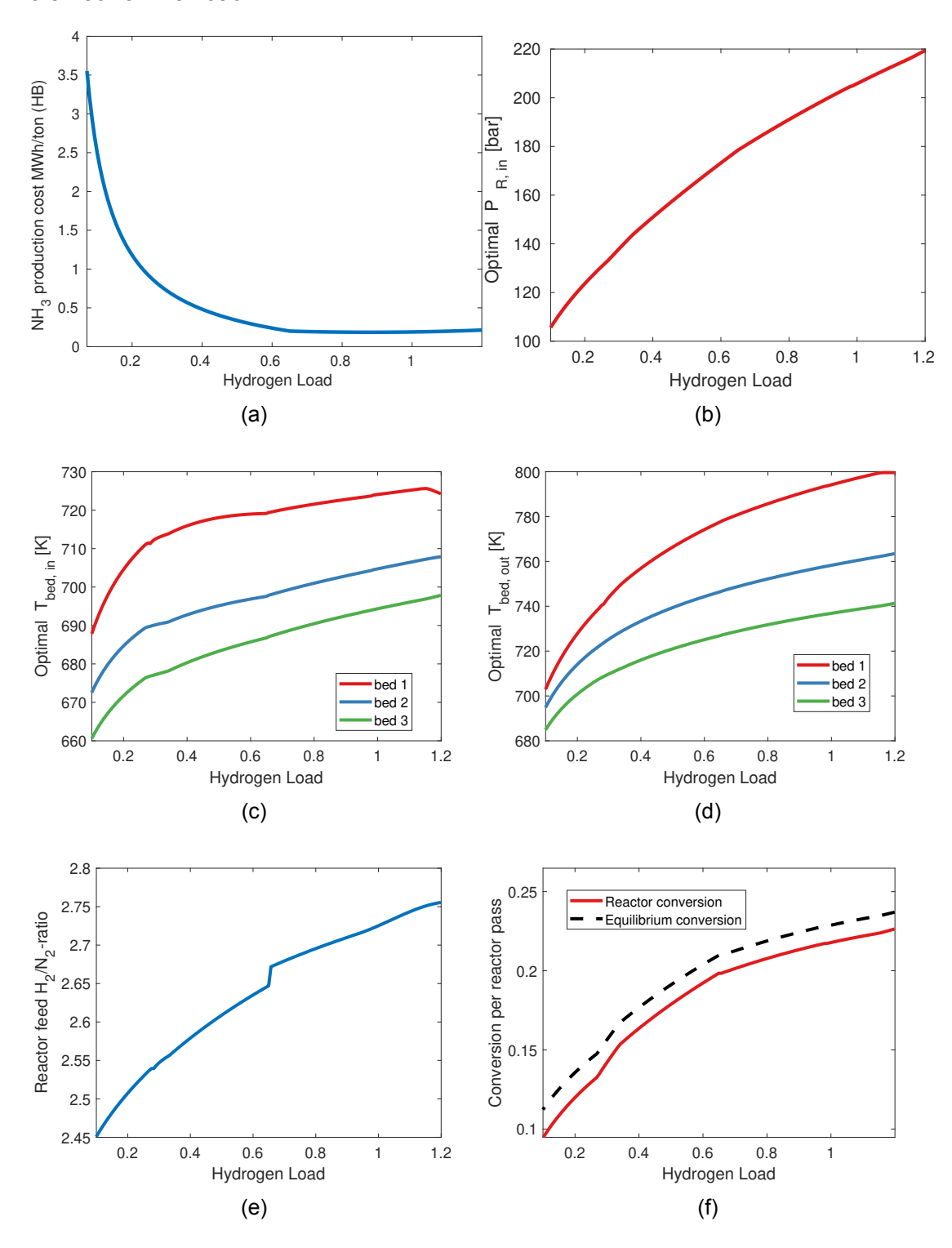


Figure 6.7: Selected optimal operating parameters as a function of the synthesis loop load, $d_1 = F_{f, \, \text{H}_2}$. a) Specific ammonia production cost in MWh/ton, b) loop pressure, c) Reactor bed inlet temperatures, d) Reactor bed outlet temperatures, e) Reactor feed H_2/N_2 -ratio, and f) Conversion per reactor pass.

Figure 6.7 presents the optimal solution for selected operating parameters across the PtA operating window. As shown in Figure 6.7b, the optimal synthesis loop pressure decreases at lower loads, which accounts for the modest reduction in feed compressor power observed in Figure 6.6a for hydrogen loads below the surge threshold. This reduction in pressure shifts the chemical equilibrium towards the reactants (see Figure 6.7f), thereby decreasing the reactant conversion per reactor pass. To partially mitigate this limitation, the reactor bed inlet and outlet temperatures are reduced (see Figure 6.7c and 6.7d). Lowering the reactor temperatures favours the exothermic ammonia synthesis reaction, thereby shifting the equilibrium towards the ammonia product. The lower temperature additionally slows down the reaction; however, the decreased flow rates at low loads ensure sufficient residence time. A more detailed explanation of this is provided in Rosbo et al. (2024a).

Figure 6.7e indicates that it is advantageous to operate the reactor with a H_2/N_2 -ratio slightly below the stoichiometric value of three at the reactor inlet. It should be noted that the make-up feed is, under steady-state conditions, supplied at the stoichiometric ratio. However, within the synthesis loop, it is possible to maintain a different H_2/N_2 -ratio. The H_2/N_2 -ratio can be dynamically adjusted by temporarily deviating from stoichiometry in the make-up feed. Due to the large recycle flow and the short residence time of reactants in the loop, the internal H_2/N_2 -ratio changes rapidly in response to such deviations.

6.7 Conclusion

In this study, a comprehensive dynamic model of the Haber–Bosch synthesis loop was developed, incorporating catalytic reactors, heat exchangers, compressors, steam turbines, and flash separators. The model was used to quantify the total electrical power utility of the loop, accounting for both power consumption and recovery.

At nominal load, the feed compressor consumed around 96% of the total electrical utility, while optimal ammonia separation was achieved using only cooling water. Approximately 60% of the compression power was recovered through the Rankine cycle.

Optimisation across a wide operating window (10–120% of nominal hydrogen feed flow) showed that loop pressure was the most influential decision variable, with optimal values ranging from above 220 bar at high load to about 110 bar at low load.

Compressor anti-surge constraints were also found to strongly affect low-load operation. Below the feed compressor surge limit at 65% hydrogen load, further reductions in power consumption were minimal.

Chapter 7

System design of compressor structure for PtA operation

In Chapter 6, a detailed model of the ammonia synthesis loop was developed and used to optimise power consumption across the full operating window. The optimisation results revealed that compressor anti-surge constraints significantly impacted the power consumption in the low load operating range.

To address this issue, this chapter explores synthesis loop compressor design with two, three, and four compressor trains operating in parallel. These configurations are evaluated for their ability to reduce power consumption and overall cost, with both performance and capital cost implications assessed over long-term operation.

This chapter contains material from the articles:

-Rosbo, J.W., Jørgensen, J.B., Jensen, A.D., Skogestad, S., Huusom, J.K., (2025). Optimisation of a Haber-Bosch Synthesis Loop for PtA. Systems Control Transactions 4, 1126–1132. doi: https://doi.org/10.69997/sct.122254.

7.1 Introduction

The previous chapter 6 showed that the specific energy cost of ammonia production relative to the synthesis loop was more than a magnitude higher at the lowest loads compared to nominal operation. This drastic increase in ammonia production cost at low loads was caused by compressor anti-surge recycling. To reduce this loss, operating with multiple compressor trains in parallel is investigated. Operating with compressors in parallel significantly extends the lower operating range for the compression before anti-surge recycling is activated. For example, a configuration with two parallel compressor trains, half the size of a corresponding single train configuration, doubles the downward operating flow range before activation of anti-surge recycle is required. Additionally, multiple parallel compressors can facilitate higher compressor efficiency as the compressor flow can be distributed closer to the optimal operating flow. Figure 7.1 illustrates the combined operating window for configurations with one, two, three and four compressors in parallel. The minimal total normalised operating flow before reaching the surge limit is respectively 65%, 32.5%, 21.7% and 16.3%

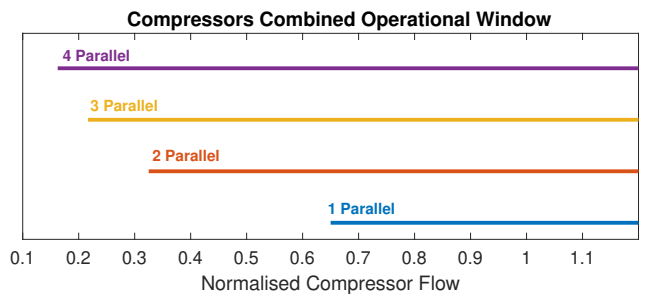


Figure 7.1: Combined operating window for configurations with one, two, three and four compressors in parallel.

While employing more, smaller compressors in parallel can reduce anti-surge losses at low loads, it also increases capital expenditure. This trade-off is therefore evaluated in this chapter.

7.2 Compressors in parallel

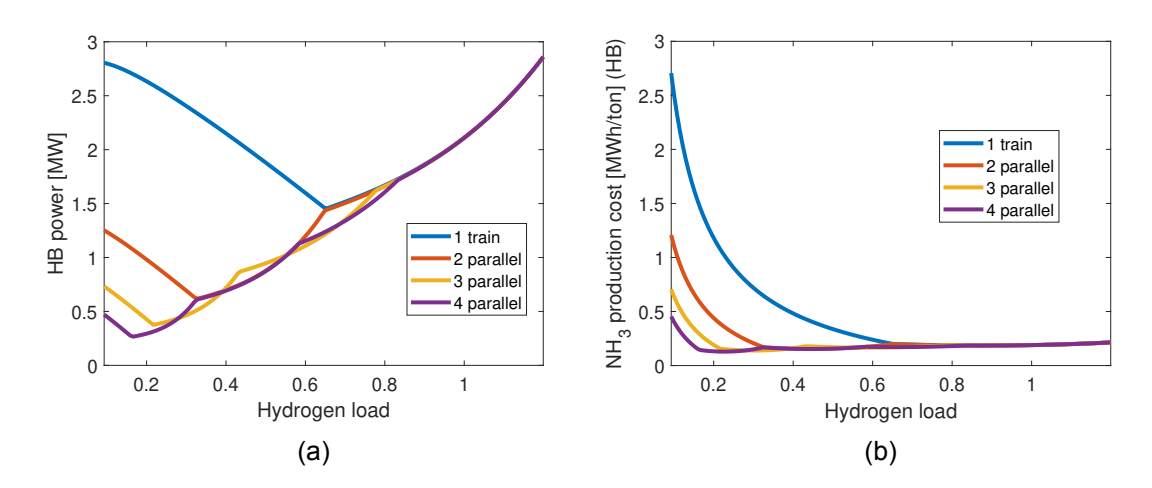


Figure 7.2: a) HB-power requirement and b) Specific ammonia production cost across the operating envelope with one, two, three and four parallel compressor trains.

The optimisation problem in Eq. 6.29a is solved across the operating window with two, three, and four parallel compressor trains. Figure 7.2a displays the optimal HB-loop power for different compressor configurations, showcasing a significant reduction in HB-power by operating with multiple parallel compressor trains. At around 80% hydrogen feed load, the configurations with 3 and 4 parallel compressor trains reduce the HB-power due to improved compressor efficiency achieved by pausing one compressor. However, the substantial reduction in HB-power occurs below the compressor surge limit, as the antisurge recycling is shifted to 32.5%, 21.7% and 16.3% of nominal hydrogen load for two, three and four parallel compressor trains, respectively. Figure 7.2b shows the specific ammonia production cost across the operating envelope. Clearly, multiple parallel compressors significantly decrease production costs. At 10% load, the ammonia production cost is reduced by 55%, 74% and 84% for two, three and four parallel compressor trains, respectively.

7.3 Economic Comparison

Figures 7.2 illustrates that operating with multiple parallel compressor trains significantly reduces the HB-loop power during part-load operation. However, to evaluate the economic benefits, it is essential to consider the distribution of operating hours across the hydrogen loads. This is an extensive optimisation problem depending on factors such as the local wind and solar power distribution, the relative size of renewable power to the electrolyser and synthesis loop capacity, hydrogen storage size and electricity price. Performing this optimisation is not the scope of this paper, but it was assessed by Armijo and Philibert (2020), Schulte Beerbühl et al. (2015) and Maggi et al. (2023). They concluded that wind and solar-powered PtA plants optimally operate mainly at minimum load, during periods of limited renewable power, or nominal load and above, during periods of surplus renewable energy. Complete reactor shutdown should be avoided as start-up times are extensive and frequent shutdowns damage the reactor catalyst (Armijo and Philibert, 2020).

7.3.1 Mean power for the HB-loop

Based on this, an HB-loop capacity factor of 70% is assumed. The corresponding hydrogen load distribution is illustrated in Figure 7.3. The mean power consumption of the HB-loop is found from the probability density function, p, via,

$$\bar{W}_{\mathsf{HB}} = \int_{0.1}^{1.2} W_{\mathsf{HB}}(\mathsf{HL}) \cdot p(\mathsf{HL}) \, d\mathsf{HL}$$
 (7.1)

Note, p is a piecewise function from the distribution in Figure 7.3. Table 7.1 summarises the mean HB-loop power for the four parallel compressor configurations. Approximately 26% reduction in mean HB-power is achieved by operating with two parallel compressors, while further power savings are less significant for three and four parallel compressors.

Parallel Compressors	Mean HB-Power [MW]
1	2.37
2	1.75
3	1.55
4	1.44

Table 7.1: Mean HB-power with one, two, three or four compressor trains in parallel.

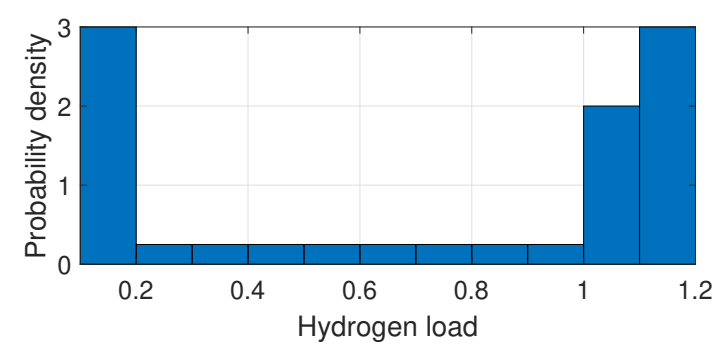


Figure 7.3: Probability density distribution of the synthesis loop load.

7.3.2 Capital Cost Estimation

The compressor capital costs are estimated using the bare module cost (BMC) method presented in (Kenneth Guthrie, 1974; Peters et al., 2002). The bare cost (BC) of an operating unit is given by an exponential expression,

$$BC = C_0 \left(\frac{S}{S_0}\right)^{\alpha} \tag{7.2}$$

where S is the capacity of the unit, and S_0 and C_0 are reference capacities and costs. α is the exponent around 0.6 to 0.85, reflecting the lower relative cost of larger equipment. For centrifugal compressor $C_0=74.6$ kWh, $S_0=\$23,000$, and $\alpha=0.8$. The Bare Module Cost (BMC) is the installed cost of the unit, including foundations, wiring, piping, instrumentation, etc. The BMC is given by,

$$BMC = UF \cdot BC \cdot (MPF + MF - 1) \tag{7.3}$$

where UF is the update factor relating the cost from the original work to the present value. The CEPCI index (2024) was used to update the cost,

$$UF = \frac{CEPCI_{2024}}{CEPCI_{1974}} = \frac{798.8}{165.4} = 4.83$$
 (7.4)

The module factor MF accounts for the total installation cost of unit and depends on the bare cost;

- MF = 3.11 for BC < 200,000 USD
- MF = 3.01 for 200,000 < BC < 400,000 USD
- MF = 2.97 for 500,000 < BC < 600,000 USD
- MF = 2.96 for 600,000 < BC < 800,000 USD
- MF = 2.93 for 800,000 < BC < 1,000,000 USD

Finally, MPF is the material and pressure correction factor, which for centrifugal compressors is one, MPF = 1 (Kenneth Guthrie, 1974).

7.3.3 Operational cost

Electricity is the only operational cost of the ammonia synthesis loop in a PtA setting. Figure 7.4 presents the hourly electricity spot prices for Western Denmark (DK1) from 1 January to 31 December 2024. The DK1 price index represents a region with a high share of renewable energy in the grid, making it particularly relevant for PtA studies. The spot prices show substantial hourly fluctuations throughout the year.

Table 7.2: Statistical values for hourly electricity spot price in Western Denmark (DK1) in 2024 (Els).

	Mean	Max	Min	1st Quartile	2nd Quartile	3rd Quartile
Value (USD/MWh)	77.8	1029	-66.0	44.7	74.8	104.7

Table 7.2 summarises the mean, minimum, maximum, and quartiles of the spot prices for the same period. Notably, the data includes extreme values, with a minimum of –66.0 USD/MWh and a maximum of 1029 USD/MWh. However, the quartile values are more reasonably distributed around the mean.

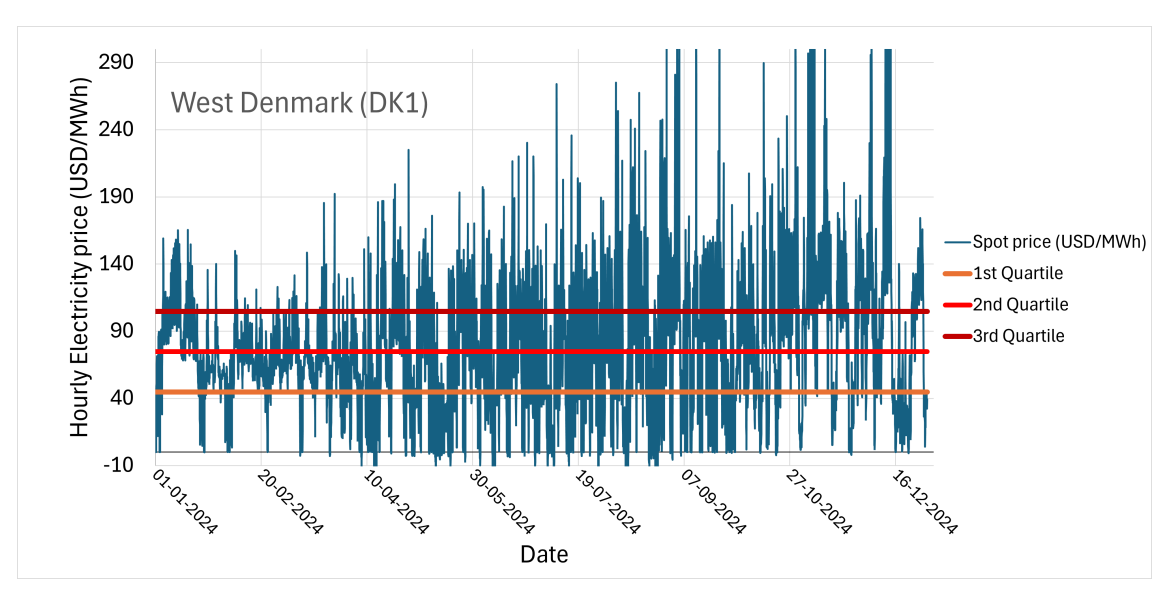


Figure 7.4: Hourly electricity spot prices for Western Denmark (DK1) in 2024 (Els).

.

Figure 7.4 illustrates that defining a single average electricity price does not describe the energy market well. Instead, the spot price dataset is used to define distinct price regions, corresponding to the probability density function (PDF) shown in Figure 7.3.

For example, from Figure 7.3, the synthesis loop operates 30% of the time in the low-load operating region. The electricity price for this region is therefore defined as the average of the lowest 30% of spot price values in the dataset. With this definition, the resulting prices for all the operating regions are shown in Figure 7.5.

The average operation cost of the HB-synthesis loop can then be calculated via,

$$OPEX_{\mathsf{HB}} = \int_{0.1}^{1.2} W_{\mathsf{HB}}(\mathsf{HL}) \cdot p(\mathsf{HL}) \cdot C_{elec.}(\mathsf{HL}) \, d\mathsf{HL}$$
 (7.5)

The average operating expenses (OPEX) for the different compressor configurations are evaluated, and the results are presented in Table 7.3. As shown, the relative reduction in OPEX achieved by operating with multiple trains in parallel is significantly greater than the energy savings reported in Table 7.1. This is because the parallel configurations primarily reduce energy consumption at low loads (see Figure 7.2), where electricity prices are higher, as illustrated in Figure 7.5.

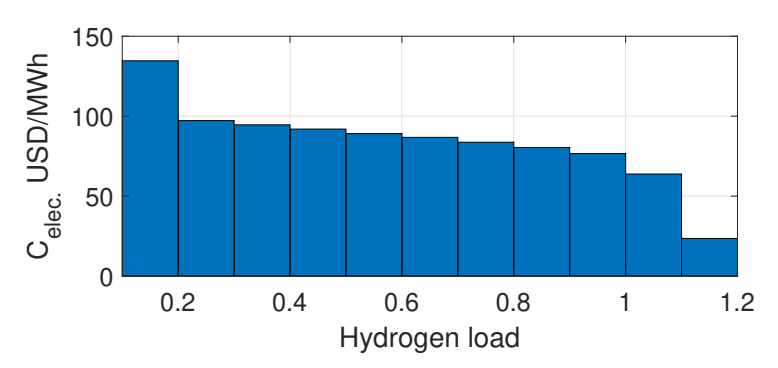


Figure 7.5: Average electricity prices at the HB-loop loads.

Parallel Compressors	Average OPEX [USD/h]
1	191.5
2	113.9
3	90.4
4	79.2

Table 7.3: Average OPEX for the HB-synthesis loop with one, two, three or four compressor trains in parallel.

7.3.4 Total cost

With the capital cost estimation method presented in Section 7.3.2 and the average operational cost described above, the total cost, TC, of a compressor system after n_h hours of operation is given by

$$TC = BMC + OPEX \cdot n_h \tag{7.6}$$

Figure 7.6 shows the total cost of the compressor systems (CAPEX + OPEX) as a function of years of operation. A compressor lifetime of 15 years is assumed, in line with literature values (Maggi et al., 2023).

As expected, the initial capital cost increases with the number of parallel compressors. However, the reduction in average operational cost quickly outweighs the higher capital investment. After 15 years of operation, configurations with two, three, and four parallel compressor trains achieve cost savings of 7.9, 9.8, and 10.4 million USD, respectively, compared to a single train configuration. This corresponds to total cost reductions of 19.1%, 23.9%, and 25.4%.

In addition to the economic benefits, the redundancy provided by multiple parallel compressors significantly improves the reliability of the synthesis loop. For example, with three parallel trains, near full-load operation can be maintained using the remaining two compressors if one train is out of service. However, increasing the number of parallel trains also adds operational complexity, including more frequent startups and shutdowns.

Considering the trade-off between economic benefits, improved reliability, and operational complexity, configurations with two or three parallel compressors are recommended for PtA plant operation.

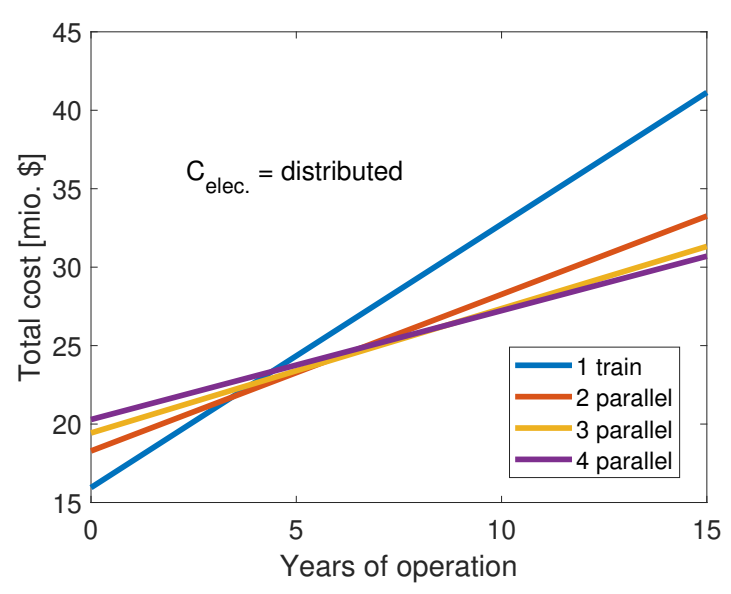


Figure 7.6: Total compressor cost (CAPEX + OPEX) for 15 years of operation with one, two, three or four compressor trains in parallel.

7.4 Conclusion

A static model of the Haber–Bosch synthesis loop was developed to evaluate the total power demand of the system. The model was used to optimise the synthesis loop with respect to key operating parameters, including reactor bed inlet temperatures, loop pressure, separator temperature, and the N_2/H_2 feed ratio, over a wide operating range representative of PtA operation.

The optimisation results highlighted that compressor anti-surge limitations significantly increase power consumption at low loads. Introducing multiple parallel compressor trains was shown to substantially reduce HB-loop power requirements in this regime, offering both economic and operational advantages. In addition to lowering energy use, parallel compressors improve process reliability by enabling continued high-load operation in the event of a compressor outage.

Considering the trade-off between capital investment, operational savings, and increased operational complexity, configurations with two or three parallel compressor trains were identified as the most attractive options for PtA applications.

Chapter 8

Sensitivity analysis and self -optimising variables

In Chapter (6), a detailed model of the ammonia synthesis loop was developed and used to optimise power consumption across the full operating window. The analysis revealed that compressor anti-surge constraints limit the reduction of power demand during low-load operation. To address this, a design incorporating multiple parallel compressor trains for feed and recycle compression was proposed.

Building on this, the present chapter continues the analysis for a synthesis loop configuration with two parallel compressor trains for both feed and recycle compression. The sensitivity of the optimisation results is assessed for realistic process disturbances, including reductions in catalyst activity, variations in argon concentration, and changes in cooling water temperature.

The chapter further investigates potential controlled variables with self-optimising properties: variables that, when held constant across the operating range, lead to minimal additional power consumption compared to full re-optimisation. The study shows that maintaining constant reactor bed inlet temperatures and H_2/N_2 -ratio in the reactor feed results in only minor efficiency losses, whereas keeping loop pressure constant causes substantial power penalties at load extremes. Operating with fixed parameters can reduce the frequency of set-point changes during load-flexible operation, simplifying control strategies and enhancing the lifetime of critical equipment.

Thus, this chapter answers the second part of research question 3.

This chapter contains material from the article:

-Rosbo, J.W., Jørgensen, J.B., Jensen, A.D., Skogestad, S., Huusom, J.K., (2025). Optimisation and Robust Control of a Load-Flexible Haber-Bosch Ammonia Synthesis Loop. Submitted to Computer Computers & Chemical Engineering

8.1 Introduction

Based on the analysis in the previous chapter, the study presumes with a synthesis loop design with two parallel compressor trains for feed compression and two parallel compressors for recycle compression.

The Background Section 2.10 reviewed strategies for load-flexible operation, as presented by, among others, Fahr et al. (2025), Cheema and Krewer (2018), Schiedeck et al. (2025), and Sun et al. (2024). These approaches demonstrate flexible operation across wide load ranges but do not achieve optimal performance across the entire operating envelope. In contrast, the previous chapter identified optimal synthesis loop operating parameters throughout the full load range.

However, implementing flexible operation with a real-time optimiser (RTO) that continuously updates synthesis loop set-points according to load introduces unnecessary complexity to the control system. In this context, the concept of self-optimising controlled (SOC) variables (Skogestad, 2000) offers an appealing alternative. An SOC variable incurs only minimal losses from the optimum when held constant across the operating window. By selecting appropriate SOC variables, it is possible to achieve near-optimal operation while maintaining relatively stable internal conditions in the Haber–Bosch loop, even as the external hydrogen feed varies between 10% and 120% of nominal capacity. Such stable operating conditions are additionally beneficial for preserving catalyst lifetime and structural strength, as large and frequent fluctuations in temperature and pressure can be damaging due to thermal and mechanical stress (Morud and Skogestad, 1998).

8.2 Optimasation of synthesis loop with two parallel compressor trains

The optimisation problem in Eq. (6.29a) is solved for the synthesis loop configured with two parallel compressor trains for compression across the entire operating window. Figure

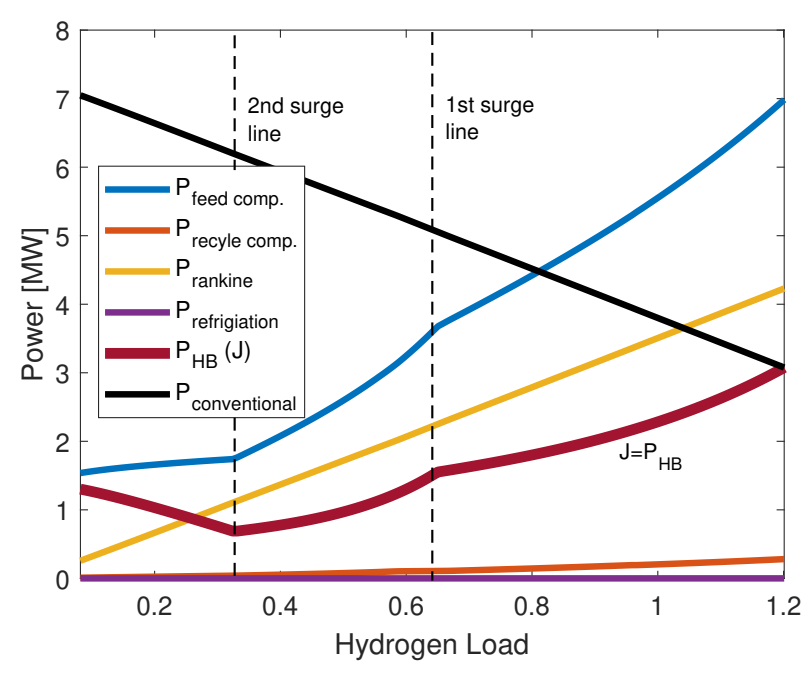


Figure 8.1: Optimal distribution of the power utilities across the operating envelope from 10% to 120% of the nominal hydrogen feed flow.

8.1 illustrates the resulting optimal power distribution. Overall, the distribution exhibits similar characteristics to the single-compressor configuration presented in Section 6.6, Figure 6.6a. However, in Figure 8.1 two distinct changes in the trajectory of the power curves can be observed. The first occurs at the 1st surge line, where one compressor train is taken offline below 65% of nominal hydrogen feed flow. The second occurs at the 2nd surge line, corresponding to 32.5% hydrogen load, where anti-surge recycling is activated for the remaining active compressor train.

Figure 8.1 also presents the power demand of the Haber- Bosch synthesis loop under a conventional pressure control strategy (black line), as described in Speth et al. (2023); Maurizio (2022); Gorval and Kein (2025). These patents propose regulating loop pressure and make-up feed flow by adjusting the recycle flow around the compressors, while maintaining constant compressor power. Under this control approach, the HB power requirement increases linearly as the hydrogen load decreases, as shown in Figure 8.1.

Figure 8.2 presents the optimal operating parameters across the PtA operating window for the synthesis loop equipped with two parallel compressor trains. Overall, the trends are very similar to those observed for the single-train configuration in Figure 6.7. However, the graphs exhibit two distinct discontinuities, corresponding to the two surge lines identified in Figure 8.1.

8.3 Sensitivity to process disturbances

The optimisation results presented above inherently depend on the assumed values for system parameters shown in Table 6.1. In the real plant, some of these parameters may differ and are subject to temporal variations. Important process disturbances for the synthesis loop include:

- Hydrogen feed flow (load), $d_1 = F_{f, H_2}$.
- Catalyst activity and effectiveness, $d_2 = \alpha$.
- Argon content in the nitrogen feed, $d_3 = x_{f, Ar}$.
- Cooling water temperature, $d_4 = T_{cool}$.

The hydrogen synthesis feed flow disturbance reflects the intermittency of renewable energy and constitutes the primary fluctuating disturbance to the synthesis loop. At the same time, it also functions as a decision variable at the plant-wide level, where a scheduling optimisation determines the synthesis load based on renewable energy forecasts and the level of hydrogen inventory in storage. However, from the perspective of the synthesis loop, the specified hydrogen feed flow acts as a disturbance ranging from 10% to 120% of its nominal value. Figure 8.3 presents an evaluation of the sensitivity of the remaining disturbances across this entire hydrogen load operating range. Note that each curve represents a reoptimised solution for the specified perturbation of the disturbance variables.

Changes in catalyst activity and effectiveness factor are not directly measurable disturbances. Both affect the reaction rate of the ammonia formation, but arise from distinct underlying phenomena. Variations in catalyst activity are associated with changes in the intrinsic reaction kinetics and typically occur over long time scales due to progressive catalyst deactivation throughout its operational lifetime. In contrast, the catalyst effectiveness factor accounts for transport limitations and is influenced by external factors such as gas-phase composition, flow rate, temperature, pressure and particle size. Notably, the catalyst effectiveness factor can vary as reactor operating conditions shift across the PtA operating window. Although these two phenomena originate from different mechanisms,

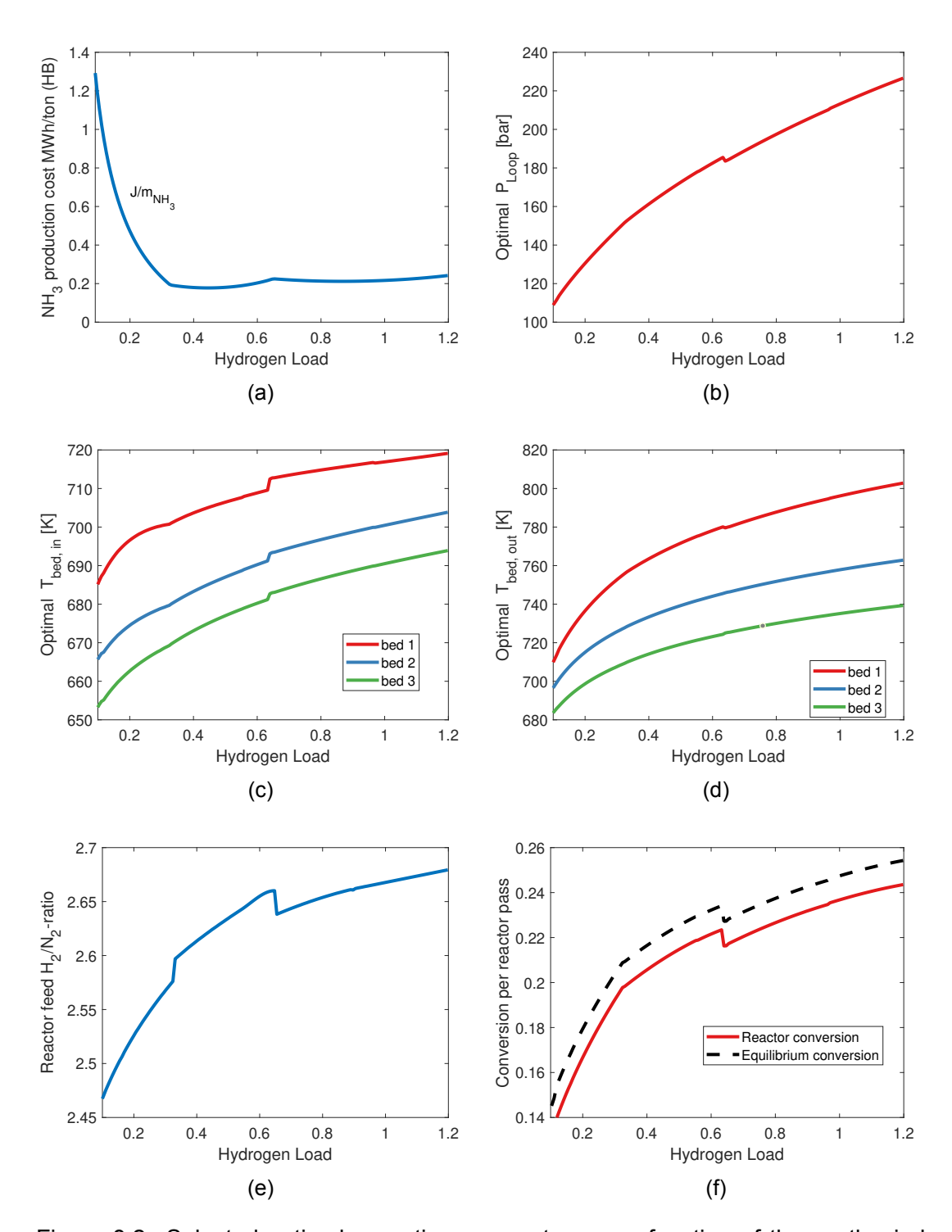


Figure 8.2: Selected optimal operating parameters as a function of the synthesis loop load, $d_1 = F_{f,\, H_2}$. a) Specific ammonia production cost in MWh/ton, b) loop pressure, c) Reactor bed inlet temperatures, d) Reactor bed outlet temperatures, e) Reactor feed H_2/N_2 -ratio, and f) Conversion per reactor pass.

both ultimately affect the overall reaction rate of ammonia formation. Therefore, their impact on the optimisation results can be jointly assessed by introducing an activity factor, α , which scales the reaction rate relative to its nominal value,

$$r_{adj} = \alpha \cdot r_{nom}, \tag{8.1}$$

Figure 8.3a illustrates the impact of perturbations in reaction activity on the cost function (loop power) when reoptimising across the load range. As expected, the loop power increases with decreasing catalyst activity factor. This effect is primarily due to increased feed compressor work, as the system compensates for reduced catalyst activity by elevating the loop pressure. The figure shows that reducing the catalyst activity to $\alpha=10\%$ results in a 20–40% increase in the loop power consumption across the load range. In practice, catalyst replacement or regeneration would be considered if the activity factor falls below approximately 30%, which is typically reached after decades of gradual degradation in a conventional plant (Kohli et al., 2008).

On shorter time scales, changes in reaction rate may result from variations in catalyst effectiveness during flexible operation. The dependence of the catalyst effectiveness factor on changes in operating parameters such as pressure, temperature, flow rate, and gas composition is not described in the presented reactor models. Such variations in catalyst effectiveness are expected to correspond to effective activity factors ranging from 70% to 120% of the nominal reaction rate, leading to changes in the HB-loop power of approximately $\pm 5\%$ across the operating envelope. Appendix E contains an analysis of the HB-loop power consumption for a broad range of catalyst activities, $\alpha \in [0.1,\ 100]$.

As described in section 6.3, the argon content in the nitrogen feed is assumed significantly lower than in conventional ammonia plants ($f_{Ar,\ nom}=0.1\%$), due to the use of air separation. Nonetheless, some variation in f_{Ar} is expected across the operational envelope of the PtA plant. Figure 8.3c-d show the HB-loop power and percentage increase in HB-loop power for different values of f_{Ar} . The HB-loop power increases substantially — by up to 35% — as the argon content approaches the conventional level of approximately 1.2%. However, in systems employing air separation, the argon content is not expected to exceed 0.3%, as argon predominantly separates with oxygen Rosbo et al. (2024b).

Figure 8.3e illustrates the influence of the cooling water temperature, T_{cool} , on the loop power. The cooling water temperature primarily affects the vapour–liquid equilibrium in the flash separator. While seasonal variations are the dominant source of long-term fluctuation in the cooling water temperature, short-term changes may occur due to weather conditions or local flow patterns in the cooling water source. Although the impact is less pronounced compared to variations in catalyst activity or argon content, the cooling water temperature still has a notable effect on the HB-loop power demand. Contrary to the disturbances for catalyst activity and $f_{\rm Ar}$, the cooling water temperature is easy to measure. Thus, the optimal operating conditions can quickly be updated by rerunning the optimisation with the given cooling water temperature.

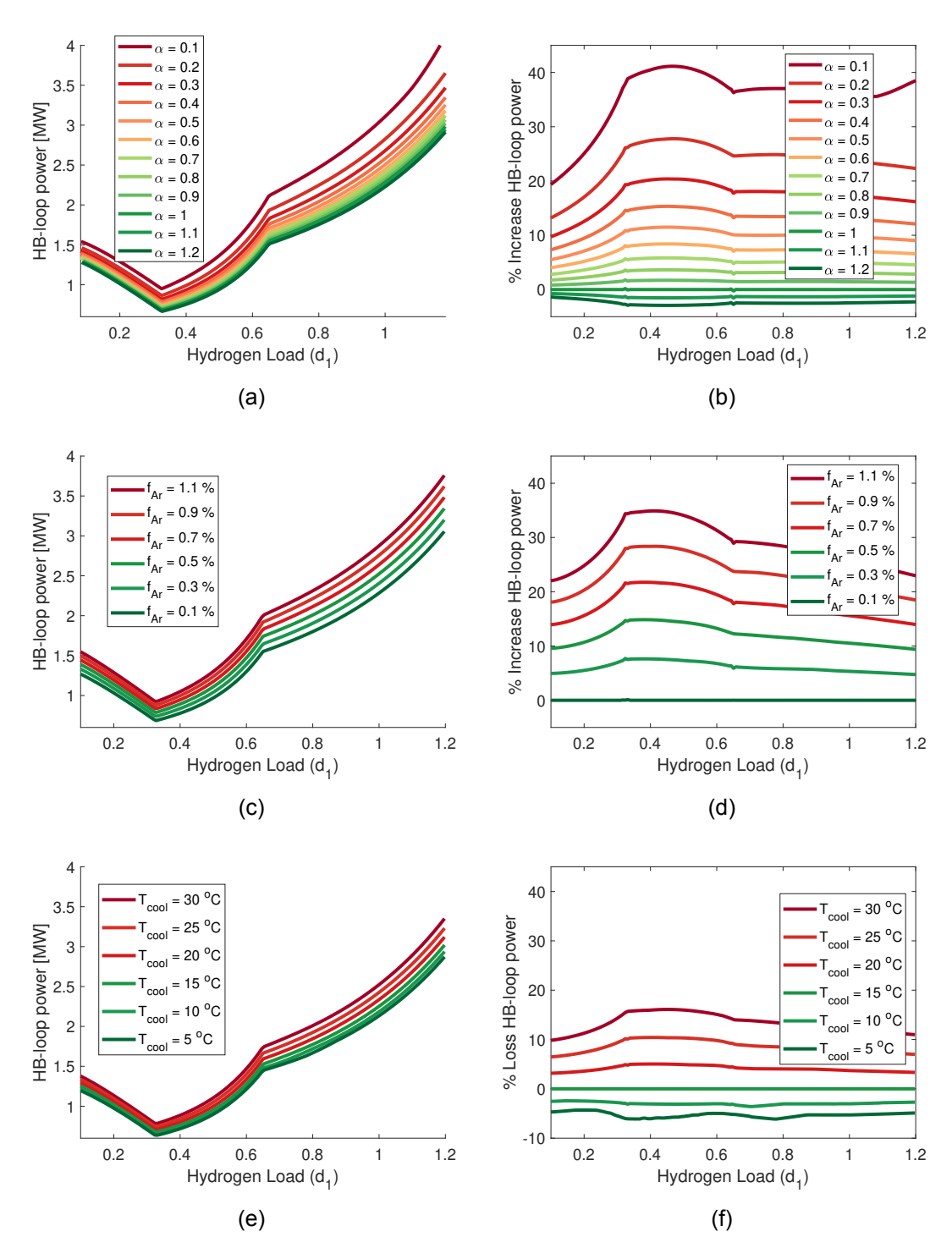


Figure 8.3: Reoptimised loop power as a function of the load (d_1) to disturbances in a) catalyst activity (d_2) , c) argon content in the nitrogen feed (d_3) , and e) cooling water temperature (d_4) . b), d) and f) show the corresponding percentage increase in HB-power compared to the nominal solution ($\alpha = 1$, $f_{Ar} = 0.1\%$, $T_{cool} = 15^{\circ}\text{C}$).

8.4 Self-optimising variables for control

The optimisation problem in Eq. (6.29a) involves six degrees of freedom. Thus, to operate the synthesis loop at the optimal points, six controlled variables must be identified.

However, since the optimal cooling in the flash separator was found to be always at the maximum cooling water flow limit, this degree of freedom is effectively fixed. As a result, the control problem reduces to identifying five controlled variables.

The following candidates for controlled variables are identified,

- Reactor bed inlet temperatures, $T_{bed, in}$.
- Reactor bed outlet temperatures, $T_{bed, out}$.
- Loop pressure, P_{loop} .
- Hydrogen to nitrogen ratio in the reactor feed, $R_{\text{H}_2/\text{N}_2}$.
- Hydrogen to nitrogen ratio in the synthesis feed, $R_{f, H_2/N_2}$.
- Liquid level in the flash tanks, ${\cal V}^l_{flash}$

Note that the liquid level in the flash tanks does not influence the steady-state cost function. Consequently, optimal steady-state operation can, in principle, be achieved at any liquid level. For this reason, the liquid levels in the flash tanks are not considered in the following analysis.

As illustrated in Figure 8.2, the optimal values of the remaining variables change with the hydrogen load. Consequently, maintaining optimal operation requires frequent updates to the set-points of the controlled variables, particularly in a PtA plant supplied by intermittent renewable energy. To minimise the need for such frequent set-point updates, a promising approach is to employ self-optimising control (SOC) variables. The concept of self-optimising variables is introduced in Skogestad (2000)

"Self-optimising control is when we can achieve an acceptable loss with constant setpoint values for the controlled variables (without the need to reoptimise when disturbances occur)."

Self-optimising control has demonstrated the ability to maintain near-optimal operation across a range of systems subject to disturbances (Krishnamoorthy and Skogestad, 2022). According to Skogestad (2000), a good self-optimising control variable should satisfy four key criteria:

- Requirement 1: Its optimal value should be insensitive to disturbances.
- Requirement 2: It should be easy to measure and control accurately.
- Requirement 3: Its value should be sensitive to changes in the manipulated variables.
- Requirement 4: For cases with two or more controlled variables, the selected variables should not be closely correlated.

Following the procedure in Skogestad (2000), The synthesis loop exhibits an external H_2/N_2 -ratio in the make-up feed, $R_{f, H_2/N_2}$, and an internal loop ratio in the reactor feed, R_{H_2/N_2} . The internal hydrogen-to-nitrogen ratio does not satisfy Requirement 2, as gasphase compositions are challenging to measure in real-time. Typically, offline gas chromatography is required, with sampling cycles from 10 to 20 minutes (Speth et al., 2023).

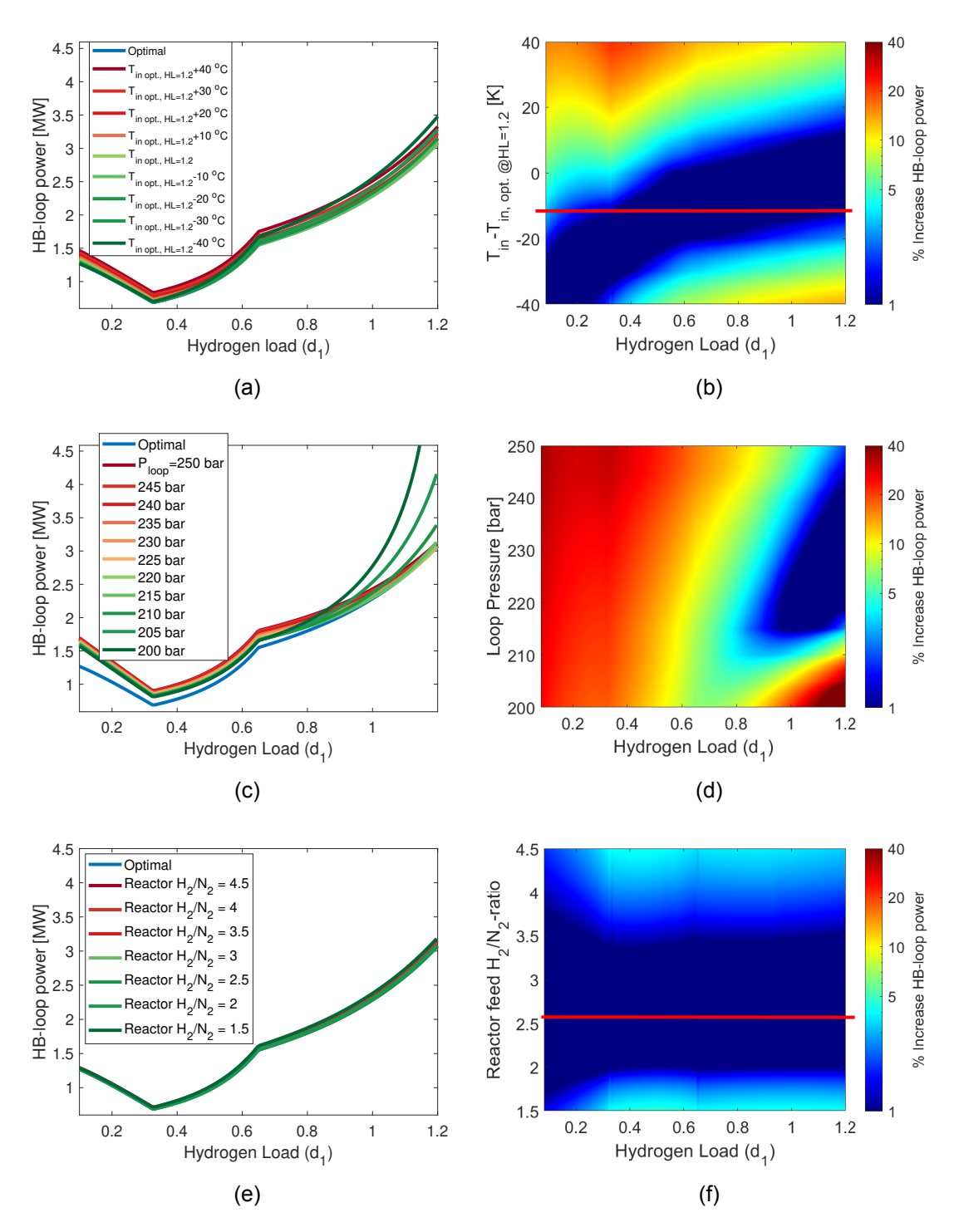


Figure 8.4: Optimal HB-loop power as a function of the load with constant values of a) reactor bed inlet temperature, c) loop pressure, and e) reactor feed H_2/N_2 -ratio. b), d) and f) show contour plots of the percentage increase in the power compared to the optimal solution for constant reactor bed inlet temperature, loop pressure and reactor feed H_2/N_2 -ratio, respectively. The red lines indicate the values for self-optimising control yielding the smallest loss in the objective function.

In contrast, the H_2/N_2 -ratio in the synthesis feed is relatively easy to control via a flow controller. However, purely controlling the feed H_2/N_2 -ratio is impractical in the presence of

implementation errors, as even minor deviations from stoichiometry amplify rapidly within the synthesis loop, as shown in Luyben (2012). Moreover, controlling H_2/N_2 -ratio in the synthesis feed loses feedback information within the synthesis loop. Therefore, controlling the H_2/N_2 -ratio within the synthesis loop appears as the most promising solution, although measurements are infrequent.

Similarly, the reactor bed outlet temperatures fail to meet Requirement 2. As shown by Luyben (2012), controlling the bed outlet temperatures is difficult due to the significant time delays associated with the high thermal inertia of packed-bed reactors. In addition, setting the reactor outlet temperatures may be infeasible if the desired setpoints exceed the achievable equilibrium temperatures.

Given these observations, the following remain as viable candidates for self-optimising control variables:

- Reactor bed inlet temperatures, $T_{bed1,\ in}$, $T_{bed2,\ in}$, $T_{bed3,\ in}$.
- Loop pressure, P_{loop} .
- Hydrogen to nitrogen ratio in the reactor feed, $R_{\text{H}_2/\text{N}_2}$.

The self-optimising properties of the candidate controlled variables are assessed by fixing each candidate variable and reoptimising the synthesis loop over the remaining degrees of freedom. The resulting increase in the objective function (loop power) is assessed over the entire hydrogen load (d_1) operating window. The nominal point for the candidate-controlled variables corresponds to the optimal solution at the maximum hydrogen load (120%). This nominal point is selected because it represents the condition with the shortest catalyst residence time, thereby ensuring that the system remains closed-loop stable throughout the entire operating range.

Figure 8.4 illustrates the sensitivity of HB-loop power to fixing candidate controlled variables at constant values. The variables are evaluated under several perturbations around the optimal point at maximum hydrogen load, enabling the identification of an optimal constant setpoint.

Figure 8.4a presents the optimal loop power when the reactor bed inlet temperatures are kept constant across the full operating window. Figure 8.4b shows a contour plot of the corresponding relative increase in power consumption compared to the fully optimised solution. The results show that the additional HB-power required when fixing the bed inlet temperatures is relatively modest across the range of hydrogen loads. The highest penalty occurs when the bed inlet temperatures are fixed 40 °C above the nominal optimum at maximum load, resulting in a maximum increase of up to 20% in HB-power.

Observe from Figure 8.4b, that fixing the bed inlet temperatures around 0-20°C below the optimum at maximum load results in negligible additional HB-power throughout the operating envelope. This suggests that fixing bed inlet temperatures to a constant value approximately 10°C below the optimal at maximum load, makes the system practically insensitive to moderate implementation errors in the bed inlet temperature. Based on this analysis, the bed inlet temperatures present strong candidates for self-optimising control.

The small impact of the bed inlet temperatures on HB-loop power can be understood by revisiting the optimisation results presented in Figure 8.1, which illustrated that the power required for recycle compression is negligible compared to the power consumed by the feed compressors. Since the bed inlet temperatures influence the per-pass reactor conversion, deviations from the optimal temperatures lead to reduced conversion and,

consequently, increased recycle flow. However, because the power demand for recycling is minimal, this increase in flow has only a marginal effect on the total loop power.

In Figure 8.4c, the sensitivity of HB-loop power to fixed loop pressure values is depicted, while Figure 8.4d presents a contour plot of the corresponding percentage increase in HB-power requirements relative to optimal operation. Compared to the case of fixed bed inlet temperatures, the use of constant loop pressures results in a substantially higher increase in HB-power. The most pronounced power penalties occur at low hydrogen loads, where maintaining a high constant loop pressure leads to excessive HB-power demands up to 30% higher than the fully optimised solution. These results align with the optimal loop pressure trends observed in Figure 8.2b, where the pressure decreases to approximately 110 bar at the lower load limit. Conversely, adopting a lower fixed reactor pressure to match low-load conditions leads to significant increases in HB-power at high loads. Additionally, operating with insufficient pressure at high loads can compromise reactor stability due to inadequate conversion per pass, which may ultimately lead to a reactor blowout.

However, note that, relative to the conventional strategy of maintaining constant compressor power (see Figure 8.1), a control strategy based on constant loop pressure results in a comparatively modest increase in HB-power. In particular, for hydrogen loads above 50% of the nominal value, the additional power requirement remains relatively small, highlighting the potential viability of constant pressure control within this operational range. Nonetheless, across the full operational range, maintaining a constant loop pressure results in an unacceptably high increase in HB-power. Especially, considering the power utility at low loads should be regarded as more valuable, as this likely represents operation during periods of insufficient renewable power. Therefore, this strategy is considered suboptimal, and a load-dependent real-time optimisation (RTO) approach is recommended to ensure energy-efficient operation at reduced loads.

Figure 8.4e illustrates the sensitivity of HB-loop power to operating with a constant H_2/N_2 -ratio in the reactor feed. The contour plot in Figure 8.4f clearly shows that variations in the H_2/N_2 -ratio within a reasonable range have only a limited impact on the required HB-power. Similar to the case of the bed inlet temperatures, the H_2/N_2 -ratio primarily influences the recycle flow rate and therefore has a minimal effect on the total HB-power.

This negligible sensitivity of the H_2/N_2 -ratio is particularly advantageous, considering the practical challenges associated with accurate and continuous online measurement of gas compositions. In practice, the analysis suggest that tight control of the H_2/N_2 -ratio is unnecessary. Maintaining the H_2/N_2 -ratio within the range from 2 to 4, using infrequent measurements, results in only a modest increase in HB-power, making it a viable approach as a self-optimising variable.

To summarise, near-optimal operation can be achieved across the operating envelope by operating with constant bed inlet temperature and reactor H_2/N_2 -ratio, while updating the loop operating pressure in response to changes in the load. The optimal constant values for the bed inlet temperatures have been identified as 10 K below the optimal solution for maximum load operation (indicated by the red line in Figure 8.4b). For the reactor H_2/N_2 -ratio the optimal constant value is 2.6. Table 8.1 presents the selected self-optimising control variables and a justification for each choice, based on the analysis conducted across the hydrogen load operating envelope.

The make-up feed flow is the primary varying disturbance from the perspective of the HB-loop. However, other process disturbances may also impact operation (as discussed in

Section 8.3). Therefore, to assess the robustness of the proposed self-optimising variables, the resulting power loss under the disturbances presented in Section 8.3 are evaluated.

Table 8.1: Justification for the selection of self-optimising variables.

Candidate CV	SOC?	Reasoning
Bed Inlet Temperatures	Yes	 Near optimal operation across the PtA operating envelope with constant bed inlet temperatures in the range ±20 K of the optimal solution at 120% load. Controllable through manipulation of the reactor feed splits.
Loop Pressure	No	 Constant loop pressure leads to a significant increase in HB-loop power at reduced hydrogen loads Control is fast through the recycle compressor power (see Chapter 10).
Reactor H ₂ /N ₂ -ratio	Yes	 Negligible influence of the reactor feed H₂/N₂-ratio on the HB-power. The use of offline gas measurements complicates tight control of the reactor feed H₂/N₂-ratio. However, the low sensitivity of the HB-loop power to variations in H₂/N₂-ratio makes tight control unnecessary.

Figure 8.5 shows the increase in power consumption when using the self-optimising control strategy under perturbations in catalyst activity, argon feed fraction, and cooling water temperature. The evaluated disturbance ranges are $0.8 \le \alpha \le 1.2,\, 0.005\% \le f_{\rm Ar} \le 0.02\%$, and $10^{\rm o}{\rm C} \le T_{cool} \le 25^{\rm o}{\rm C}$. The disturbances are perturbed in a closer neighbourhood around the nominal load compared to the results presented in Section 8.3. This reflects the assumption that these disturbances change on a slower time-scale than the hydrogen load fluctuations. Thus, a persistent shift in the disturbance variables can be adjusted for by periodic reoptimisation. Across the full hydrogen load envelope, the additional power requirement due to fixed self-optimising variables remains below 10% compared to the fully re-optimised solutions. This demonstrates the effectiveness of the proposed strategy, as such a loss is acceptable for the considered disturbance perturbations.

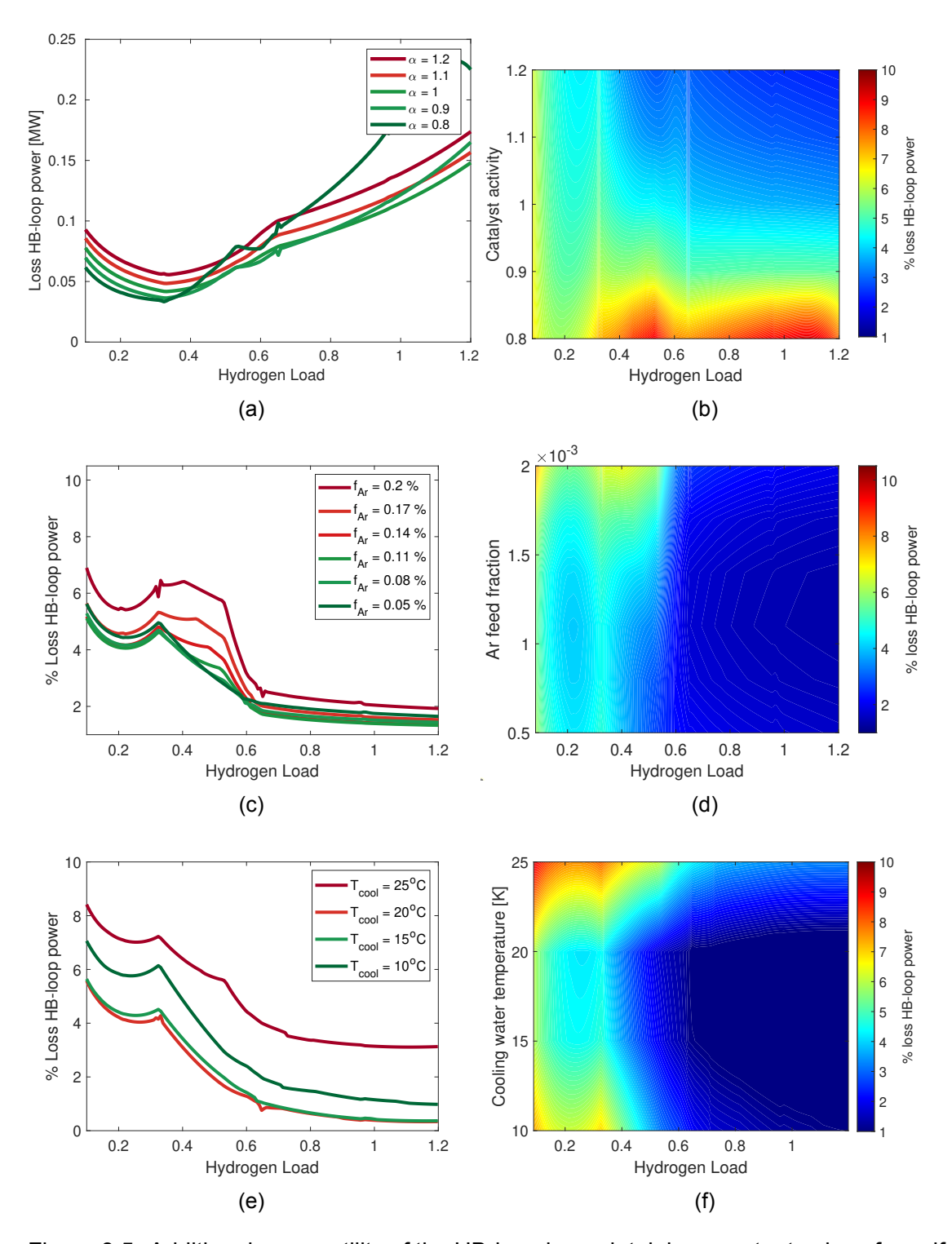


Figure 8.5: Additional power utility of the HB-loop by maintaining constant values for self-optimising variables across the operating envelope compared to the optimal solution for disturbances in a) catalyst activity, c) argon content in the nitrogen feed, and e) cooling water temperature. b), d) and f) show the corresponding contour plots for the percentage increase in HB-power compared to the optimal solution.

8.5 Conclusion

This chapter extended the optimisation study from Chapter 6 by considering a synthesis loop design with two parallel compressor trains for both make-up feed and recycle compression. This configuration was shown to significantly reduce power consumption at low-load operation compared to a single-compressor setup, mitigating the limitations caused by anti-surge constraints.

A sensitivity analysis demonstrated that the optimal power consumption is relatively modestly affected even under significant process variations, including reductions in catalyst activity, changes in argon concentration, and variations in cooling water temperature.

Furthermore, the study identified controlled variables with self-optimising properties. Maintaining constant reactor bed inlet temperatures and a fixed H_2/N_2 -ratio provided near-optimal performance across the operating window. In contrast, keeping loop pressure constant resulted in significant efficiency penalties at load extremes, suggesting that real-time optimisation is more appropriate for loop pressure control. Employing a self-optimising strategy for selected variables reduces the need for frequent set-point adjustments, thereby simplifying control implementation and extending equipment lifetime while maintaining high energy efficiency.

Chapter 9

Open-loop simulations of the Haber-Bosch synthesis loop

Chapter 8 illustrated the sensitivity of the Haber-Bosch synthesis loop to disturbances in catalyst activity, argon feed fraction, and cooling water temperature across the hydrogen load operating window. This demonstrated that a strategy employing self-optimising controlled variables for the reactor bed inlet temperatures and H_2/N_2 -ratio in the reactor feed achieved near optimimal operation for all the disturbances across the load range.

This Chapter investigates the open-loop dynamics and stability of the ammonia synthesis loop. The open-loop behaviour of the system is important for formulating an effective control architecture.

This chapter contains material from the article:

-Rosbo, J.W., Jørgensen, J.B., Jensen, A.D., Skogestad, S., Huusom, J.K., (2025). Optimisation and Robust Control of a Load-Flexible Haber-Bosch Ammonia Synthesis Loop. Submitted to Computer Computers & Chemical Engineering

9.1 Introduction

Chapter 5 investigated the dynamic behaviour of individual reactor configurations, showing that the optimal operating points for maximum conversion often lie close to the extinction boundary. In particular, open-loop simulations of the AICR demonstrated that even small disturbances in reactor feed temperature or feed flow could drive the system to extinction. In the synthesis loop, these instabilities may be further amplified through the large reactant recycling. For instance, an increase in reactor flow reduces the per-pass conversion, which in turn raises the recycle flow, reinforcing the disturbance through a negative feedback loop.

Despite the critical importance of these dynamics for flexible Power-to-Ammonia operation, relatively few studies in the literature have examined the open-loop behaviour of ammonia synthesis loops. Sun et al. (2024) presented open-loop step responses of an ammonia loop to changes in feed flows and compressor power, while most other works focus primarily on closed-loop simulations (Luyben, 2012; Araújo and Skogestad, 2008; Wen et al., 2024; Rovaglio et al., 2001).

To address this gap, this chapter investigates the open-loop dynamics and stability of a synthesis loop equipped with an AICR reactor. Step-change simulations are performed in key manipulated variables, including compressor powers, reactor feed splits, and make-up flows, to analyse the resulting responses of the main controlled variables. These results reveal the degree of nonlinearity, cross-coupling, and potential instabilities in the synthesis loop, providing critical insight for assessing operational risks.

The simulations form the foundation for the subsequent development of a control architecture in Chapter 10.

9.2 Step-responses to manipulated variables

Chapter 8 identified the best selection of controlled variables in the synthesis loop (bed inlet temperatures, loop pressure and H_2/N_2 -ratio in the reactor feed). The following investigates the open-loop response of these controlled variables to step changes in relevant manipulated variables (MVs).

The synthesis loop includes the following manipulated variables:

- Reactor beds feed splits, q_R .
- External heat exchanger (eHex1) bypass, q_{ex}
- Recycle compressor power, $P_{looncomp}$.
- Loop compressor anti-surge recycle flow, $Q_{loopcomp, recycle}$.
- Feed compressor power, $P_{feedcomp}$.
- Feed compressor anti-surge recycle flow, $Q_{feedcomp, recyle}$.
- Nitrogen make-up feed, F_{f, N_2} .
- Liquid flow exiting flash 1, Q_{flash1}^l .
- Liquid flow exiting flash 2, Q_{flash2}^l .
- Flow of saturated water to the Rankine cycle, $Q_{rankine, water}$.

Note that some of these variables, such as split fractions and flow rates, cannot be directly manipulated. However, we assume they are rapidly regulated via cascade control

loops acting through the valve positions, which allows us to regard them as manipulated variables in the control structure. The dynamics of the Rankine cycle are not included in the synthesis loop model (only the overall energy balance described in Section 6.2.8). Instead, we employ the temperature of stream 12, T_{S12} , as a manipulated variable, which is cascade controlled via the flow of water through the Rankine cycle. The cascade loop from $Q_{rankine,\ water}$ to T_{S12} follows the dynamics in the Rankine cycle and therefore cannot be assumed infinitely fast.

The most influential MVs affecting the synthesis loop dynamics are the compressor powers, the reactor bed feed splits, and the nitrogen make-up feed flow, F_{f, N_2} . In contrast, the outlet liquid flow from the flash tanks primarily influences the local tank dynamics, while the anti-surge recycle flow mainly affects the compressors. Consequently, the dynamic analysis focuses on these key MVs and the corresponding responses in the controlled variables identified in Chapter 8.4.

The in investigated manipulated (u) and controlled variables (c) are given in Eq. (9.1).

$$\mathbf{u} = \begin{bmatrix} u_1 \\ u_2 \\ u_3 \\ u_4 \\ u_5 \\ u_6 \end{bmatrix} = \begin{bmatrix} q_{\text{R1}} \\ q_{\text{R2}} \\ q_{\text{ex}} \\ P_{\text{loopcomp}} \text{ [kW]} \\ P_{\text{feedcomp}} \text{ [MW]} \\ F_{f, N_2} \text{ [kmol/s]} \end{bmatrix}$$

$$\begin{bmatrix} c_1 \end{bmatrix} \begin{bmatrix} T_{\text{bed1, in}} \text{ [K]} \end{bmatrix}$$

$$\mathbf{c} = \begin{bmatrix} c_1 \\ c_2 \\ c_3 \\ c_4 \\ c_5 \\ c_6 \end{bmatrix} = \begin{bmatrix} T_{\text{bed1, in }} [\mathbf{K}] \\ T_{\text{bed2, in }} [\mathbf{K}] \\ T_{\text{bed3, in }} [\mathbf{K}] \\ P_{\text{bed1, in }} [\mathbf{bar}] \\ F_{f, H_2} [\mathbf{kmol/s}] \\ S_{R, H_2/N_2} \end{bmatrix}$$
(9.1b)

Note, the make-up hydrogen feed flow ($c_5 = F_{f,\, {\rm H_2}}$) is included in the list of controlled variables. As described in Section 8.3, the hydrogen synthesis feed flow is the primary disturbance to the synthesis loop from an optimisation perspective. However, it also acts as a decision variable at the plant-wide level. It is assumed that a high-level scheduling optimisation determines the desired hydrogen consumption of the synthesis loop. In dynamic operation, the hydrogen feed flow is therefore treated as a controlled variable, with its set-point adjusted according to the desired synthesis load. For this reason, the dynamic response of the hydrogen make-up feed flow is also included in the step-response analysis.

The step responses are all initiated from the optimal operating point at the nominal hydrogen feed flow identified in Section 8.2.

The nitrogen make-up feed, $F_{f,\,N_2}$, is the most intuitive manipulated variable (MV) for controlling the reactor H_2/N_2 -ratio, R_{H_2/N_2} . However, during load-flexible operation, the slow sampling rate of the reactor H_2/N_2 -ratio (discussed in Section 8.4) can lead to large deviations from stoichiometry in the make-up feed if the hydrogen feed flow changes rapidly. To address this, a cascade control strategy is proposed, where the make-up feed ratio, $R_{f,;H_2/N_2}$, is controlled via the nitrogen feed flow. In this approach, the make-up feed H_2/N_2 -ratio acts as the MV, ensuring that it remains close to the stoichiometric value.

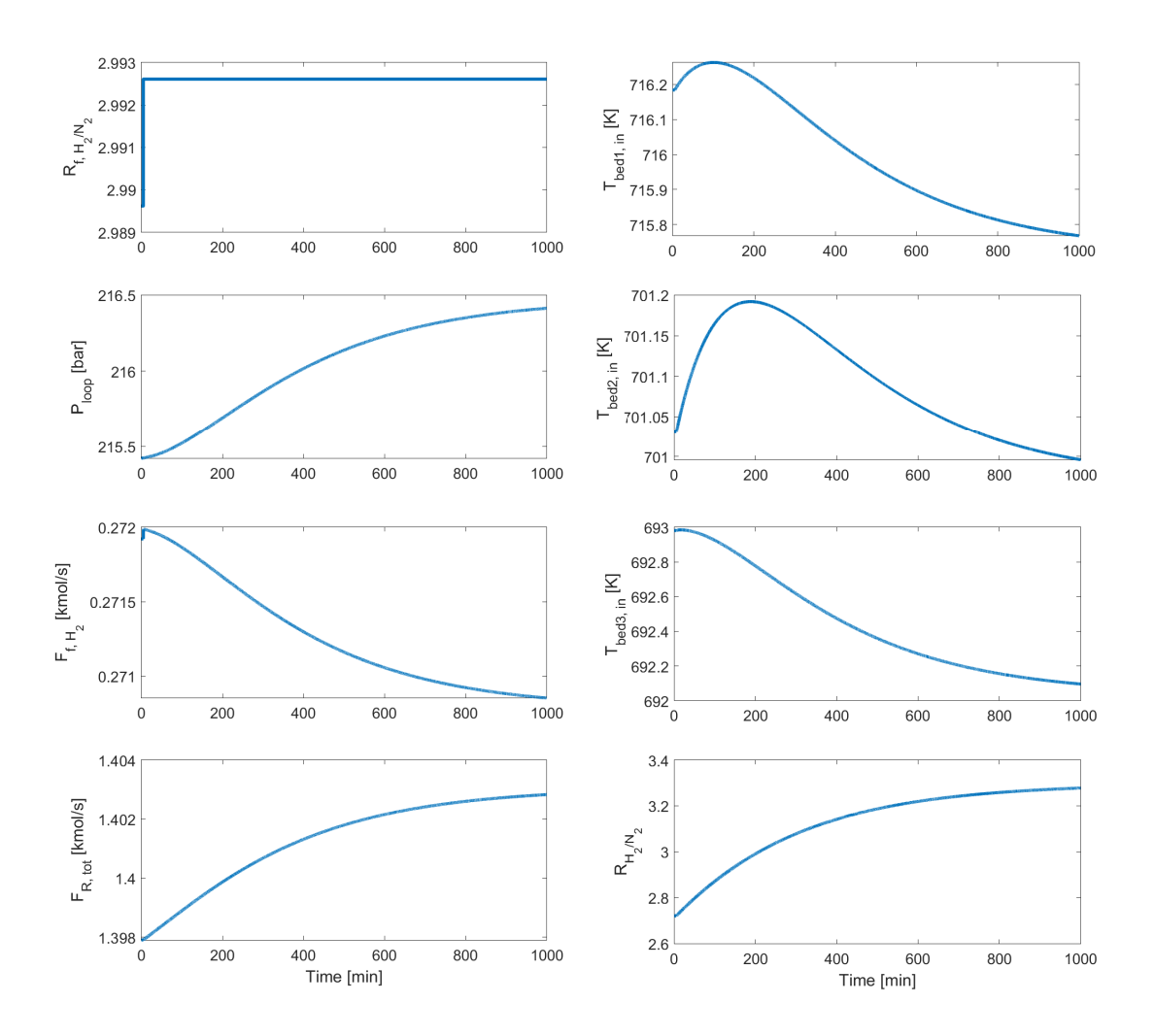


Figure 9.1: Open loop response of selected variables to a 0.1% step-change in feed H_2/N_2 -ratio.

Figure 9.1 shows the open-loop responses of the synthesis loop to a 0.1% step-change in the feed $\rm H_2/N_2$ -ratio. The reponse is illustrated for the selected controlled variables ($T_{bed1:3, in}, P_{loop}, F_{f, H_2}$, and $R_{\rm H_2/N_2}$). The upper left plot shows the step change in feed $\rm H_2/N_2$ -ratio, illustrating that the ratio is slightly deviating from the stoichiometric value due to differences in solubility of hydrogen and nitrogen in ammonia. The bed inlet temperatures respond modestly, with changes of less than 1 K. The loop pressure exhibits a slightly larger increase of about 1 bar, which in turn reduces the hydrogen feed flow, as the higher compression ratio is offset by reduced flow at constant compressor power.

As expected, the reactor H_2/N_2 -ratio, R_{H_2/N_2} , exhibits a significant response, increasing from approximately 2.7 to 3.2. This corresponds to a gain of about 150 from the external to the internal loop H_2/N_2 -ratio. Such a large increase in R_{H_2/N_2} reduces reactor conversion, which in turn increases the overall loop flow, as shown in the lower-left plot. The large gain between the external and internal H_2/N_2 -ratios suggests that these variables should be paired in the control structure.

It is worth noting that the transients induced by changes in the external H₂/N₂-ratio have

relatively slow time constants, on the order of several hours. Therefore, the slow sampling time of the reactor H_2/N_2 -ratio, discussed in Section 8.4, is less problematic. Based on these observations, the subsequent step-response analysis focuses on the remaining manipulated and controlled variables.

Figures 9.2-9.4 show the open-loop responses of the controlled variables (CVs: $T_{bed1:3, in}$, P_{loop} , F_{f, H_2}) to 1% step changes in the reactor feed splits and eHex1 bypass (MVs: q_{ex} , q_{R1} , q_{R2}). Changing the reactor split fractions and eHex 1 bypass primarily affect the reactor bed inlet temperatures.

In Figure 9.2, a negative step change in the eHex1 bypass produces a positive change in the bed inlet temperatures. This is expected, since reducing the eHex1 bypass fraction increases the reactor feed temperature (stream 10 in Figure 6.1). Because the valve dynamics are modeled with algebraic equations, the initial change in the reactor bed temperatures is instantaneous. This immediate increase propagates through the reactor beds, producing the subsequent transient rise in temperatures.

Similarly, step changes in q_{R1} and q_{R2} cause instantaneous shifts in the bed inlet temperatures, followed by continuous transients toward a new steady state. Some of these responses display notable nonlinear behavior. In particular, the responses from q_{R1} to $T_{bed2,\ in}$ and $T_{bed3,\ in}$ exhibit an initial inverse response within the first five minutes after the step change. Inverse responses can complicate closed-loop control design, highlighting the importance of careful loop pairing.

Finally, Figure 9.4 shows that $T_{bed3,\ in}$ exhibits a pronounced instantaneous inverse response, followed by a slower transient in the opposite direction.

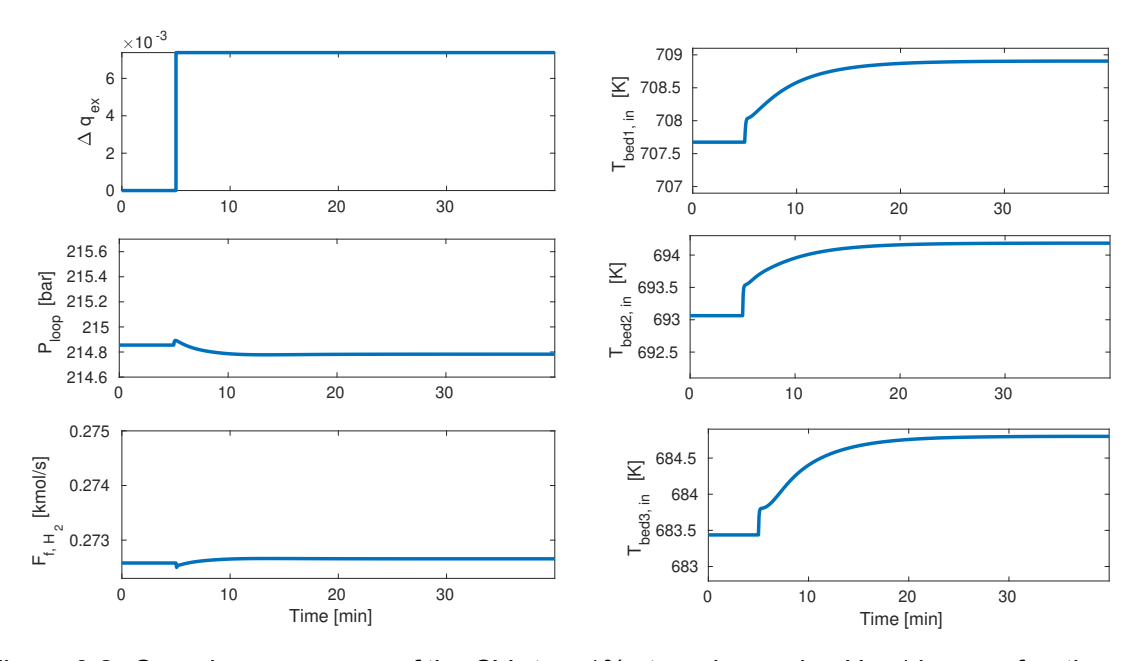


Figure 9.2: Open loop response of the CVs to a 1% step-change in eHex1 bypass fraction.

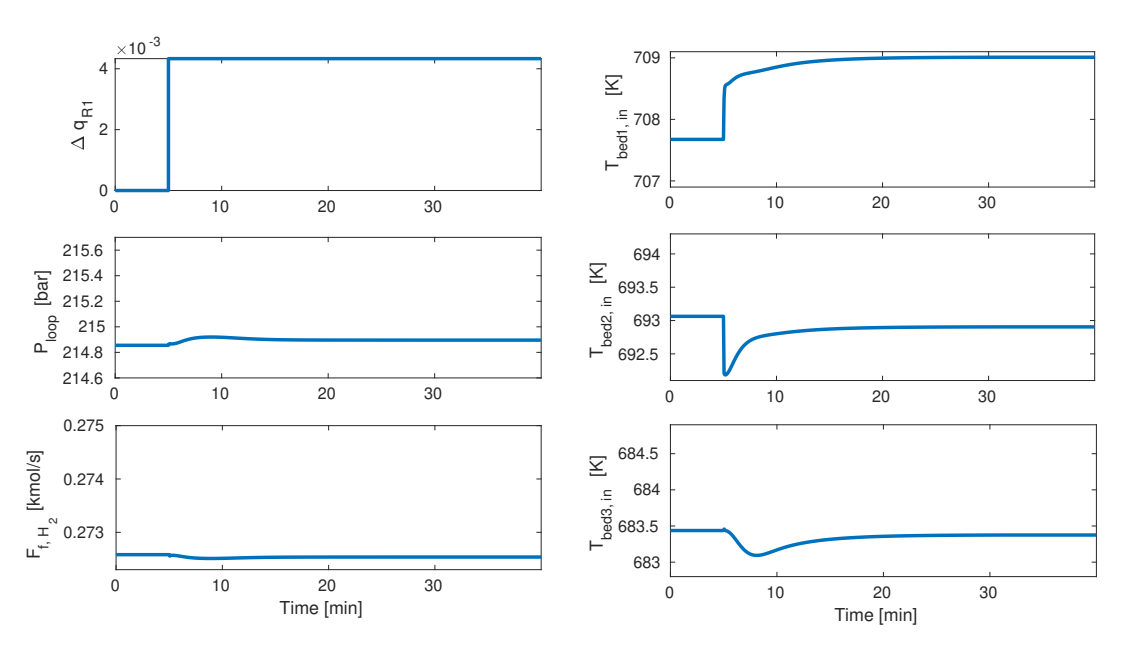


Figure 9.3: Open loop response of the CVs to a 1% step-change in reactor feed split 1, q_{R1} .

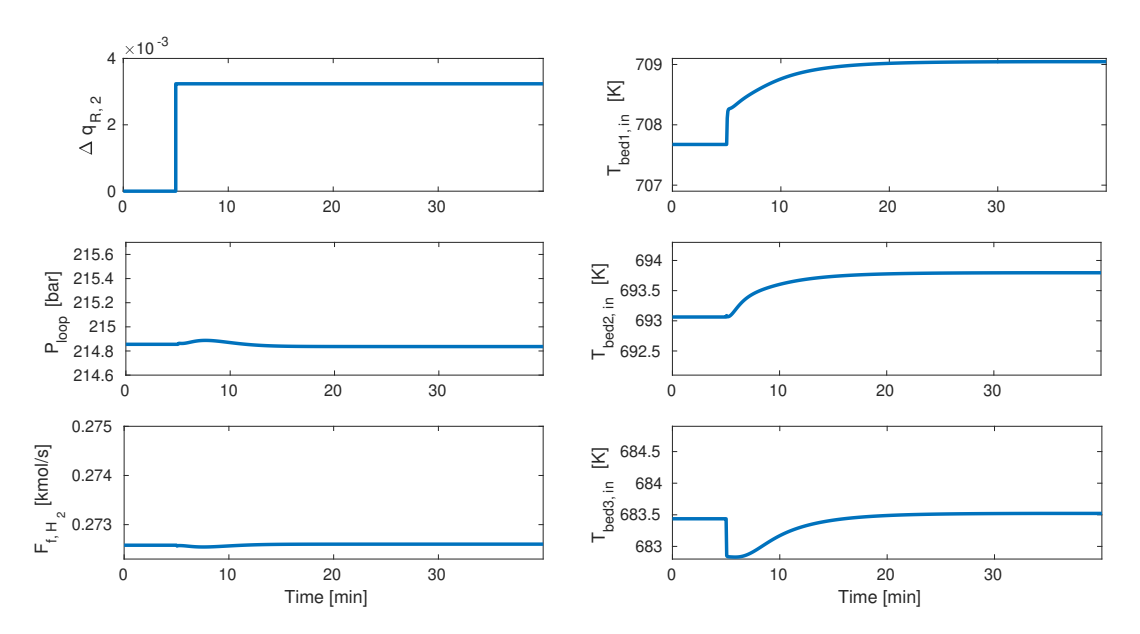


Figure 9.4: Open loop response of the CVs to a 1% step-change in reactor feed split 2, q_{R2} .

Figures 9.5–9.6 show the open-loop responses of the controlled variables to 1% step changes in the feed compressor power, $P_{feedcomp}$, and the loop compressor power, $P_{loopcomp}$.

Changing the feed compressor power has a pronounced impact on all controlled variables (Figure 9.5). The hydrogen feed flow rises almost instantaneously, as compressor dynamics are much faster than the reactor dynamics. This triggers a cascade of effects: the increased feed flow raises the loop pressure as more molecules are introduced into the loop. Higher loop pressure shifts the reactor equilibrium toward the product side, increas-

ing reactant conversion and causing the observed rise in reactor bed inlet temperatures. The higher pressure also induces a slight, gradual reduction in hydrogen feed flow after the initial peak. Eventually, the increased conversion balances the higher make-up feed rate, and a new steady state is reached.

A 1% step change in the recycle compressor power (Figure 9.6) produces smaller effects but still influences all controlled variables. The mechanisms are similar to those for the feed compressor, but partly reversed. Increasing the recycle compressor power initially increases loop circulation flow, leading to a higher absolute ammonia production rate. Since most of this ammonia is quickly removed via condensation, the total molecular hold-up in the loop decreases. This explains the drop in loop pressure when the loop compressor power increases. The reduced loop pressure slightly increases hydrogen feed flow, but also lowers per-pass reactant conversion, resulting in the observed decrease in reactor bed inlet temperatures.

These cause-and-effect sequences are summarised in the following lists:

• Figure 9.5 — Feed compressor power step

- ↑ $P_{feedcomp}$ \Rightarrow ↑ F_{f, H_2} (fast compressor dynamics)
- ↑ F_{f, H_2} ⇒ ↑ P_{loop} ⇒ ↑ reactor conversion (equilibrium shift)
- ↑ Reactor conversion \Rightarrow ↑ Bed temperatures, $T_{bed1:3, in}$
- Slight $\downarrow F_{f,\, {\rm H_2}}$ after initial peak due to higher P_{loop} reducing flow for constant compressor power

• Figure 9.6 — Loop compressor power step:

- ↑ $P_{loopcomp}$ \Rightarrow ↑ Loop circulation flow
- − ↑ Loop circulation flow \Rightarrow ↑ Ammonia formation per pass \Rightarrow faster removal via condensation \Rightarrow ↓ Loop molecular hold-up \Rightarrow ↓ P_{loop}
- ↓ P_{loop} ⇒ slight ↑ $F_{f, \, \mathsf{H_2}}$ but ↓ reactor per-pass conversion ⇒↓ $T_{bed1:3, \, in}$

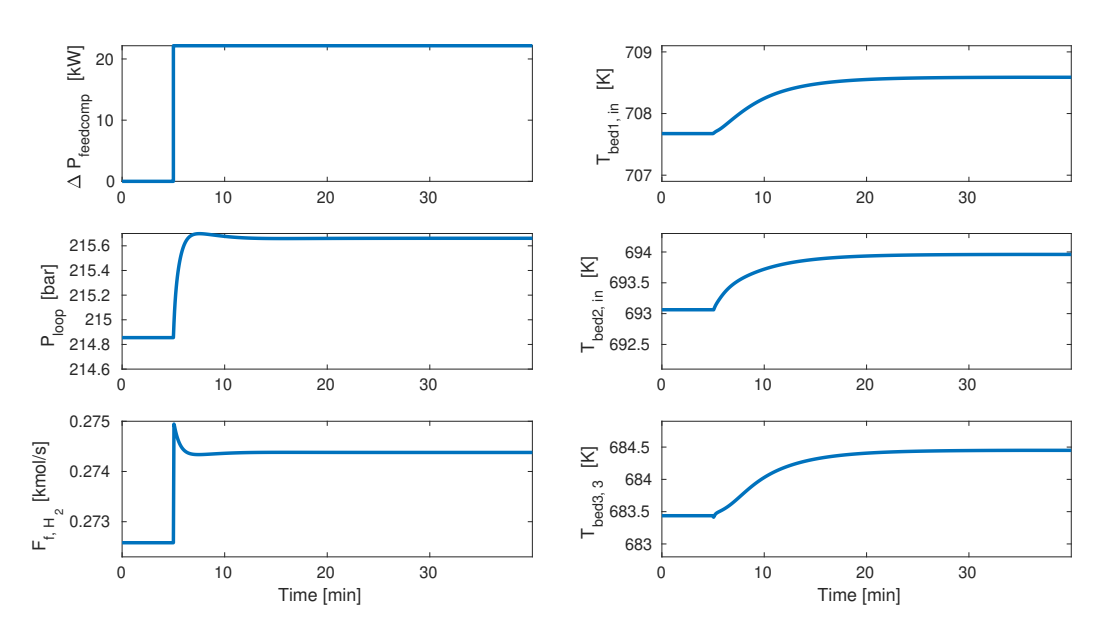


Figure 9.5: Open loop response of the CVs to a 1% step-change in feed compressor power.

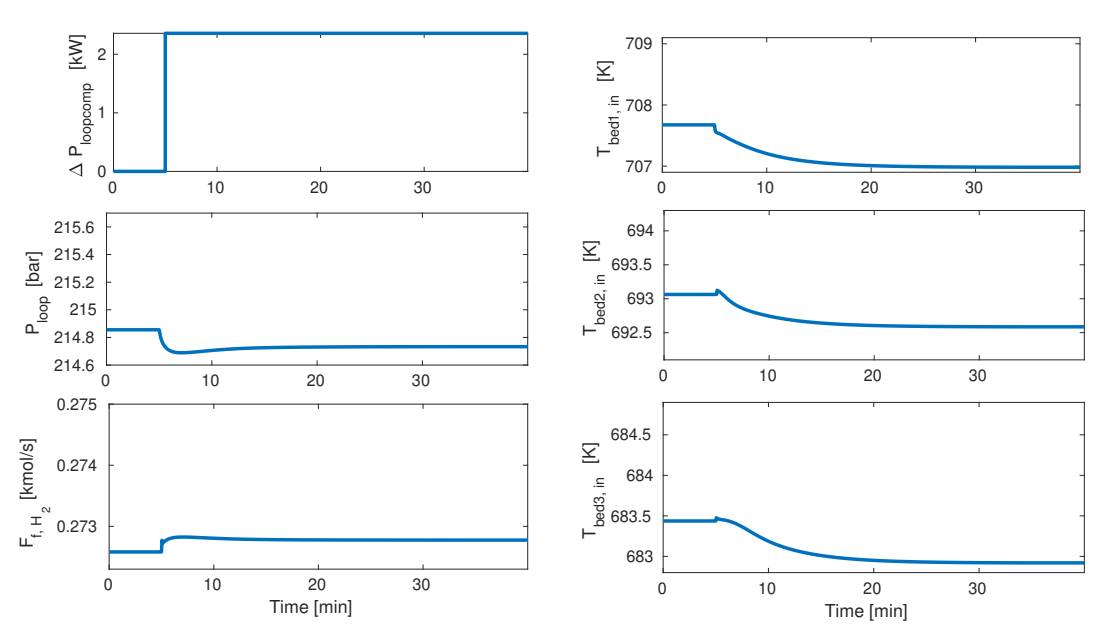


Figure 9.6: Open loop response of the CVs to a 1% step-change in loop compressor power.

9.3 Open-loop load change

The step responses discussed earlier indicate that among the manipulated variables, the synthesis loop load (hydrogen make-up feed flow) is most sensitive to changes in feed compressor power. Consequently, reducing the hydrogen load can be achieved by lowering the feed compressor power. Figure 9.7 illustrates the system response to sequential 3% reductions in feed compressor power to achieve low-load operation. The first two

reductions decrease the hydrogen load to approximately 97.5% and 95% of nominal hydrogen make-up feed flow. Simultaneously, both loop pressure and reactor bed inlet temperatures decline, consistent with the mechanisms described in Section 9.2.

However, after a cumulative 9% reduction in feed compressor power, the reactor system becomes unstable as the lower bed inlet temperatures and loop pressure fail to sustain thermal equilibrium. The resulting reduction in per-pass conversion increases recycle flow, further reducing conversion and reinforcing this feedback loop. This accelerates the drop in reactor feed temperature, and ultimately, the loop pressure begins to rise as conversion falls below the make-up feed rate, causing material accumulation in the loop. At this point, the catalyst beds are too cold to reignite, leading to reactor extinction and continuous recycling of unreacted gas.

These open-loop simulations underscore the necessity of a robust control architecture to enable safe and efficient load-flexible operation of the ammonia synthesis loop.

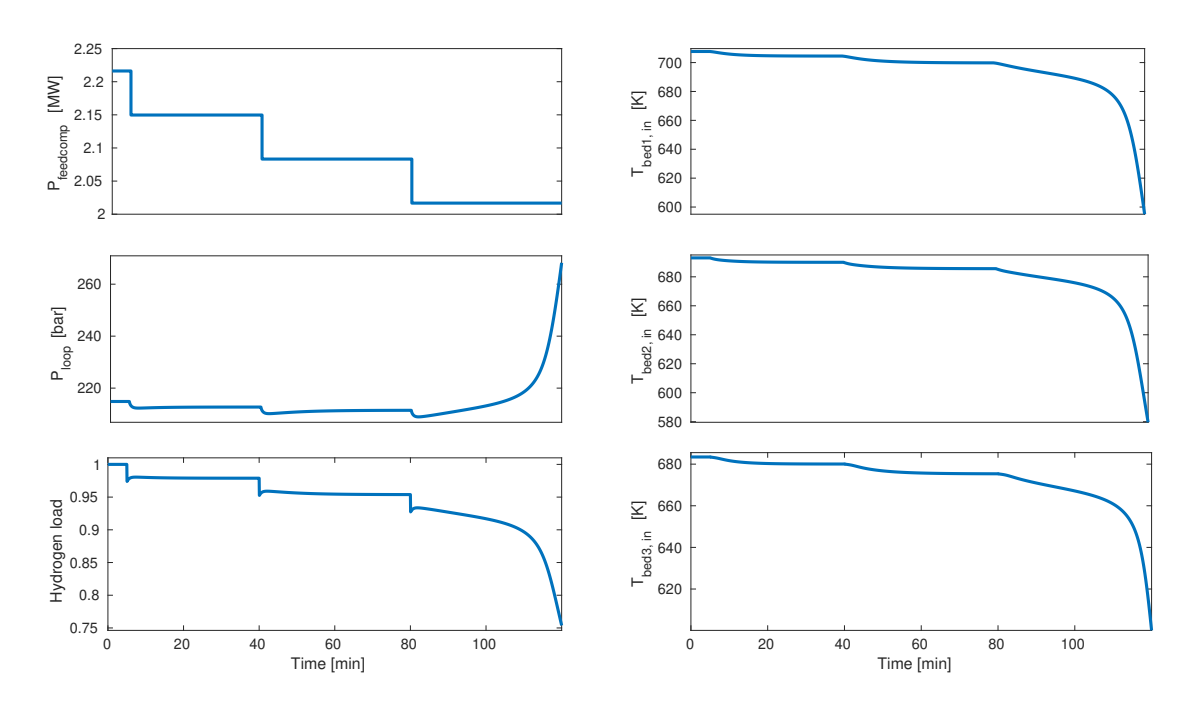


Figure 9.7: Open loop response of the CVs to a 1% step-change in loop compressor power.

9.4 Conclusion

This chapter presented open-loop simulations of the Haber–Bosch synthesis loop with an AICR reactor, focusing on the dynamic response of key process variables to step changes in the manipulated inputs. The results highlighted strong nonlinear dynamics and pronounced cross-coupling across the system, with several input–output responses exhibiting inverse behaviour.

The step-response analysis showed that the hydrogen make-up feed flow is highly sensitive to the feed compressor power. Sequential reductions in compressor power initially lowered the hydrogen load as expected, but also caused loop pressure and reactor bed inlet temperatures to fall. Already for a 9% power reduction, the system became unstable, ultimately leading to reactor extinction.

Overall, the findings underscore the challenges of operating the synthesis loop flexibly under variable renewable input. They also emphasise the need for carefully designing the control structure based on the open-loop responses.

Chapter 10

Control of a Haber-Bosch synthesis loop for load-flexible operation

This chapter develops and evaluates a control architecture for the Haber–Bosch synthesis loop in the context of flexible Power-to-Ammonia operation. Building on the optimisation and sensitivity analysis in Chapter 8, a control structure is proposed that integrates real-time optimisation with self-optimising control. The hydrogen make-up flow is treated as a controlled variable, with its set-point determined by a higher-level scheduling layer. The pairing of controlled and manipulated variables is based on steady-state gain analysis and relative gain array (RGA). The final control structure incorporates two decoupler matrices to mitigate control-loop interactions.

Dynamic simulations demonstrate that the proposed control system ensures stable operation of the synthesis loop across the full load range (10–120% of nominal feed), while maintaining power efficiency close to the optimal benchmark obtained in Chapter 6. The control structure enables accurate set-point tracking and robust performance, even under rapid load changes of up to 3% per minute.

Thus, this chapter answers research question 4.

This chapter contains material from the article:

-Rosbo, J.W., Jørgensen, J.B., Jensen, A.D., Skogestad, S., Huusom, J.K., (2025). Optimisation and Robust Control of a Load-Flexible Haber-Bosch Ammonia Synthesis Loop. Submitted to Computers & Chemical Engineering

10.1 Introduction

Early studies on the control of ammonia synthesis loops focused primarily on stabilising the reactor under relatively small disturbances, consistent with conventional plant operation (Luyben, 2012; Araújo and Skogestad, 2008; Rovaglio et al., 2001; Straus et al., 2019).

The flexible operation of the Haber–Bosch (HB) process across a wide operating envelope has only recently gained attention in the context of Power-to-Ammonia. Fahr et al. (2025) employed a UniSim® Dynamics simulator to investigate load-change strategies, achieving ramp rates up to 3%/min and stable operation down to 10% load. Similarly, Kong et al. (2024) applied nonlinear MPC to a quench-cooled HB reactor, enabling flexible operation between 50–100% load.

However, these studies did not consider optimal operation of the synthesis loop across the load range. Chapter 8 demonstrated that non-optimal operation of the synthesis loop at reduced load leads to significantly higher power consumption than the optimal benchmark. Building on this, the present chapter defines a control architecture that combines real-time optimisation and self-optimising control as identified in Chapter 8. The aim is to achieve safe, robust, and power-efficient operation of the HB synthesis loop across the full load range from 10% to 120% of the nominal hydrogen make-up feed flow.

10.2 Control architecture design

Considering the open-loop responses presented in Chapter 9, which reveal several complex and non-linear dynamics, designing a control structure for the ammonia synthesis loop is not straightforward. Therefore, a methodical approach is employed in this section to identify the best-performing configuration.

10.2.1 CV/MV pairing

For effective control, the best pairing of controlled and manipulated variables should be identified. As mentioned in Chapter 9, certain controlled and manipulated variable (CV/MV) pairings are intuitively clear. For instance, the liquid level in the flash tank is naturally regulated via the outlet liquid flow, while the total compressor flow is adjusted through the anti-surge valve.

In Chapter 9, it was established that the external feed H_2/N_2 -ratio, $R_{f, \, H_2/N_2}$, is well suited for controlling the internal reactor feed ratio, R_{H_2/N_2} . This is because the gain between the two ratios is large and their dynamics occur on a similar time scale to the slow measurement frequency of gas analysers (see Figure 9.1). Thus, the internal ratio c_6 is regulated via the nitrogen make-up feed flow, u_6 , using a cascade control strategy with the external ratio $R_{f,\,H_2/N_2}$ as the intermediate variable.

The remaining 5x5 system of manipulated and controlled variables is given in Eq. (10.1).

$$\mathbf{u} = \begin{bmatrix} u_1 \\ u_2 \\ u_3 \\ u_4 \\ u_5 \end{bmatrix} = \begin{bmatrix} q_{\text{R1}} \\ q_{\text{R2}} \\ q_{\text{ex}} \\ P_{\text{loopcomp}} \text{ [kW]} \\ P_{\text{feedcomp}} \text{ [MW]} \end{bmatrix}$$

$$\mathbf{c} = \begin{bmatrix} c_1 \\ c_2 \\ c_3 \\ c_4 \\ c_5 \end{bmatrix} = \begin{bmatrix} T_{\text{bed1, in}} \text{ [K]} \\ T_{\text{bed2, in}} \text{ [K]} \\ T_{\text{bed3, in}} \text{ [K]} \\ P_{\text{bed1, in}} \text{ [bar]} \\ F_{f, \text{H2}} \text{ [kmol/s]} \end{bmatrix}$$

$$(10.1a)$$

$$\mathbf{c} = \begin{vmatrix} c_1 \\ c_2 \\ c_3 \\ c_4 \\ c_5 \end{vmatrix} = \begin{vmatrix} T_{\text{bed1, in}} \left[\mathbf{K} \right] \\ T_{\text{bed2, in}} \left[\mathbf{K} \right] \\ T_{\text{bed3, in}} \left[\mathbf{K} \right] \\ P_{\text{bed1, in}} \left[\text{bar} \right] \\ F_{f, \, \text{H}_2} \left[\text{kmol/s} \right] \end{vmatrix}$$

$$(10.1b)$$

For the remaining variables ($c_{1:5}$ and $u_{1:5}$), the optimal CV/MV pairing is not immediately apparent. As shown in Chapter 9, the open-loop step responses of the controlled variables to perturbations in each manipulated variable revealed strong cross-coupling within the system. Changes in any manipulated variable affect all controlled variables, with several input-output responses exhibiting pronounced non-linear dynamics. To determine the most suitable pairings, the steady-state gain matrix, K, and the corresponding relative gain array (RGA) matrix are evaluated. The steady state gains are determined from the step responses in Chapter 9 via,

$$K_{ij} = \frac{\Delta c_i}{\Delta u_j} \tag{10.2}$$

where Δu_i is the size of the input step, and Δc_i is the change in the output from the initial value to the new steady-state. The full gain matrix is,

The RGA is calculated via,

$$\mathsf{RGA} = K \circ (K^{-1})' = \begin{bmatrix} 0.848 & 0.155 & 0.089 & -0.089 & -0.003 \\ 0.195 & 0.936 & -0.328 & 0.189 & 0.007 \\ -0.026 & -0.103 & 1.051 & 0.074 & 0.004 \\ -0.010 & 0.008 & 0.146 & 0.457 & 0.399 \\ -0.008 & 0.003 & 0.043 & 0.369 & 0.592 \end{bmatrix}$$
(10.4)

RGA values close to one indicate favourable candidates for CV-MV pairings (Seborg et al., 2016; Jørgensen and Jørgensen, 2000). Consequently, the RGA suggests a diagonal pairing strategy for the reactor system, yielding the following control pairings: $T_{bed1,in}$ with q_{R1} , $T_{bed2,in}$ with q_{R2} , $T_{bed3,in}$ with q_{ehex} . This pairing is somewhat surprising. Initially, one might expect q_{R1} and q_{R2} to be better suited for controlling $T_{\text{bed2,in}}$ and $T_{\text{bed3,in}}$, respectively, due to their direct coupling through the internal heat exchangers of the reactor. However, as illustrated in the step responses presented in Chapter 9 Figure 9.3-9.2, these pairings exhibit highly non-linear dynamics and ultimately small steady-state gains.

10.2.2 Decoupled system

For controlling the loop pressure and hydrogen feed flowrate, the optimal CV-MV pairing is not immediately evident, as the corresponding elements in the relative gain array (RGA) are close to one-half. This suggests a high degree of interaction between the loops, which potentially leads to competing control actions. To address this issue and reduce loop interaction, a static decoupler matrix, D_{Loop} , is introduced and defined as follows,

$$D_{Loop} = K_{Loop}^{-1} = K_{4:5,4:5}^{-1}$$
(10.5)

where K_{loop} refers to the 2x2 submatrix of K from $u_{4:5}$ to $y_{4:5}$ ($K_{4:5,4:5}$). The control input is then,

$$u_{Loop} = \begin{bmatrix} u_4 \\ u_5 \end{bmatrix} = \begin{bmatrix} P_{\text{loopcomp}} \\ P_{\text{feedcomp}} \end{bmatrix} = u_{Loop, ref.} + D_{Loop} \begin{bmatrix} v_4 \\ v_5 \end{bmatrix}$$
 (10.6)

in which $v_{4:5}$ are the decoupled controller outputs. For the temperature control in the reactor system, the RGA (Eq. 10.4) suggested a diagonal pairing. However, implementing a static decoupler may still enhance control performance by mitigating interaction effects. In Rosbo et al. (2024d), a control structure was implemented with a static decoupler for temperature control of the AICR via manipulations of the reactor feed splits. This approach proved highly effective for controlling the reactor inlet temperatures and reactor operation under varying load conditions. Continuing this strategy, a decoulper matrix of the reactor system, D_{Reac} , is defined,

$$D_{Reac} = K_{Reac}^{-1} = K_{1:3,1:3}^{-1}$$
(10.7)

with K_{Reac} being the 3x3 submatrix of K from $u_{1:3}$ to $y_{1:3}$.

Figure 10.1 illustrates the control structure. With the two decoupled loops, the gain matrix, K_{vy} and the RGA $_{yv}$ from the decoupled inputs v to the measurement y becomes,

$$K_{vy} = \begin{pmatrix} v_1 & v_2 & v_3 & v_4 & v_5 \\ \hline c_1 & 1.02 & 0.01 & 0.004 & 3.81 & -1.20 \\ c_2 & 0.02 & 1.00 & 0.001 & 2.76 & -0.73 \\ c_3 & 0.02 & 0.01 & 1.01 & 3.02 & -0.80 \\ c_4 & 0.02 & -0.07 & -0.04 & 1.04 & -0.03 \\ c_5 & -0.02 & 0.08 & 0.04 & -0.05 & 1.03 \end{pmatrix}$$
 (10.8)

$$\mathsf{RGA} = \begin{bmatrix} 1.07 & 0.001 & 0 & -0.05 & -0.02 \\ -0.01 & 0.830 & 0 & 0.14 & 0.04 \\ -0.01 & -0.01 & 0.90 & 0.08 & 0.02 \\ -0.04 & 0.13 & 0.08 & 0.83 & -0.01 \\ -0.01 & 0.04 & 0.02 & -0.01 & 0.96 \end{bmatrix} \tag{10.9}$$

The decoupled RGA illustrates that the decouplers substantially suppress steady-state cross-coupling effects within the control loops. As shown in Eq. (10.8), the diagonal elements are close to unity, while the off-diagonal elements are near zero, indicating effective static decoupling within the respective loops. Nevertheless, some interaction remains between the two decoupled subsystems. In particular, manipulations of v_4 and v_5 exhibit a significant influence on the bed inlet temperatures ($y_{1:3}$). However, since the interaction from $v_{1:3}$ to $y_{4:5}$ is minimal, this is not expected to introduce competition between the control loops.

It should be noted that evaluating the effectiveness of the decoupling strategy solely through RGA analysis based on steady-state gains may provide a misleading picture, as it does not capture dynamic interactions. A dynamic analysis is therefore essential for a more comprehensive assessment. Therefore, the open-loop responses of the controlled variables to changes in the decoupled MVs $v_{1:5}$ is investigated.

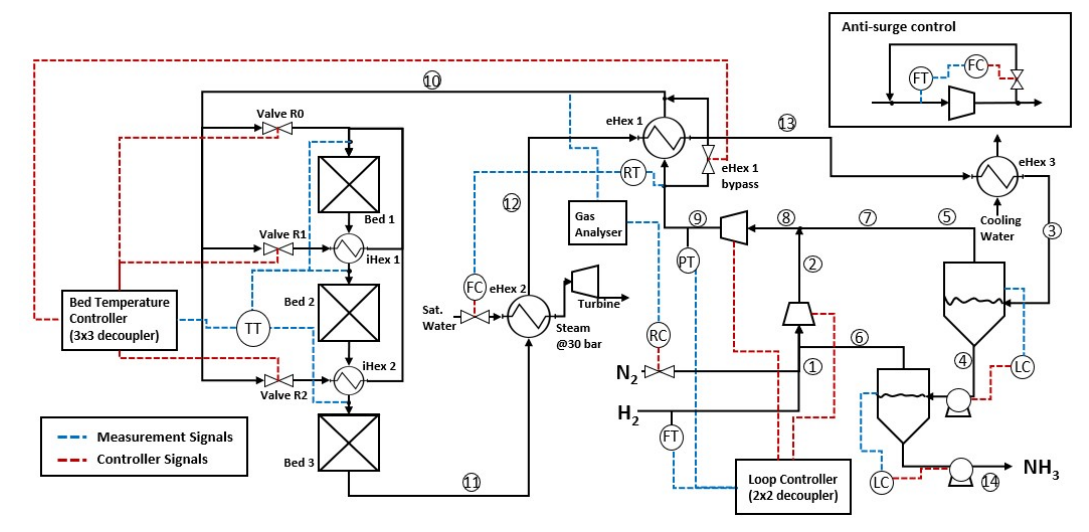


Figure 10.1: Illustration of the employed control structure. Dotted blue lined indicate transmitter signals (measurements), while dotted red lines indicate control signals (inputs). The bed temperature control is performed via a 3x3 decoupler block adjusting the reactor feed valves and eHex1 by-pass valve. The loop pressure and hydrogen synthesis feed flow are transmitted to a 2x2 decoupler block sending control signals to the feed and loop compressors. Level control in the flash tanks is achieved by manipulating the liquid outlet pumps. The size of the eHex1 bypass is adjusted through the amount of water supplied to the rankine cycle. The internal loop N_2/N_2 -ratio (stream 10) is controlled via external H_2/N_2 -ratio in the make-up feed (via cascade control through the nitrogen make-up flow).

Figure 10.2 shows open-loop unit step responses of the decoupled reactor system from $v_{1:3}$ to the bed inlet temperatures. This shows that for the temperature control significant non-linear cross-interactions persist in the bandwidth from 0-6s, especially from v_1 to $T_{bed2,\ in}$ and v_2 to $T_{bed3,\ in}$. Nonetheless, the cross-interactions are significantly reduced for the decoupled system compared to the original system responses shown Chapter 9. In particular, the loop, $T_{bed3,\ in}-v_3$, exhibits nearly decoupled behaviour, allowing it to be controlled with minimal interference. The non-linear cross-interactions $v_1-T_{bed2,\ in}$ and $v_2-T_{bed3,\ in}$ can be effectively managed by tuning the controllers with time constants sufficiently larger than the critical 6-second window, as discussed in Section 10.2.3.

Likewise, Figure 10.3 illustrates step responses from $v_{4:5}$ to the loop pressure and hydrogen feed flow. The response from v_5 to the hydrogen feed flow is effectively decoupled from the loop pressure. However, the response of v_4 exhibits fast cross-interaction with the hydrogen feed within the first 5 seconds. As described in Section 10.2.3, this is adjusted for by tuning the controllers with a sufficiently large time constant to not act on the initial non-linear dynamics.

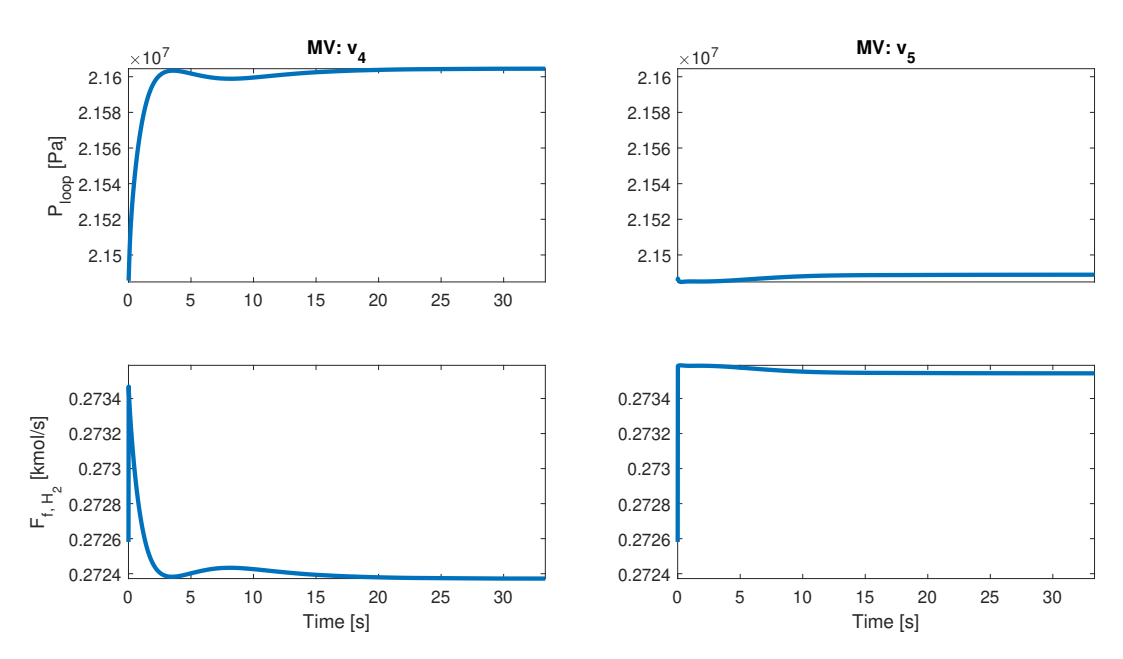


Figure 10.2: Open loop response of the bed inlet temperature to a unit-step in $v_{1:3}$ 0.

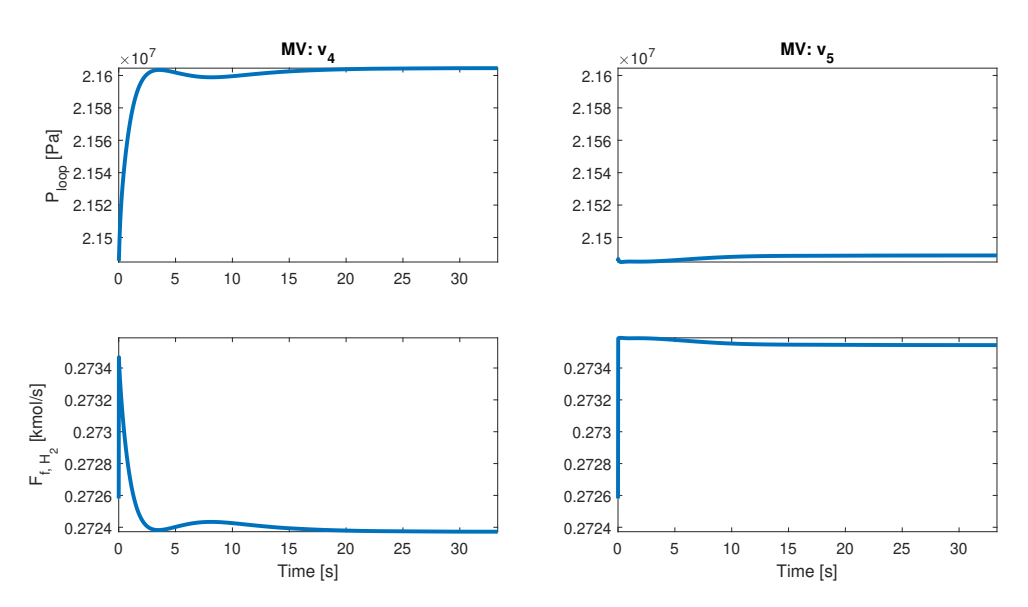


Figure 10.3: Open loop response of the loop pressure and hydrogen feed flow rate to a unit-step in $v_{4:5}$.

10.2.3 Controller tuning

The controller's structure consists of PI controllers tuned with the SIMC tuning rules presented in Skogestad (2004). The controller derivative term, D, is not included in the control laws as the simulated system response contains several instantaneous interactions (arising from pseudo steady-state model assumptions of e.g. heat-exchangers and compressors), which do not comply well with derivative control action. The tuning parameter, τ_c , represents the desired closed-loop time constants. From Figure 10.2 and 10.3 observe that the open-loop responses from $v_{1:3}$ to the bed inlet temperatures and from v_5 to the hydrogen feed flow can be approximated well as pure gain systems. Skogestad (2004) then recommends applying pure integral control,

$$K_I = \frac{1}{K\tau_c},\tag{10.10}$$

where the gain $K \approx 1$ by the decoupler design. The response from v_4 to the loop pressure (c_4) is approximated by a first-order response with a time constant of $\tau_{4,4}=2$ s. The recommended controller for a first-order response is a PI controller with,

$$K_C = \frac{\tau}{K\tau_c}, \qquad \tau_I = \tau. \tag{10.11}$$

The control loops were tuned adjusting τ_c , ensuring that τ_c sufficiently exceeds the duration of the non-linear dynamic interactions discussed in Section 10.2.2. Table 10.2 displays the tuned values for the proportional gain and integral time of the PI control loops, while Table 10.1 displays the integral gain of the integral controllers. The control of the inlet temperature to the first bed is controlled slightly more aggressively ($\tau_c = 20$ s) than the following beds ($\tau_c=40\,$ s). This relates to the initial bed being most important for reactor stability as a potential blow-out of first bed can quickly propagate through the reactor system. The hydrogen feed flow and loop pressure control loops were assigned time constants of $\tau_c=40$ s and $\tau_c=30$ s, respectively. These values enable sufficiently fast control while preventing the controllers from responding too aggressively to the initial non-linear dynamics. In particular, tight control of the loop pressure is desired to adhere to the specified ramping rates. Fast fluctuations in operating pressure can be highly damaging to both the reactor catalyst and the wall structure of the system. Given the high operating pressures of the Haber–Bosch process, even moderate pressure changes can generate substantial mechanical stresses on process equipment. The control loop from T_{S12} to q_{ex} (via the Rankine cycle water flow) ensures that the eHex1 bypass fraction, q_{ex} , is sufficiently far away from saturation (fully open, q_{ex}) for regulating the temperatures across the operating window.

Table 10.1: Tuned variables for the pure integral control loops.

CV	MV	$ au_c$	K_I
$T_{bed1, in}$	v_1	20 s	$0.05 \mathrm{K^{-1} s^{-1}}$
$T_{bed2, in}$	v_2	40 s	$0.025~{\rm K}^{-1}{\rm s}^{-1}$
$T_{bed3, in}$	v_3	40 s	$0.025~{\rm K}^{-1}{\rm s}^{-1}$
F_{f, H_2}	v_5	40 s	$0.05 \; {\rm kmol^{-1}}$
q_{ex}	T_{S12}	180 s	$0.5 {\rm K s^{-1}}$

10.3 Load-flexible operation

The set-point for the hydrogen feed flow is allowed to ramp at 3% of the nominal flow per second, adopting the fast ramping rate from Fahr et al. (2025). Changes in loop operating

Table 10.2: Tuned variables for the PI control loop gains and time constants. *Integral action based on measurement frequency.

CV	MV	$ au_c$	K_c	$ au_I$
$\overline{P_{loop}}$	v_4	30 s	$0.0667~{ m Pa}^{-1}$	2s
R_{H_2/N_2}	$R_{f,H_2/N_2}$	-	0.01	600 s*
$R_{H_2/N_2} \ V_{f,lash1}^l$	$Q_{out, flash1}^{l}$	10 s	0.1	40s
V_{flash2}^{l}	$Q_{out, \ flash2}^{l}$	10 s	0.1	40s

pressure are limited to two bars per minute to limit mechanical stress on the metal structures. Figure 10.4 shows a simulated case for load-flexible operation of the HB synthesis loop across the entire operating window. Initially, the set-point for the hydrogen feed flow is varied from 100% to 70% of the nominal feed flow over a 10-minute ramp. Then the operation is temporarily stabilised at 70% load, before two subsequent 30% load ramps down to 10% load. After an hour of stable operation at the minimum 10% load, the synthesis load is increased to 110% in ramps of 20% load. The set-point for the loop pressure is updated according to the HB-load, but with a slightly more restrictive ramping rate. The bed inlet temperatures are kept constant, complying with the self-optimising control strategy outlined in Section 8.4. Evidently, very efficient control is achieved for the hydrogen feed flow and the loop pressure as the set-points are tracked virtually perfectly. The control of the bed inlet temperatures appears slightly less smooth, as some fluctuations in the inlet temperatures are observed during load ramping. However, the scale on the y-axis shows that the bed inlet temperatures are controlled within \pm 5 K of the set-points. The fluctuations observed in the reactor bed temperatures arise from the nonlinear temperature dynamics of the reactor bed observed from the step responses in the supporting material. The severity of the temperature fluctuations is put into perspective by the simulated time of 14.5 hours, illustrating that the fluctuations are not rapid but occur on a time scale of several minutes.

Figure 10.5 provides a close-up view of hydrogen feed flow and loop pressure response to the initial set-point change in the synthesis loop load from 100% to 70%. It shows that both the hydrogen feed flow and loop pressure trail slightly behind the set-point, a natural characteristic of feedback control, which responds with some delay. The absence of overshoot at the end of the load change indicates that the controllers are not overly aggressive. This slightly conservative tuning is likely advantageous in PtA systems, as it prevents rapid changes in operating conditions during load transitions.

Figure 10.6 shows the anti-surge control of the feed and loop compressors for the load changes in Figure 10.4. Recall, the compressor stages compromise two parallel compressor trains. One compressor train is taken offline when the total combined compressor flow (middle plots) falls below 65% of the total nominal flow. This causes the sudden increase in flow through the remaining active compressor train shown in the plots on the right. The anti-surge recycle flow (left plots) activates for compressor flow below 65% of the nominal value for the single train. The anti-surge control is performed via PI control, which quickly adjusts the compressor flow to the anti-surge boundary when necessary. As feedback control is applied, some violation of the compressor surge boundary occurs. However, recall from the definition of the operating limits in Section 6.2.4 Figure 6.4 that the operating window is defined with some safety margin to the surge boundary. Thus, small violations of the assigned compressor operating window are acceptable.

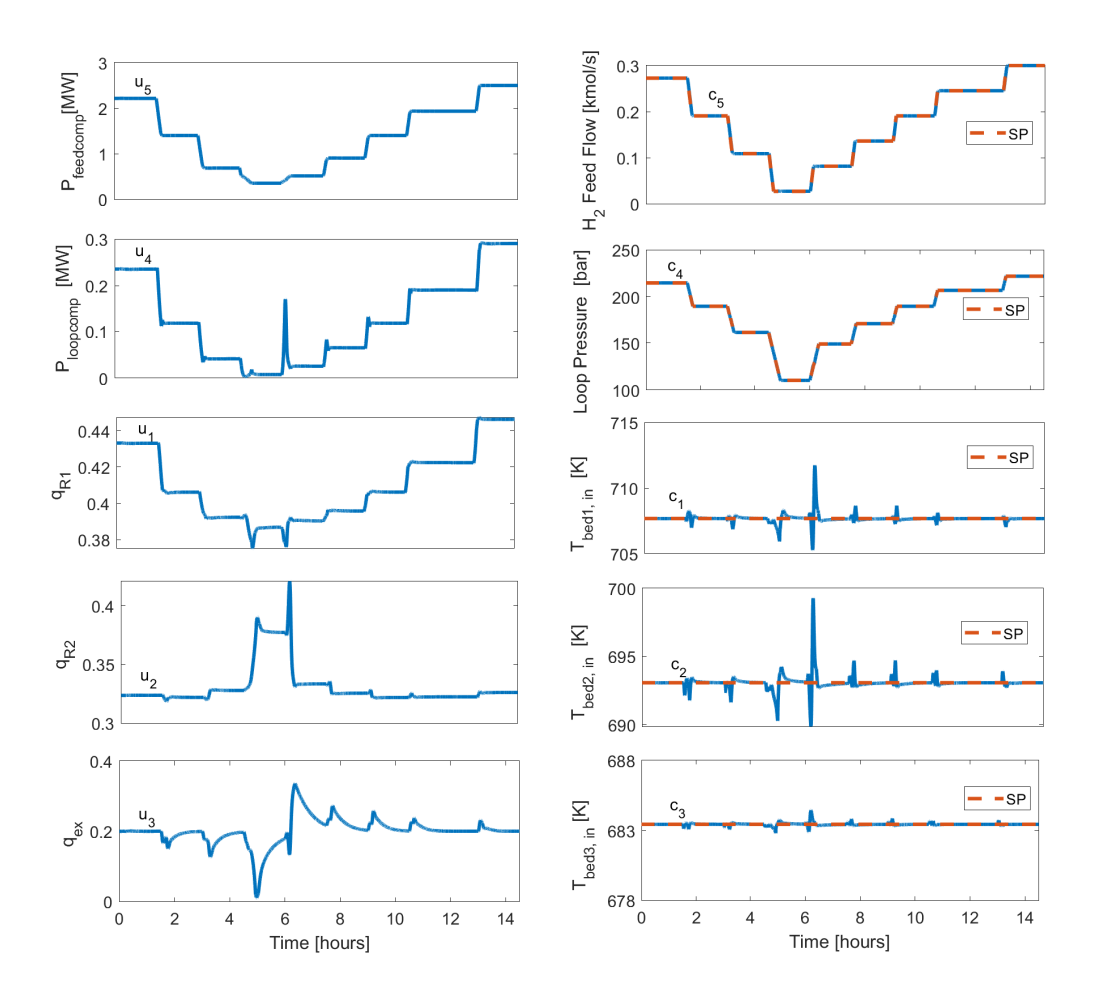


Figure 10.4: Simulated load-flexible operation of the Haber-Bosch Process. Left: manipulated variables of feed compressor power, loop compressor power, eHex1 bypass, and reactor feed split fractions. Right: controlled variables of synthesis hydrogen feed flow, loop pressure, and bed inlet temperatures.

Figure 10.7 shows the control of the eHex1 bypass fraction via the temperature of Stream S12 as the hydrogen load is adjusted according to Figure 10.4. The controller is acting slowly as the temperature of Stream S12 cannot be manipulated fast (due to the indirect control via the Rankine cycle). However, the control is sufficiently fast to avoid saturation of the bypass ($q_{ex}=0$). and keeps the bypass fraction around the desired value of 20%.

Figure 10.8 displays the control of the reactor H_2/N_2 -ratio based on simulated gas analyser measurements with a 10-minute sampling interval (red dots). The controller operates with an equally slow control loop time constant. Nevertheless, the controller maintains the internal H_2/N_2 -ratio relatively close to the set-point, facilitating near-optimal operation as described in Section 8.4.

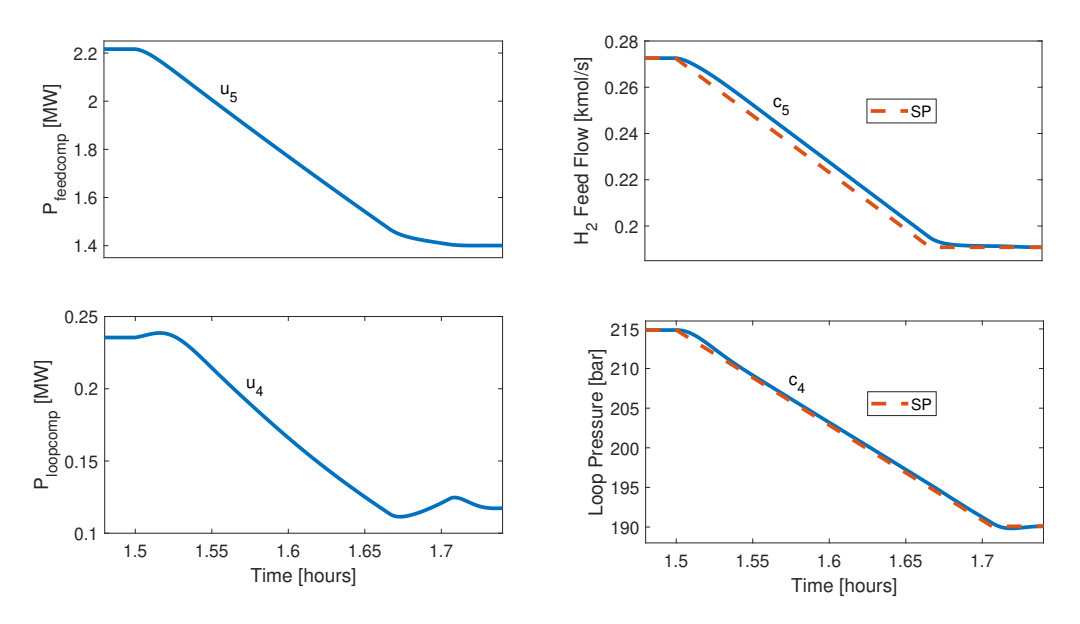


Figure 10.5: Close-up view of hydrogen feed flow and loop pressure response to the initial set-point change in the synthesis loop load from 100% to 70%.

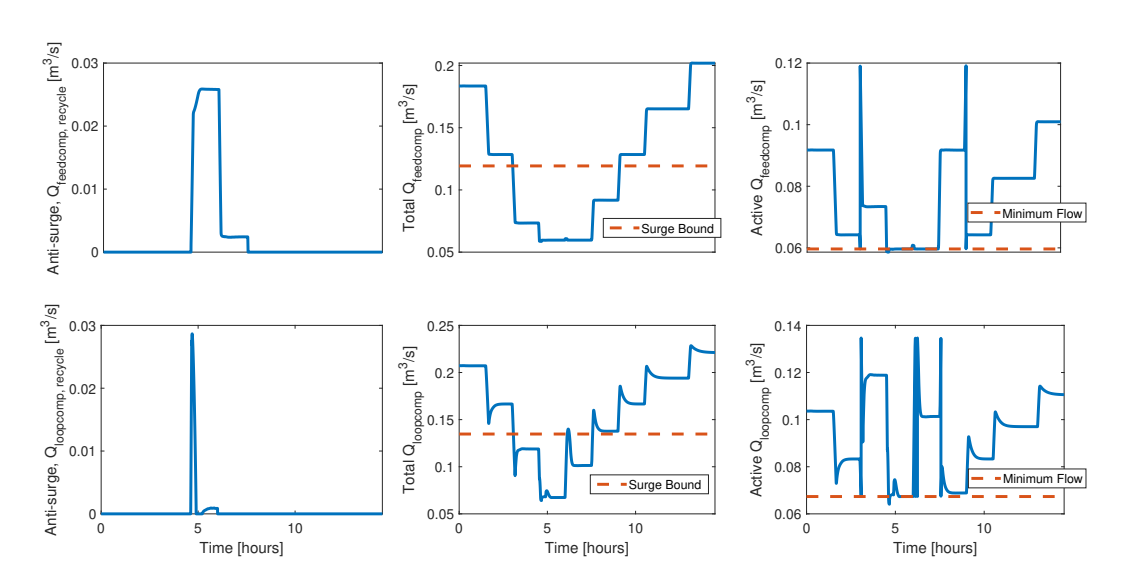


Figure 10.6: Compressor flows during for the load-flexible operation shown in figure 10.4. Left: manipulated variables of compressor anti-surge recycle flow. Middle: Total compressor flow for all active compressors. One compressor train is deactivated at the defined surge boundary (65% of nominal flow). Right: Individual compressor flow for the active compressors. The anti-surge recycle controller activates when the flow across the last remaining active compressor falls below 65% of the individual nominal flow (corresponding to 32.5% of the total nominal flow for the two parallel compressor train case).

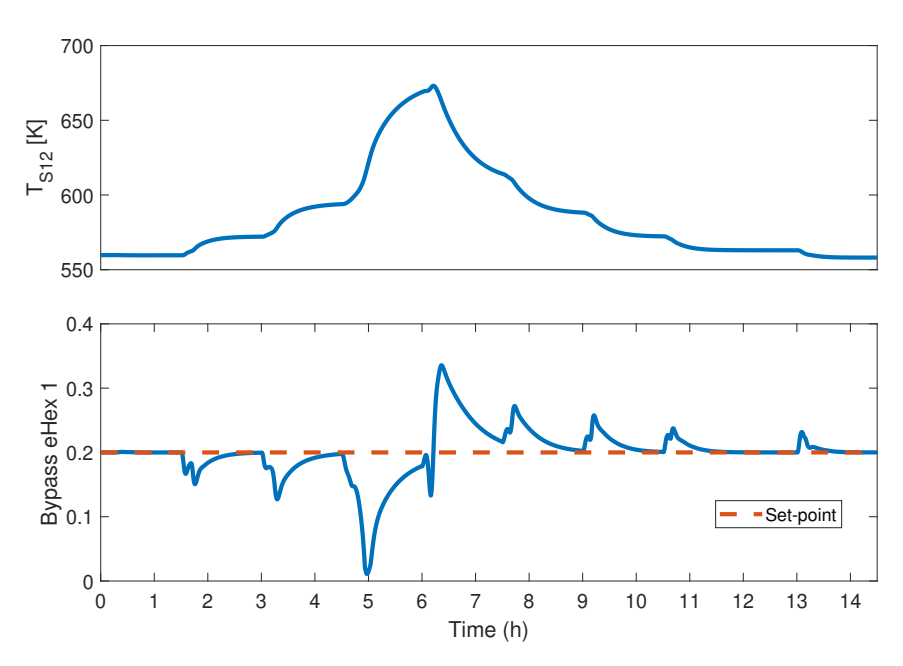


Figure 10.7: Control of the eHex1 bypass through the temperature of Stream 12 for the load changes shown in figure 10.4.

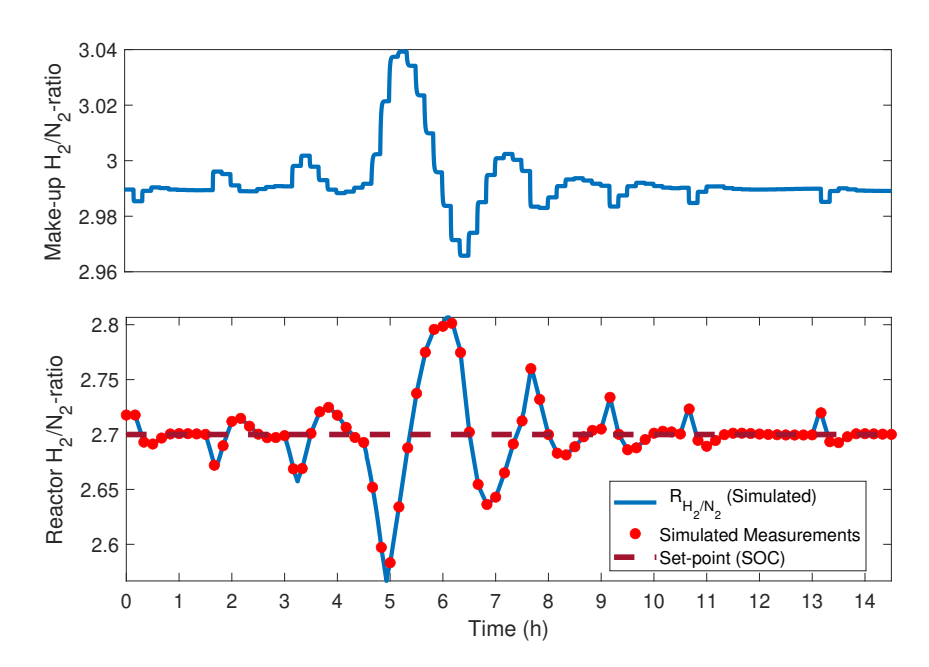


Figure 10.8: Control of the H_2/N_2 -ratio in the reactor feed via manipulation of the feed H_2/N_2 -ratio for the load changes shown in figure 10.4.

Maximum load-change

From an operational perspective, PtA plant operators may require rapid transitions between full load and the minimum load operating point to accommodate fast fluctuations in the renewable energy supply. Figure 10.9 illustrates such a controlled load change from 100% to 10% of nominal hydrogen feed flow, using a ramping rate of 3% per minute. The system is stabilised at minimum load for 1.5 hours before ramping up to 120% load. Both ramp-down and ramp-up phases exhibit stable and well-regulated dynamics, demonstrating the effectiveness of the proposed control strategy under large load variations.

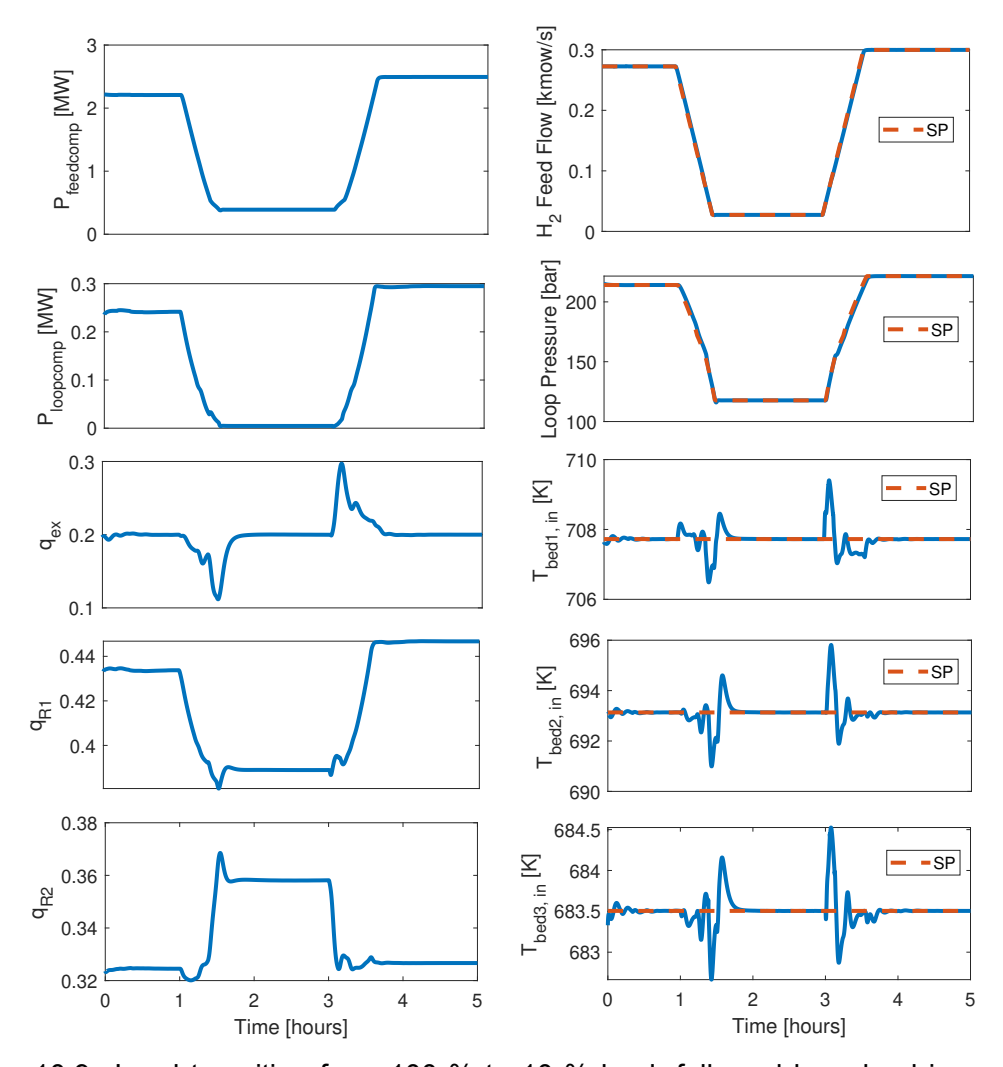


Figure 10.9: Load transition from 100 % to 10 % load, followed by a load increase to 120 %. Left: manipulated variables of feed compressor power, loop compressor power, eHex1 bypass, and reactor feed split fractions. Right: controlled variables of synthesis hydrogen feed flow, loop pressure, and bed inlet temperatures.

10.4 Conclusion

This chapter showed that safe and efficient load-flexible operation of the Haber–Bosch synthesis loop is achievable with a well-designed control architecture. By combining real-time optimisation with self-optimising control, the system continuously adapts to changing operating conditions and maintains performance close to the fully re-optimised case. Importantly, the use of decoupling and careful CV–MV pairing ensured robust behaviour despite the strong process interactions identified in Chapter 9.

Dynamic simulations confirmed that the architecture tracks load set-points accurately from minimum load at 10% to overload conditions at 120% of nominal capacity with fast ramp rates of up to 3% per minute. These results demonstrate a viable path towards realising flexible Power-to-Ammonia plants that can integrate seamlessly with intermittent renewable energy.

Chapter 11

Discussion

This chapter presents an overall discussion of the thesis's main findings, with particular attention to the modelling assumptions and their impact on the proposed optimisation strategies and control concepts for flexible Haber–Bosch operation in Power-to-Ammonia plants. The discussion also considers the integration of these strategies with upstream PtA units, including electrolysers and air separation units, and how system-wide interactions influence plant flexibility. In addition, the broader implications of the results are explored in the context of other hydrogen-based and electrified processes. Finally, the chapter outlines next steps towards realising PtA in practice, emphasising the importance of demonstration projects and the further development of advanced control and optimisation strategies.

11.1 Operating window

The reader may have observed that the operating windows considered throughout this thesis varied slightly: 20–120% in Chapter 4, 30–130% in Chapter 5, and 10–120% in Chapters 6–10. This evolution reflects both the state of the art in the literature at the time the work was conducted and the process insights gained during the project.

At the start of this work in 2022, most scheduling and techno-economic studies assumed minimum loads of 20% for the Haber–Bosch synthesis loop in PtA plants (Armijo and Philibert, 2020; Schulte Beerbühl et al., 2015; Nayak-Luke et al., 2018; Nayak-Luke and Bañares-Alcántara, 2020; Salmon and Bañares-Alcántara, 2023). Some studies applied even more conservative ranges, limiting part-load operation to 50% or higher (Fischer and Freund, 2020; Allman et al., 2017). Despite these differences, all studies agreed that increased flexibility significantly reduces the levelised cost of green ammonia.

However, at that time, very few works addressed the dynamic feasibility of such significant load reductions. Cheema and Krewer (2018) suggested achieving $\approx 33\%$ load by operating at highly non-stoichiometric H_2/N_2 ratios, while earlier dynamic studies by Araújo and Skogestad (2008) and Luyben (2012) demonstrated only minor load reductions (around 15%). This highlighted a research gap in developing strategies for stable and dynamic operation down to 20% load, as often assumed in scheduling studies.

Chapter 4 addressed this gap, demonstrating dynamic and stable operation of an AQCR system from 20–120% hydrogen load using a regulatory control structure combined with real-time optimisation for reactor set-points (Rosbo et al., 2023a). The overload operation of 120% is consistent with the optimal solution to the sizing and scheduling studies presented in Armijo and Philibert (2020) and Maggi et al. (2023). Although a simplified model was used for the synthesis loop, the results illustrated key challenges for flexible operation, such as ramping constraints and reactor blowout.

In Chapter 5, the three general reactor types (AQCR, AICR, IDCR) were compared across a window of 30–130% reactor load (RL), defined relative to reactor feed flow. It is important to distinguish this from the synthesis loop hydrogen load (HL), defined relative to make-up hydrogen feed. The two metrics are linked through the reactor hydrogen conversion, as expressed in Equation 11.1, Thus, the choice of investigating the operation window from 30% to 130% was based on the idea, that the reactor flow changes less across the operating window than the make-up feed flow as illustrated in Fahr et al. (2023) and Rosbo et al. (2023a). However, this depends on how the reactor is operated, as the hydrogen conversion rate of the reactor gives the relationship between the internal reactor load and external hydrogen load. For a given reactor hydrogen conversion, $X_{Rn,\ H_2}$, and reactor hydrogen feed flow $F_{Rf,\ H_2}$, the hydrogen load is,

$$HL = \frac{F_{f, H_2}}{F_{fn, H_2}} = \frac{X_{R, H_2} F_{Rf, H_2}}{X_{Rn, H_2} F_{Rfn, H_2}} = \frac{X_{R, H_2}}{X_{Rn, H_2}} RL$$
(11.1)

where X_{Rn,H_2} is per-pass hydrogen conversion and F_{Rf,H_2} the reactor hydrogen feed flow. Because optimisation in Chapter 5 increased per-pass hydrogen conversion at low RL, the variation in HL was narrower, approximately 40–125%. While this differs slightly from the intended hydrogen load range, the qualitative findings remain valid and can be extrapolated to lower loads.

This analysis underscores the importance of considering the entire synthesis loop dynamics when determining feasible operating windows. As Chapter 6 showed, minimum load operation is most effectively obtained by simultaneously reducing reactor feed flow and loop pressure, lowering both X_{Rn,H_2} and F_{Rf,H_2} .

Recent studies further motivated this broader perspective. For example, Smith and Torrente-Murciano (2024) demonstrated that extending flexibility down to 10% load can further lower the levelised cost of ammonia, while Fahr et al. (2025) successfully demonstrated safe dynamic operation between 10–100% load. Consequently, the final contribution of this thesis (Rosbo et al. (2025a)) investigated optimal HB-loop operation across 10–120% hydrogen load, reflecting the latest flexibility targets for PtA systems.

11.2 Model assumptions

Several simplifying assumptions were made in the development of the synthesis loop model. The assumptions of the bed model were already discussed in the model validation section (4.7). There, it was shown that the model reproduced industrial data with high accuracy under conventional operating conditions (loop pressure >200 bar). However, moderate deviations were observed when benchmarking against the low-pressure case presented in Shamiri and Aliabadi (2021). Since all beds were operating close to equilibrium, this suggested that the Temkin–Pyzhev rate expression does not fully capture the equilibrium behaviour of ammonia synthesis at pressures near 100 bar.

This observation is relevant in the context of Chapter 6, where the optimal loop pressure was shown to gradually decrease across the operating window, reaching approximately 100 bar at 10% load. This finding motivates the use of more comprehensive equilibrium expressions valid over a wider pressure range. Nevertheless, small modelling errors such as deviations in equilibrium prediction are unlikely to significantly affect the identified optimal operation. As shown in Chapter 8, the essence of the self-optimising control strategy is to maintain near-optimal performance even in the presence of modelling errors or disturbances. While equilibrium deviations were not specifically tested as disturbances, other perturbations influencing reactor conversion per pass (such as argon content in the feed and separator temperature) demonstrated the robustness of the self-optimising control strategy. Ultimately, this robustness stems from the fact that recycle compressor work is small compared to feed compressor work, meaning that disturbances in per-pass conversion have limited impact on total power consumption.

In the full synthesis loop model, heat exchangers and the rotating parts of compressors were described using steady-state equations, assuming that their dynamics are fast compared to those of the reactor beds. For compressors, this assumption is valid, since rotational acceleration and deceleration occur on a timescale of seconds. For heat exchangers, however, the relatively thick pressure shells required at high operating pressures introduce thermal inertia. This inertia would smooth the pure-gain behaviour observed in the dynamic responses of Chapter 9. Incorporating heat-exchanger thermal inertia would therefore likely simplify, rather than complicate, the reactor dynamics. Moreover, the proposed control structure was designed with conservative gains to avoid amplification of inverse responses at the reactor bed inlets, meaning that potential fast heat-exchanger dynamics would not compromise control system stability.

Finally, the heat transfer coefficients (U) of heat exchangers were assumed constant across the operating window. In reality, U depends on operating conditions such as flow velocity, viscosity, density, and temperature, all of which vary during flexible operation. For example, Fahr et al. (2023, 2025) modelled U as proportional to the molar flows on both sides of the exchanger raised to the power of 0.7. Furthermore, Fahr et al. (2023) showed that heat recovery could constrain minimum-load operation, while Fahr et al. (2024) proposed heat-exchanger design adaptations to overcome this limitation.

For the operating strategy proposed in this study, reactor outlet temperatures decrease

at low loads. This occurs because the inlet temperatures remain fixed while the perpass conversion falls due to reduced operating pressure. As a result, the driving force for heat recovery in the exchangers is diminished. However, this is partially offset by a simultaneous reduction in reactor flow, which increases the relative exchanger area per unit flow.

These effects are ultimately managed through adjustment of the bypass fraction around the feed–effluent heat exchanger (Figure 6.1: eHex1). As shown in Figure 10.7, the bypass fraction approaches full closure at low hydrogen loads, indicating that heat recovery would become a limiting factor without this adjustment. The corresponding rise in the temperature of stream S12 suggests a modest reduction in heat withdrawn to the steam cycle, which avoids saturation of the eHex1 bypass. In the case of a load-dependent heat transfer coefficient, the same bypass mechanism would compensate automatically, ensuring that heat-recovery limitations are avoided by the control structure design.

11.3 Integration with the entire PtA process

This study focused specifically on the ammonia synthesis loop, whereas the complete PtA process also comprises electrolysis, air separation, and reactant storage, as illustrated in Figure 2.3 in Chapter 2. The decision to isolate the synthesis loop was based on two main arguments. First, the electrolyser and air separation unit are not expected to limit the load-switching rate of the PtA plant. Instead, the flexibility of the synthesis loop ultimately dictates the overall PtA flexibility. Second, the synthesis loop design employed in Chapter 6, which omitted a purge stream, effectively decoupled loop optimisation from the other PtA units. As a result, the optimisation results presented in this work are largely independent of the chosen electrolyser technology (alkaline, PEM, or solid oxide) and air separation technology (cryogenic or pressure swing adsorption).

Flexible operation of air separation units (ASUs) is currently being developed on an industrial scale. Linde reports that their flexible ASU systems can ramp between 20% and 100% load within approximately ten minutes (Linde, 2023; Klein et al., 2021). This ramping capability is of the same order of magnitude as the demonstrated load-change rate of 3% per minute for the HB synthesis loop, suggesting that both units can follow each other without major bottlenecks.

Electrolysers, on the other hand, operate in a different frequency domain. State-of-theart alkaline and PEM systems have been reported to cover load ranges of 10–110% with ramping rates (up or down) of approximately 10% per second (Weiss and Ikäheimo, 2024; Schmidt et al., 2017; Graber et al., 2024; Siemens Energy, 2020). These dynamics are sufficient to follow fluctuations in renewable power generation from wind and solar sources in real time.

This contrast in dynamic response times between the electrolyser and the HB synthesis loop (and ASU) has important implications. While electrolysers can seamlessly follow second-by-second variations in renewable supply, the HB synthesis loop can only adjust on a slower timescale. To fully exploit the fast-response capability of electrolysers, a hydrogen storage system is therefore required. Storage acts as a buffer that absorbs short-term fluctuations in renewable generation, while the HB loop follows the smoothed load trajectory on its slower timescale. For example, if the HB synthesis loop can safely ramp at 3%/min, a full load change from 100% to 10% load requires 30 minutes. Electrolysers can achieve the same change in under 10 seconds. Without buffering, this mismatch would lead to curtailed renewable power. Hydrogen storage equivalent to 15–30 minutes of full-load operation is sufficient to bridge this gap. Figure 11.1 illustrates this dynamic.

The electrolyser ramps down from 100% load to 10% load within seconds, while the HB synthesis loop requires 30 minutes for the load changes. The area between the load curves of the electrolyser and the HB-loop represents the required size of the storage.

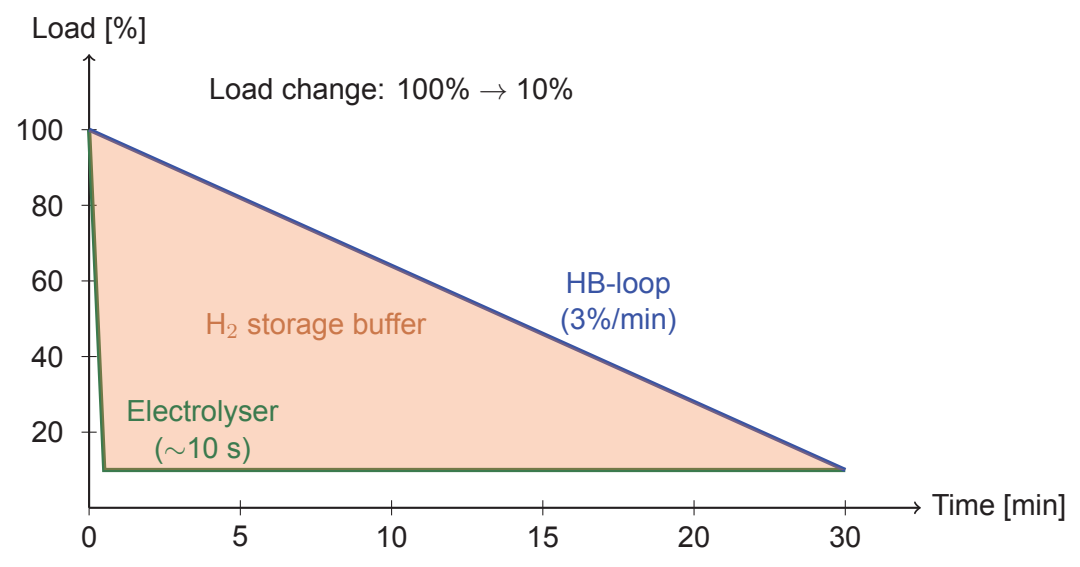


Figure 11.1: Dynamic responses of the electrolyser (fast) and HB synthesis loop (slow) to a load change. Hydrogen storage smooths fluctuations and bridges the timescale gap.

Larger-scale hydrogen storage can enable low-load operation of the HB synthesis loop while the electrolysers are running idle. Electrolysis accounts for roughly 90% of the total energy input to a PtA plant, making it the single largest contributor to production costs. Thus, supplying hydrogen from storage during periods of high electricity prices can improve system economics. However, for this, storage capacity on the order of several days of low-load operation is required, corresponding to about 3–10 hours of full-load hydrogen production. Determining the optimal sizing and technology for hydrogen storage requires detailed techno-economic optimisation and integration with renewable generation profiles, which was not the scope of this study.

The influence of storage also extends to the dynamics of the HB loop. The optimisation studies in Chapters 6–8 were conducted under steady-state assumptions, compressing the make-up feed from 5 bar to the optimised loop pressure. These results remain valid for dynamic operation in configurations without storage, or with only small storage sufficient to buffer short-term fluctuations (15–30 minutes at full load). Accordingly, the flexible operation demonstrated in Chapter 10 is optimal for systems with limited storage.

In contrast, when large-scale storage is included, the operational strategy changes. Storage tanks would be filled during periods of surplus renewable generation and emptied during shortages. Depending on storage pressure, the make-up feed may be supplied to the loop passively, driven by the pressure differential, or require reduced compressor work. Literature reports storage pressures in the range of 50–500 bar (Armijo and Philibert, 2020; Ikäheimo et al., 2018). Consequently, there may be periods during dynamic operation where the synthesis loop pressure is dictated by the storage system rather than by optimisation results.

This interaction between storage and the synthesis loop was beyond the scope of this work. Nevertheless, the proposed control architecture is expected to remain effective, with only minor adjustments required. For instance, in the case of high-pressure stor-

age, hydrogen feed flow control could be implemented via a throttling valve instead of compressor power manipulation.

11.4 Process electrification

The flexible operation regime investigated in this thesis is a natural requirement for Powerto-X (PtX) processes supplied by renewable energy sources. The analysis presented here can be extended to other PtX technologies. In particular, methanol synthesis exhibits strong similarities to the Haber–Bosch process. It is likewise based on a high-pressure synthesis loop with fixed-bed catalytic reactors. Furthermore, the methanol formation reaction is exothermic, leading to comparable reactor designs with inter-bed cooling or direct heat removal. As in ammonia synthesis, the per-pass conversion is limited to approximately 20–30% (Stoica et al., 2015), necessitating recycle operation. Therefore, strategies to achieve flexible operation of the ammonia process presented in this chapter can likely be applied effectively on a green methanol process with small adjustments.

Additional process with green hydrogen as a feed stock include oil refining (e.g. hydrotreating and hydrocracking), production of e-fuels such as synthetic jet fuel and direct reduction of iron (DRI) with hydrogen. By replacing coal with hydrogen in the iron reduction step, CO₂ emissions can be cut by more than 90% compared to blast furnaces (Weiss and Ikäheimo, 2024). In all of these processes, hydrogen demand must be matched dynamically to renewable availability, and flexible compression, heat integration, and control strategies will be key to efficient operation.

However, the concept of flexible operation may in the future also become relevant for several other processes as part of the broader electrification of the process industry. Industrial electrification is considered vital for achieving net-zero climate targets due to its dual benefits of decarbonising energy use and improving energy efficiency (Rosenow et al., 2025). With fluctuating electricity prices, electrified processes may likewise adopt flexible operation strategies for economic benefits, although likely on a less extensive scale than in PtX plants.

In particular, processes with large thermal inventories, such as distillation columns, have been proposed to act as a form of "thermal battery," where energy stored in the system is released during periods of high electricity prices (Udugama et al., 2024). In such cases, low-load operation of auxiliary units such as compressors may occur when the process "battery" is discharged. Parallel compressor configurations, as discussed in Chapter 7, could therefore play a key role in enabling efficient low-load operation in future electrified processes.

Carbon capture and storage (CCS) systems is one example, which rely on energy-intensive separation and compression. Therefore, CCS might benefit from flexible operation strategies to reduce costs under volatile electricity markets.

In this broader perspective, these examples illustrate that the methodologies developed in this work, such as parallel compressor design, optimisation across operating windows, and self-optimising control, may find broader application well beyond PtA, serving as a general framework for flexible and efficient operation in an electrified process industry.

11.5 Next steps toward enabling PtA

This thesis has developed modelling frameworks, optimisation strategies, and control architectures for flexible operation of the Haber–Bosch synthesis loop, which was demonstrated through simulation studies. The next critical step toward enabling Power-to-Ammonia

(PtA) is therefore the validation of the proposed strategies in pilot and demonstration plants.

In this context, the PtA demonstration facility currently under construction in Ramme, Western Denmark, is a very interesting opportunity. The facility is designed to couple renewable energy sources directly to ammonia production, making it an ideal test case for the operating strategies and control concepts proposed in this work. Skovgaard Energy is a partner in the Dynflex project, which has funded this PhD study, and the author of this thesis has visited the plant in April 2025. Unfortunately, the Ramme plant did not become operational during the course of this project, preventing direct validation of the developed methods.

Nevertheless, once operational, demonstration plants such as Ramme will provide an important opportunity to evaluate several of the strategies proposed in this thesis under real operating conditions:

- Operating the ammonia reactors with a stability margin: Assessing whether approaches such as operating with stability margins can support safe reactor behaviour during load changes.
- **Self-optimising control**: Testing the ability of the proposed control concepts to maintain near-optimal performance in the presence of disturbances and modelling uncertainties.
- Integrated Self-optimising and RTO control architecture: Evaluating the performance of the developed control architecture combining self-optimising control and real-time optimisation in achieving stable, efficient, and flexible operation across a wide load range.

Such demonstrations would offer valuable insights into the practical feasibility of flexible Power-to-Ammonia plants and help guide future scale-up efforts. In addition, follow-up work should investigate long-term catalyst behaviour under fluctuating loads and include techno-economic studies using real electricity market data to evaluate the economic potential of flexible operation strategies.

11.5.1 Model predictive control for PtA

The control strategies developed in this thesis focused on self-optimising control in combination with real-time optimisation, providing a relatively simple and robust framework for enabling flexible operation of the Haber–Bosch synthesis loop. While this approach is effective and practical, more advanced control methodologies could further enhance the performance of PtA plants. In particular, Model Predictive Control (MPC) offers unique advantages in the context of power-to-X.

One of the key benefits of MPC lies in its ability to incorporate forecasts of external disturbances, such as fluctuations in wind and solar power availability, into the control decision-making. By utilising renewable energy forecasts, MPC can establish the future plant operating trajectory and adjust the synthesis loop set-points proactively, rather than reacting only once changes in hydrogen feed have already occurred, which is one of the main drawbacks of traditional PID control.

By acting on anticipated fluctuations in renewable supply, MPC can initiate gradual adjustments in loop pressure, reactor temperatures, or compressor loading ahead of time. This enables the HB synthesis loop to adapt more rapidly to load changes, which is particularly valuable as electrolysers can ramp almost instantaneously. A faster response in

the synthesis loop would therefore improve the overall utilisation of hydrogen or reduced the required size of the hydrogen storage.

Additionally, MPC is naturally suited to processes with strong nonlinearities and operating constraints. By embedding constraint such a maximum ramp range on loop pressure, and reactor stability margins directly into the optimisation problem, MPC can ensure that flexible operation remains both safe and efficient. In this way, MPC could complement the self-optimising control and RTO framework proposed in this work. Self-optimising variables as set-points for the MPC can still provide simple near-optimal operating conditions, while MPC is employed at the supervisory level to anticipate renewable fluctuations and manage fast load changes within operational constraints.

Ultimately, the use of MPC may allow PtA plants to achieve faster and more reliable transitions across the full operating window, further improving the ability of PtA plant to follow intermittent renewable energy supply and improving the economic case for green ammonia production.

Chapter 12

Conclusion

This thesis has addressed one of the key challenges for future green ammonia production: enabling the Haber–Bosch (HB) process to operate flexibly in Power-to-Ammonia (PtA) plants powered by intermittent renewable energy. The work combines rigorous modelling, optimisation, and control design to develop strategies that ensure safe and efficient operation across a wide load range.

To reach this goal, the four research questions were raised. The answers to the research questions are summarised in the following conclusion. The first research question is:

Research question 1

How does an ammonia reactor dynamically respond to load changes in a PtA system? Can load variability lead to open-loop instabilities or unsafe operating conditions?

To answer this, a dynamic fixed-bed reactor model was developed as the foundation of the study, using a novel formulation of the governing partial differential—algebraic equations to achieve significantly faster simulations compared to conventional approaches. The model accurately captures the nonlinear dynamics and thermal behaviour characteristic of ammonia synthesis, enabling detailed analysis of stability and transient behaviour. The model was extended to represent an adiabatic quench-cooled reactor (AQCR), revealing the risk of oscillatory behaviour and extinction during load changes. Optimisation studies highlighted the trade-off between conversion efficiency and stability, while a basic control strategy was proposed to enable safe operation under moderate ramp rates.

Research Question 2 focused on identifying which reactor configuration is best suited for flexible PtA operation:

Research Question 2 Among the three general reactor types, which configuration offers the best combination of stability, conversion efficiency, and controllability for flexible operation in a PtA system?

To address this, the scope was expanded to include the two other main industrial reactor designs: the adiabatic indirect-cooled reactor (AICR) and the internal direct-cooled reactor (IDCR). A systematic comparison across a wide operating window of reactor loads showed that the AICR and IDCR deliver superior conversion performance and improved stability compared to the AQCR. Introducing a modest thermal stability margin was shown to substantially enhance robustness without significantly sacrificing efficiency.

Research Question 3 examined the optimal operation and sensitivity of the entire synthesis loop:

Research question 3

What are the optimal operating parameters for a Haber-Bosch synthesis loop across the PtA operating envelope? How sensitive are the optimisation results to process disturbances?

To answer this, a comprehensive dynamic model of the entire HB synthesis loop was developed, incorporating reactors, compressors, steam turbines, and flash separators. Steady-state optimisation identified loop pressure as the most critical degree of freedom, varying significantly across the load range. However, anti-surge constraints on the main feed compressor were shown to limit efficiency gains at low load, motivating alternative design solutions.

Building on these findings, the thesis investigated synthesis-loop compressor configurations featuring multiple parallel compressor trains. The analysis demonstrated that such designs dramatically reduce energy penalties at low load, achieving power reductions of 55% for a double train configuration compared with a single-train design. An economic assessment confirmed that configurations with two or more trains offer a significant reduction in overall compressor cost over the plant lifetime. A sensitivity study further revealed that optimal power consumption is only modestly affected by disturbances such as catalyst deactivation, changes in argon concentration, and cooling water temperature, demonstrating the robustness of the optimised designs.

Finally, Research Question 4 addresses the design of a control architecture for load-flexible operation of the Haber–Bosch synthesis loop:

Research question 4

How can a control architecture be developed that supports fast, robust, and efficient load-flexible operation of the Haber–Bosch synthesis loop? Can the control strategy be designed to reduce mechanical and thermal stress on process equipment while maintaining near-optimal operation?

To this end, the concept of self-optimising control was introduced for the HB synthesis loop as a means of simplifying control while maintaining energy efficiency. Sensitivity analysis identified controlled variables that deliver near-optimal performance when kept constant across the operating range. In particular, fixing the reactor bed inlet temperatures and the H_2/N_2 -ratio provided minimal deviation from the optimal benchmark, whereas holding loop pressure constant resulted in significant energy penalties at high and low loads. These findings motivated a hybrid control strategy, combining self-optimising control principles for selected variables with real-time optimisation for pressure, ensuring both stability and economic performance.

Complementing this, the dynamic behaviour of the full synthesis loop was explored through open-loop simulations for step-changes in key manipulated variables, including compressor powers and reactor feed splits. The results highlighted strong nonlinear dynamics and intricate process interactions, underlining the challenges of load-flexible operation. These insights provided the basis for developing a robust control architecture capable of achieving safe and efficient operation across the full load range.

The final contribution of the thesis was a control architecture for the HB synthesis loop, integrating real-time optimisation with self-optimising control principles. Variable pairing was assessed through open-loop simulations and a relative gain array analysis, and decoupling was implemented to mitigate interactions between loops. Dynamic simulations demonstrated that the proposed control system ensures stable operation from 10% to 120% load, maintains energy consumption close to the theoretical optimum, and enables fast load changes of up to 3% per minute. The self-optimising control approach reduces the frequency of set-point changes, improving equipment lifetime while ensuring high energy efficiency.

In summary, this thesis provided a framework for enabling flexible operation of the Haber-

Bosch process in Power-to-Ammonia systems. The work presents three main contributions:

- i An efficient dynamic modelling framework for ammonia reactors and synthesis loops.
- ii An optimisation and design strategy for reactor systems and compressor configurations under wide load variations.
- iii A practical yet effective control architecture that combines self-optimising principles with real-time optimisation to achieve near-optimal performance during highly flexible operation.

Hopefully, these contributions can support the deployment of future PtA plants capable of operating reliably, flexibly and efficiently under the variability of renewable energy supply.

Bibliography

- Elspot Prices. URL: https://www.energidataservice.dk/tso-electricity/Elspotprices.
- Afif, A., Radenahmad, N., Cheok, Q., Shams, S., Kim, J. H., and Azad, A. K. (2016). Ammonia-fed fuel cells: A comprehensive review. *Renewable and Sustainable Energy Reviews*, 60(February 2020):822–835. DOI: 10.1016/j.rser.2016.01.120.
- Akpa, J. G. and Raphael, N. R. (2014). Optimization of an Ammonia Synthesis Converter. World Journal of Engineering and Technology, 02(04):305–313. DOI: 10.4236/w-jet.2014.24032.
- Al-Aboosi, F. Y., El-Halwagi, M. M., Moore, M., and Nielsen, R. B. (2021). Renewable ammonia as an alternative fuel for the shipping industry. *Current Opinion in Chemical Engineering*, 31:100670. DOI: 10.1016/j.coche.2021.100670.
- Allman, A. and Daoutidis, P. (2018). Optimal scheduling for wind-powered ammonia generation: Effects of key design parameters. *Chemical Engineering Research and Design*, 131:5–15. DOI: 10.1016/j.cherd.2017.10.010.
- Allman, A., Daoutidis, P., Tiffany, D., and Kelley, S. (2017). A Framework for Ammonia Supply Chain Optimization Incorporating Conventional and Renewable Generation. *AIChE Journal*, 59(4):215–228. DOI: 10.1002/aic.
- Allman, A., Palys, M. J., and Daoutidis, P. (2019). Scheduling-informed optimal design of systems with time-varying operation: A wind-powered ammonia case study. *AIChE Journal*, 65(7). DOI: 10.1002/aic.16434.
- Andersen, B. R. (1999). *Nonlinear Dynamics of Catalytic Ammonia Reactors*. PhD thesis, DTU; Technical University of Denmark.
- Anh-Nga, N. T., Tuan-Anh, N., Tien-Dung, V., and Kim-Trung, N. (2017). Multivariable optimization of an auto-thermal ammonia synthesis reactor using genetic algorithm. *AIP Conference Proceedings*, 1878(November). DOI: 10.1063/1.5000192.
- Appl, M. (2006). Ammonia. In Ullmann's Encyclopedia of Industrial Chemistry.
- Araújo, A. and Skogestad, S. (2008). Control structure design for the ammonia synthesis process. *Computers and Chemical Engineering*, 32(12):2920–2932. DOI: 10.1016/j.compchemeng.2008.03.001.
- Araya, S. S., Cui, X., Li, N., Liso, V., and Sahlin, S. L. (2022). Technology overview, possibilities and challenges.
- Armijo, J. and Philibert, C. (2020). Flexible production of green hydrogen and ammonia from variable solar and wind energy: Case study of Chile and Argentina. *International Journal of Hydrogen Energy*, 45(3):1541–1558. DOI: 10.1016/j.ijhydene.2019.11.028.
- Ash, N. and Scarbrough, T. (2019). Sailing on Solar Could green ammonia decarbonise international shipping? *Ricardo Energy & Environment*, (May):1–63.
- Atchison, J. (2022). Skovgaard renewable ammonia project orders electrolysers from Nel. URL: https://ammoniaenergy.org/articles/skovgaard-renewable-ammonia-projectorders-electrolysers-from-nel/.

- Azarhoosh, M. J., Farivar, F., and Ale Ebrahim, H. (2014). Simulation and optimization of a horizontal ammonia synthesis reactor using genetic algorithm. *RSC Advances*, 4(26):13419–13429. DOI: 10.1039/c3ra45410j.
- Baddour, R. F., Brian, P. L., Logeais, B. A., and Eymery, J. P. (1965). Steady-state simulation of an ammonia synthesis converter. *Chemical Engineering Science*, 20(4):281–292. DOI: 10.1016/0009-2509(65)85017-5.
- Balmer, R. T. (2011a). Chapter 13 Vapor and Gas Power Cycles. pages 447–534. Academic Press, Boston.
- Balmer, R. T. (2011b). Chapter 14 Vapor and Gas Refrigeration Cycles. pages 535–590. Academic Press, Boston.
- Bird, F., Clarke, A., Davies, P., and Surkovic, E. (2020). *Ammonia: zero-carbon fertiliser, fuel and energy store*. URL: https://royalsociety.org/-/media/policy/projects/green-ammonia/green-ammonia-policy-briefing.pdf.
- Burrows, L. and Bollas, G. M. (2022). Stability Assessment of Small-Scale Distributed Ammonia Production Systems. *Industrial and Engineering Chemistry Research*, 61(43):16081–16092. DOI: 10.1021/acs.iecr.2c00631.
- Business analytiq (2025). Business analytiq. URL: https://businessanalytiq.com/procurementanalytics/index/ammonia-price-index/.
- Cheema, I. I. and Krewer, U. (2018). Operating envelope of Haber-Bosch process design for power-to-ammonia. *RSC Advances*, 8(61):34926–34936. DOI: 10.1039/c8ra06821f.
- Cheema, I. I. and Krewer, U. (2020). Optimisation of the autothermal NH3 production process for power-to-ammonia. *Processes*, 8(1):1–21. DOI: 10.3390/pr8010038.
- Chehade, Z., Mansilla, C., Lucchese, P., Hilliard, S., and Proost, J. (2019). Review and analysis of demonstration projects on power-to-X pathways in the world. *International Journal of Hydrogen Energy*, 44(51):27637–27655. DOI: 10.1016/j.ijhydene.2019.08.260.
- Danish Ministry of Climate (2022). The Government's strategy for Power-to-X.
- Dansk Energi (2020). Anbefalinger til en dansk strategi for Power-to-X. (November):78.
- de Wasch, A. P. and Froment, G. F. (1972). Heat transfer in packed beds. *Chemical Engineering Science*, 27(3):567–576. DOI: https://doi.org/10.1016/0009-2509(72)87012-X.
- Delbeke, J., Runge-Metzger, A., Slingenberg, Y., and Werksman, J. (2019). The paris agreement. *Towards a Climate-Neutral Europe: Curbing the Trend*, pages 24–45. DOI: 10.4324/9789276082569-2.
- Delgado, J. M. (2006). A critical review of dispersion in packed beds. *Heat and Mass Transfer/Waerme- und Stoffuebertragung*, 42(4):279–310. DOI: 10.1007/s00231-005-0019-0.
- Edwards, M. F. and Richardson, J. F. (1968). Gas dispersion in packed beds. *Chemical Engineering Science*, 23(2):109–123. DOI: 10.1016/0009-2509(68)87056-3.
- El-Gharbawy, M., Shehata, W., and Gad, F. (2021). Ammonia converter Simulation and Optimization Based on an Innovative Correlation for (KP) Prediction. *Jour-*

- nal of University of Shanghai for Science and Technology, 23(12):323–338. DOI: 10.51201/jusst/21/121034.
- El-Shafie, M., Harada, H., Yajima, T., Tsuda, S., Inazu, K., and Kawajiri, Y. (2024). A comprehensive analysis of ammonia synthesis over a commercial iron-based catalyst using differential and integral reactor models. *International Journal of Hydrogen Energy*, 58(November 2023):1009–1019. DOI: 10.1016/j.ijhydene.2024.01.173.
- Erisman, J. W., Sutton, M. A., Galloway, J., Klimont, Z., and Winiwarter, W. (2008). How a century of ammonia synthesis changed the world. *Nature Geoscience*, 1(10):636–639. DOI: 10.1038/ngeo325.
- European Council (2014). Euco 169/14. European Council, (October):1-15.
- European Gas Hub. Market outlook for renewable Ammonia. URL: https://www.europeangashub.com/report-presentation/market-outlook-for-renewable-ammonia.
- European Union (2020). EU Climate Target Plan 2030 Building a modern, sustainable and resilient Europea. *European Union*, pages 1–2. DOI: 10.2834/42397.
- Fahr, S., Kender, R., Bohn, J. P., Rehfeldt, S., Peschel, A., and Klein, H. (2025). Dynamic simulation of a highly load-flexible Haber–Bosch plant. *International Journal of Hydrogen Energy*, 102(September 2024):1231–1242. DOI: 10.1016/j.ijhydene.2025.01.039.
- Fahr, S., Schiedeck, M., Reinke, M., Bohn, J. P., Rehfeldt, S., Peschel, A., and Klein, H. (2024). Simultaneous design and part-load optimization of an industrial ammonia synthesis reactor. *Chemical Engineering Journal*, 480(November 2023):148302. DOI: 10.1016/j.cej.2023.148302.
- Fahr, S., Schiedeck, M., Schwarzhuber, J., Rehfeldt, S., Peschel, A., and Klein, H. (2023). Design and thermodynamic analysis of a large-scale ammonia reactor for increased load flexibility. *Chemical Engineering Journal*, 471(June):144612. DOI: 10.1016/j.cej.2023.144612.
- Fischer, K. L. and Freund, H. (2020). On the optimal design of load flexible fixed bed reactors: Integration of dynamics into the design problem. *Chemical Engineering Journal*, 393(March):124722. DOI: 10.1016/j.cej.2020.124722.
- Forzatti, P. and Lietti, L. (1999). Catalyst deactivation. *Catalysis Today*, 52(2):165–181. DOI: https://doi.org/10.1016/S0920-5861(99)00074-7.
- Froment, Gilbert F. Bischoff, K. B. and De Wilde, J. (2010). *Chemical Reactor Analysis and Design*. Wiley, 3rd edition.
- Gaines, L. D. and Gani, R. (1977). Optimal Temperatures for Ammonia Synthesis Converters. *Industrial and Engineering Chemistry Process Design and Development*, 16(3):381–389. DOI: 10.1021/i260063a024.
- Gorval, E. and Kein, B. (2025). Ammonia synthesis plant for partial-load operation which changes, and method for operating an ammonia synthesis plant. URL: https://lens.org/095-600-620-098-340.
- Graber, G., Calderaro, V., Galdi, V., Ippolito, L., De Caro, F., and Vaccaro, A. (2024). Day-Ahead Optimization of Proton Exchange Membrane Electrolyzer Operations Considering System Efficiency and Green Hydrogen Production Constraints Imposed by the European Regulatory Framework. *Energies*, 17(22). DOI: 10.3390/en17225713.

- Hangos, K. (2001). *Process modelling and model analysis / K.M. Hangos, I.T. Cameron*. Process systems engineering; 4. Academic Press, San Diego.
- Holman, J. P. (2002). *Heat Transfer*. Irwin/McGraw-Hill Series in Operations and Decision Sciences. McGraw-Hill. URL: https://books.google.dk/books?id=yh6xzQEACAAJ.
- HøstP2X (2021). Hoest PtX Esbjerg. URL: https://hoestptxesbjerg.dk/.
- Ikäheimo, J., Kiviluoma, J., Weiss, R., and Holttinen, H. (2018). Power-to-ammonia in future North European 100 % renewable power and heat system. *International Journal of Hydrogen Energy*, 43(36):17295–17308. DOI: 10.1016/j.ijhydene.2018.06.121.
- Inamuddin, Boddula, R., and Asiri, A. (2020). *Sustainable Ammonia Production*. Springer Nature Switzerland. DOI: 10.1007/978-3-030-35106-9_4.
- Innovation fund (2020). ELYgator. Technical Report November.
- Institute for Sustainable Process Technology (2017). Power to Ammonia. *Institute for Sustainable Process Technology*, pages 1–98.
- IRENA and AEA (2022). Innovation Outlook: Renewable Ammonia.
- Jiang, P., Wang, C., Li, L., Ji, T., Mu, L., Lu, X., and Zhu, J. (2025). Green impacts of transforming green electricity into microwave for ammonia and urea production. *AIChE Journal*, (January). DOI: 10.1002/aic.18743.
- Jinasena, A., Lie, B., and Glemmestad, B. (2018). Dynamic model of an ammonia synthesis reactor based on open information. *Proceedings of The 9th EUROSIM Congress on Modelling and Simulation, EUROSIM 2016, The 57th SIMS Conference on Simulation and Modelling SIMS 2016*, 142:998–1004. DOI: 10.3384/ecp17142998.
- Jørgensen, J. B. and Jørgensen, S. B. (2000). Towards automatic decentralized control structure selection. *Computers and Chemical Engineering*, 24(2-7):841–846. DOI: 10.1016/S0098-1354(00)00337-9.
- Jorqueira, D. S. S., Neto, A. M. B., and Rodrigues, M. T. M. (2018). Modeling and Numerical Simulation of Ammonia Synthesis Reactors Using Compositional Approach. *Advances in Chemical Engineering and Science*, 08(03):124–143. DOI: 10.4236/aces.2018.83009.
- Kenneth Guthrie (1974). *Process plant estimating evaluation and control*. CRAFTSMAN BOOK COMPANY OF AMERICA, 1st edition.
- Khademi, M. H. and Sabbaghi, R. S. (2017). Comparison between three types of ammonia synthesis reactor configurations in terms of cooling methods. *Chemical Engineering Research and Design*, 128:306–317. DOI: 10.1016/j.cherd.2017.10.021.
- Klein, H., Fritsch, P., Haider, P., Kender, R., Rößler, F., Rehfeldt, S., Freko, P., Hoffmann, R., Thomas, I., and Wunderlich, B. (2021). Flexible Operation of Air Separation Units. *ChemBioEng Reviews*, 8(4):357–374. DOI: 10.1002/cben.202100023.
- Kohli, V., Mason, J., Timbres, D., and Ormsbee, C. (2008). Replacement of an S-200 basket with an S-300 basket in a 24-year-old ammonia plant. *Ammonia Plant Safety and Related Facilities*, 49:91–109.
- Kong, B., Zhang, Q., and Daoutidis, P. (2024). Nonlinear model predictive control of flexible ammonia production. *Control Engineering Practice*, 148(April):105946. DOI: 10.1016/j.conengprac.2024.105946.

- Krishnamoorthy, D. and Skogestad, S. (2022). Real-Time optimization as a feedback control problem A review. *Computers & Chemical Engineering*, 161:107723. DOI: 10.1016/j.compchemeng.2022.107723.
- Laursen, R. (2018). (Slides) Ship Operation Using LPG and Ammonia As Fuel on MAN B&W Dual Fuel ME-LGIP Engines. *NH3 Fuel Conference*.
- Linde (2023). Flexible air separation for a sustainable energy economy. URL: https://www.linde-engineering.com/en/about-linde-engineering/success-stories/flexible-air-separation.html.
- Liu, X., Elgowainy, A., and Wang, M. (2020). Life cycle energy use and greenhouse gas emissions of ammonia production from renewable resources and industrial by-products. *Green Chemistry*, 22(17):5751–5761. DOI: 10.1039/d0gc02301a.
- Luyben, W. L. (2012). Design and Control of a Cooled Ammonia Reactor. *Plantwide Control: Recent Developments and Applications*, pages 273–292. DOI: 10.1002/9781119968962.ch13.
- MacFarlane, D. R., Cherepanov, P. V., Choi, J., Suryanto, B. H., Hodgetts, R. Y., Bakker, J. M., Ferrero Vallana, F. M., and Simonov, A. N. (2020). A Roadmap to the Ammonia Economy. *Joule*, 4(6):1186–1205. DOI: 10.1016/j.joule.2020.04.004.
- Maggi, A., Bremer, J., and Sundmacher, K. (2023). Multi-period optimization for the design and operation of a flexible power-to-methanol process. *Chemical Engineering Science*, 281:119202. DOI: https://doi.org/10.1016/j.ces.2023.119202.
- Mancusi, E., Maffettone, P. L., Gioia, F., and A, S. C. (2001). Nonl i n e a r analysis of an industrial a m m o n i a reactor with h e t e r o g e n e o u s model. (1998):225–230.
- Mancusi, E., Maffettone, P. L., Gioia, F., and Crescitelli, S. (2009). Nonlinear analysis of heterogeneous model for an industrial ammonia reactor. *Chemical Product and Process Modeling*, 4(2). DOI: 10.2202/1934-2659.1296.
- Manenti, F. and Bozzano, G. (2013). Optimal control of methanol synthesis fixed-bed reactor. *Industrial and Engineering Chemistry Research*, 52(36):13079–13091. DOI: 10.1021/ie401511e.
- Martinsen, E. S., Rosbo, J. W., Andersen, A. H. D., Ritschel, T. K. S., Hørsholt, S., Huusom, J. K., and Jørgensen, J. B. (2023). Modeling and Simulation of a Single Catalytic Fixed Bed in an Ammonia Reactor. *IFAC-PapersOnLine*, 56(2):6906–6912. DOI: https://doi.org/10.1016/j.ifacol.2023.10.497.
- Matthey, J. (2021). Safe handling of ammonia synthesis catalysts. (April).
- Maurizio, R. (2022). Control of an ammonia synthesis loop at partial load. URL: https://lens.org/097-741-947-746-874.
- Michels, A., Dumoulin, E., and Van Dijk, J. J. (1961). Gas-liquid phase equilibrium in the system NH3-A. *Physica*, 27(9):886–892. DOI: 10.1016/0031-8914(61)90088-X.
- Michels, A., Skelton, G. F., and Dumoulin, E. (1950). Gas-liquid phase equilibrium in the system ammonia-hydrogen-nitrogen. *Physica*, 16(11):831–838. DOI: https://doi.org/10.1016/0031-8914(50)90092-9.
- Moghaddam, A. A. and Krewer, U. (2020). Poisoning of ammonia synthesis catalyst considering off-design feed compositions. *Catalysts*, 10(11):1–16. DOI: 10.3390/catal10111225.

- Morgan, E., Manwell, J., and McGowan, J. (2014). Wind-powered ammonia fuel production for remote islands: A case study. *Renewable Energy*, 72:51–61. DOI: 10.1016/j.renene.2014.06.034.
- Morud, J. C. and Skogestad, S. (1998). Analysis of Instability in an Industrial Ammonia Reactor. *AIChE Journal*, 44(4):888–895. DOI: 10.1002/aic.690440414.
- Naess, L., Mjaavatten, A., and Li, J. O. (1992). Using dynamic process simulation from conception to normal operation of process plants. *Computers and Chemical Engineer*ing, 16:S119–S130. DOI: 10.1016/S0098-1354(09)80014-8.
- Nayak-Luke, R., Bañares-Alcántara, R., and Wilkinson, I. (2018). "green" Ammonia: Impact of Renewable Energy Intermittency on Plant Sizing and Levelized Cost of Ammonia. *Industrial and Engineering Chemistry Research*, 57(43):14607–14616. DOI: 10.1021/acs.iecr.8b02447.
- Nayak-Luke, R. M. and Bañares-Alcántara, R. (2020). Techno-economic viability of islanded green ammonia as a carbon-free energy vector and as a substitute for conventional production. *Energy and Environmental Science*, 13(9):2957–2966. DOI: 10.1039/d0ee01707h.
- Nielsen, A. (1953). Latest Developments in Ammonia Synthesis. *Advances in Catalysis*, 5(C):1–37. DOI: 10.1016/S0360-0564(08)60639-2.
- Nielsen, A., Kjaer, J., and Hansen, B. (1964). Rate equation and mechanism of ammonia synthesis at industrial conditions. *Journal of Catalysis*, 3(1):68–79. DOI: 10.1016/0021-9517(64)90094-6.
- Osozawa, M., Hori, A., Fukai, K., Honma, T., Oshima, K., and Satokawa, S. (2022). Improvement in ammonia synthesis activity on ruthenium catalyst using ceria support modified a large amount of cesium promoter. *International Journal of Hydrogen Energy*, 47(4):2433–2441. DOI: https://doi.org/10.1016/j.ijhydene.2021.10.204.
- Peters, M. S., Timmerhaus, K. D., and West, R. E. (2002). *Plant design and economics for chemical engineers*. 5th edition.
- Pistolesi, C., Giaconia, A., and Bassano, C. (2025). Flexible Green Ammonia Production: Impact of Process Design on the Levelized Cost of Ammonia. *Fuels*, pages 1–21.
- Poling, B. E., Prausnitz, J. M., and O'Connell, J. P. (2001). *The Properties of Gases and Liquids*. McGraw-Hill Education.
- Quintero-Masselski, C., Portha, J. F., and Falk, L. (2022). Conception and optimization of an ammonia synthesis superstructure for energy storage. *Chemical Engineering Research and Design*, 177:826–842. DOI: 10.1016/j.cherd.2021.11.039.
- Rabchuk, K., Lie, B., Mjaavatten, A., and Siepmann, V. (2014). Stability map for Ammonia Synthesis Reactors. *Proceedings from the 55th Conference on Simulation and Modelling (SIMS 55)*, 21-22 October, 2014. Aalborg, Denmark, (Sims 55):159–166.
- Ravn, S. (2020). Danish partnership sets out to build world's first commercial scale green ammonia plant. URL: https://www.topsoe.com/press-releases/partnership-sets-out-to-build-worlds-first-commercial-scale-green-ammonia-plant.
- Rawlings, J. B. and Ekerdt, J. G. (2013). *Chemical Reactor Analysis and Design Fundamentals*. Nob Hill Publishing, 2nd edition.

- Recke, B., Rønde Andersen, B., and Bay Jørgensen, S. (2000). Bifurcation Control of Sample Chemical Reaction Systems. *IFAC Proceedings Volumes*, 33(10):569–574. DOI: 10.1016/s1474-6670(17)38601-9.
- Reddy, K. V. and Husain, A. (1982). Modeling and Simulation of an Ammonia Synthesis Loop. *Industrial and Engineering Chemistry Process Design and Development*, 21(3):359–367. DOI: 10.1021/i200018a001.
- Ritschel, T. K., Capolei, A., Gaspar, J., and Jørgensen, J. B. (2018). An algorithm for gradient-based dynamic optimization of UV flash processes. *Computers and Chemical Engineering*, 114:281–295. DOI: 10.1016/j.compchemeng.2017.10.007.
- Ritschel, T. K. S., Gaspar, J., Capolei, A., and Jørgensen, J. B. (2016). An open-source thermodynamic software library. DTU Compute-Technical Report-2016 No. 12. Technical report, DTU: Technical University of Denmark.
- Ritschel, T. K. S., Gaspar, J., and Jørgensen, J. B. (2017). A Thermodynamic Library for Simulation and Optimization of Dynamic Processes. *IFAC-PapersOnLine*, 50(1):3542–3547. DOI: 10.1016/j.ifacol.2017.08.951.
- Rosbo, J. W., Jensen, A. D., Jørgensen, J. B., and Huusom, J. K. (2024a). Comparison, operation and cooling design of three general reactor types for Power-to-Ammonia processes. *Chemical Engineering Journal*, 496:153660. DOI: https://doi.org/10.1016/j.cej.2024.153660.
- Rosbo, J. W., Jensen, A. D., Jørgensen, J. B., and Huusom, J. K. (2024b). Design of an Indirect Cooled Reactor for Power to Ammonia. *Computer Aided Chemical Engineering*.
- Rosbo, J. W., Jensen, A. D., Jørgensen, J. B., and Huusom, J. K. (2024c). Efficient Numerical Methods for Dynamic Simulation of Fixed-bed Reactors. In *Computer Aided Chemical Engineering*, volume 53, pages 1111–1116.
- Rosbo, J. W., Jensen, A. D., Jørgensen, J. B., and Huusom, J. K. (2024d). Optimal flexible operation of an AICR for P2A. In Manenti, F. and Reklaitis, G. V. B. T. C. A. C. E., editors, 34 European Symposium on Computer Aided Process Engineering / 15 International Symposium on Process Systems Engineering, volume 53, pages 1771–1776. Elsevier.
- Rosbo, J. W., Jensen, A. D., Jørgensen, J. B., Skogestad, S., and Huusom, J. K. (2025a). Optimisation and Robust Control of a Load-Flexible Haber-Bosch Ammonia Synthesis Loop. *Submitted to Computers & Chemical Engineering*.
- Rosbo, J. W., Jørgensen, J. B., Jensen, A. D., Skogestad, S., and Huusom, J. K. (2025b). Optimisation of a Haber-Bosch Synthesis Loop for PtA. *Systems & Control Transactions*, 4:1126–1132. DOI: https://doi.org/10.69997/sct.122254.
- Rosbo, J. W., Ritschel, T. K., Hørsholt, S., Jensen, A. D., Jørgensen, J. B., and Huusom, J. K. (2023a). *Optimal power distribution in a P2A plant*, volume 52. Elsevier Masson SAS. DOI: 10.1016/B978-0-443-15274-0.50282-1. URL: https://doi.org/10.1016/B978-0-443-15274-0.50282-1.
- Rosbo, J. W., Ritschel, T. K. S., Hørstholt, S., Huusom, J. K., and Jørgensen, J. B. (2023b). Flexible operation, optimisation and stabilising control of a quench cooled ammonia reactor for Power-to-Ammonia. *Computers & Chemical Engineering*, 176(108316). DOI: https://doi.org/10.1016/j.compchemeng.2023.108316.
- Rosenow, J., Arpagaus, C., Lechtenböhmer, S., Oxenaar, S., and Pusceddu, E. (2025).

- The heat is on: Policy solutions for industrial electrification. *Energy Research & Social Science*, 127:104227. DOI: https://doi.org/10.1016/j.erss.2025.104227.
- Rouwenhorst, K., Krzywda, P., Benes, N., Mul, G., and Lefferts, L. (2021). *Ammonia Production Technologies*. Elsevier Inc. DOI: 10.1016/b978-0-12-820560-0.00004-7. URL: http://dx.doi.org/10.1016/B978-0-12-820560-0.00004-7.
- Rouwenhorst, K. H. R. and Brown, T. (2023). *Techno-economic Considerations for Ammonia Production, Storage, and Transportation*. Springer Nature Singapore. DOI: 10.1007/978-981-19-4767-4. URL: http://dx.doi.org/10.1007/978-981-19-4767-4₄7.
- Rouwenhorst, K. H. R., Travis, A. S., and Lefferts, L. (2022). 1921–2021: A Century of Renewable Ammonia Synthesis. *Sustainable Chemistry*, 3(2):149–171. DOI: 10.3390/suschem3020011.
- Rovaglio, M., Manca, D., Cortese, F., and Mussone, P. (2001). Multistability and robust control of the ammonia synthesis loop. *Computer Aided Chemical Engineering*, 9:723–730.
- Salmon, N. and Bañares-Alcántara, R. (2023). Impact of process flexibility and imperfect forecasting on the operation and design of Haber-Bosch green ammonia. *RSC Sustainability*, 1(4):923–937. DOI: 10.1039/d3su00067b.
- Sánchez, A., Castellano, E., Martín, M., and Vega, P. (2021). Evaluating ammonia as green fuel for power generation: A thermo-chemical perspective. *Applied Energy*, 293(February):116956. DOI: 10.1016/j.apenergy.2021.116956.
- Sánchez, A. and Martín, M. (2018a). Optimal renewable production of ammonia from water and air. *Journal of Cleaner Production*, 178:325–342. DOI: 10.1016/j.jclepro.2017.12.279.
- Sánchez, A. and Martín, M. (2018b). Scale up and scale down issues of renewable ammonia plants: Towards modular design. *Sustainable Production and Consumption*, 16:176–192. DOI: 10.1016/j.spc.2018.08.001.
- Sawant, M. R., Patwardhan, A. W., Gaikar, V. G., and Bhaskaran, M. (2006). Phase equilibria analysis of the binary N2-NH3 and H2-NH3 systems and prediction of ternary phase equilibria. *Fluid Phase Equilibria*, 239(1):52–62. DOI: 10.1016/j.fluid.2005.10.014.
- Saygin, D., Blanco, H., Boshell, F., Cordonnier, J., Rouwenhorst, K., Lathwal, P., and Gielen, D. (2023). Ammonia Production from Clean Hydrogen and the Implications for Global Natural Gas Demand. *Sustainability (Switzerland)*, 15(2). DOI: 10.3390/su15021623.
- Schiedeck, M., Nogueira, R., and Lund, H. (2025). Energy Heat integration and part-load performance of an SOEC-coupled Haber Bosch process. *International Journal of Hydrogen Energy*, 116(November 2024):242–256. DOI: 10.1016/j.ijhydene.2025.02.335.
- Schmidt, O., Gambhir, A., Staffell, I., Hawkes, A., Nelson, J., and Few, S. (2017). Future cost and performance of water electrolysis: An expert elicitation study. *International Journal of Hydrogen Energy*, 42(52):30470–30492. DOI: https://doi.org/10.1016/j.ijhydene.2017.10.045.
- Schulte Beerbühl, S., Fröhling, M., and Schultmann, F. (2015). Combined scheduling and capacity planning of electricity-based ammonia production to integrate renewable energies. *European Journal of Operational Research*, 241(3):851–862. DOI: 10.1016/j.ejor.2014.08.039.

- Seborg, D. E., Edgar, T. F., and Mellichamp, D. A. (2016). Process Dynamics and Control. In *Process Dynamics and Control*, chapter 18. Multil. John Wiley & Sons, Ltd, 4th editio edition.
- Shamiri, A. and Aliabadi, N. (2021). Modeling and Performance Improvement of an Industrial Ammonia Synthesis Reactor. *Chemical Engineering Journal Advances*, 8:100177. DOI: 10.1016/j.ceja.2021.100177.
- Siemens Energy (2020). Overview of the PEM Silyzer Family. Technical report.
- Singh, C. P. and Saraf, D. N. (1979). Simulation of Ammonia Synthesis Reactors. *Industrial and Engineering Chemistry Process Design and Development*, 18(3):364–370. DOI: 10.1021/i260071a002.
- Skogestad, S. (2000). Plantwide control: The search for the self-optimizing control structure. *Journal of Process Control*, 10(5):487–507. DOI: 10.1016/S0959-1524(00)00023-8.
- Skogestad, S. (2004). Simple analytic rules for model reduction and PID controller tuning. *Modeling, Identification and Control*, 25(2):85–120. DOI: 10.4173/mic.2004.2.2.
- Smith, C., Hill, A. K., and Torrente-Murciano, L. (2020). Current and future role of Haber-Bosch ammonia in a carbon-free energy landscape. *Energy and Environmental Science*, 13(2):331–344. DOI: 10.1039/c9ee02873k.
- Smith, C. and Torrente-Murciano, L. (2024). The importance of dynamic operation and renewable energy source on the economic feasibility of green ammonia. *Joule*, 8(1):157–174. DOI: 10.1016/j.joule.2023.12.002.
- Speth, H. C., Hultqvist, M., and Han, P. A. (2023). Method for the control of pressure in a loop for the preparation of ammonia or methanol. URL: https://lens.org/001-351-524-916-804.
- Stoica, I., Banu, I., Bobarnac, I., and Bozga, G. (2015). Optimization of a methanol synthesis reactor. *UPB Scientific Bulletin, Series B: Chemistry and Materials Science*, 77(4):134–146.
- Straus, J. (2018). *Optimal Operation of Integrated Chemical Processes*. PhD thesis, NTNU: Norwegian University of Science and Technology.
- Straus, J., Krishnamoorthy, D., and Skogestad, S. (2019). On combining self-optimizing control and extremum-seeking control Applied to an ammonia reactor case study. *Journal of Process Control*, 78:78–87. DOI: 10.1016/j.jprocont.2019.01.012.
- Straus, J. and Skogestad, S. (2017). Economic NMPC for heat-integrated chemical reactors. *Proceedings of the 2017 21st International Conference on Process Control, PC 2017*, pages 309–314. DOI: 10.1109/PC.2017.7976232.
- Straus, J. and Skogestad, S. (2018). Self-Optimizing Control in Chemical Recycle Processes. *IFAC-PapersOnLine*, 51(18):536–541. DOI: 10.1016/j.ifacol.2018.09.369.
- Sun, Z., Zhang, Y., Huang, H., Luo, Y., Lin, L., and Jiang, L. (2024). Modeling and simulation of dynamic characteristics of a green ammonia synthesis system. *Energy Conversion and Management*, 300(July 2023):117893. DOI: 10.1016/j.enconman.2023.117893.
- Topsoe (2008). KM1/KM1R The Heart of the Ammonia Plant.
- Tripodi, A., Conte, F., and Rossetti, I. (2021). Process Intensification for Ammonia Synthesis in Multibed Reactors with Fe-Wustite and Ru/C Catalysts. *Industrial and Engineering Chemistry Research*, 60(2):908–915. DOI: 10.1021/acs.iecr.0c05350.

- Udugama, I. A., Taube, M. A., Kirkpatrick, R., Bayer, C., and Young, B. R. (2024). Implications for control systems in highly volatile energy markets: Using a high purity distillation electrification case study. *Chemical Engineering Research and Design*, 203:431–440. DOI: https://doi.org/10.1016/j.cherd.2024.02.001.
- Valera-Medina, A., Xiao, H., Owen-Jones, M., David, W. I. F., and Bowen, P. J. (2018). Ammonia for power. *Progress in Energy and Combustion Science*, 69:63–102. DOI: https://doi.org/10.1016/j.pecs.2018.07.001.
- van Heerden, C. (1953). Autothermic Processes. *Industrial & Engineering Chemistry*, 45(6):1242–1247. DOI: 10.1021/ie50522a030.
- Verleysen, K., Parente, A., and Contino, F. (2021). How sensitive is a dynamic ammonia synthesis process? Global sensitivity analysis of a dynamic Haber-Bosch process (for flexible seasonal energy storage). *Energy*, 232(May). DOI: 10.1016/j.energy.2021.121016.
- Vieri, H. M., Badakhsh, A., and Choi, S. H. (2023). Comparative Study of Ba, Cs, K, and Li as Promoters for Ru/La2Ce2O7-Based Catalyst for Ammonia Synthesis. *International Journal of Energy Research*, 2023(1):2072245. DOI: https://doi.org/10.1155/2023/2072245.
- Wang, C., Walsh, S. D., Longden, T., Palmer, G., Lutalo, I., and Dargaville, R. (2023). Optimising renewable generation configurations of off-grid green ammonia production systems considering Haber-Bosch flexibility. *Energy Conversion and Management*, 280(February):116790. DOI: 10.1016/j.enconman.2023.116790.
- Wang, G., Mitsos, A., and Marquardt, W. (2017). Conceptual Design of Ammonia-Based Energy Storage System: System Design and Time-Invariant Performance. *AIChE Journal*, 63. DOI: 10.1002/aic.15660.
- Wang, G., Mitsos, A., and Marquardt, W. (2020). Renewable production of ammonia and nitric acid. *AIChE Journal*, 66(6):1–9. DOI: 10.1002/aic.16947.
- Weiss, R. and Ikäheimo, J. (2024). Flexible industrial power-to-X production enabling large-scale wind power integration: A case study of future hydrogen direct reduction iron production in Finland. *Applied Energy*, 365:123230. DOI: https://doi.org/10.1016/j.apenergy.2024.123230.
- Wen, L., Huang, C., Dai, Z., Nie, L., Ji, X., and Dai, Y. (2024). Dynamic Simulation and Optimization for Load Regulation Strategies of the Green Ammonia Synthesis Process. *Industrial and Engineering Chemistry Research*. DOI: 10.1021/acs.iecr.4c02410.
- Wiebe, R. and Tremearne, T. H. (1934). The Solubility of Hydrogen in Liquid Ammonia at 25, 50, 75 and 100° and at Pressures to 1000 Atmospheres. *Journal of the American Chemical Society*, 56(11):2357–2360. DOI: 10.1021/ja01326a039.
- Woolf, P. J. (2009). *Chemical Process Dynamics and Controls*. University of Michigan. URL: https://eng.libretexts.org/@go/page/22355.
- Wulf, C., Linßen, J., and Zapp, P. (2018). Review of power-to-gas projects in Europe. *Energy Procedia*, 155:367–378. DOI: 10.1016/j.egypro.2018.11.041.
- Wulf, C., Zapp, P., and Schreiber, A. (2020). Review of Power-to-X Demonstration Projects in Europe. *Frontiers in Energy Research*, 8(September):1–12. DOI: 10.3389/fenrg.2020.00191.
- Yakhnin, V. Z. and Menzinger, M. (1999). Convective instability and its suppression in

- packed-bed- and monolith reactors. *Chemical Engineering Science*, 54(20):4547–4557. DOI: 10.1016/S0009-2509(99)00137-2.
- Zhai, Y., He, Y., Shao, J., Zhang, W., Tong, X., Wang, Z., and Weng, W. (2024). Review of Hydrogen-Driven Power-to-X Technology and Application Status in China. *Processes*, 12(7). DOI: 10.3390/pr12071518.
- Zhang, C., Vasudevan, S., and Rangaiah, G. P. (2010). Plantwide Control System Design and Performance Evaluation for Ammonia Synthesis Process. *Industrial & Engineering Chemistry Research*, 49(24):12538–12547.

Appendix A

Explicit ODE system for the fixed bed

In this appendix material, the explicit ODE form of the fixed-bed reactor is derived. In this appendix, the following derivative notation is used to make the expressions more compact,

$$\partial_x y \equiv \left(\frac{\partial y}{\partial x}\right) \tag{A.1}$$

In chapter 3, the material and energy balances for a finite volume are expressed on pervolume basis (States: c, \hat{u}_R). The absolute moles, n_k , and internal energy, U_k , balances for a finite volume are achieved by multiplying by the cell volume,

$$\Delta V_{k+1/2}^g \partial_t c_k = \partial_t n_k = A^g N_{k-1/2} - A^g N_{k+1/2} + \Delta V_{k+1/2}^g R_k, \tag{A.2a}$$

$$\Delta V_{R,k} \partial_t \hat{u}_{R,k} = \partial_t U_k = A^g \bar{H}_{k-1/2} - A^g \bar{H}_{k+1/2},$$
 (A.2b)

with the interfacial mole and enthalpy flux from cell k to k+1,

$$N_{k+1/2} = v_{k+1/2}c_k$$
 $\left\lceil \frac{\mathsf{mol}}{\mathsf{s}} \right
ceil$, (A.3a)

$$\bar{H}_{k+1/2} = \mathcal{H}(T_k, P_k, N_{k+1/2}) = \hat{h}_k v_{k+1/2}$$
 $\left[\frac{\mathsf{J}}{\mathsf{s} \, \mathsf{m}^2}\right],$ (A.3b)

The volumetric enthalpy, \hat{h}_k , is given by

$$\hat{h}_k = \mathcal{H}(T_k, P_k, c_{k+1/2})$$
 (A.4)

Inserting (A.3a) in A.2 yields,

$$\partial_t n_k = A^g c_{k-1} v_{k-1/2} - A^g c_k v_{k+1/2} + \Delta V_{k+1/2}^g R_k,$$
 (A.5a)

$$\partial_t U_k = A^g \hat{h}_{k-1} v_{k-1/2} - A^g \hat{h}_k v_{k+1/2},$$
(A.5b)

For the finite volume, the algebraic constraints give,

$$\Delta V_{k+1/2}^g = \mathcal{V}(T_k, \ P, \ n_k) \tag{A.6a}$$

$$U_k = \mathcal{U}_{\mathcal{R}}(T_k, P, n_k) \tag{A.6b}$$

A.0.1 Substituting internal energy for temperature

The temperature derivative wrt. time can be expressed by applying the chain rule to the total internal energy of the cell,

$$\partial_t U_k = \partial_T U_k^g \ \partial_t T_k + \partial_P U_k \ \partial_t P + \partial_n U_k^g \ \partial_t n_k = \partial_T V_k^g \ \partial_t T_k + \partial_n V_k^g \ \partial_t n_k \tag{A.7}$$

where it has been used that $\partial_t P = 0$ as the pressure is assumed constant. Note, $\partial_T U_k$ is a combination of the temperature derivative for the gas and catalyst phase,

$$\partial_T U_k = \partial_T U_k^g + \partial_T U_k^s = \partial_T U_k^g + c_p^s \rho^s (1 - \epsilon_B) \Delta V_R \tag{A.8}$$

Inserting the energy balance (A.5b) on the left-hand side and the material balance (A.5a) on the right-hand side of (A.7) yields,

$$A^{g}\hat{h}_{k-1}v_{k-1/2} - A^{g}\hat{h}_{k}v_{k+1/2} = \partial_{n}U_{k}^{g}(A^{g}c_{k-1}v_{k-1/2} - A^{g}c_{k}v_{k+1/2} + V^{g}R_{k}) + \partial_{T}U_{k}^{g}\partial_{t}T_{k}$$

$$= \partial_{n}U_{k}^{g}(a_{k} - A^{g}c_{k}v_{k+1/2}) + \partial_{T}U_{k}^{g}\partial_{t}T_{k}$$
(A.9)

in which, a_k , is defined as

$$a_k = A^g c_{k-1} v_{k-1/2} + v_{k+1/2}^g R_k$$
 (A.10)

Isolating for the temperature derivative,

$$\partial_t T_k = \frac{A^g \hat{h}_{k-1} v_{k-1/2} - A^g \hat{h}_k v_{k+1/2} - \partial_n U_k^g (a_k - A^g c_k v_{k+1/2})}{\partial_T U_k} \tag{A.11}$$

which expresses the time-wise derivative of the temperature.

Flow over cell interfaces - ideal pressure control

In the following, let's denote,

$$\Delta V_k^g = V_k^g \tag{A.12}$$

As the volume of each cell is fixed, the cell volume is constant in time,

$$\partial_t V_k^g = 0 \tag{A.13}$$

Applying the chain rule,

$$\partial_t V_k^g = \partial_T V_k^g \ \partial_t T_k + \partial_P V_k^g \ \partial_t P + \partial_n V_k^g \ \partial_t n_k = 0 \tag{A.14}$$

From the assumption of constant pressure, $\partial_t P = 0$,

$$0 = \partial_T V_k^g \ \partial_t T_k + \partial_n V_k^g \ \partial_t n_k \tag{A.15}$$

Inserting the material balance (A.5a) yields,

$$0 = \partial_T V_k^g \ \partial_t T_k + \partial_n V_k^g a_k - \partial_n V_k^g A^g c_k v_{k+1/2}$$
(A.16)

The temperature derivative wrt. time was derived in the section above. Thus, inserting (A.11) in (A.16),

$$0 = \partial_T V_k^g \frac{A^g \hat{h}_{k-1} v_{k-1/2} - A^g \hat{h}_k v_{k+1/2} - \partial_n U_k^g (a_k - A^g c_k v_{k+1/2})}{\partial_T U_k} + \partial_n V_k^g a_k - \partial_n V_k^g A^g c_k v_{k+1/2}$$
(A.17)

And gathering common terms,

$$0 = \frac{\partial_T V_k^g}{\partial_T U_k} A^g \hat{h}_{k-1} v_{k-1/2} + \left[\partial_n V_k^g - \partial_T V_k^g \frac{\partial_n U_k}{\partial_T U_k} \right] a_k - \left[\frac{\partial_T V_k^g}{\partial_T U_k} A^g \hat{h}_k + \partial_n V_k^g - \partial_T V_k^g \frac{\partial_n U_k}{\partial_T U_k} A^g c_k \right] v_{k+1/2}$$
(A.18)

The flow velocity out of the cell can then be isolated,

$$v_{k+1/2} = \frac{\frac{\partial_T V_k^g}{\partial_T U_k} A^g \hat{h}_{k-1} v_{k-1/2} + \left[\partial_n V_k^g - \partial_T V_k^g \frac{\partial_n U_k}{\partial_T U_k} \right] a_k}{\frac{\partial_T V_k^g}{\partial_T U_k} A^g \hat{h}_k + \left[\partial_n V_k^g - \partial_T V_k^g \frac{\partial_n U_k}{\partial_T U_k} \right] A^g c_k}$$
(A.19)

Define the coefficients,

$$\phi_T \equiv \frac{\partial_T V_k^g}{\partial_T U_k}, \qquad \phi_n \equiv \partial_n V_k^g - \frac{\partial_T V_k^g}{\partial_T U_k} \partial_n U_k$$
 (A.20)

then

$$v_{k+1/2} = \frac{\phi_T \,\hat{h}_{k-1} \,v_{k-1/2} \,+\, \frac{\phi_n}{A_g} \,a_k}{\phi_T \,\hat{h}_k \,+\, \phi_n \,c_k} \tag{A.21}$$

which is the explicit expression for velocity across the cell interfaces. The derivatives in (A.19) can all be evaluated directly in Thermolib. Note additionally, the derivatives in (A.19) are the definition for,

$$\partial_T V^g = \alpha_V, \quad \partial_n V^g = \mathbf{v}$$
 (A.22a)

$$\partial_T U^g = \partial_T H^g - P \partial_T V^g = C_P - P \alpha_V \tag{A.22b}$$

$$\partial_n U^g = \partial_n H^g - P \partial_n V^g = \mathbf{h} - P \mathbf{v}$$
 (A.22c)

where α_V is the thermal expansion coefficient, C_P is the constant pressure heat capacity, and **h** and **v** are vectors containing the component molar enthalpies, h_i , and volumes, v_i .

A.0.2 Explicit ODE formulation

Summarising, the final form of the ODE for the fixed bed is,

$$\partial_t c_k = \frac{N_{k-1/2} - N_{k+1/2}}{\Delta l} + R_k,$$
 (A.23a)

$$\partial_t T_k = \frac{A^g \hat{h}_{k-1} v_{k-1/2} - A^g \hat{h}_k v_{k+1/2} - \partial_n U_k^g (a_k - A^g c_k v_{k+1/2})}{\partial_T U_k},\tag{A.23b}$$

in which, a_k , is defined as,

$$a_k = A^g c_{k-1} v_{k-1/2} + v_{k+1/2}^g R_k.$$
 (A.24)

And the velocity across the cell surfaces

$$v_{k+1/2} = \frac{\phi_T \,\hat{h}_{k-1} \,v_{k-1/2} \,+\, \frac{\phi_n}{A_g} \,a_k}{\phi_T \,\hat{h}_k \,+\, \phi_n \,c_k} \tag{A.25}$$

with

$$\phi_T = \frac{\partial_T V_k^g}{\partial_T U_k}, \qquad \phi_n = \partial_n V_k^g - \frac{\partial_T V_k^g}{\partial_T U_k} \partial_n U_k$$
(A.26)

Appendix B

Steady-State solution method (New-ton's Method)

The residual function for the steady state, **R**, is defined as,

$$\mathbf{z} = \begin{bmatrix} \mathbf{x} \\ \mathbf{y} \end{bmatrix}, \tag{B.1a}$$

$$\mathbf{R} = \mathbf{R^{ss}}(\mathbf{z}) = \mathbf{R^{ss}} \begin{pmatrix} \begin{bmatrix} \mathbf{x} \\ \mathbf{y} \end{bmatrix} \end{pmatrix}$$

$$= \begin{bmatrix} f(\mathbf{x}, \mathbf{y}) \\ g(\mathbf{x}, \mathbf{y}) \end{bmatrix},$$
(B.1b)

The steady state is satisfied when $\mathbf{R^{ss}} = \mathbf{0}$, which is solved via Newton's method. The iteration matrix, M^{SS} , is constructed via the partial derivatives,

$$M^{SS} = \frac{\partial \mathbf{R^{ss}}}{\partial \mathbf{z}} = \begin{pmatrix} \frac{\partial \mathbf{R^{ss}}}{\partial \mathbf{x}} & \frac{\partial \mathbf{R^{ss}}}{\partial \mathbf{y}} \end{pmatrix} = \begin{pmatrix} \frac{\partial f}{\partial \mathbf{x}} & \frac{\partial f}{\partial \mathbf{y}} \\ \frac{\partial g}{\partial \mathbf{x}} & \frac{\partial g}{\partial \mathbf{y}} \end{pmatrix}, \tag{B.2}$$

Starting from an initial guess for the solution, $\mathbf{z^{ss}}_0$, a better approximation is obtained at iteration w+1 via,

$$\mathbf{z}_{w+1}^{ss} = \mathbf{z}_w^{ss} - \left(M^{ss} \left(\mathbf{z}_w^{ss} \right) \right)^{-1} \mathbf{R}^{ss} \left(\mathbf{z}_w^{ss} \right)$$
(B.3)

The iteration procedure terminates, when the infinity norm for the absolute value of the normalized elements in $\mathbf{R^{ss}}$ is smaller than a predetermined value, e,

stop when
$$L_{\infty} \left| \frac{\mathbf{R^{ss}}}{\mathbf{R_{norm}^{ss}}} \right| \le e$$
 (B.4)

in which normalization vector $\mathbf{R_{norm}^{ss}}$ insures equal weighting of the equations contained in $\mathbf{R^{ss}}$. In this work, a tolerance of $e=10^{-6}$ was used.

The initial guess for the Steady State solution is provided by solving equation B.5 in the standard way by integrating along the reactor length via Matlab's built-in ODE solver ode15s.

$$\frac{dN}{dl} = R ag{B.5a}$$

$$\frac{dl}{\partial l} = \frac{\Delta H_r r^g}{c_p^g} \tag{B.5b}$$

where ΔH_r is the heat of reaction for the ammonia formation and C_p^g is the heat capacity for the flux N in unis of $J/(K \ s \ m^2)$.

Appendix C

Derivation of Equation (5.18) in the main manuscript.

In this section, the expression for the reactor flow of ammonia given in Equation (5.18) is derived. The mole fraction of a component i is given by,

$$x_i = \frac{F_{Rf, i}}{\sum_{j \neq i} F_{Rf, j}}.$$
 (C.1)

Assuming constant mole fraction of component *i* over the operational window,

$$\frac{F_{Rf, i}}{\sum_{j \neq i} F_{Rf, j}} = \frac{F_{Rfn, i}}{\sum_{j \neq i} F_{Rfn, j}}.$$
 (C.2)

Isolating for the reactor flow of component *i*,

$$F_{Rf, i} = F_{Rfn, i} \frac{\sum_{j \neq i} F_{Rf, j}}{\sum_{j \neq i} F_{Rfn, j}}.$$
 (C.3)

For ammonia, this gives Equation (C.4),

$$F_{Rf, \text{ NH}_3} = F_{Rfn, \text{ NH}_3} \left(\frac{F_{Rf, \text{ H}_2} + F_{Rf, \text{ N}_2} + F_{Rf, \text{ Ar}}}{F_{Rfn, \text{ H}_2} + F_{Rfn, \text{ N}_2} + F_{Rfn, \text{ Ar}}} \right). \tag{C.4}$$

Appendix D

Vapour-Liquid Equilibrium: H₂, N₂, NH₃, Ar

As described in Section 6.2.5, the vapour liquid equilibrium of the $[H_2, N_2, NH_3, Ar]$ -mixture at temperature, T, and pressure, P is found when component chemical potentials of the vapour and liquid phases are identical,

$$0 = \mu_i^g(T, P, n^g) - \mu_i^l(T, P, n^l), \tag{D.1}$$

The chemical potentials of the gas and liquid mixtures are calculated using the Peng-Robinson equation of state using the thermodynamic tool Thermolib (Ritschel et al., 2016, 2017). This requires providing the binary interaction parameters, k_{ij} for the liquid interactions in the matrix.

$$K = \begin{bmatrix} 0 & k_{\text{H}_2, \text{N}_2} & k_{\text{H}_2, \text{NH}_3} & k_{\text{H}_2, \text{Ar}} \\ k_{\text{N}_2, \text{H}_2} & 0 & k_{\text{N}_2, \text{NH}_3} & k_{\text{N}_2, \text{Ar}} \\ k_{\text{NH}_3, \text{H}_2} & k_{\text{NH}_3, \text{N}_2} & 0 & k_{\text{NH}_3, \text{Ar}} \\ k_{\text{Ar}, \text{H}_2} & k_{\text{Ar}, \text{N}_2} & k_{\text{Ar}, \text{NH}_3} & 0 \end{bmatrix} = \begin{bmatrix} 0 & 0 & 0.32 & 0 \\ 0 & 0 & 0.21 & 0 \\ 0.32 & 0.21 & 0 & 0.30 \\ 0 & 0 & 0.30 & 0 \end{bmatrix}$$
 (D.2)

The values of the binary interaction parameters are estimated by solving the equilibrium and minimising the error to experimental data. It is assumed, that the light components (H₂, N₂, Ar) are sufficiently dilute in the liquid mixture that the binary interactions between the light components can be neglected. Therefore, the binary interaction matrix only contains values on the 3rd row and column, representing the interactions with ammonia. Appl (2006) provides data for the [H₂, N₂, NH₃]-equilibrium at a range of temperatures and pressures. The equilibrium is for a mixture with overall composition of 3:1 hydrogen to nitrogen and around 50% ammonia. Data for the Ar-NH₃ equilibrium is obtained from Michels et al. (1961). The experimental solubility data (X) for H₂, N₂, and Ar are provided in Figure D.1 along with the simulated equilibrium data (-). The simulated equilibrium data match the experimental data relatively well, with some minor deviations. However, especially in the relevant range ($T \in [280 \text{ K}; 320 \text{ K}]$ and $P \in [10 \text{ MPa}; 25 \text{ MPa}]$), the simulated VLE agrees very well with the provided data. Note, the data for Ar-NH₃ equilibrium (Figure D.1d) displays the pressure on the x-axis, which was chosen because the experimental equilibrium data were only reported for three temperatures.

Interestingly, the liquid mole fraction of the light component in ammonia increases with temperature. This is the opposite of typical behaviour for the solubility of lighter components in a less volatile medium. However, this phenomenon is well documented in the literature and has been attributed to non-ideal interactions between the solute and ammonia (Wiebe and Tremearne, 1934; Sawant et al., 2006).

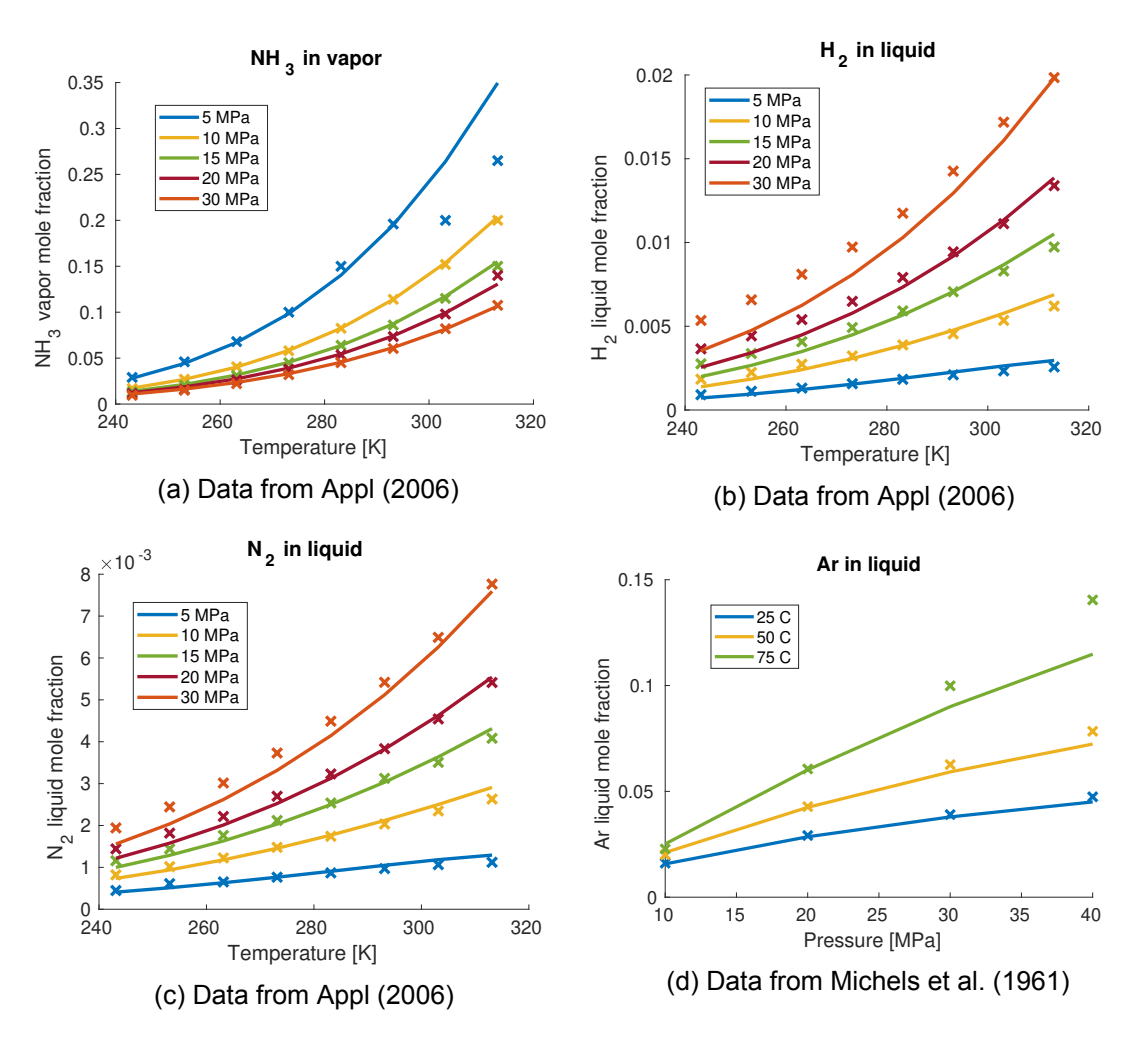


Figure D.1: Simulated vapour-liquid equilibrium (-) and experimental data (x) for the $[H_2, N_2, NH_3, Ar]$ -system. Data from Appl (2006) and Michels et al. (1961).

Appendix E

Influence of catalyst activity on synthesis loop power

In recent decades, substantial research has focused on alternatives to the traditional iron-based catalysts used in ammonia synthesis. Among these, ruthenium (Ru)-based catalysts have attracted particular attention due to their much higher intrinsic activity. Several studies report that Ru catalysts can be up to an order of magnitude more active than iron, and in some cases exhibit 10–20 times higher activity under comparable conditions (Vieri et al., 2023; El-Shafie et al., 2024; Osozawa et al., 2022). This high activity suggests the potential for significantly lower operating pressures and temperatures, thereby improving the overall electrical energy efficiency of ammonia production. Improved power efficiency is naturally interesting for PtA, where electrical power is the direct feedstock.

However, Ru catalysts also face important drawbacks. Ruthenium is a scarce and expensive noble metal, making large-scale deployment economically challenging. Furthermore, Ru catalysts are highly sensitive to poisoning by trace impurities and to hydrogen inhibition, often requiring under-stoichiometric operating conditions to maintain activity (Tripodi et al., 2021). These challenges currently limit their adoption compared to the more robust and well-established iron-based systems.

In this appendix, the influence of increased catalyst activity on the power consumption of the HB synthesis loop is investigated. Figure E.1 shows the optimal loop power demand as a function of catalyst activity, $\alpha \in [0.1,100]$, relative to the nominal reaction rate applied in this work. At low activity ($\alpha=0.1$), the HB-loop requires approximately 4.0 MW, decreasing to 2.4 MW at nominal activity ($\alpha=1$) and 1.8 MW at very high activity ($\alpha=100$). The main reduction is linked to the lower optimum loop pressure (Figure E.2a), which reduces feed compression work. Note, for low catalyst activity, the optimal pressure is at the upper constraint of 300 bar. The reduction in HB-loop power quickly levels off, reaching a plateau once the relative catalyst activity exceeds about $\alpha=10$. Beyond this point, the decrease in feed compressor power achieved by lowering the loop pressure is offset by higher energy demand in the recycle compressor. Operating at reduced pressure also lowers the per-pass conversion, which increases the recycle flow rate. In addition, the larger volumetric flow at lower pressure causes higher pressure drops across the synthesis loop, further balancing out the potential energy savings.

Figure E.2b illustrates that the optimal reactor feed temperature does not fall below 510 K. This limit corresponds to the temperature of steam generated in the Rankine cycle. If the feed temperature drops below this threshold, the reaction heat cannot be fully utilised for steam generation, explaining the lower bound.

Although a detailed economic analysis of catalyst materials lies beyond the scope of this thesis, the potential power savings from increased activity appear modest once above $\alpha \approx 10$. Nevertheless, higher activity can also reduce the required catalyst volume, which may strengthen the economic case for advanced catalysts.

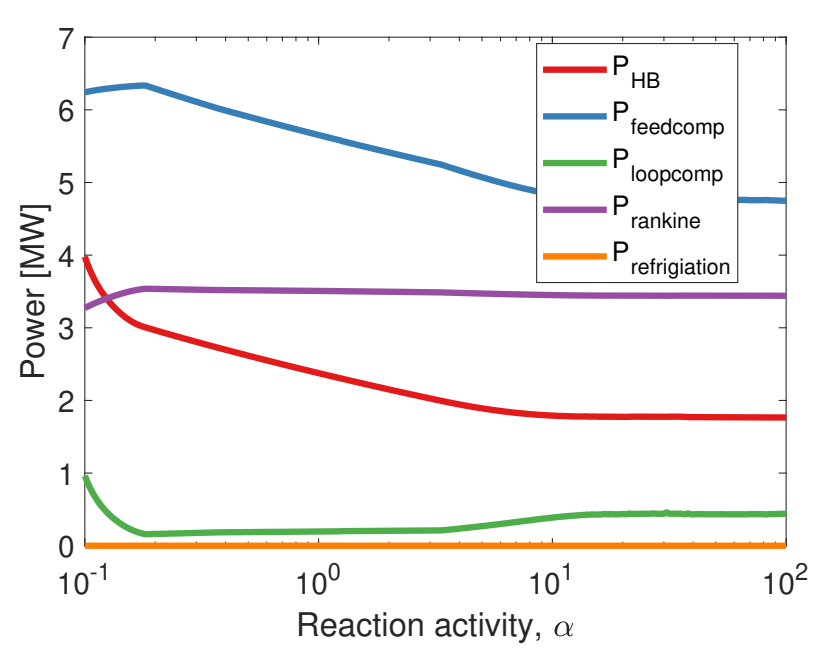


Figure E.1: Optimal distribution of the power utilities across the operating envelope from 10% to 120% of the nominal hydrogen feed flow.

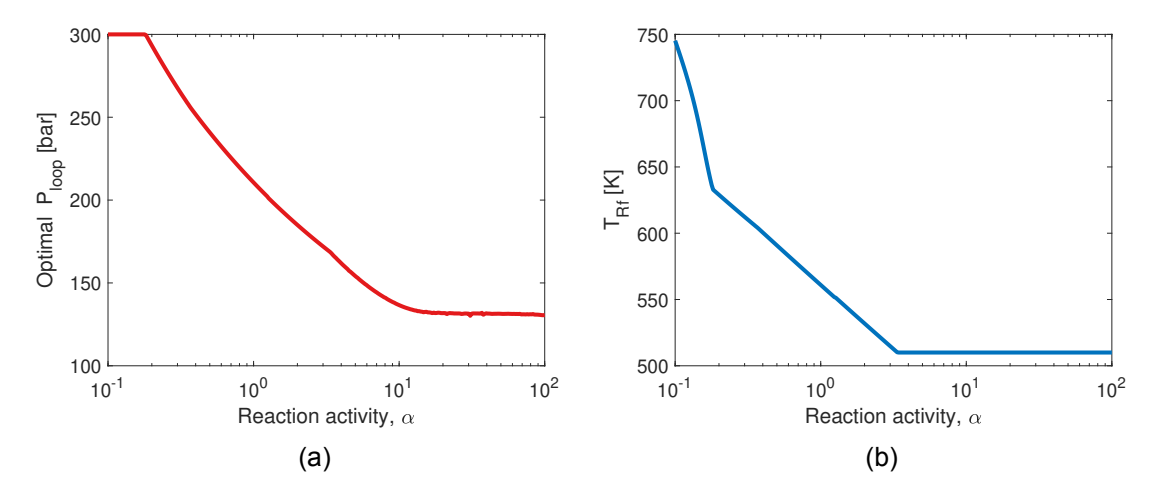


Figure E.2: a) Optimal loop pressure and b) reactor feed temperature as a function of catalyst activity.

Technical University of Denmark

Søltofts Plads, Building 228A 2800 Kgs. Lyngby Tlf. 4525 1700

www.kt.dtu.dk